University of Calgary

PRISM Repository **https://prism.ucalgary.ca**

The Vault Open Theses and Dissertations

2017

Effects of Nanopores on Carbon Dioxide Enhanced Oil Recovery in Tight Oil Reservoirs

Zhang, Kai

Zhang, K. (2017). Effects of Nanopores on Carbon Dioxide Enhanced Oil Recovery in Tight Oil Reservoirs (Doctoral thesis, University of Calgary, Calgary, Canada). Retrieved from https://prism.ucalgary.ca. doi:10.11575/PRISM/25829

http://hdl.handle.net/11023/3835

Downloaded from PRISM Repository, University of Calgary

UNIVERSITY OF CALGARY

Effects of Nanopores on Carbon Dioxide Enhanced Oil Recovery in Tight Oil Reservoirs

by

Kai Zhang

A THESIS

SUBMITTED TO THE FACULTY OF GRADUATE STUDIES

IN PARTIAL FULFILMENT OF THE REQUIREMENTS FOR THE

DEGREE OF DOCTOR OF PHILOSOPHY

GRADUATE PROGRAM IN CHEMICAL AND PETROLEUM ENGINEERING

CALGARY, ALBERTA

MAY, 2017

© Kai Zhang 2017

Abstract

Horizontal well drilling with multi-stage hydraulic fracturing is mainly applied in tight oil exploitation. In some tight carbonate reservoirs like Pekisko, acidizing is applied. The primary recovery factor, however, remains below 10% even with advanced technologies. Water flooding has also been proposed for tight oil development, but water can form a membrane up to 43 *nm*, which tremendously hinders water injectivity. A CO_2 miscible process seems a promising technique to enhance tight oil recovery.

The mechanism of CO_2-oil miscibility is the separation of oil molecules by the CO_2 introduced; van der Waals forces that hold the oil molecules together need to be overcome. The process is similar to the vaporization of a liquid. The energy added into the liquid is used to overcome the van der Waals forces that hold the molecules of the liquid together, separate the liquid molecules and split them into the gas phase.

In a nanoscale pore medium, variations in molecular orientation and molecules arrangement result in an alteration in the van der Waals forces, thereby creating unique thermal dynamic properties. These contribute to changes in CO_2-oil miscibility compared to that in conventional reservoirs. At present, no systematical study addresses CO_2-oil miscibility in nanopores.

To unlock the mysteries of CO_2 in enhanced oil recovery (EOR) in nanopores, the interactions between nanopores and molecules are studied using armchair, a zig-zag carbon nanotube, cubic shape smooth and rough nano-channels, and nano-channels with a functional group OH. The molecules trajectory and potential energy can be recorded by molecular dynamics simulations. The

CO_2-oil miscibility in nanopores is further presented including phase equilibrium, vaporizing and condensing drive, immiscible and miscible processes, and solubility parameters. The nanopore effect can be applied in screening candidate reservoirs for CO_2 flooding and in selecting CO_2 parameters by reservoir simulations.

The thesis can be very revealing to researchers in the area of CO_2-oil miscibility in nanopores.

Acknowledgements

I am privileged to have worked in the Reservoir Simulation Group. I am grateful to my supervisor Dr. Zhangxing (John) Chen for his supervision, guidance and support during my PhD studies at the University of Calgary. I also thank: Dr. Nancy Chen, Dr. Jalel Azaiez, Dr. Robert Gordon Moore, Dr. David Eaton, Dr. Keliu Wu and Mr. Gary Jing from the University of Calgary; Dr. Ole Torsæter from the Norwegian University of Science and Technology; Dr. Shirish Patil from the King Fahd University of Petroleum and Minerals and Mr. Jun Hu from Baker Hughes for their suggestions and review of this thesis.

I am grateful to everyone in the Reservoir Simulation Group in the Department of Chemical and Petroleum Engineering, the University of Calgary for providing a positive, supportive environment, conductive to my area of study.

The research is partly supported by NSERC/AIEES/Foundation CMG, AITF (iCore), IBM Thomas J. Watson Research Center, and the Frank and Sarah Meyer FCMG Collaboration Center for Visualization and Simulation.

Finally, I would like to thank my family for their support and love.

I was grabbed as a child, and released as a man.

Table of Content

Chapter 1. Introduction 1

1.1. Literature Review for CO_2 Enhanced Oil Recovery 1

1.2 Literature Review for Effects of Nanopores 2

1.3 Objective 3

1.4 Effects of Nanoscale Pores on CO_2 EOR Process 3

1.5 Application of Nanoscale Pore Effects to CO_2 EOR Process 5

1.6 Structure of Thesis 5

1.7 Novelty of the Thesis 8

Chapter 2. What Makes Tight Oil Different? 10

2.1 Background of Tight Oil Resources 10

2.2 Production Characteristics of Tight Oil Exploitation 14

2.3 Effects of Confinement 23

2.4 Effects of Nanoscale Pore Confinement on Multi-components Phase Equilibrium 28

Chapter 3. Effects of Nanoscale Pore Confinement on CO_2 Injection in Tight Oil Reservoirs 55

3.1 Effects of Nanoscale Pore Confinement on the CO_2 Injection Process 70

3.2 Effects of Nanoscale Pore Confinement on CO_2 Minimum Miscibility Pressure 89

3.3 Correlation and Prediction of MMP for CO_2 Injection in Nanopores 95

3.4 Effects of Nanoscale Pore Confinement on CO_2 Immiscible and Miscible Flooding ... 105

3.5 Effects of Nanoscale Pore Confinement on Relative Permeability Alteration during CO_2

Flooding 114

3.6 Applications 119

Chapter 4. Reservoir Models 121

Chapter 5. Integrated Method to Screen CO_2 Flooding for Tight Oil Reservoirs 127

5.1 Least Squares Method 128

5.2 Reservoir Simulation 132

5.3 Fuzzy Analytical Hierarchy Process 134

5.4 Ranking Candidate Reservoirs 136

5.5 Pros and Cons 143

Chapter 6. CO_2 Parameters Selection 145

6.1 CO_2 Operation Pressure 145

6.2 Pure or Impure Gas 153

Chapter 7. CO_2 Performance Improvement 157

7.1 Water Alternating CO_2 Flooding 161

7.2. Nanofluid Alternating CO_2 Flooding 168

Chapter 8. Conclusions and Future work 187

References 204

Appendix A: Phase Behavior 230

Appendix B: Molecular Dynamics 237

Appendix C: Reservoir Simulation 243

List of Figures

Figure 1. 1 Structure of Thesis 7

Figure 1. 2 Previous Study on Phase Equilibrium in Pore Scale 9

Figure 1. 3 Novelty of the Thesis 9

Figure 2. 1 Tight Oil Exploitation (Laredo Energy, 2017) 13

Figure 2. 2 Fluid Level Alteration during a Swab Test (Zhang, 2015) 15

Figure 2. 3 Transition Zone for Convention and Tight Oil Reservoirs (Zhang, 2015) 16

Figure 2. 4 Water Cut at 1st Month and 36th Month for Cardium Sandstone Reservoir (Zhang, 2015) 17

Figure 2. 5 Water Cut at 1st Month and 36th Month for Pekisko Limestone Reservoir (Zhang, 2015) 18

Figure 2.6 Oil Production Profiles (Zhang, 2015) 19

Figure 2. 7 Idealized Stages in GOR History of a Multi-stage Fractured Horizontal Well (Steven, 2016) 20

Figure 2.8 Fluid Injection in Conventional (Left) and Tight Oil Reservoirs (Right) 21

Figure 2.9 Molecules and Reservoir Scale (Nelson, 2009) 23

Figure 2.10 Core Porosity vs. Permeability Cross Plot for Well 04-32-047-10W5 (Nicholas, 2015) 24

Figure 2.11 Plot of Pore Type vs. Depth for Well 04-32-047-10W5 (Nicholas, 2015) 24

Figure 2. 12 C_2H_6 Molecule Orientation Alteration (Zhang, 2016) 25

Figure 2. 13 Energy of C_2H_6 in a Nanotube (Zhang, 2016) 26

Figure 2.14 Molecular Orientation in Bulk System and Confined System (Pitakbunkate, 2015) 27

Figure 2.15 Fluid Molecules in a Nanopore (Jensen, 1997) 27

Figure 2.16 Effect of Pore Size on the CO_2 Density Distribution (Liu, 2012) 28

Figure 2.17 Reservoir Fluid Phase Envelop (Zhang, 2016) 36

Figure 2.18 Critical Pressure Alteration with Confinement (Zhang, 2016) 37

Figure 2.19 Critical Temperature Alteration with Confinement (Zhang, 2016) 38

Figure 2.20 Fluid Enthalpy (Zhang, 2016) 39

Figure 2.21 Flash Calculation of a Fluid Sample (Zhang, 2016) 40

Figure 2.22 Effect of Confinement at Various Pore Radii on Phase Envelope (Zhang, 2016) 41

Figure 2.23 Fugacity of Light and Heavier Components (Zhang, 2016) 42

Figure 2.24 Phase Envelope of Equilibrium Composition (Zhang, 2016) 42

Figure 2.25 Total Energy of CH_4 or C_2H_6 in Nanotube (Zhang, 2016) 43

Figure 2.26 Hydrocarbons Coexist in Nanopores (Zhang, 2016) 44

Figure 2.27 CH_4 in Nanotubes (Zhang, 2016) 45

Figure 2.28 Schematic View of Rebounds of Gas Molecules on Solid Surface (Shindo, 1983) .. 46

Figure 2.29 Schematic View of Collision and Rebound for Molecules in Gas-Phase Flow Influenced by Surface Potential Energy (Shindo, 1983) 47

Figure 2. 30 Armchair Nanotube (Left) vs. Zig-zag Arrangement of Carbon Nanotube (Right), the Grey Atoms Represent the Carbon and the White Molecules are Hydrogens. 48

Figure 2. 31 Example for the Nano-Cube (Left) vs. Rough Nano-Cube (Middle) vs. Rough Nano-Cube with Functional Group (Right), the Red Molecules are Functional Group OH. 51

Figure 3.1 Relative Oil Volume vs Pressure at 144° *F*, West Texas Fluid (Holm, 1974) 61

Figure 3. 2 CO_2 Drive Mechanisms Illustration (Zhang, 2016) 62

Figure 3.3 The Vaporizing Gas Drive Process (Martin, 1982) 63

Figure 3.4 The Condensing Gas Drive Process (Martin, 1982)..... 65

Figure 3.5 Change in Volume of Mead Strawn Stock Tank Oil (Holm, 1974)..... 67

Figure 3.6 Pseudo-ternary Diagram (Martin, 1982) 68

Figure 3.7 The Impact of CO_2 Concentration on Phase Envelope (Zhang, 2015)..... 71

Figure 3. 8 Phase Envelope Alteration with Effects of CO_2 Injection and Confinement (Zhang, 2015) 72

Figure 3.9 Process Path for CO_2 Injection in Conventional and Tight Oil Reservoirs (Zhang, 2015) 73

Figure 3.10 Phase Envelope for Reservoir Fluid Contacts with 20% CO_2 (Zhang, 2016) 74

Figure 3. 11 Vaporizing Gas Drive (Zhang, 2016)..... 76

Figure 3.12 Condensing Gas Drive (Zhang, 2016)..... 76

Figure 3.13 Pseudo-ternary Representation of Multi-contact Vaporizing and Condensing Drive (Zhang, 2016)..... 78

Figure 3.14 Molecular Dispersion in Bulk System (Left) and Confined System (Right) (Zhang, 2016) 78

Figure 3.15 Phase Viscosity with Confinement Effect (Zhang, 2016) 79

Figure 3.16 Liquid-vapor Viscosity Ratio (Zhang, 2016)..... 80

Figure 3.17 Liquid-vapor Viscosity Ratio at Various Radii (Zhang, 2016)..... 80

Figure 3. 18 Gas-oil Interface at Very Low Gas Injection Rate (Left) and Very High Gas Injection Rate (Right) (Kleppe, 2016) 81

Figure 3.19 Dietz Analysis (Hawthorne, 1960) 82

Figure 3.20 Threshold Velocity for Stable Displacement (Zhang, 2016) 84

Figure 3. 21 Threshold Velocity for Stable CO_2 Displacement at Various Radii (Zhang, 2016).. 85

Figure 3. 22 Viscous Finger Illustration (Perkins, 1965)..... 86

Figure 3.23 Growth of Fingers (Zhang, 2016)..... 88

Figure 3. 24 Growth of Fingers with Confinement Effect (Zhang, 2016)..... 88

Figure 3.25 Slim Tube Displacements at Various Pressures (Wu, 1990)..... 90

Figure 3. 26 Miscibility vs. Vaporization Process 91

Figure 3.27 Solubility Parameters with the Confinement Effect (Zhang, 2016)..... 93

Figure 3.28 Semi-analytical Methods to Evaluate CO_2 MMP (Zhang, 2016)..... 94

Figure 3.29 Density of CO_2 Required for Miscible Displacement (Holm, 1982) 97

Figure 3. 30 CO_2 Flooding Schematic (Zhang, 2016) 106

Figure 3.31 Gas-oil Interfacial Tension versus Pore Radius (Zhang, 2016).....111

Figure 3.32 Remaining Oil Saturation in Immiscible Zone (Zhang, 2016).....112

Figure 3. 33 Immiscible Zone Length Reduction (Zhang, 2016) 113

Figure 3.34 Relative Permeability Alteration during CO_2 Injection with Confinement Effect (Zhang, 2016).....116

Figure 3.35 Contact Angle Hysteresis (Zhang, 2016).....117

Figure 3.36 Relative Permeability with Hysteresis (Zhang, 2016).....119

Figure 4. 1 Permeability Distribution for Reservoir Models 122

Figure 4. 2 Reservoir Fluid Composition 123

Figure 4. 3 Permeability in Fractures Varies with Distance to Wellbore 124

Figure 4. 4 Initial Water Saturation Configuration 124

Figure 4. 5 Pressure Dependent Rock Compaction for Hydraulic Fractures..... 125

Figure 4. 6 Hydraulic Fracturing Distribution 125

Figure 5. 1 Reservoir Simulations for Base Model (Zhang, 2015)..... 134

Figure 5. 2 Reservoir Fluids Composition (Zhang, 2015) 138

Figure 5. 3 CO_2 Flooding Reservoir Simulation for Reservoir 1 (Zhang, 2015)..... 141

Figure 5. 4 Solid Precipitation Prediction (Zhang, 2015)..... 142

Figure 5. 5 Screen for Asphaltene Precipitation (Boer, 1995) 143

Figure 6. 1 Oil Recovery Factor with Various CO_2 Operation Conditions (Zhang, 2015)..... 147

Figure 6. 2 Liquid-vapor Viscosity Ratio (Zhang, 2016)..... 148

Figure 6. 3 Oil Production for CO_2 Near-miscible and Miscible Process with 50 *nm* Pores (Zhang, 2015) 149

Figure 6. 4 CO_2 Injection for Near-miscible and Miscible Process with 50 *nm* Pores (Zhang, 2015)

..... 150

Figure 6. 5 Oil Production for CO_2 Near-miscible and Miscible Process with 10 *nm* Pores (Zhang, 2015) 151

Figure 6. 6 CO_2 Injection for Near-miscible and Miscible Process with 10 *nm* Pores (Zhang, 2015) 152

Figure 6. 7 Gas Injection Field Experience (Christensen, 1998) 153

Figure 6. 8 Diffusion Coefficient at Different Pore Pressure (Wu, 2015) 154

Figure 6. 9 Impure CO_2 MMP and Flooding Performance (Zhang, 2015) 156

Figure 7. 1 Typical Behavior of Relationships for Mobilization of Residual Oil (Lake, 1989) . 158

Figure 7. 2 Cumulative Oil Production versus Different Parameters 159

Figure 7. 3 Gas Saturation Profile during CO_2 Injection 161

Figure 7. 4 WAG Cycle Length Investigations 162

Figure 7. 5 WAG Performance 164

Figure 7. 6 Fluid Zone Illustration in Analytical Model (Jenkins, 1984) 167

Figure 7. 7 Zone Boundaries for Different VGR in a Rectangular Homogeneous Reservoir. (Jenkins, 1984) 168

Figure 7. 8 Nanoparticle Structuring in the Wedge Film (Kondiparty, 2012) 170

Figure 7. 9 Pressure on the Walls of Wedge for 0.5°Contact Angle at the Vertex as a Function of Radial Distance (Kondiparty, 2012) 171

Figure 7. 10 Multiple Relative Permeability Sets (Zhang, 2015) 180

Figure 7. 11 Nanofluids Concentration in a Reservoir after 3 Years' Injection for Homogeneous (left) and Heterogonous (right) Model (Zhang, 2015)..... 181

Figure 7. 12 Nanofluids Concentration in Reservoir after 3 Years' Injection for Matrix (left) and Fracture (right) in Dual Porosity Model (Zhang, 2015) 183

Figure 7. 13 Cumulative Oil Production for Homogeneous Model (Zhang, 2015)..... 184

Figure 7. 14 Cumulative Oil Production for Heterogeneous System (Zhang, 2015) 184

Figure 7. 15 Cumulative Oil Production for Dual Porosity Model (Zhang, 2015)..... 185

Figure 7. 16 Countercurrent Flow vs. Cocurrent Flow during Water Flooding (Zhang, 2015).. 186

Figure 8. 1 Armchair Nanotube (Left) vs. Zig-zag Arrangement of Carbon Nanotube (Right); the Grey Atoms Represent the Carbon and the White Molecules are Hydrogens. 189

Figure 8. 2 Mean Square Displacement in a Nanotube 190

Figure 8. 3 Diffusion in a Nanotube 191

Figure 8. 4 Surface Roughness Variation in the Nano-channel 192

Figure 8. 5 Mean Square Displacement in a Nano-channel..... 193

Figure 8. 6 Diffusion in a Nano-channel 194

Figure 8. 7 Mean Square Displacement in Smooth and Rough Pore Walls (Sofos, 2010)..... 195

Figure 8. 8 Diffusion Coefficient of Pore Wall Roughness (Sofos, 2010)..... 195

Figure 8. 9 Diffusion Coefficient in Smooth and Rough Pore Walls (Sofos, 2010)..... 196

Figure 8. 10 Energy Difference in Smooth Nano-channel..... 197

Figure 8. 11 Energy Difference in Rough Nano-channel 198

Figure 8. 12 Functional Group OH in the Rough Nano-channel 199

Figure 8. 13 Mean Square Displacement in the Rough Nano-channel with Functional Group OH 200

Figure 8. 14 Diffusion in the Rough Nano-channel with Functional Group OH..... 201

Figure 8. 15 Pore Connections 202

Figure A. 1 Gibbs Energy Surface for a Binary System (Curtis, 2000)..... 233

Figure C. 1 Knudsen Number of Reservoir Gas 244

Figure C. 2 Knudsen Number of Equilibrium Gas during CO2 Flooding..... 245

Figure C. 3 Reynolds Number of Reservoir Oil 246

Figure C. 4 Reynolds Number of Equilibrium Oil during CO2 Flooding 246

List of Table

Table 2. 1 Recombined Bottom Sample Analysis (Zhang, 2016) 33

Table 2. 2 Parachors for Pure Components and Compound Groups (Curtis, 2000) 34

Table 2. 3 Molecules Movement in Armchair Nanotube (Zhang, 2016) 49

Table 2. 4. Molecules Movement in Zig-zag Nanotube 50

Table 2. 5 Molecular Movement in Nano-cube 52

Table 2. 6 Molecular Movement in Rough Nano-cube 52

Table 2. 7 Molecular Movement in Rough Nano-cube with Functional Group 53

Table 3. 1 Field Case of CO2 Flooding (Leena, 2008) 56

Table 3. 2 CO2 Minimum Miscible Pressure versus Various Pore Radius (Zhang, 2015) 94

Table 3. 3 Common CO2 MMP Correlations (Zhang, 2016) 98

Table 3. 4 Live Oil Samples (Ghaderi, 2012; Teklu, 2014) 102

Table 3. 5 CO2 MMP Correlation Validation for Each Category (Zhang, 2016) 103

Table 3. 6 CO2 MMP Correlation Validation for Nanoscale Pore (Zhang, 2016) 104

Table 3. 7 Reference Parameters for the Immiscible/Miscible Process Calculation 110

Table 4. 1 Reservoir Properties (Zhang, 2015) 121

Table 4. 2 Hydraulic Fracturing Properties (Zhang, 2015) 126

Table 5. 1 CO2 Miscible Flooding Checklist (Carcoana, 1982; Taber, 1983; Klins, 1984; Zhao, 2001; Bachu, 2004; Zhang, 2009) 128

Table 5. 2 Scale for Two Properties Comparison (Zhang, 2000) 131

Table 5. 3 Relative Significance Matrix 132

Table 5. 4 Candidate Reservoirs for CO2 Screen Process (Zhang, 2015) 137

Table 5. 5 Weight for Each Property (Zhang, 2015) 139

Table 5. 6 Grades for Candidate Reservoirs (Zhang, 2015) 139

Table 6. 1 Impure Gas MMP (Zhang, 2015) 156

Table 7. 1 Pros and Cons of CO2 Flooding 157

Table 7. 2 Various Scenarios for WAG Cycle Length 162

Table 7. 3 WAG Ratio Investigation for Reservoir 1 163

Table 7. 4 Density and Viscosity Measurement (Anne, 2013) 173

Table 7. 5 Oil/Water Contact Angle Measurement (Manrique, 2010) 174

Table 7. 6 Interfacial Tension Reduction by Nanoparticles (Gunnar, 2014) 175

Table 7. 7 Berea Sandstone Core Flooding Summary (Gunnar, 2014) 176

Table 7. 8 Porosity and Permeability Measurement Scenarios (Anne, 2013) 177

Table 7. 9 Porosity and Permeability Measurement (Anne, 2013) 178

Table 7. 10 Permeability Modification Based on Nanoparticle Concentration (Zhang, 2015) .. 182

Table B. 1 Sample Models Description 239

Table B. 2 Force-Field Parameters for MM2 (Allinger,1977): 240

Table B. 3 Reference Parameters for Molecular Interaction (Liu. 2016) 242

Nomenclature

$a^* b^*$	EOS constants
a_0	Capillary force term
$a - e$	Constant, for a in **Equation (5.10)**, $0 < a \leq 0.5$
a_{adj}	Adjusted parameter
α	Angle between interface and horizontal plane
a_{ij}	Base matrix
α_j	The slope for parameter *j*
A_{ij}	Varying parameters
A_1	Coefficient, a function of pressure, A_1 =1 at $p=p_{sc}$ and A_1=0 at $p=p_k$.
A_2	Coefficient, ranging from 0.5 to 0.8
A_p	$\pi(r_p/\sigma)^2$, transversal section area of the pore
A	Cross section of the core (ft^2)
AB	Length from A to B
b_{adj}	Adjusted parameter
b_0	Gravity force term
b_{ij}	Decisive matrix
β	Angle between interface and layer
B_{ob}	Oil formation volume factor at bubble point pressure (*STB/Bbl*)
c_0	The ratio of gravity force to capillary force

c_i	Quantity term
C1-C7	Mole fraction
CD	Length from C to D
d_p	Particle diameter, *(ft)*
D_o	Molecular diffusion coefficient, (ft^2/s)
Ej	Information term
$\mathrm{E_{tot}}$	Total oil recovery efficiency, based on original oil in place
$\mathrm{E_{wf}}$	Recovery efficiency of waterflood only based on OOIP
$\mathrm{E_s}$	Energy variation by stretching
$\mathrm{E_\theta}$	Energy variation by bending
$\mathrm{E_{s\theta}}$	Energy variation by stretching-bending
$\mathrm{E_{\theta_t}}$	Energy variation by torsion
$\mathrm{E_{ij}}$	Energy variation by van der Waals
E_t	Total Energy
f_w	Fraction of mixture that is water
$\mathrm{f_g}$	Fraction of mixture that is gas. Note that $\frac{\mathrm{f_w}}{\mathrm{f_g}} = \mathrm{WAG}$ ratio
F_v	Vapor fraction
F_g	Gas term for recombining analysis
F	Formation electrical resistivity factor
g	Gravity (ft^2/s)

h	Total reservoir height, (*ft*)
h_w	Height of the water zone, *(ft)*
h_m	Height of the mixture zone, *(ft)*
h_g	Height of the gas zone, *(ft)*
$H(w)$	The squares of weight errors
H	Height of the medium, (*ft*)
hBp	Terms for bubble point pressure
hDp	Terms for bubble point pressure and dew point pressure
ΔH	Heat of vaporization
i	Candidate reservoirs *i*, ranging from 1 to *n*
j	Specific property
k'_{ro}	Oil relative permeability
k'_{rg}	Gas relative permeability
k	Permeability, *(md)*
k_w	Effective permeability of the wetting phase
k_{nw}	Effective permeability of the nonwetting phase
k_V	Vertical permeability of reservoir, (*md*)
k_B	Boltzmann constant
k_s	Stretching Coefficient
k_θ	Bending Coefficient

$k_{s\theta}$	Stretching-Bending Coefficient
K_i	K-value for each component
L_c	Length of the core (*ft*)
L_{im}	Immiscible portion length
L_m	Miscible portion length
L_t	Total CO_2 flux portion length
L_z	Pore length
L	Length of the fingered region in a linear system, (*ft)*
L_r	Length of reservoir, *(ft)*
L_G	Distance in reservoir at which segregation is complete, (*ft)*
m	Number of reference experts based on **Table 5.1**, *m* is 5 in this case.
M	Molecular weight, subscript C_{7+} represents hydrocarbons above C7+
M_l	Mobility ratio for the linear system
M_e	The endpoint mobility ratio
M_w	Mobility of wetting phase
M_{nw}	Mobility of nonwetting phase
M_{eff}	Effective mobility
MMP	CO_2 minimum miscibility pressure (*psi*)
M_{gm}	Ratio: gas mobility in gas zone to gas mobility in mixture zone
M_{gw}	Ratio: gas mobility in gas zone to water mobility in water zone

n	Number of properties
N_{ge}	The endpoint gravity number
N_{wt}	Cumulative volume of wetting phase get into the core
N	Number of particles
N_B^{-1}	The inverse bond number
N_i	Amount of oil originally in place, *(Bbl)*
N_{wf}	Oil produced up to the end of waterflood, *(Bbl)*
N_{WAG}	Oil produced up to the end of WAG flood, *(Bbl/day)*
p_w	Pressure of the wetting phase
p_{nw}	Pressure of the nonwetting phase
p_{nw}	Pressure of the nonwetting phase
p_w	Pressure of the wetting phase
p_c	Capillary pressure
p_{zz}	Axial pressure
p	Pressure
P_i	Parachors
P_{ci}	Critical pressure
P_k	Convergence pressure
P_{ri}	Reduced pressure
P_{cp}	Pore critical pressure (*psi*)

P_{cb}	Bulk critical pressure (*psi*)
P_b	Bubble point pressure (*psi*)
P_A	Pressure at point A
P_B	Pressure at point B
P_C	Pressure at point C
P_D	Pressure at point D
P_{go}	Gas oil capillary pressure
P_{ow}	Oil water capillary pressure
ΔP_c^*	Relative critical pressure shift (dimensionless)
P_{ij}	Each property j of the reservoir *i*
P_r	A reference value given by experts for property *j*
p_{ij}	Normalized matrix
P_{oj}	Optimistic value in property *j* refer to oil production Q_{oil} or CO_2 utilization
P_{wj}	Worst value in property *j* refer to oil production Q_{oil} or CO_2 utilization
$q_i \ \ q_j$	The charges of atoms *i* and *j*, respectively
q	Flow rate
q_t	Total flow rate, *(Bbl/day)*
q_g	Flow rate in the gas zone, *(Bbl/day)*
q_m	Flow rate in the mixture zone, *(Bbl/day)*
q_w	Flow rate in the water zone, *(Bbl/day)*

r_p	Pore throat radius (nm)
r_{ij}	Separation between two atoms i and j
r_j	Relative significance matrix
R_s	Gas oil ratio
R	Gas constant
R_t	Total recovery
R_{im}	Recovery in the immiscible portion of the displacement
R_m	Recovery in the miscible portion of the displacement
R_g	The final grade for reservoirs
R_0	Recovery
R^*	Normalized recovery
S_{orm}	Residue oil saturation during CO_2 flooding
S_{orw}	Residue oil saturation during water flooding
S_{wf}	Wetting saturation at flux front
S_{wi}	Initial water saturation
t	Flux time (s)
t_d	Dimensionless time
T	Temperature
T_{cb}	Bulk critical temperature (F)
T_{cp}	Pore critical temperature (F)

T_{ri}	Reduced temperature
ΔT_c^*	Relative critical temperature shift (dimensionless)
u_{ginj}	Maximum fluid velocity
U	Average velocity, (*ft/s)*
U_f	Velocity of forward projecting finger, (*ft/s)*
U_b	Velocity of the backward-projecting finger, (*ft/s)*
v_w	Volumetric fluxes of the wetting phase
v_{nw}	Volumetric fluxes of the nonwetting phase
v	Molar volume
v_c	Bulk critical specific volume
v_{cp}	Pore critical specific volume
V	Volume, subscript $\bar{g}, \bar{o}$ represents gas and oil term at the standard condition
V_1, V_2, V_3	Torsion Coefficient
V_p	$A_p L_z$, volume of the pore
VGR	Viscosity- gravity ratio
V_{oj}	Oil production Q_{oil} or CO_2 utilization for optimistic case
V_{wj}	Oil production Q_{oil} or CO_2 utilization for worst case
w_j	Weight for each property j
w	Weight fractions
ω_i	Acentric factor

WAG	Water- gas ratio of injection mixture
W	Width of reservoir, *(ft)*
W_{ij}	Weighted grading matrix
W_o	The weighted matrix using the optimistic value for each property *j*
x_i	Liquid composition
x_f	Position of the flux front
Δx	Distance between A and D or B and C
x	Distance along reservoir, *(ft)*
X_b	Distance traveled by the backward-projecting finger, (*ft)*
X_f	Distance traveled by the forward-projecting finger, (*ft)*
X_o	Mean distance at which fingers are initiated, (*ft)*
X_m	Mean invaded distance, (*ft)*
X	Distance measured from original position of an interface, (*ft)*
X_{ij}	Normalized parameter
y_i	Gas composition
Y_l	Width of a transverse mixed zone in a linear system, (*ft)*
z_i	Mixture composition
Δz	Thickness of layer, the distance between A and B or C and D

Greek Letter

γ	Gas specific gravity (dimensionless)

ρ	Density
ρ_r	Reduced density
$\rho_r(liq)$	Reduced density of the gas compressed to a liquid state
ρ_w	Density of the wetting phase
ρ_{nw}	Density of the nonwetting phase
$\Delta\rho$	Density difference between wetting and nonwetting phase
ε_{ij}	Lennard-Jones potential well depth
σ_{ij}	The distance at which the intermolecular potential between two particles is zero
σ_{go}	Interfacial tension (IFT) (*dyne/cm*)
σ	A measure of the inhomogeneity of a particle pack
σ_{LJ}	Lennard-Jones size parameter (the collision diameter in *nm*)
δ	Solubility Parameters
θ	Time, (*s)*
ϕ	Porosity, (fraction)
μ	Viscosity, (*cp)*
μ_w	Viscosity of the wetting phase
μ_{nw}	Viscosity of the nonwetting phase
λ	Lagrangian multiplier
λ_{gg}	Gas relative mobility in gas zone
λ_{gm}	Gas relative mobility in mixture zone

λ_{wm}	Water relative mobility in mixture zone
λ_{ww}	Water relative mobility in water zone

SI Metric Conversion Factors

ft	0.3048 m
API	$\frac{141.5}{\text{specific gravity}} - 131.5$
Bbl	0.158987 m^3
°F	$1.8K - 459.67$
lb	0.4536 *kg*
fs	10^{-15} *s*
ps	10^{-12} *s*
dyne	10^{-5} *N*
cm	10^{-2} *m*
psi	6894.75729 *Pa*
md	9.869233×10^{-16} m^2

Chapter 1. Introduction

1.1. Literature Review for CO_2 Enhanced Oil Recovery

The oil production rate in tight oil reservoirs highly depends on enlarging a contact area between a well and the target formation, improving oil relative permeability, reducing oil viscosity and altering wettability (Zhang, 2015). Since 1970, CO_2 flooding has been considered one of the most promising gas injection processes in the U.S. (Holm, 1976; Goodrich, 1980; Klins, 1984). Recovery mechanisms related to CO_2 flooding include a swelling effect, viscosity reduction, interfacial tension reduction and light components extraction (Pittaway, 1985). The CO_2 flooding process is regarded as a promising enhanced oil recovery (EOR) technique for tight oil reservoirs (Manrique, 2006). CO_2 in either a miscible or a near-miscible condition, contributes to better oil recovery as compared to a water flooding process (Shyeh, 1991; Hadlow, 1992; Bardon, 1994; Thomas, 1994; Dong, 2001; Sohrabi, 2005; Arshad, 2009; Bui, 2010; Ren, 2011; Tsau, 2014). Changing a well from water to gas injection, after a prolonged water cycle, can lead to a short-lived increment in production (Lake, 1989). In general, the WAG (water alternating gas) process provides higher oil recovery as compared to continuous water or gas injection (Wilson, 2014) and is a promising process to extract oil from a tight formation (Figuera, 2014). Wettability alteration is one of the main residual oil mobilizing mechanisms during the WAG process (Teklu, 2015).

Although many CO_2 field applications in low permeability reservoirs have been recorded as successful, a number of CO_2 injection trials in tight formations have proven to be uneconomic (Leena, 2008). The CO_2 EOR process in tight oil reservoirs needs to be investigated in detail to set

guidelines for screening candidate reservoirs and parameters.

1.2 Literature Review for Effects of Nanopores

Unlike conventional oil reservoirs, ultralow in-situ permeability is very common in tight oil reservoirs due to the huge chance that nanoscale pores exist. The common pore diameter is approximately 30 *nm* to 2,000 *nm* in tight sandstone reservoirs and 2 *nm* to 100 *nm* in shale reservoirs (Nelson, 2009). Many pore diameters are within 2 to 20 *nm* in shale reservoirs (Nagarajan, 2013) and 30 to 100 *nm* in sandstone reservoirs (Nicholas, 2015). Dominant pore radii of most shale reservoirs are smaller than 10 *nm* (Swami, 2012).

In such nanoscale pore media, variations in molecular orientation and molecules arrangement result in unique thermal dynamic properties (Pitakbunkate, 2015). This is caused by the geometric constraint limiting fluid molecules (Zarragoicoechea, 2002) and the interactions between surface walls and fluid molecules (Zhang, 2006). In these circumstances, the critical temperature and critical pressure of a pure component reduce as a pore size decreases (Morishige, 1997; Vishnyakov, 2001; Zarragoicoechea, 2004; Singh, 2009; Jana, 2009; Akkutlu, 2013; Pitakbunkate, 2014; Islam. 2015). For a nanoscale porous system, a two-phase region shrinks as compared to their bulk state (Ma, 2014; Wang, 2014; Sanaei, 2014; Rahmani, 2015) and the nanoscale pore confinement has a different effect on phase behavior in sandstone reservoirs with that in carbonate reservoirs because of the wettability variation (Teklu, 2013). The shrinkage in the phase diagram indicates that oil properties are altered as well (Ma, 2013; Jin, 2013; Ma, 2014; Qanbari, 2014; Xiong, 2014; Wang, 2014; Li, 2015; Jin, 2015). The bubble point pressure is depressed by

nanoscale pore confinement; thus, single phase production over extended periods is possible (Honarpour, 2012). The alteration in critical gas saturation by the pore confinement is proposed as well (Nagarajan, 2013; Khoshghadam, 2015). Furthermore, CO_2 minimum miscibility pressure (MMP) can be reduced with the consideration of nanoscale pore confinement (Teklu, 2013; Teklu, 2014; Teklu, 2014; Teklu, 2014).

Current research regarding a nanoscale pore effect focuses primarily on phase behavior alteration. No systematic study on a nanoscale pore effect on the CO_2 EOR process exists.

1.3 Objective

The objective of this research is to study the nanoscale pore effect on CO_2 EOR, which can help to accurately screen candidate tight oil reservoirs for CO_2 flooding, select CO_2 parameters and improve CO_2 performance.

1.4 Effects of Nanoscale Pores on CO_2 EOR Process

In Canada's Cardium tight sandstone and the Monteny liquid rich shale plays, horizontal wells with multistage hydraulic fracturing are the main method to extract the oil underground. In the Pekisko tight carbonate reservoir, the wells are partly vertical and partly horizontal with acidizing, and may or may not include hydraulic fracturing. However, tight oil reservoirs have a primary recovery of as low as 5.0-15.0% of original oil in place (OOIP) even with horizontal wells and massive hydraulic fracturing (Manrique, 2010).

Since water injection offers benefits for reservoir pressure maintenance and economic feasibility, a waterflooding process is proposed to improve tight oil recovery in previous

experimental and simulation work (Raju, 2004; Raju, 2005; Yong, 2012; Thomas, 2014). But water can form a membrane up to 43 *nm* in porous media; the critical pore size for water injection is around 90 *nm*, which can impair water injectivity in tight reservoirs (Yang, 2013). A CO_2 miscible flooding process is regarded as a primary enhanced oil recovery (EOR) technique for light oil reservoirs (Zhang, 2015) and a number of CO_2 field applications in low permeability reservoirs have been recorded as successful (Leena, 2008). Also, after water breakthrough in a producer, the CO_2 injection can still extract oil even at a very high water cut (Bui, 2010). Oil displaced by CO_2 can develop miscibility through the extraction of light hydrocarbon components into a CO_2-rich phase (Orr, 1981). A great change in gas-oil relative permeability occurs when the interfacial tension drops to 0.04 *dyne/cm* by the CO_2 miscible flooding (Longeron, 1980). CO_2 also contributes to a change in oil viscosity and oil swelling, resulting in improved oil recovery (Mohammed, 2006).

Since nanoscale pores are extensively distributed in tight formations, the associated confinement can affect component orientation and arrangement, resulting in a variation in hydrocarbon phase behavior (Teklu, 2013; Teklu, 2014). Taking the confinement effect into consideration, variations exist in the CO_2 EOR process between tight oil and conventional oil reservoirs.

In this study, the unique properties in tight oil reservoirs are investigated. The interactions between nanopores and molecules are studied by using Armchair, a Zig-zag carbon nanotube, cubic shape smooth and rough nano-channels, and nano-channels with a functional group –OH. The molecule's movement and potential energy can be studied through molecular dynamics

simulations. The CO_2-oil miscibility in nanopores is further presented including phase equilibrium, vaporizing and condensing drive, immiscible and miscible processes, and solubility parameters.

1.5 Application of Nanoscale Pore Effects to CO_2 EOR Process

As the nanopore effect can alter phase equilibrium and CO_2 MMP, which includes key parameters for the CO_2 EOR process, it can be applied in screening tight oil candidate reservoirs and selecting parameters for CO_2 flooding. Taking the geometric constraint effect into consideration, screening tight oil reservoirs for the CO_2 injection process can be more accurate, selecting CO_2 parameters can be more reasonable and improving tight oil recovery can be more productive.

1.6 Structure of Thesis

The thesis contains two parts: a theory of the nanoscale pore effect on the CO_2 EOR process and its applications, which are shown in **Figure 1.1**.

In **Chapter 1**, the background of the CO_2 EOR process, and previous research on the nanopore effects are presented.

In **Chapter 2**, the tight oil production characteristics are analyzed and the effects of nanopores on phase equilibrium are presented to prepare for the CO_2-oil miscibility study.

In **Chapter 3**, the nanopore effects on CO_2 EOR, including miscibility alteration, vaporizing and condensing drive, immiscible and miscible processes, and solubility parameters and hysteresis, are presented. Furthermore, the applications of the nanopore effects are summarized.

In **Chapter 4**, theoretical reservoir models are introduced to help to perform the simulations.

In **Chapter 5**, an integrated method to screen tight oil reservoirs for CO_2 flooding is proposed.

In **Chapter 6**, CO_2 parameter selection is presented with the nanopore effect.

In **Chapter 7**, CO_2 performance improvement is investigated with the consideration of nanopores.

In **Chapter 8**, conclusions and future work are presented.

In **Appendix A**, the process of the phase behavior calculations is provided.

In **Appendix B**, the molecular models description and molecular dynamic calculations are presented.

In **Appendix C**, the non-Darcy effects are clarified and the equations related to reservoir simulations are provided.

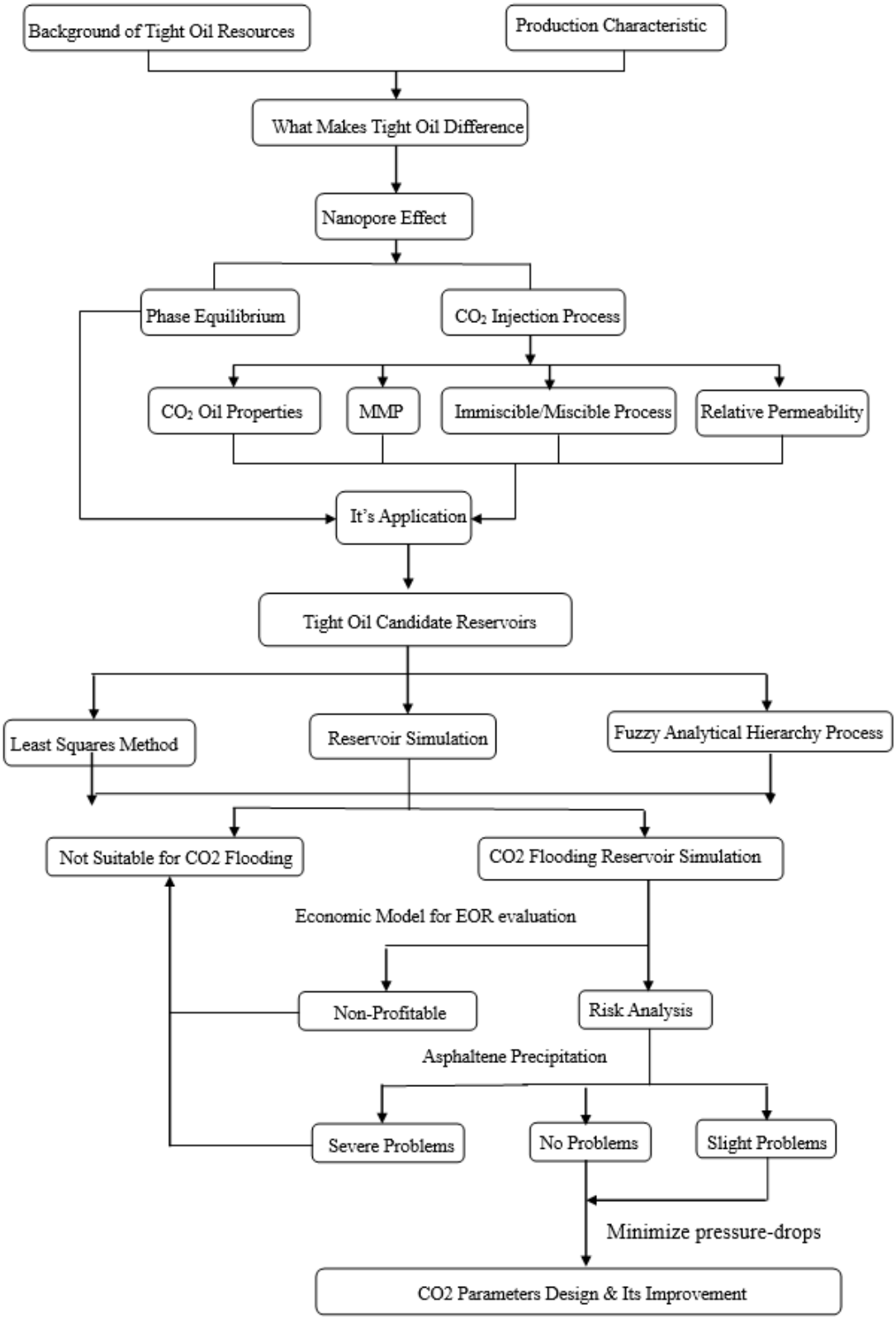

Figure 1. 1 Structure of Thesis

1.7 Novelty of the Thesis

As shown in **Figure 1.2**, previous studies showed that the phase behavior was not affected by porous media since 1949 (Weinaug, 1949); later, the phase equilibrium was found to be related to the pore scale (Sadyk, 1963). A breakthrough in this area was found that the phase equilibrium varies in the neighborhood of microscale (Sigmund, 1973). Afterwards, experiments and mathematical models have helped to determine the phase equilibria, which is characterized by pore proximity or a confinement effect (Yanis, 2001). The shifts of component critical properties in nanopores were characterized (Zarragoicoechea, 2002) and validated by molecular dynamic simulations (Singh, 2011). At that time, the pore scale was characterized in detail (Nelson, 2009). Since then, studies on tight reservoirs mainly have focused on the phase equilibria in nanopores incorporating the capillary pressure or the critical properties shifts (Teklu, 2014; Pitakbunkate, 2016). Different hydrocarbon and non-hydrocarbon gases MMP in nanopores have been calculated (Teklu, 2014). However, there is no systematical study on the CO_2-oil miscibility in nanopores. The novelty of the thesis covers the contents of the light blue sections in **Figure 1.3**, except for the calculation of the CO_2-oil MMP in nanopores. The theory behind the CO_2-oil miscibility was not given and the reason why the CO_2-oil miscibility alters in nanopores was not provided. Furthermore, under what condition the effect of nanopores on CO_2-oil miscibility works and the amount of alteration in the CO_2-oil miscibility in nanopores were not present. In addition, the applications of CO_2-oil miscibility in nanopores was not investigated.

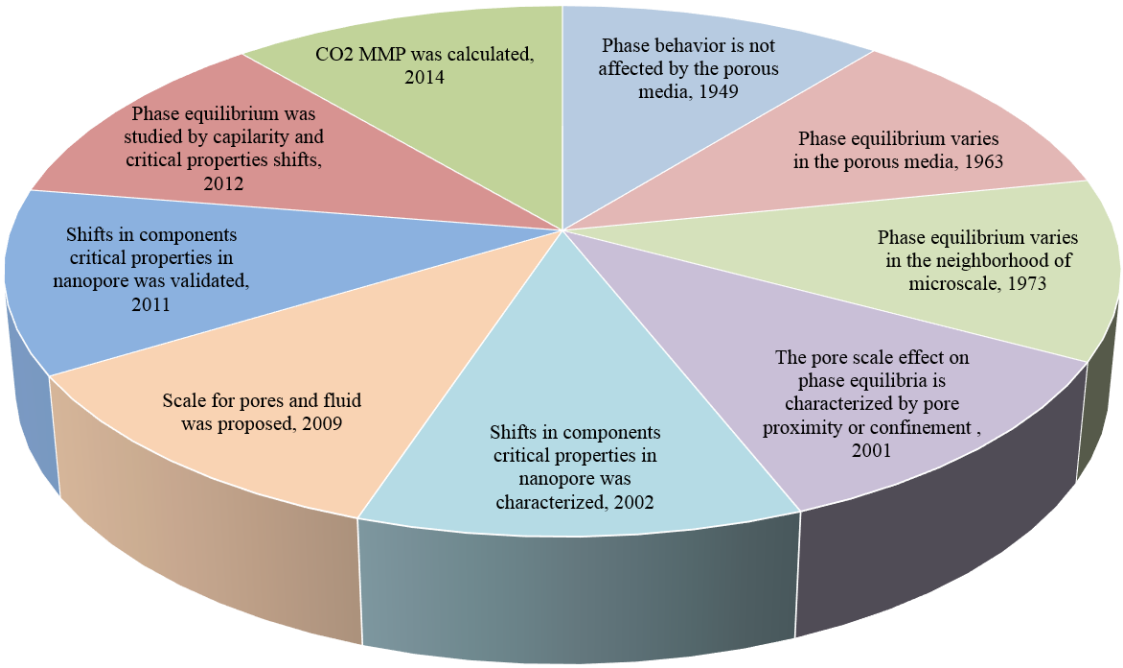

Figure 1. 2 Previous Study on Phase Equilibrium in Pore Scale

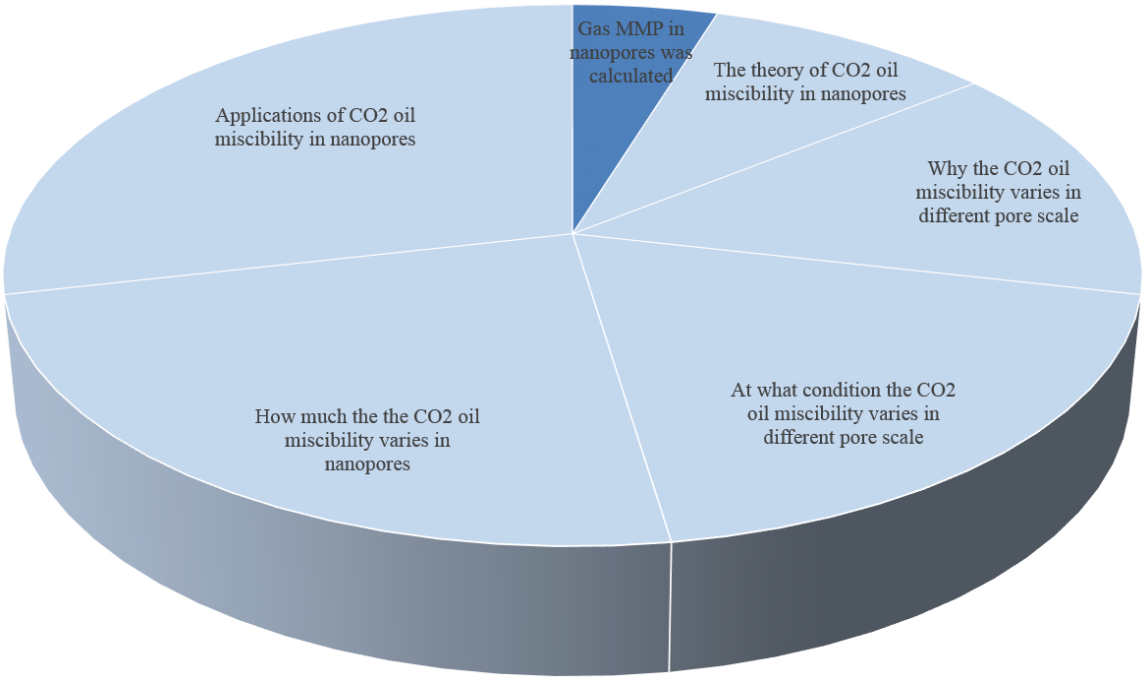

Figure 1. 3 Novelty of the Thesis

Chapter 2. What Makes Tight Oil Different?

2.1 Background of Tight Oil Resources

Tight oil is light crude oil contained in formations with a permeability lower than 0.1 *md* (Clarkson, 2011). The flow of oil from rock to wellbore is limited by the largely impermeable fine-grained nature of an oil-hosting rock, the cause for the term "tight". While some tight light oil plays produce oil directly from shale, most tight oil is produced from low-permeability sandstones, limestones and dolomites that are associated with the shale from which oil has been generated (Clarkson, 2011).

The oil itself requires very little refinement and is extensively distributed with two times deepwater hydrocarbon resources (Ashraf, 2013). The total tight oil reserves in North America are estimated to be more than 30 billion barrels contained in 24 oil reservoirs, among which only 14 reservoirs are under development (Forrest, 2011).

The tight oil exploration and development stages are listed as follows by Canadian Society for Unconventional Resources (CSUR, 2017):

Stage 1: Identify tight oil resources

Gathering all existing information for a review of a basin, a fairway or a play, characterizing geologic formations and their stratigraphy within the survey area. The subsurface information and seismic data are used to indicate the presence of potential oil- and gas-bearing structures.

Stage 2: Resource evaluation

In this stage, core samples are collected. Land acquisition and the securing of seismic data lead to

drilling location permits and land use agreements; vertical wells are drilled initially to evaluate reservoir properties and resources potential.

Stage 3: Pilot production evaluation

Initial horizontal wells and potential completion techniques help to determine production potential. Multi-stage fracturing may apply at this point. In this stage, planning and acquisition of pipeline right-of-ways for field development also occur.

Stage 4: Pilot production testing

Multiple horizontal wells from a single pad are drilled; micro-seismic surveys are conducted and completion techniques include drilling, multi-stage fracturing are optimized; pipeline right-of-ways for field development are planned.

Stage 5: Commercial development

Optimization of completion techniques, including multiple horizontal wells, multi-stage fracturing and micro-seismic monitoring, is presented at this stage. Drilling and completion proceeds, based on the field development plan as defined by regulatory well spacing. Government approvals are obtained for the construction of facilities and applicable technologies are identified during the evaluation stage.

Stage 6: Project completion and reclamation

At the final stage, completion of a project and reclamation of development sites and well pads to regulatory standards occur.

Every tight oil reservoir is unique and the stimulation and completion method is determined

based on its individual petrophysical attributes (Rickman, 2008). The oil extracted from a tight reservoir is the same type of oil produced from a conventional reservoir. It is the advanced technology that drives this extraction to be unconventional.

As shown in **Figure 2.1**, wells are initially drilled vertically to a certain depth above a tight oil reservoir, and then the wells are kicked off (turned) at an increasing angle until they run parallel within the reservoir. Once horizontal, the wells are drilled to a selected length which can extend up to 9000 *ft*. Stimulation is needed in the tight formation once the wells have been drilled. Through applying pressure by pumping fluids into wellbore, pathways are created in the reservoir through which the oil can flow to the wellbore (Laredo Energy, 2017).

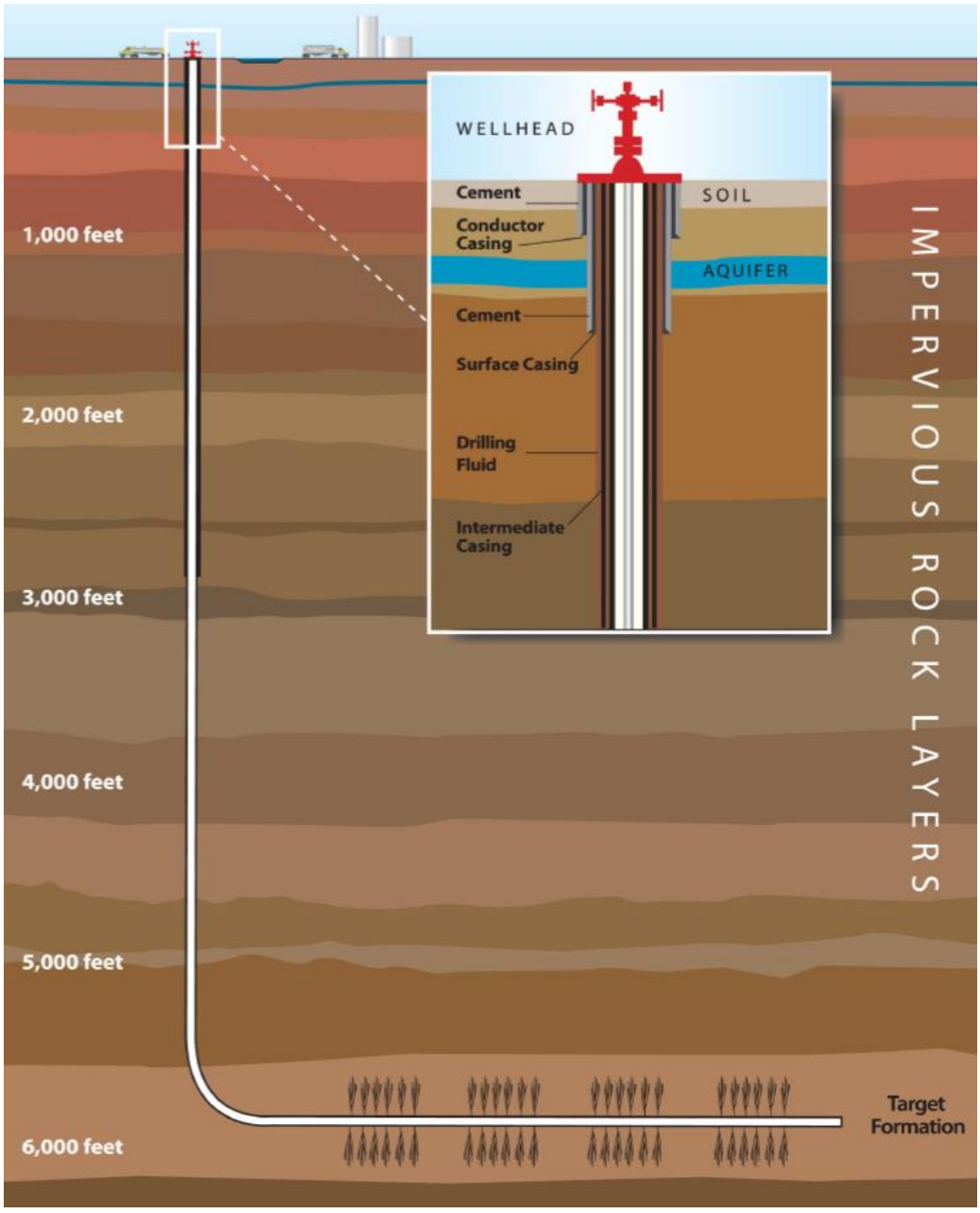

Figure 2. 1 Tight Oil Exploitation (Laredo Energy, 2017)

2.2 Production Characteristics of Tight Oil Exploitation

As conventional resources are gradually declining, unconventional resources, such as tight oil, have attracted extensive attention. Its production characteristics, however, are still unclear.

As noted, nanoscale pores are extensively distributed in tight oil reservoirs (Pitakbunkate, 2015) and a pore structure can affect fluid distribution, resulting in a variation in hydrocarbon production characteristics between conventional oil reservoirs and tight oil reservoirs. In this part, the primary, secondary and tertiary recovery aspects in tight oil exploitation are presented.

First, production behavior is observed during reservoir depletion for tight oil reservoirs, including oil production profiles, water cut and producing GOR. Then the comparison is made for a fluid flooding response between conventional oil and tight oil reservoirs.

With the consideration of the nanopore effect, a transition zone will become quite broad in tight oil reservoirs. Its production can experience a significant variation compared to that in conventional oil reservoirs.

In the case of insufficient bottomhole pressure in oil wells, a surface flow rate cannot be measured. A swabbing unit can be run to maintain fluid flowing from a formation continuously. The volume of a fluid recovered from each swabbing run as a function of time is recorded, which can be used to determine the rate of fluid feed-in from the formation to a wellbore (Whittaker, 1987). The fluid level in a well varies over the course of several hours in tight oil reservoirs as identified during a swab test. As shown in **Figure 2.2**, for conventional reservoirs, the amount of fluids produced can be filled by fluids coming from the reservoir as the flow capacity of

conventional reservoirs is high. While the reservoir fluids delivery is quite poor in tight oil reservoirs, the fluid level in a well may change within several hours. It is important to keep downhole flowing pressure above the saturation pressure since liberated gas impedes the flow of oil through a porous medium.

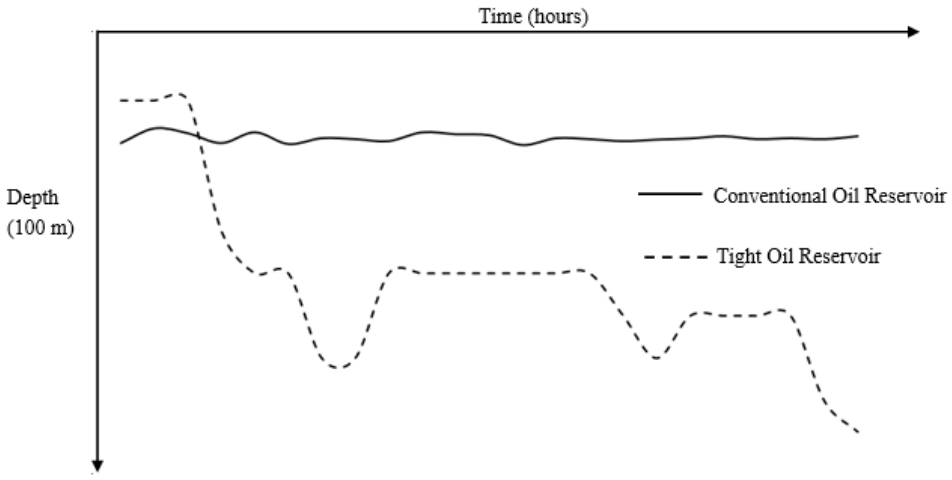

Figure 2. 2 Fluid Level Alteration during a Swab Test (Zhang, 2015)

Nanoscale pores can affect fluid distribution underground, resulting in a variation in production behavior. Capillary pressure can be negligible in conventional reservoirs, but in tight oil reservoirs it can have a tremendous effect on fluid distribution. As shown in **Figure 2.3**, transition zones including an oil + mobile water zone and a gas + oil + immobile water zone are quite broad in tight formations (Gregory, 2010). Associated with ultra-low reservoir permeability, production characteristics of tight oil reservoirs during primary recovery may vary considerably when compared with that of conventional oil reservoirs.

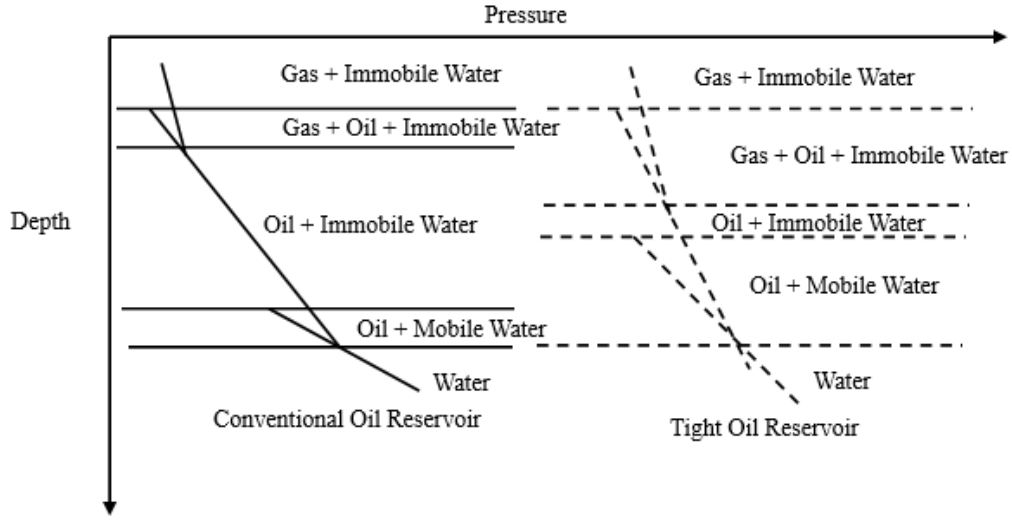

Figure 2. 3 Transition Zone for Convention and Tight Oil Reservoirs (Zhang, 2015)

Numerous field productions are investigated, including the Cardium sandstone reservoir and the Pekisko limestone reservoir. The phenomenon that gas and oil or water and oil are co-produced at an early stage of production has been observed. In addition, the water cut in many tight oil producers remains constant or undergoes a reduction as production continues over the first 36 months, as shown in **Figures 2.4** and **2.5**. Because water coexists with oil in a tight formation, an oil and immobile water zone is too thin while an oil and mobile water zone is quite broad. Thus, water produced at the early stage is coming from a transition zone. Once oil produced from a tight formation and mobile water in a transition zone has been depleted, the water cut will drop to a relatively low level. The wells in Cardium Reservoirs have been hydraulically fractured and there is a possibility of high water cut at the very beginning of production after wells are fractured. However, the wells in Pekisko are not hydraulically fractured, and the same phenomena in water cut has been recorded, which eliminates the effects of the flow back of a fracturing fluid (Zhang,

2015).

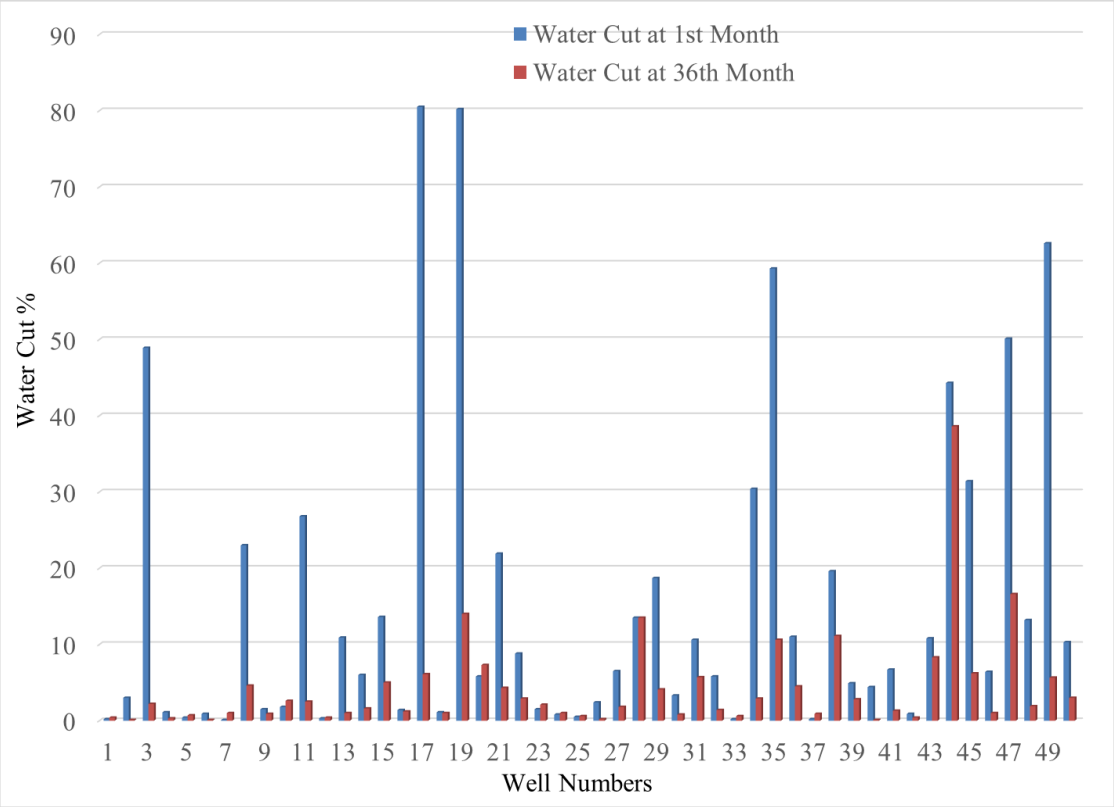

Figure 2. 4 Water Cut at 1st Month and 36th Month for Cardium Sandstone Reservoir (Zhang, 2015)

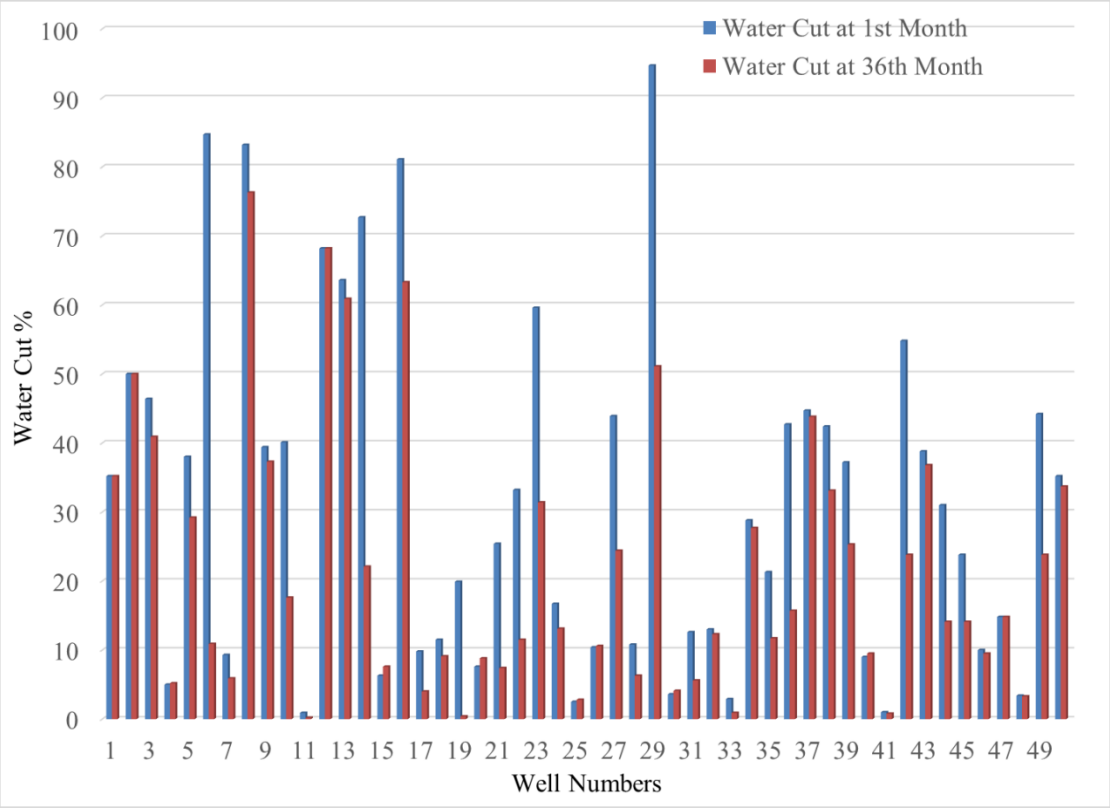

Figure 2. 5 Water Cut at 1st Month and 36th Month for Pekisko Limestone Reservoir (Zhang, 2015)

Generally, tight oil exploitation has no natural or low production capacity and the production cycle of a single well is quite long. As shown in **Figure 2.6**, for conventional reservoirs, oil production can sustain a plateau for a certain period of time. In tight oil reservoirs, the oil production rate declines rapidly and stabilizes at a low rate of decline between 9 to 12 months (Zhang, 2014).

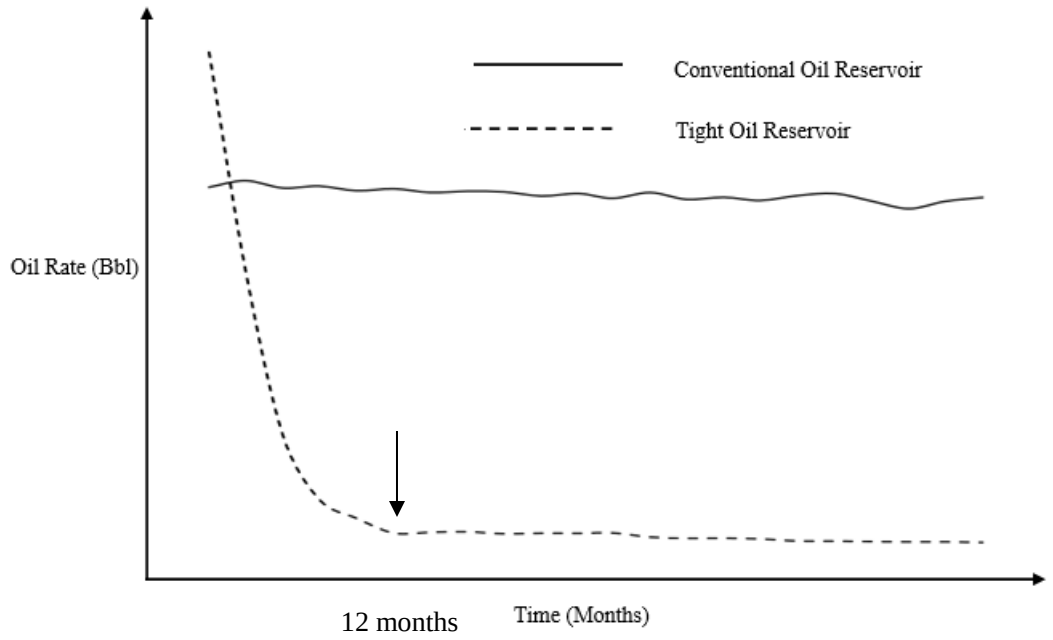

Figure 2.6 Oil Production Profiles (Zhang, 2015)

The producing gas-oil ratio (GOR) in tight oil reservoirs with multi-stage fractured horizontal wells is heavily related to the flowing bottom hole pressure due to the nature of pressure gradients near fractures (Steven, 2016).

As shown in **Figure 2.7**, the following idealized stages of GOR history are identified in chronological order (Steven, 2016):

a. GOR = R_{si}. The production starts while the flowing bottom hole pressure is above the bubble point, and GOR remains flat at the initial gas-oil ratio;

b. GOR rises due to $p_{wf} < p_b$. Shortly after the production, the well bottom hole pressure drops below the bubble point pressure and the GOR will rise up dramatically.

c. A transient GOR plateau. After the rise of the GOR due to the bottom hole flow pressure below the bubble point pressure, a transient GOR plateau may occur when the flowing bottom hole

pressure reaches a minimum and becomes constant. GOR stabilizes at a level well above R_{si}, and remains there throughout the transient linear flow. The duration of the transient linear flow highly depends on the fracture conductivity and fracture half length.

d. GOR rises during boundary-dominated flow (BDF). Once the pressure depletion approaches the boundary, the boundary dominated flow begins, the fracture pressure decreases and the average gas saturation in the drainage area increases due to depletion between fractures.

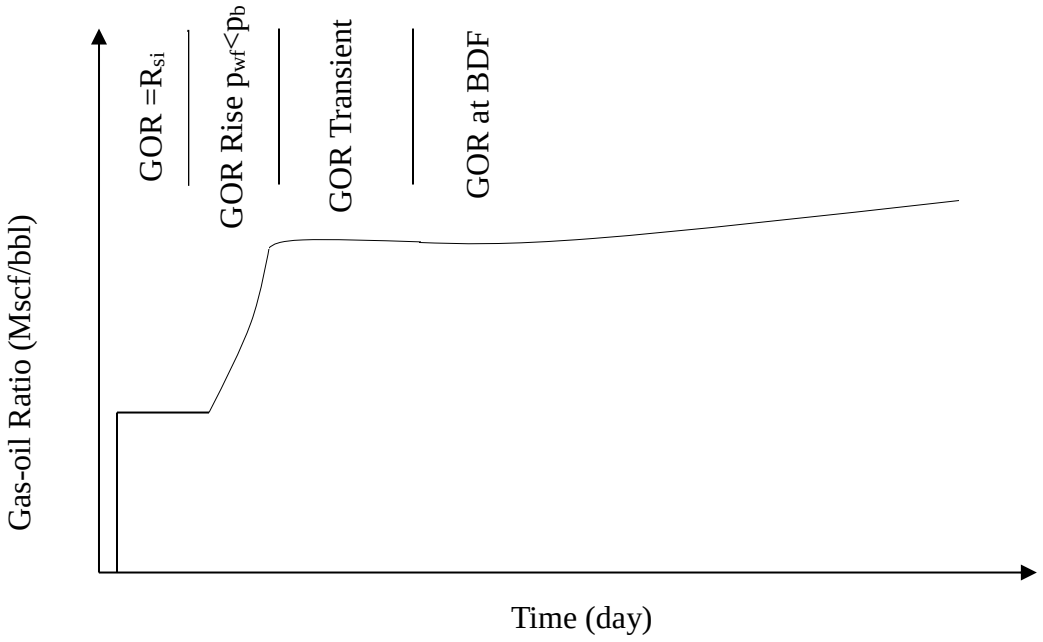

Figure 2. 7 Idealized Stages in GOR History of a Multi-stage Fractured Horizontal Well (Steven, 2016)

In contrast to primary recovery, fluid injection, including water, gas and chemical treatments, can maintain reservoir pressure and sustain oil production in tight oil reservoirs. For conventional oil reservoirs, an injected fluid can suddenly increase an oil production rate which then drops after certain time of production, as shown in **Figure 2.8**. For tight oil reservoirs, the response of fluid

injection is not as significant.

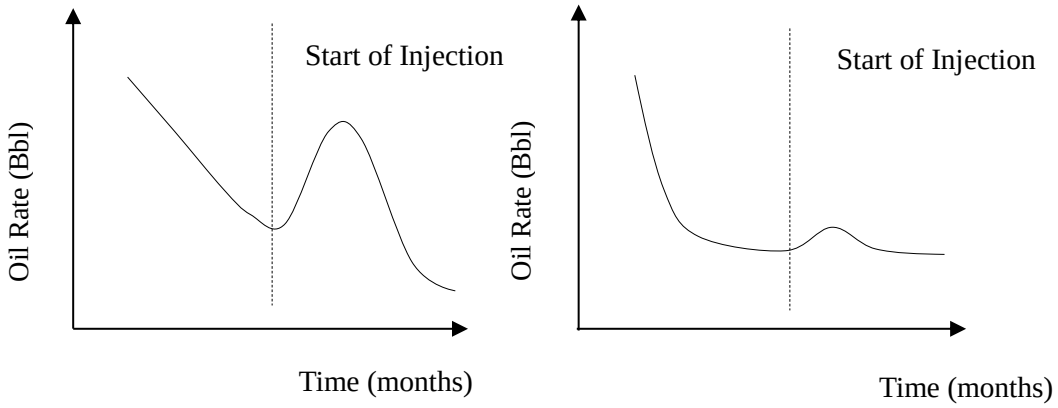

Figure 2.8 Fluid Injection in Conventional (Left) and Tight Oil Reservoirs (Right)

Field production data shows that gas and oil or water and oil are co-produced at an early stage of production. Many tight oil producers see that the water cut remains constant or undergoes a reduction as production goes on within the first 36 months. Additionally, fluid flooding can maintain reservoir pressure and keep the oil production rate for tight oil reservoirs. For conventional oil reservoirs, fluid flooding can suddenly increase an oil rate which then drops after a certain time of production. If pores are small, without much standard deviation, then interfacial tension optimization will be key to oil recovery. If pores are big and in a broader variation, the viscosity force will dominate in determining an oil rate (Lake, 1989).

As seen, the reservoir delivery is very poor in tight oil reservoirs and, even with the contribution of a fluid coming from outside the reservoirs, the production profile cannot be altered significantly. All of the unique production characteristics are caused by nanoscale pores underground.

The following figure shows the sizes of molecules and pore sizes on a logarithmic scale including seven orders of magnitude. Measurement methods are listed at the top of the plot and scales used for mineral particles are shown at the lower right. The symbols show pore sizes for sandstone, tight sandstone and shale reservoirs. Ranges of clay mineral spacing, diamondoids, and oil samples, and molecular diameters of water, mercury, and three gases are also given in the plot. The sources of data and measurement methods for each sample set are discussed in the text (Nelson, 2009).

Research shows that the pore scale for tight sandstone reservoirs is around 30 to 2000 *nm*; for shale reservoirs, the pore diameter is around 2 to 100 *nm* (Nelson, 2009), as shown in **Figure 2.9**. The molecular diameter of CO_2 is around 0.36 *nm*, H_2O is around 0.29 *nm*, CH_4 is around 0.38 *nm*, and N_2 is around 0.33 *nm* (Xiao, 1992). All of these fluids have the potential to improve tight oil production. The proper way to enhance oil recovery in tight oil reservoirs is proposed and the effects of nanopores on the flooding performance are presented in the following content.

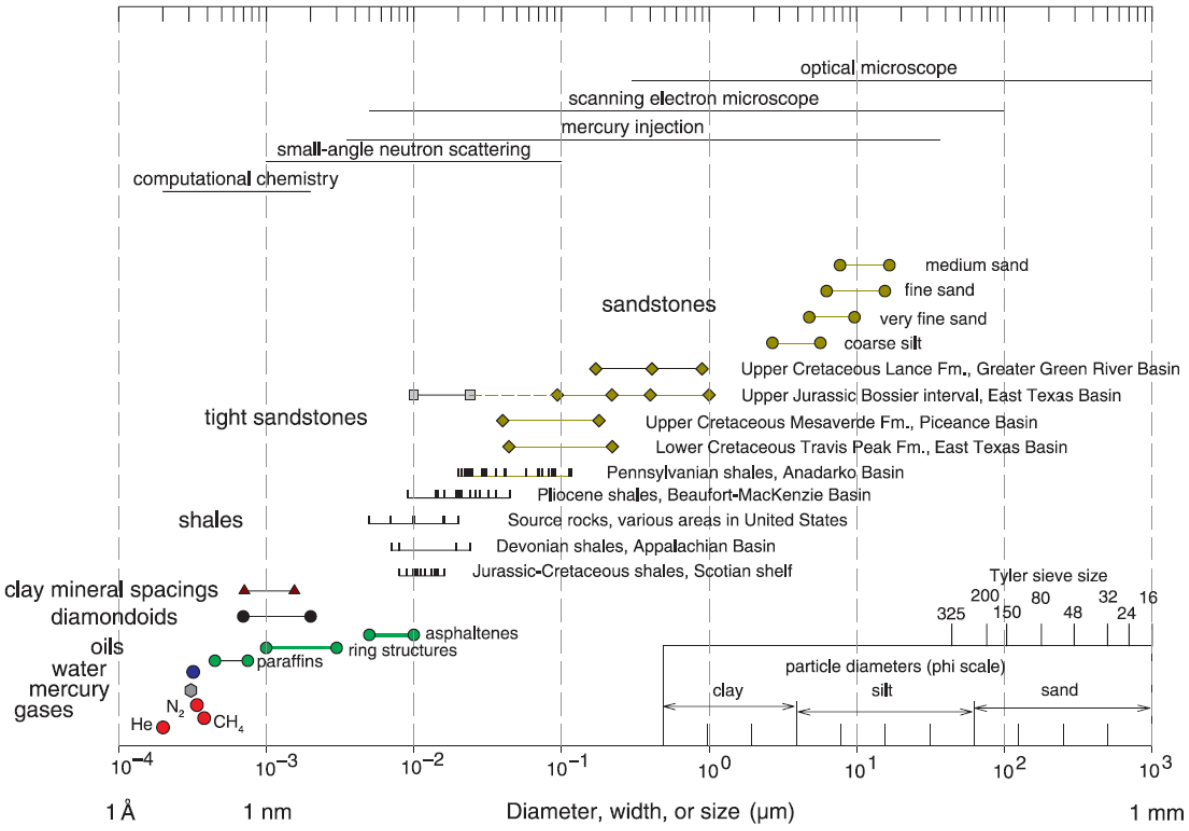

Figure 2.9 Molecules and Reservoir Scale (Nelson, 2009)

2.3 Effects of Confinement

The pore structure in tight formations is complex, including micro-pores (a pore diameter < 2 *nm*), meso-pores (a pore diameter is 2-100 *nm*) and macro-pores (a pore diameter > 100 *nm*) (Ross, 2009; Chalmers, 2012; Clarkson, 2013).

Based on a Barnett shale pore structure analysis, the pore size is around 1/400 of sandstone and has an assembly of 40 CH_4, a diameter 0.38 *nm* of each (Lin, 2011; Loucks, 2009). For well index 04-32-047-10W5 in the Cardium sandstone reservoir, its permeability and pore size distribution are shown in **Figures 2.10** and **2.11**. There is a significant chance of nanoscale pores in tight reservoirs.

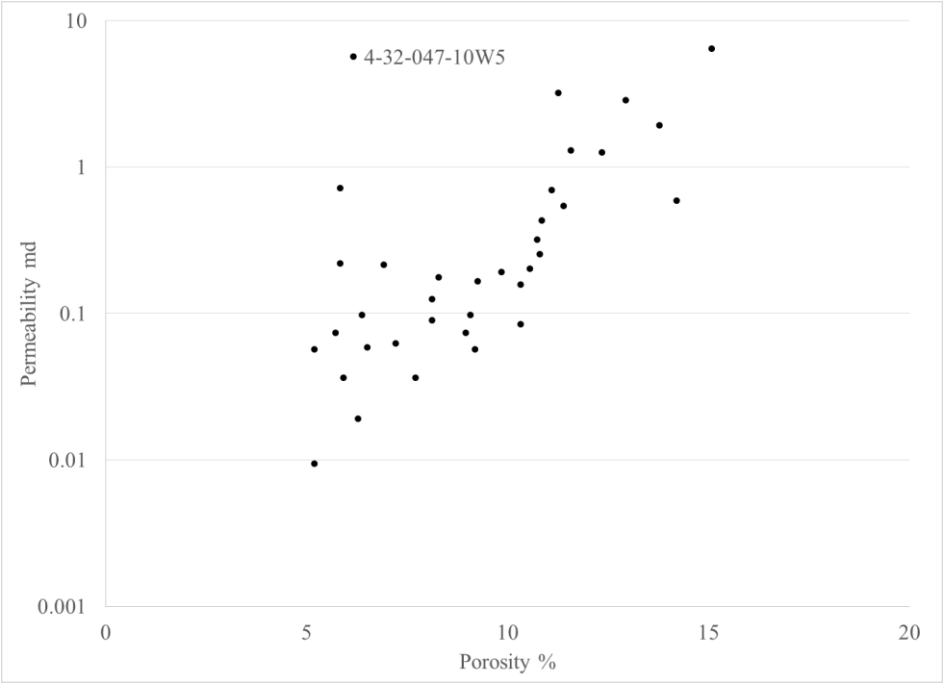

Figure 2.10 Core Porosity vs. Permeability Cross Plot for Well 04-32-047-10W5 (Nicholas, 2015)

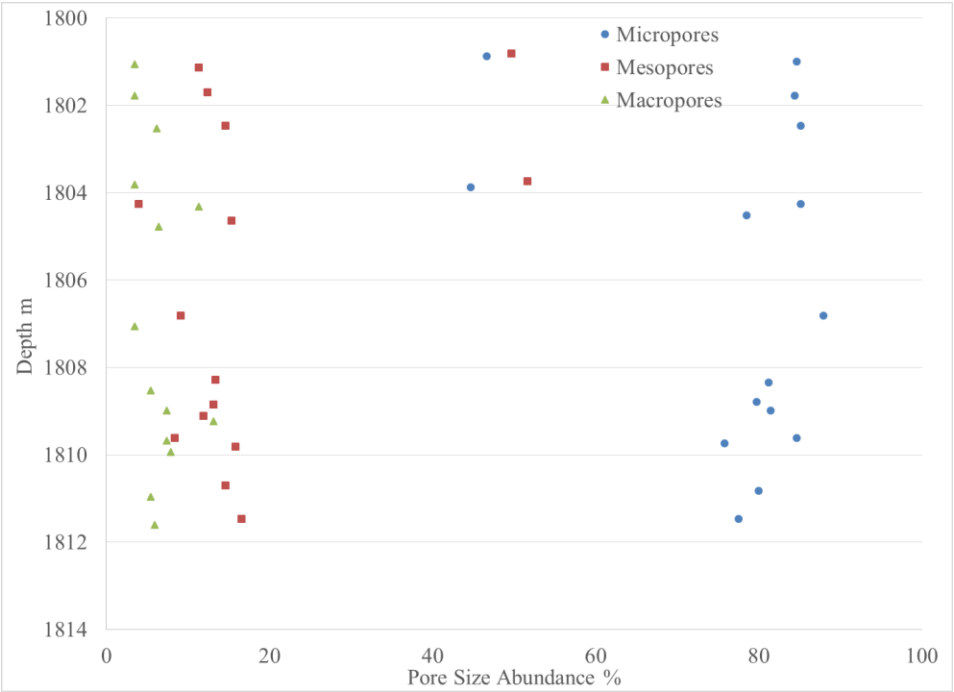

Figure 2.11 Plot of Pore Type vs. Depth for Well 04-32-047-10W5 (Nicholas, 2015)

In a nanoscale confined space, the molecular orientation can be altered. Molecular dynamics can help to characterize the interaction between molecules and solid surfaces. In molecule dynamics simulation, because molecules will behave in a steady state after a certain time, the average velocity and position, acceleration of the molecule and the energy of the system can be obtained.

A C_2H_6 molecule sets up in a different way in an Armchair (10,10) carbon nanotube: One is parallel to the nanotube surface, and another is perpendicular to the nanotube surface, as shown in **Figure 2.12**.

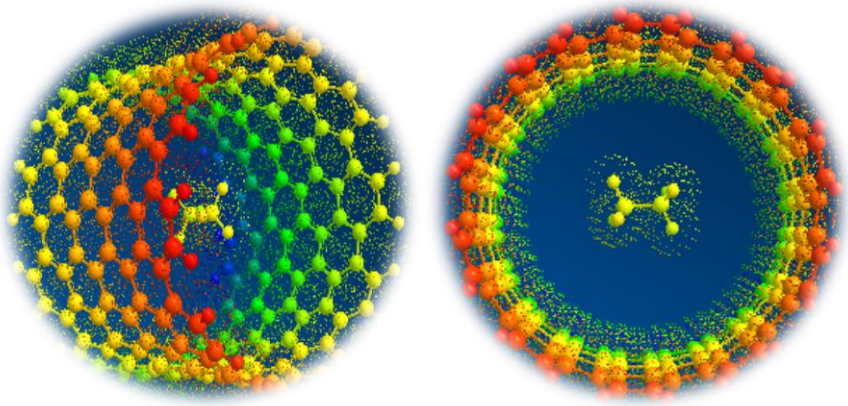

Figure 2. 12 C_2H_6 Molecule Orientation Alteration (Zhang, 2016)

The variation between the energy at a specific position and the energy at the center of the nanotube are recorded in **Figure 2.13**. The C_2H_6 molecule in a parallel configuration to the surface has larger bond energy parameter at the molecular separation distance, where the attraction and repulsion forces are equal, which indicates the system has minimum energy. The molecule will prefer to stay parallel to the surface of the nanotube.

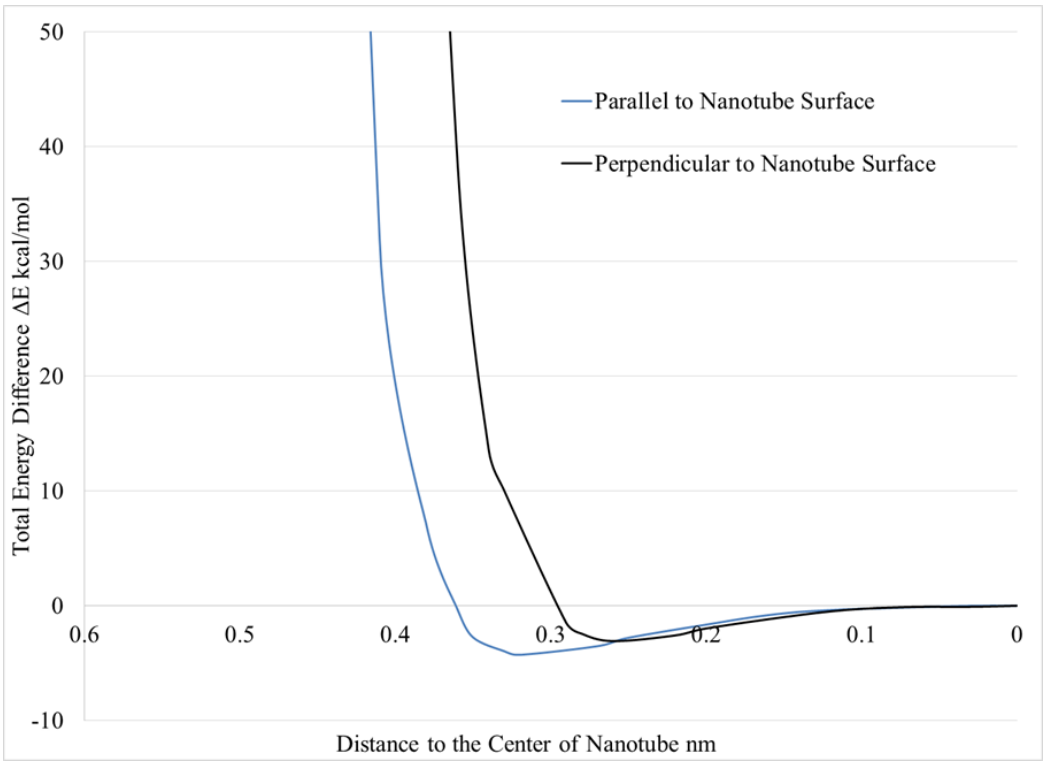

Figure 2. 13 Energy of C_2H_6 in a Nanotube (Zhang, 2016)

The orientation alteration of molecules in the nanotube can cause component critical properties alteration as bond energy and size parameters change at the molecular separation distance. The shifts of confined fluid critical properties in nanopores can be characterized.

The molecular orientation alteration by nanoscale pore confinement, as shown in **Figure 2.14**, is consistent with the previous research. In this way, interactions between surface walls and fluid molecules cause a change in the thermal dynamic behavior of the hydrocarbon phases, resulting in a variation in critical pressure and temperature (Pitakbunkate, 2015).

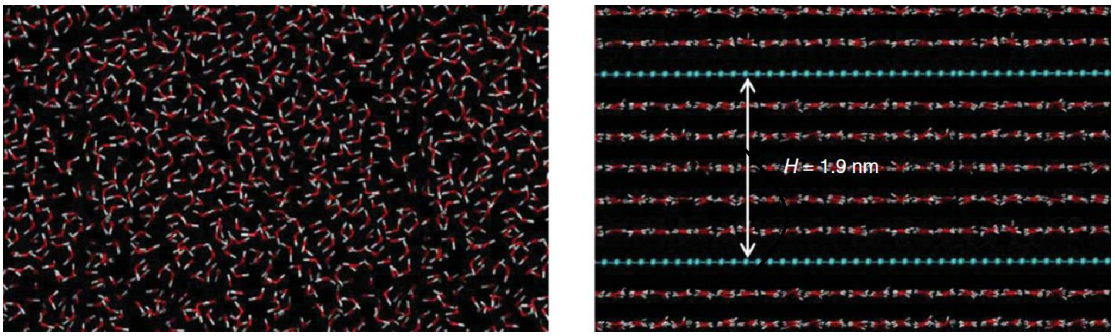

Figure 2.14 Molecular Orientation in Bulk System and Confined System (Pitakbunkate, 2015)

In nanopores, molecules conceptually divide a pore volume into two "spaces", as shown schematically in **Figure 2.15**. In space I, close to the pore wall surface, the molecules strongly interact with the pore surface. On the other hand, in space II, further from the adsorbent surface, molecules interact with molecules in space I but not directly with the pore surface. The variation in fluid interactions accounts for the inherent nonuniformity of fluid molecules in a nanopore (Jensen, 1997).

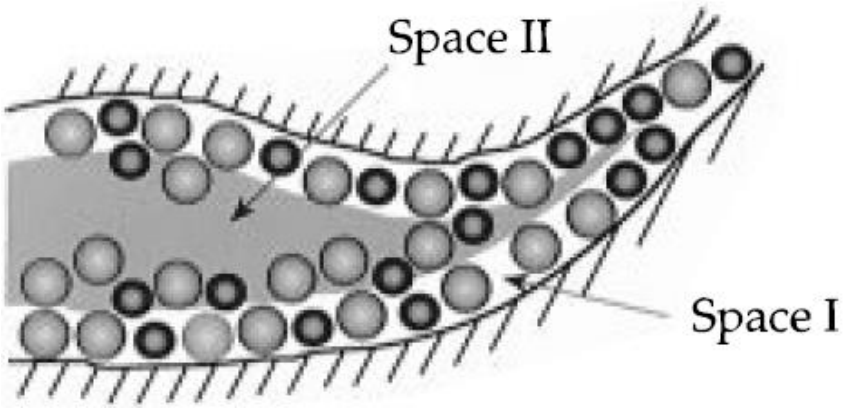

Figure 2.15 Fluid Molecules in a Nanopore (Jensen, 1997)

The nonuniformity distribution of fluid molecules causes different fluid properties in a nanopore. As shown in **Figure 2.16**, it can be seen that the CO_2 density near pore walls is higher than that in

pore centers (Liu, 2012).

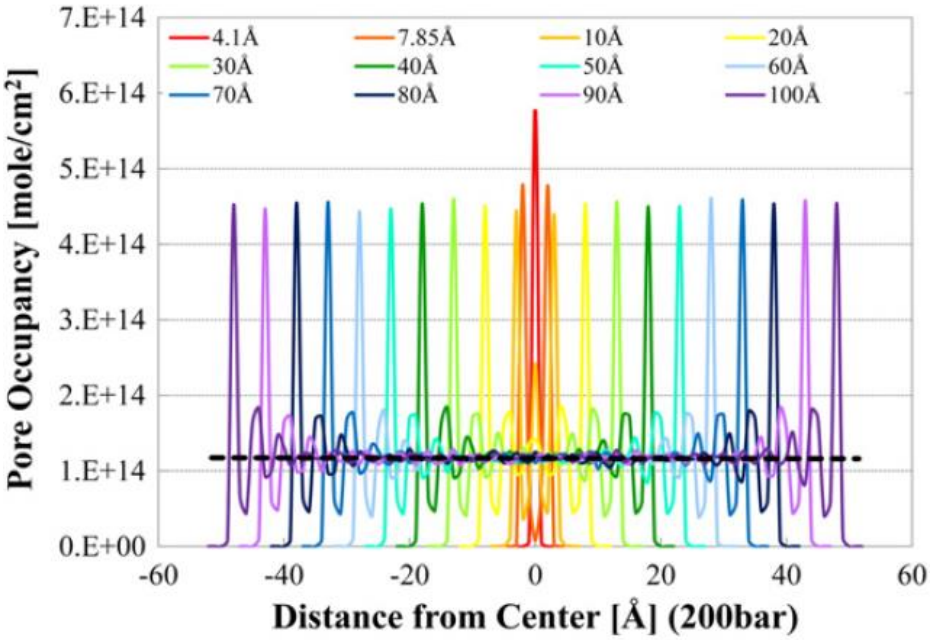

Figure 2.16 Effect of Pore Size on the CO_2 Density Distribution (Liu, 2012)

The nanopore confinement can affect the fluid orientation alteration and the inherent nonuniformity interactions between fluid molecules and pore wall surfaces, which can result in a variation in phase equilibrium.

2.4 Effects of Nanoscale Pore Confinement on Multi-components Phase Equilibrium

As noted, the production characterization of tight oil reservoirs is quite different from that of conventional ones (Zhang, 2015). The fluid level in a well varies over the course of several hours in tight oil reservoirs, as determined during a swab test. Reservoir fluid delivery is quite poor in tight oil reservoirs, as the fluid level in a well may change even within several hours. In addition, transition zones, including an oil + mobile water zone and a gas + oil + immobile water zone are quite broad in tight formations. Also, the oil production rate declines rapidly and stabilizes at low

declining rates after about 9 to 12 months (Gregory, 2010). The production characteristic highly relates to the reduction of hydraulic fractures conductivity during the primary depletion and the poor reservoir fluid delivery from nanoscale pores in the reservoir.

The effect of the reservoir pore scale on the fluid phase equilibrium was investigated experimentally and theoretically. Earlier results reported indicated that the vapor-liquid equilibria was not affected by the presence of a porous medium (Weinaug, 1949; Smith,1968). On the other hand, fluid mixtures were shown to behave differently in porous media from those observed in the conventional PVT cells (Sadyk, 1963; Trebin, 1968; Sadyk, 1968). Tindy and Raynal reported that the saturation pressures of the oil mixture in a porous medium were different from those measured in conventional test cells (Tindy, 1966). Sigmund claimed that the finest pores were occupied by connate water. Saturation pressure is independent of the presence of a porous medium at very high curvatures (curvature radius >1000 *nm*) (Sigmund, 1973). In a reservoir porous medium, the effect of capillarity can affect phase equilibrium in the neighborhood of a 1 - micron pore radius (Lee, 1989). Brusilovsky proposed a mathematical model including capillarities to capture the vapor/liquid equilibria (Brusilovsky, 1992). The results are consistent throughout several studies. The capillarities can affect the multi-components phase equilibrium (Guo, 1994; Shapiro, 1996; Guo, 1996). Later on, the alteration of phase equilibria in a porous medium is named pore proximity or the confinement effect (Yanis, 2001; Kanda, 2004; Devegowda, 2012; Milad, 2014). With the rapid growth of computing, molecular simulation becomes an important approach in understanding the fluid behavior in a confined system. Both the Gibbs Ensemble Monte Carlo

(GEMC) simulation and Molecular Dynamic Simulation, for instance, can estimate the components' properties. In a Monte Carlo molecular simulation, ensemble probability is estimated with the setup of molecules' configuration. In a Molecular Dynamic Simulation, because molecules behave in a steady state after a certain time, their average velocity, position, and acceleration can be obtained. Molecular simulation studies show that the critical properties of fluids under confinement deviate from their bulk properties (Panagiotopoulos, 1987; Vishnyakov, 2001). As a result, fluid phase diagrams can be a function of a pore size (Singh, 2011; Devegowda, 2012). In characterizing the confinement effect or pore proximity, an additional term is introduced in the PR-EOS equation to account for the molecule-wall interaction (Dhanapal, 2014) and the capillary pressure between the vapor and liquid phases is included in the fugacity evaluation (Wang, 2014; Li, 2016). The confinement effect is incorporated by the shifts in critical pressure and temperature (Xiong, 2013; Qanbari, 2014). The correlations with the shifts in critical properties are easily generalized and incorporated into any numerical simulator framework (Devegowda, 2012), they are also more widely investigated.

Recent studies of tight reservoirs have mainly focused on fluid phase behavior (Jin, 2013; Dhanapal, 2014; Wang, 2014; Li, 2014; Sanaei, 2014; Ma, 2014; Jin, 2015; Li, 2015; Luo, 2015; Pitakbunkate, 2016). In tight sandstone reservoirs, a pore diameter is about 30 to 2000 *nm*, while a pore diameter in shale reservoirs is about 2 to 100 *nm* (Nelson, 2009). In such a nanoscale porous medium, a variation in molecular orientation and molecules arrangement in a bulk state result in unique thermal dynamic properties (Pitakbunkate, 2016). In a nanopore, the heavier components

tend to have a higher concentration close to the pore surface (Ma, 2014). If the pore size is taken into account in the phase equilibrium calculations, the nanoscale pore confinement has a noticeable influence on fluid saturation pressures and phase behavior (Akkutlu, 2013; Didar, 2013; Allawe, 2015; Li, 2015; Zhang, 2015; Siripatrachai, 2016). This is caused by the geometric constraint limiting fluid molecules (Zarragoicoechea, 2002) and the interactions between surface walls and fluid molecules (Zhang, 2006). In this way, a fluid can have an inhomogeneous density distribution inside a pore, resulting in shifts in critical properties (Teklu, 2014; Pitakbunkate, 2014; Jin, 2016; Pitakbunkate, 2016). The critical temperature and critical pressure of a pure component reduce as a pore size decreases (Morishige, 1997; Vishnyakov, 2001; Zarragoicoechea, 2004; Jana, 2009; Singh, 2009; Akkutlu, 2013; Pitakbunkate, 2014; Islam, 2015). For a nanoscale porous system, the two-phase region shrinks compared to their bulk state (Ma, 2014; Sanaei, 2014; Wang, 2014; Rahmani, 2015). In addition, the nanoscale pore confinement is highlighted for mixtures that are rich in lighter components such as CH_4 (Rahmani, 2015), resulting in larger fractions of light components dissolved in liquid phase equilibrium (Ma, 2013; Li, 2015). Furthermore, confinement contributes to the production of more valuable components by keeping fluids in a single phase (Devegowda, 2012; Xiong, 2013; Wang, 2014; Parsa, 2015; Zhang, 2015). In some cases, geomechanics including rock compaction with further a pore radius reduction and complex pore throat distribution can further exaggerate the confinement effect (Xiong, 2014).

At present, no systematic statement to explain the confinement effect on phase equilibrium exists. As well, the range for the confinement effect to be insignificant is not recorded.

In this section, a fluid sample is used to investigate the multi-component phase equilibrium with the confinement effect. The enthalpy and fugacity of the fluid are recorded in the equilibrium calculations. Afterwards, by performing molecular dynamic simulations, carbon nanotubes are used to study the flow of molecules inside a nanopore.

Phase Envelope Calculation

First, convergence pressure is calculated by matching either the bubble point or dew point. Afterwards, the convergence pressure is used to attain saturation pressures at different temperatures. The following gives an example to calculate a phase envelope.

A well stream sample is given as a mole fraction in **Table 2.1** and the separator oil and gas compositions are provided.

Table 2. 1 Recombined Bottom Sample Analysis (Zhang, 2016)

Component	Separator Oil (%)	Separator Gas (%)	Well Stream (%)
N_2	0.0077	5.58096	3.01508
CO_2	0.00834	0.55164	0.30151
CH_4	0.23819	49.52578	26.83417
C_2H_6	0.62984	19.95022	11.05528
C_3H_8	1.62073	12.58602	7.53769
IC_4	0.49796	1.43765	1.00503
NC_4	2.64179	5.19607	4.0201
IC_5	1.79464	1.26258	1.50754
NC_5	3.39816	1.75698	2.51256
FC_6	6.88961	1.19935	3.8191
C_{7+}	82.27305	0.95276	38.39196

M_o = 124.82, M_{oC7+}=136.59, M_{gC7+}=100.75, GOR =432.75 *Scf/Bbl*, γ_o = 0.74, γ_g = 1.02

Bubble point pressure is 1800 psi and convergence pressure is 3153.2 psi at 156 F.

Separator is at standard conditions.

For multicomponent mixtures, the gas-oil interfacial tension can be evaluated by the following equation (Weinaug, 1943), where the parachors P_i can be obtained from **Table 2.2**:

$$\sigma_{go}^{1/4} = \sum_{i=1}^{N} P_i \left(x_i \frac{\rho_o}{M_o} - y_i \frac{\rho_g}{M_g} \right) \quad (2.1)$$

Table 2. 2 Parachors for Pure Components and Compound Groups (Curtis, 2000)

Pure Component	
C1	71
C2	111
C3	151
C4	191
C5	231
C6	271
C7	311
C8	351
C9	391
C10	431
N2	35
CO2	49
H2S	80
Group	
C	9
H	15.5
CH3	55.5
CH2	40

N	17.5
O	20
S	49.1

Example: CH4,

PC1= PC + 4(PH) = 9 + 4(15.5) = 71.

An equation of state is readily available to calculate the phase behavior of the crude oil and CO_2 mixture. The Peng-Robinson EOS is shown as follows: The calculations of the phase envelope, enthalpy, and fugacity are performed by Winprop, CMG:

$$P = \frac{RT}{v-b^*} - \frac{a^*}{v(v+b^*)+b^*(v-b^*)} \tag{2.2}$$

where

$$a^* = \frac{0.45724R^2T_c^2}{P_c}\alpha(T) \tag{2.3}$$

$$b^* = \frac{0.0778RT_c}{P_c} \tag{2.4}$$

$$\alpha(T) = exp\left((2 + 0.836T_r)\left(1 - T_r^{0.134+0.508\omega-0.0467\omega^2}\right)\right) \tag{2.5}$$

As an example, a reservoir fluid phase envelop is shown in **Figure 2.17.**

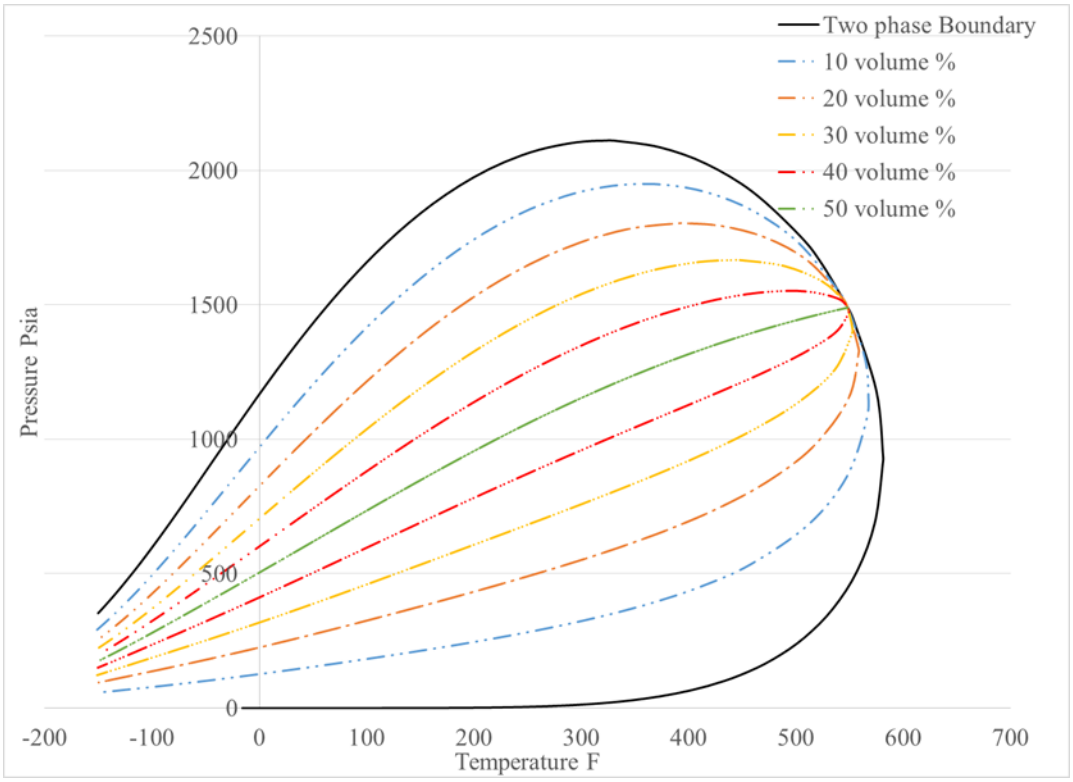

Figure 2.17 Reservoir Fluid Phase Envelop (Zhang, 2016)

The critical properties shifts are summarized by the following equations (Singh, 2009):

$$\Delta T_c^* = \frac{T_{cb} - T_{cp}}{T_{cb}} = a\frac{\sigma_{LJ}}{r_p} - b\left(\frac{\sigma_{LJ}}{r_p}\right)^2 \quad (2.6)$$

$$\Delta P_c^* = \frac{P_{cb} - P_{cp}}{P_{cb}} = a\frac{\sigma_{LJ}}{r_p} - b\left(\frac{\sigma_{LJ}}{r_p}\right)^2 \quad (2.7)$$

and

$$\sigma_{LJ} = c\sqrt[3]{\frac{T_{cb}}{P_{cb}}} \quad (2.8)$$

In a nanopore system, the geometric constraint limits fluid molecules (Zarragoicoechea, 2002) and the interactions between surface walls and fluid molecules (Zhang, 2006) contribute to the alteration of components' critical properties. As shown in **Figures 2.18** and **2.19**, the critical pressure and temperature are reduced as the pore size decreases.

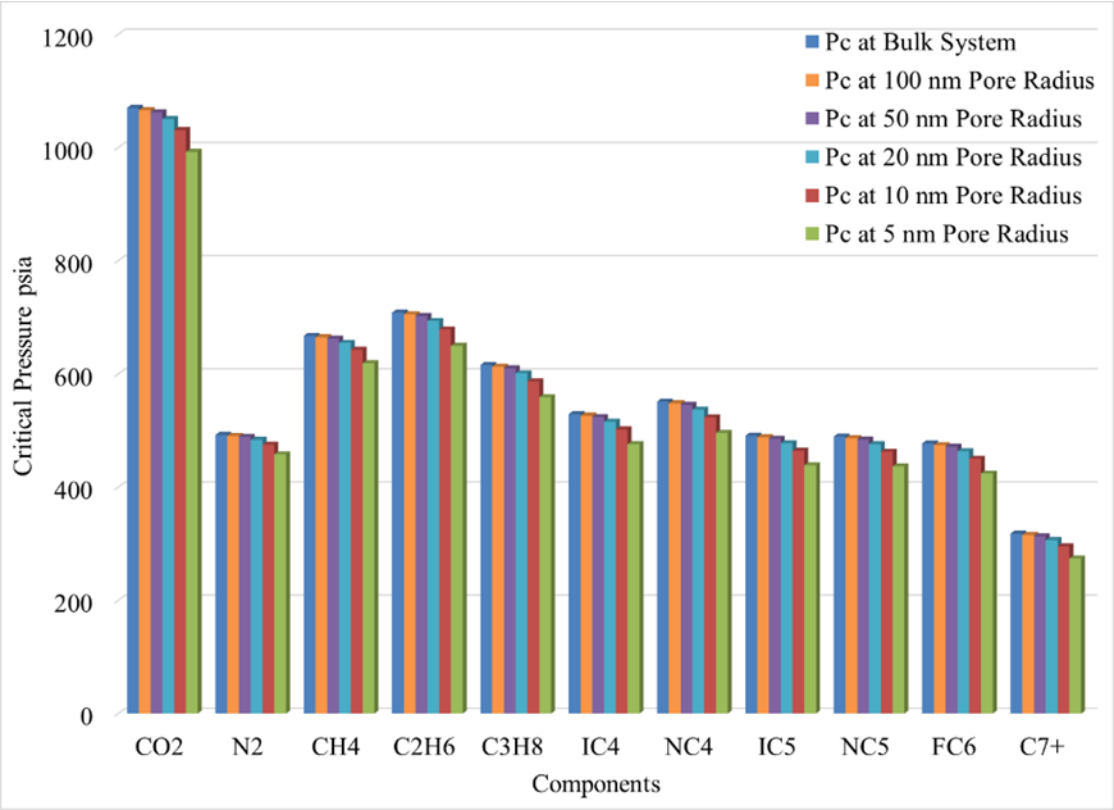

Figure 2.18 Critical Pressure Alteration with Confinement (Zhang, 2016)

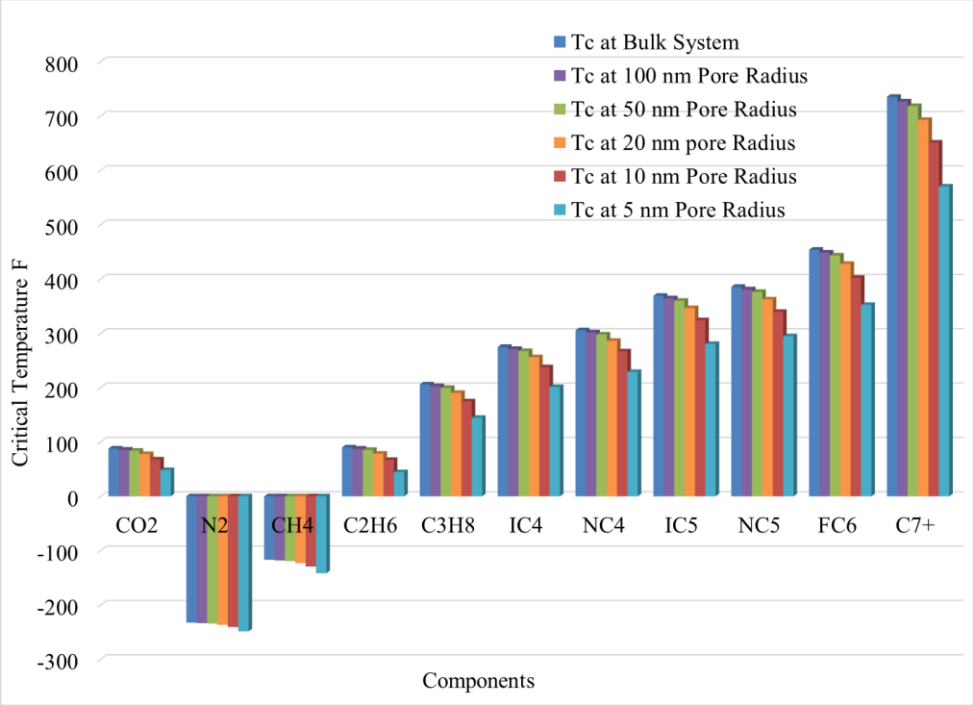

Figure 2.19 Critical Temperature Alteration with Confinement (Zhang, 2016)

Enthalpy is the nature of a chemical bond, which represents the energy absorbed or released during reaction. As confinement increases from a big pore to a small pore, the enthalpy of the fluid system is increased, as shown in **Figure 2.20**. As discussed above, the molecules prefers to stay parallel to the pore wall surface, the disorder of the system is reduced and the entropy of the system decreases. The Gibbs free energy involves a positive enthalpy and a negative entropy term, therefore, the reduction in the entropy and increases in the enthalpy can increase the Gibbs free energy in the nanoscale pores. As the Gibbs free energy indicates the energy needed to introduce into the system to create a new system. It indicates that the confinement effect helps to keep the system in a single phase, so the energy needed to create a new phase will be enlarged by the confinement effect. As shown in **Figure 2.21**, when the fluid sample is flashed at 1200 *psia* and

156 *F*, the vapor fraction is reduced by the confinement effect. With a pore size of 100 *nm* or less, the confinement effect will not be negligible.

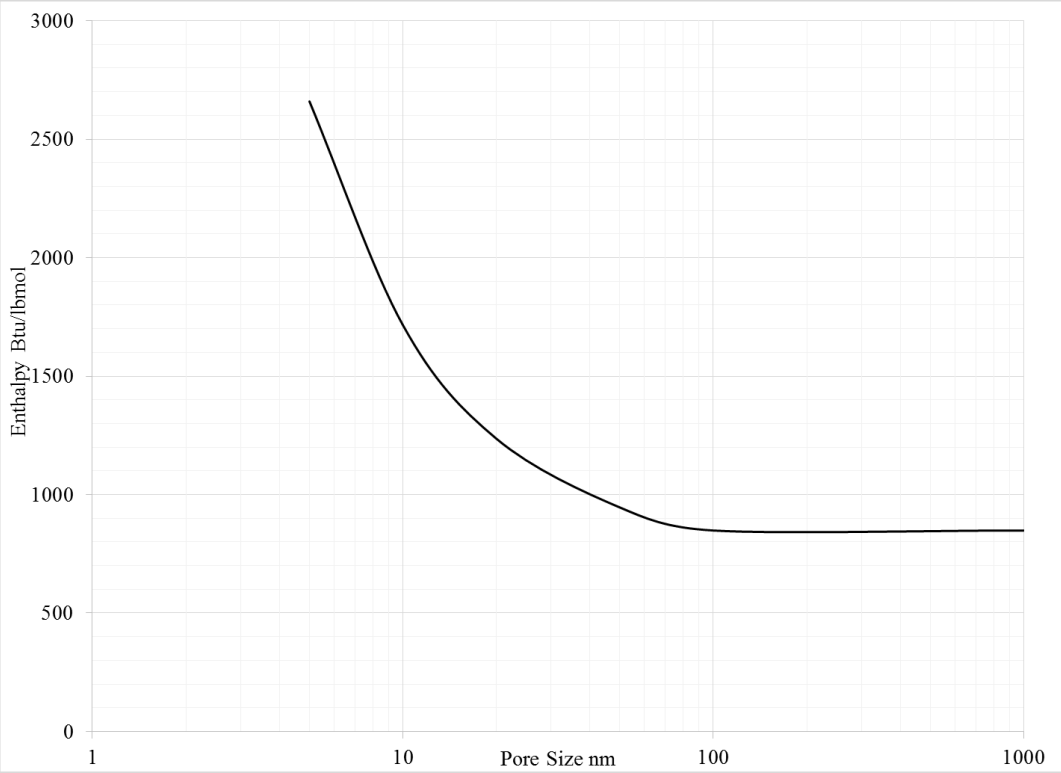

Figure 2.20 Fluid Enthalpy (Zhang, 2016)

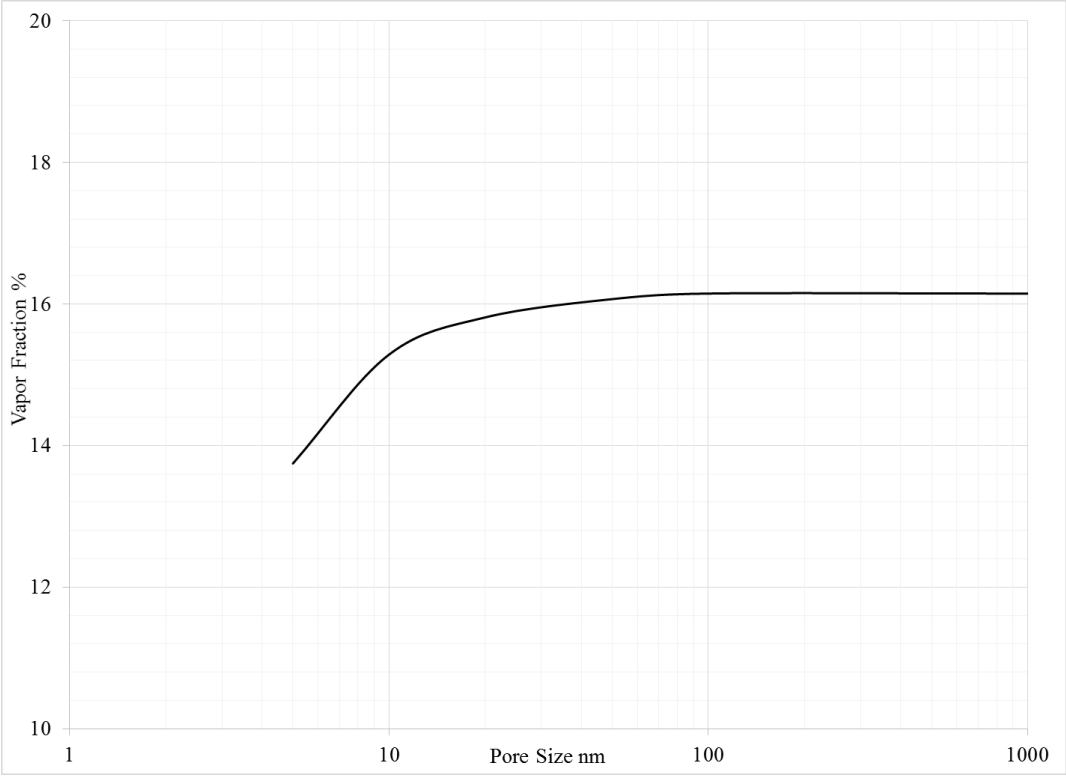

Figure 2.21 Flash Calculation of a Fluid Sample (Zhang, 2016)

The phase envelope is created and shown in **Figure 2.22**. The saturation pressure is altered by the confinement effect, which is not negligible when the pore size is 100 *nm* or less.

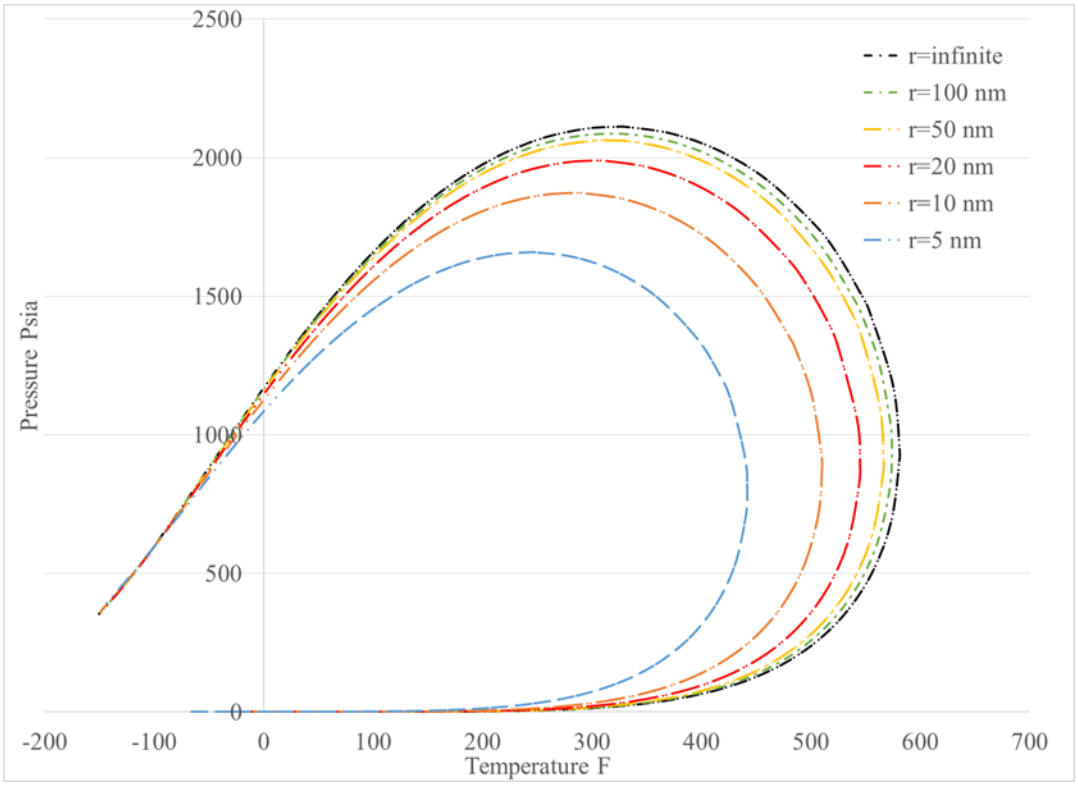

Figure 2.22 Effect of Confinement at Various Pore Radii on Phase Envelope (Zhang, 2016)

In addition, the fugacities of CH_4 and C_6H_{12} are recorded and shown in **Figure 2.23**. The fugacity of a light hydrocarbon component, like CH_4, is reduced by the confinement effect. The fugacity of a heavier hydrocarbon component, however, is increased by the confinement effect. Fugacity indicates the tendency of the molecule to escape into a gas phase. It means that CH_4 prefers to stay in the liquid phase while heavier components will enter the gas phase with the confinement effect. In this case, the vapor and liquid phase compositions will become closer to each other. As shown in **Figure 2.24**, the fluid sample is flashed at 1200 *psia* and 156 *F*; the liquid phase is closer to the fluid sample as the vapor fraction is reduced by the confinement effect. The equilibrium vapor and liquid phases become closer to each other with the confinement effect, which is shown as a dashed line in the plot.

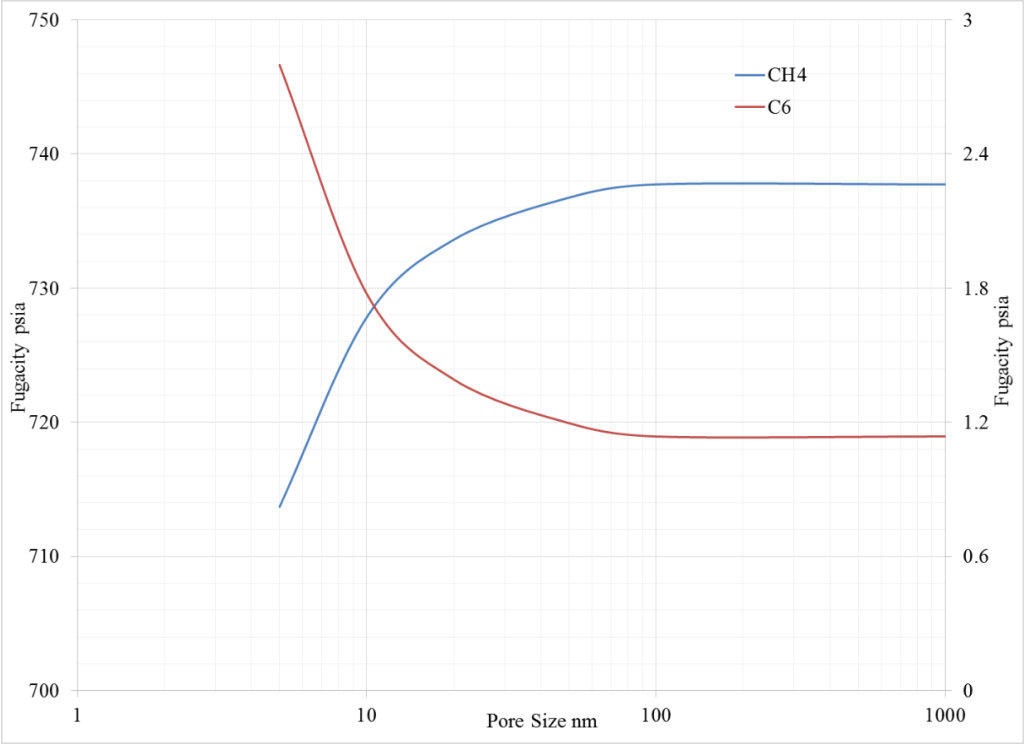

Figure 2.23 Fugacity of Light and Heavier Components (Zhang, 2016)

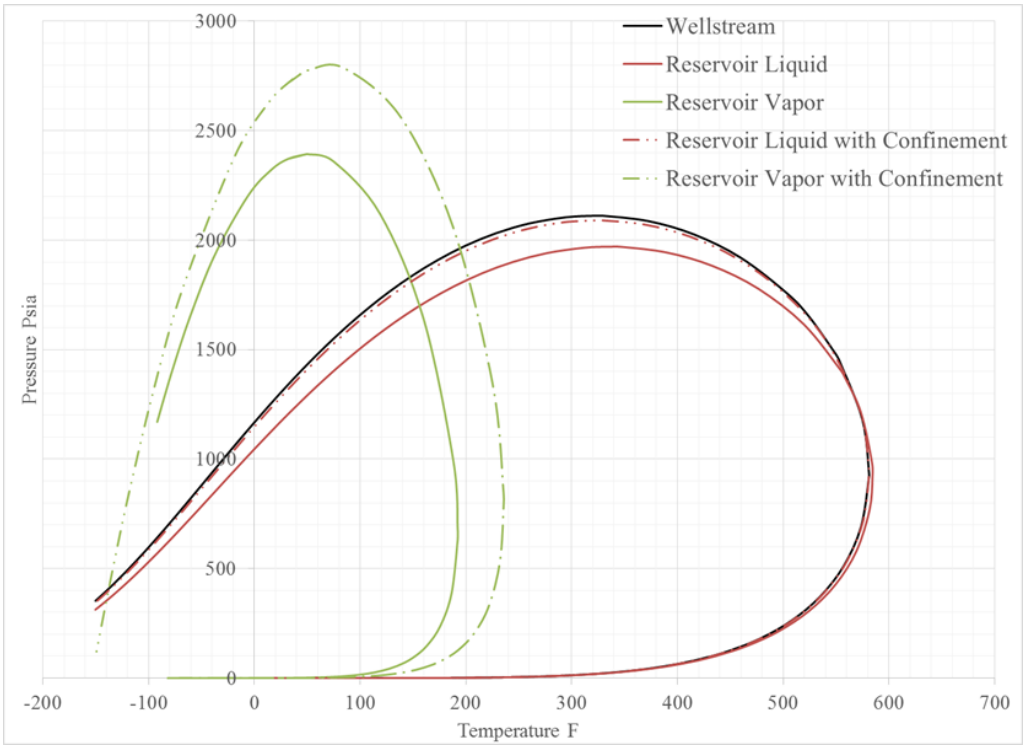

Figure 2.24 Phase Envelope of Equilibrium Composition (Zhang, 2016)

Light and heavy components exist in nanopores; the variation between the energy at specific positions and the energy at the center of the nanotube is recorded in **Figure 2.25**. The case of C_2H_6 inside the nano-channel has larger bond energy parameter compared to the case of CH_4 at the molecular separation distance, where the attraction and repulsion forces are equal, which indicates CH_4 has less interaction in a nanopore. The light components are absorbed less in the nanopore, as they have a higher diffusivity and can move out of the pore more easily. When the CH_4 and C_2H_6 molecules coexist in the nanopore, CH_4 can flow out of the pore first because the interaction between CH_4 and the pore surface is less than that of C_2H_6 as shown in **Figure 2.26**.

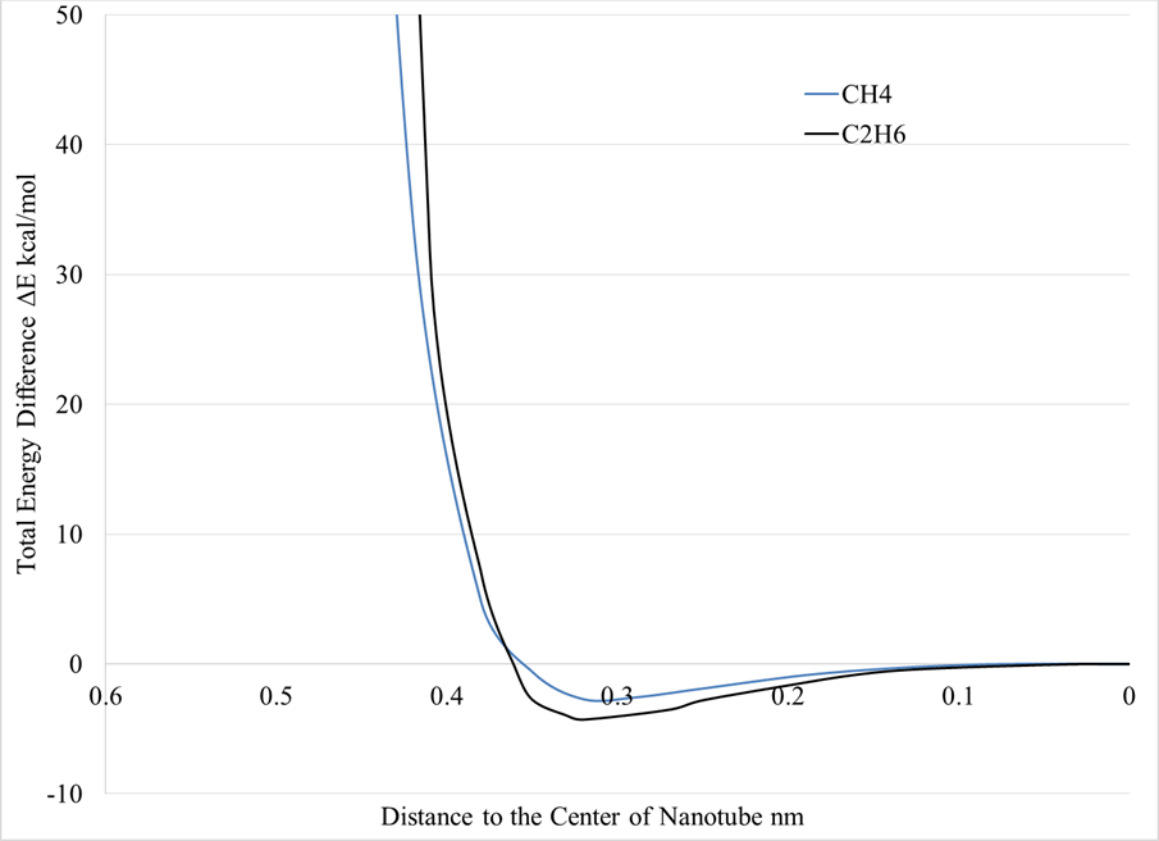

Figure 2.25 Total Energy of CH_4 or C_2H_6 in Nanotube (Zhang, 2016)

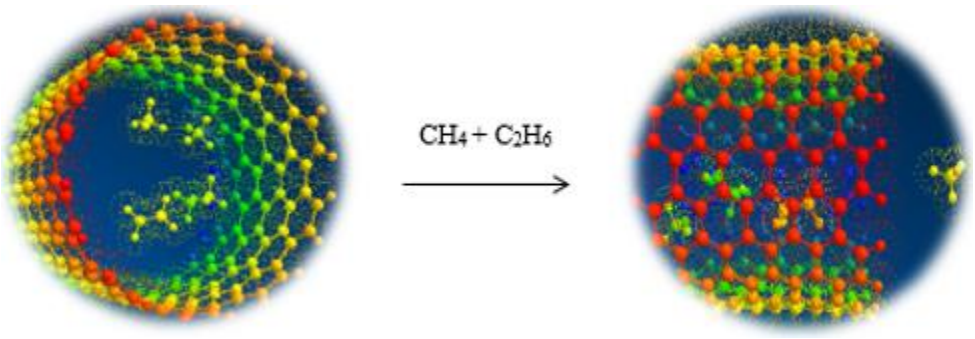

Figure 2.26 Hydrocarbons Coexist in Nanopores (Zhang, 2016)

Considering a hydrocarbon component is in a nanopore, the interaction between the molecule and the pore surface is presented. As shown in **Figure 2.27**, CH_4 is inside the center of the carbon nanotube with different pore sizes. The total energy of the system is recorded; the interaction between the molecule and the pore wall surface becomes stronger as the pore size decreases. It indicates that more work is needed to break the current equilibrium. In this way, the movement of molecules becomes more difficult.

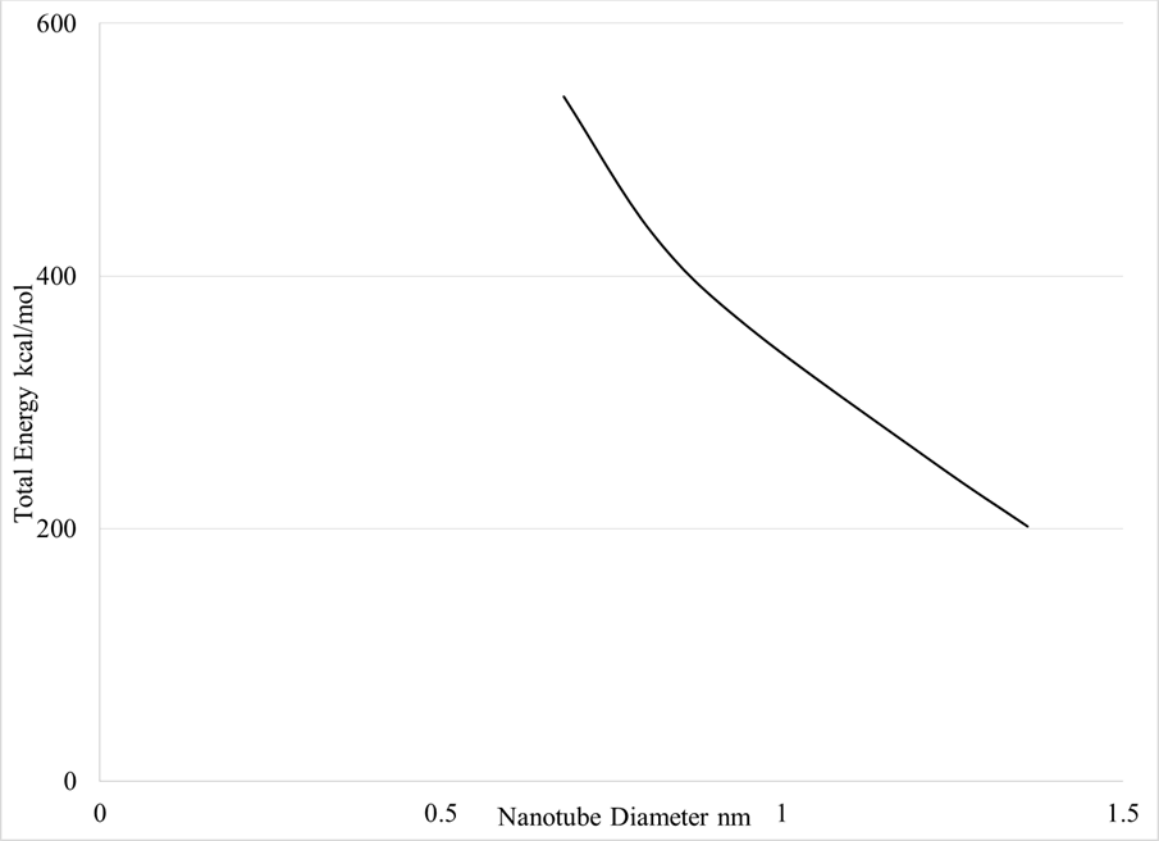

Figure 2.27 CH_4 in Nanotubes (Zhang, 2016)

Once a molecule is transported through a narrow system, there is a potential-energy barrier for the molecule to travel from one side of the wall surface to another. If the molecules do not have the enough energy to balance the potential-energy barrier, the molecules will creep along the pore walls and keep to collide with the pore wall surfaces in a slow motion (Derycke, 1991).

The magnitude of the potential-energy barrier on the pore surface depends on the interaction of energy between a molecule and the pore surface, which is called surface potential energy ε_s, which controls the magnitude of the potential energy barrier. Within a certain distance from the pore wall surface, a potential field including the attraction and repulsion forces is available. The collisions and rebounds of molecule are under the influence of the potential field. The molecule

rebounds with a different direction and kinetic energy at each collision. The rebounding molecules can be classified into two groups based on the differences in their molecular kinetic energy ε_v and surface potential energy ε_s, as shown in **Figure 2.28** (Shindo, 1983).

When $\varepsilon_v < \varepsilon_s$, the molecules unable to pass through the porous system will continue to collide with and stay along the pore wall surface.

When $\varepsilon_v > \varepsilon_s$, molecules may travel through the potential field and continue to collide with another pore surface. The collision direction can be altered by the pore wall surface, as shown in **Figure 2.29** (Shindo, 1983).

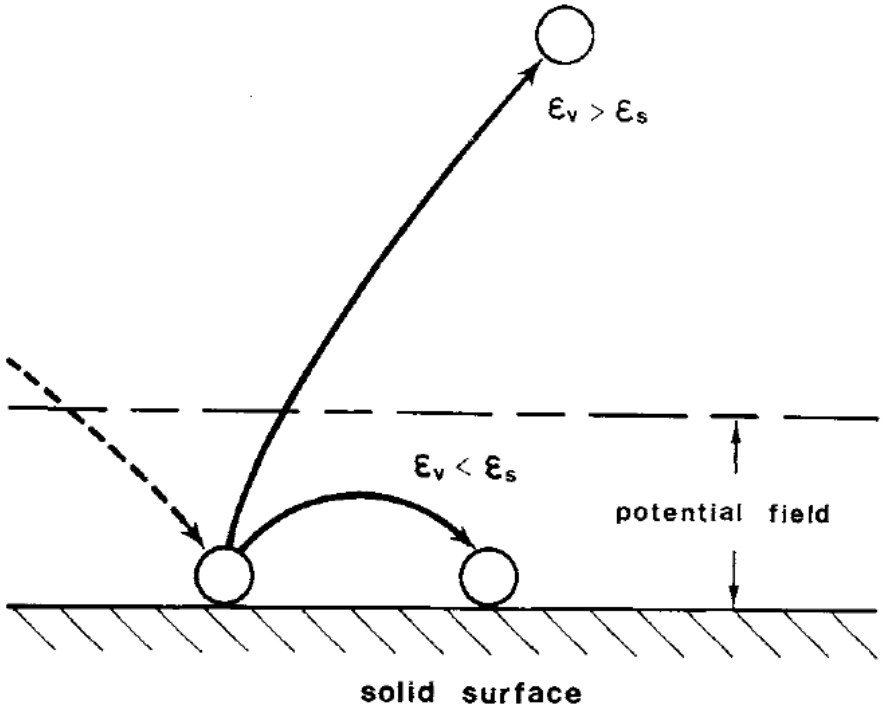

Figure 2.28 Schematic View of Rebounds of Gas Molecules on Solid Surface (Shindo, 1983)

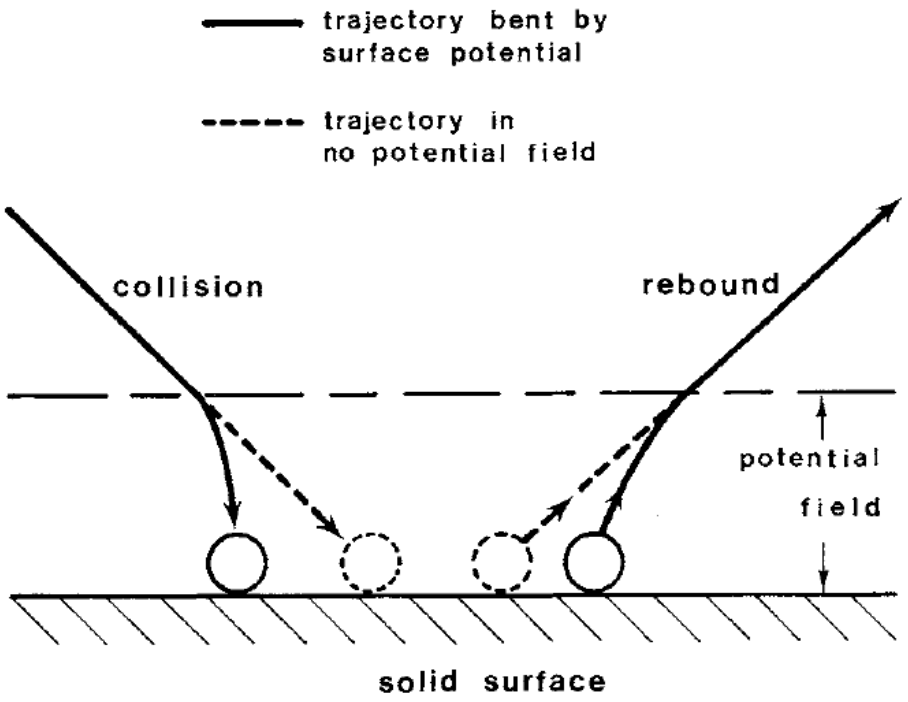

Figure 2.29 Schematic View of Collision and Rebound for Molecules in Gas-Phase Flow Influenced by Surface Potential Energy (Shindo, 1983)

Based on the above analysis, the confinement effect becomes negligible when a pore diameter is 100 *nm* or larger. There is a possibility of no apparent flow in a pore of a significantly small size. To investigate the critical pore size for molecules to flow, numerous scenarios made by molecular dynamic simulations are carried out in nano-channels with various characteristics.

As shown in **Figure 2.30**, an Armchair nanotube is shown on the left and a Zig-zag arrangement nanotube is shown on the right. The grey atoms represent the carbon and the white terms are the hydrogen atoms. The movement of CH_4, C_2H_6, C_6H_6, and C_6H_{12} molecules inside the nano-channels is tested. Results are presented in **Table 2.3**.

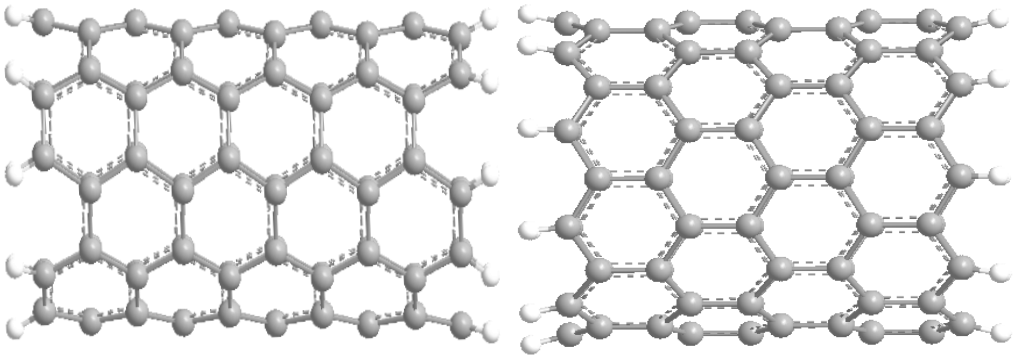

Figure 2. 30 Armchair Nanotube (Left) vs. Zig-zag Arrangement of Carbon Nanotube (Right), the Grey Atoms Represent the Carbon and the White Molecules are Hydrogens.

In the armchair carbon nanotubes, CH_4 with a diameter of 0.38 *nm* gets stuck inside the armchair (5,5) nanotube with a diameter of 0.68nm; however, it travels through the armchair (6, 6) nanotube with a diameter of 0.81 *nm*. When C_2H_6 has a diameter of 0.44 *nm*, it is difficult to move through the nanotube with a diameter of 0.81 *nm*. Instead, it goes out through the nanotube of 0.95 *nm*, which is more than two times that of the molecule size. There is a possibility for the molecule to transport through the pore with at least two times the molecular diameter. This tendency also works for the other molecules in the investigation, including C_6H_6 and C_6H_{12}.

Table 2. 3 Molecules Movement in Armchair Nanotube (Zhang, 2016)

Molecules Property		Armchair Nanotube Diameter in *nm*						
Type	Diameter in *nm* (Xiao, 1992)	1.36	1.22	1.09	0.95	0.81	0.68	0.41
CH_4	0.38	√	√	√	√	√	×	×
C_2H_6	0.44	√	√	√	√	×	×	×
C_6H_6	0.585	√	√	×	×	×	×	×
C_6H_{12}	0.6	√	√	×	×	×	×	×

√ indicates molecules can flow through the nanotube. However, × means the molecule will be trapped in the nanotube

The geometry alteration of carbon bonds in the nanotube may affect the interaction between a molecule and the nanotube. The zig-zag carbon nanotubes are built to study the effect of various carbon bond arrangement on the critical pore size for molecules to flow. As shown in **Table 2.4**, when CH_4 has a diameter of 0.38 *nm*, it gets stuck inside the zig-zag (9, 0) nanotube with a diameter of 0.71 *nm*; it does, however, move through the Zig-zag (10,0) nanotube with a diameter of 0.78 *nm*. The same experience occurs with the Armchair nanotube: The molecules can move through the pore with at least two times the molecular diameter.

Table 2. 4. Molecules Movement in Zig-zag Nanotube

Molecules Property		Zigzag Nanotube Diameter in nm									
Type	Diameter in *nm* (Xiao, 1992)	1.41	1.33	1.25	1.18	1.10	1.02	0.94	0.86	0.78	0.71
CH_4	0.38	√	√	√	√	√	√	√	√	√	×
C_2H_6	0.44	√	√	√	√	√	√	√	×	×	×
C_6H_6	0.585	√	√	√	×	×	×	×	×	×	×
C_6H_{12}	0.6	√	√	√	×	×	×	×	×	×	×

√ indicates molecules can flow through the nanotube. However, × means the molecule will be trapped in the nanotube

In addition to the different geometries of the nanotube, the shape and roughness of the pore structure can also affect the interaction between molecules and the pore wall surface, resulting in a variation in molecules' movement. As shown in **Figure 2.31**, instead of a spherical surface, a cube-shaped nano-channel is created. On the left, the cube-shape nano-channel is used to investigate the molecules movement; afterwards, the surface roughness is modified to observe its effect on molecules' movement. In addition, the functional group -OH is added into the system to further test movement.

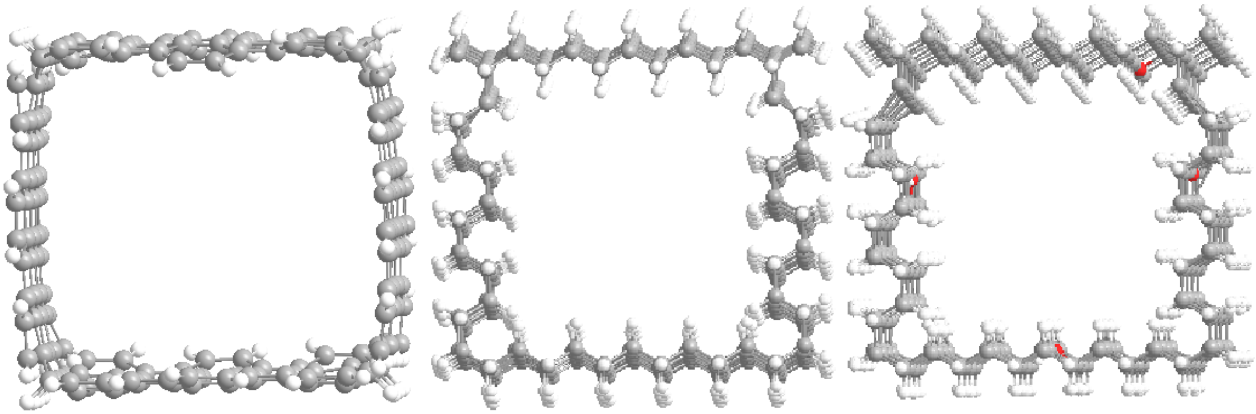

Figure 2. 31 Example for the Nano-Cube (Left) vs. Rough Nano-Cube (Middle) vs. Rough Nano-Cube with Functional Group (Right), the Red Molecules are Functional Group OH.

The nano-cubes are used to test molecules' movement. The results are shown in **Tables 2.5** and **2.6**. In the smooth nano-channel, the same results can be obtained: Molecules can get through a nano-channel with at least two times molecules' size. In the case of the rough nano-cube, the roughness of the nano-cube decreases the mean square displacement and diffusion of the molecules, to some extent. In the case of C_6H_6, it cannot go through the rough nano-cube with a lateral of 1.03 *nm*; it can, however, cross the rough nano-cube with a lateral of 1.18 *nm*, which is around 2.5 times the molecule. The same is experienced with molecules of C_2H_6.

Table 2. 5 Molecular Movement in Nano-cube

Molecules Property		Nano-Cube Lateral in *nm*				
Type	Diameter in *nm* (Xiao, 1992)	1.98	1.53	1.21	1.01	0.79
CH_4	0.38	√	√	√	√	√
C_2H_6	0.44	√	√	√	√	×
C_6H_6	0.585	√	√	√	×	×
C_6H_{12}	0.6	√	√	×	×	×

√ indicates molecules can flow through the nanotube. However, × means the molecule will be trapped in the nanotube

Table 2. 6 Molecular Movement in Rough Nano-cube

Molecules Property		Rough Nano-Cube Lateral in *nm*				
Type	Diameter in *nm* (Xiao, 1992)	2.01	1.51	1.18	1.03	0.77
CH_4	0.38	√	√	√	√	×
C_2H_6	0.44	√	√	√	×	×
C_6H_6	0.585	√	√	×	×	×
C_6H_{12}	0.6	√	√	×	×	×

√ indicates molecules can flow through the nanotube. However, × means the molecule will be trapped in the nanotube

The functional group OH is added into the rough nano-channel to investigate the movement of molecules. The results are shown in **Table 2.7**. As the functional group -OH is hydrophilic, it will help to repel the hydrocarbons. The molecules can get through the nano-channel with around two times molecules' size.

Table 2. 7 Molecular Movement in Rough Nano-cube with Functional Group

Molecules Property		Rough Nano-Cube Lateral in nm				
Type	Diameter in *nm* (Xiao, 1992)	2.01	1.51	1.18	1.03	0.77
CH_4	0.38	√	√	√	√	√
C_2H_6	0.44	√	√	√	√	×
C_6H_6	0.585	√	√	√	×	×
C_6H_{12}	0.6	√	√	√	×	×

√ indicates molecules can flow through the nanotube. However, × means the molecule will be trapped in the nanotube

Since the oil in tight oil reservoirs is mainly light oil and without aggregated asphaltene, the maximum molecule diameter is around 2 *nm* (Nelson, 2009). There is a possibility for the molecules to transport through the pore with twice the biggest molecular diameter. Therefore, the pores having a diameter of 5 *nm* and above are possible for exploitation.

The confinement effect works in any pore size, however, it is negligible when a pore diameter is larger than 100 *nm*. The confinement effect becomes stronger with a reduction in the pore size.

If the pore diameter is less than 5 *nm*, the heavy components in the reservoir oil are difficult to cross over. The confinement effect mainly applied to the range of a pore diameter from 100 *nm* to 5 *nm*.

Chapter 3. Effects of Nanoscale Pore Confinement on CO_2 Injection in Tight Oil Reservoirs

Hydraulic fracturing is capable of boosting well productivity by enlarging a contact area between a well and a target formation (Ghaderi, 2012). For the Cardium tight sandstone reservoir and the Monteny liquid rich shale reservoir, horizontal wells with multistage hydraulic fracturing are the main way to unlock the oil. For the Pekisko tight limestone reservoir, the wells are partly vertical and partly horizontal, with acidizing and maybe with or without a hydraulic fracturing technique. An oil production rate declines rapidly and stabilizes at a low decline rate after about 9 to 12 months (Zhang, 2014). Primary recovery of tight oil reservoirs is as low as 5.0-15.0% of original oil in place (OOIP) even with horizontal wells and massive hydraulic fracturing (Manrique, 2010).

Since water injection offers benefits for reservoir pressure maintenance and economic feasibility, a waterflooding process is proposed to improve tight oil recovery in previous experimental and simulation work (Raju, 2004; Raju, 2005; Yong, 2012; Thomas, 2014;). Water, however, can form a film on a solid surface in a porous medium and the water membrane formed on the matrix surface can be up to 43 *nm*, which can drive water injectivity to a low extent in tight oil reservoirs (Yang, 2013). The critical pore diameter for water injection is around 90 *nm* (Yang, 2013). In tight oil reservoirs, the common pore diameter is approximately 30 *nm* to 2000 *nm* in tight sandstone reservoirs and 2 *nm* to 100 *nm* in shale reservoirs (Nelson, 2009). It is extremely difficult for water to imbibe into the liquid-rich shale plays. For the tight sandstone and limestone reservoirs, there is a possibility for water injection to boost oil recovery. In this case, the water injectivity cannot be high.

A CO_2 miscible flooding process is regarded as a primary EOR technique for light oil reservoirs (Zhang, 2015). Many CO_2 field applications in low permeability reservoirs have been recorded as successful (Leena, 2008). As shown in **Table 3.1**, for reservoir permeability ranging from 0.1 to 20 *md*, around 66% of CO_2 flooding processes in the USA are economically profitable. The projected formations are mainly sandstone, dolomite and limestone.

Table 3. 1 Field Case of CO_2 Flooding (Leena, 2008)

Field	Area	Formation	Poro	Perm	Depth		Oil	Prev.	Proj.
	acres		*%*	*md*	*ft*	API	*°F*	prod.	eval.
Slaughter	569	Dolo	12.5	6	4900	32	110	WF	Succ.
Slaughter	8559	Dolo	10	3	5000	32	107	WF	Succ.
Rangely Weber Sand	18000	S	12	10	6000	35	160	WF	Succ.
Mabee	3600	Dolo	9	4	4700	32	104	WF	Succ.
Slaughter Sundown	5500	Dolo	11	6	4950	33	105	WF	Succ.
South Cowden	4900	Dolo	11.7	11	4500	38	101	Prim.	Succ.
Vaccum	4900	Dolo	11.7	11	4500	38	101	Prim.	Succ.
Charlton 6	60	LS/Dolo		0.1-100	5450	43	103	Prim.	TETT
Charlton 30-31	285	LS/Dolo		0.1-100	5450	42	103	Prim.	Succ.
Dover 33	120	LS/Dolo	7	10	5400	43	108	Prim.	Succ.

Dover35	80	LS/Dolo	7	5	5400	43	108	Prim.	Succ.
Dover 35	70	LS/Dolo	5	0.1-100	5500	41	101	Prim.	Succ.
Dover36	200	LS/Dolo	7	5	5500	41	108	Prim.	TETT
Dover 36	190	LS/Dolo	3	0.1-100	5600	42	102	Prim.	Succ.
East Penwell (SA) Unit	1020	Dolo	10	4	4000	34	86	WF	Prom.
Greater Aneth Area	13440	LS	14	5	5600	41	125	Prim.	Succ.
Hanford	1120	Dolo	10.5	4	5500	32	104	Prim.	Succ.
Hanford East	340	Dolo	10	4	5500	32	104	WF	Succ.
Adair San Andres Unit	1100	Dolo	15	8	4852	35	98	WF	Prom.
Seminole Unit-Main Pay Zone	15699	Dolo	12	1.3-123	5300	35	104	WF	Succ.
Seminole Unit-ROZ Phase 1	500	Dolo	12	1.3-123	5500	35	104	none	Prom.
Seminole Unit-ROZ Phase 2	480	Dolo	12	1.3-123	5500	35	104	none	Prom.
Seminole Unit-ROZ Phase 1	480	Dolo	12	1.3-123	5500	35	104	none	Prom.

SACROC	49900	LS	4	19	6700	39	135	Prim./WF	Succ.
Lost Soldier	790	S/LS-Dolo	10.3	4	5400	35	181	WF	Succ.
Lost Soldier	120	S	7	10	7000	35		WF	Succ.
Wertz	1400	S	10	20	6000	35	163	WF	Succ.
Wertz	810	S/LS-Dolo	10	5	6400	35	170	WF	Succ.
Cedar Lake	2870	Dolo	14	5	4800	32	102	WF	Succ.
Cogdell	2684	LS	13	6	6800	40	130	WF	Succ.
Igoe Smith	1235	Dolo	11	4	5040	34	105	WF	Succ.
Levelland	1179	Dolo	12	2	4900	34	108	WF	Succ.
Mid Cross-Devonian Unit	1326	Tripol	18	2	5400	42	104	Prim., GI	Disc.
North Hobbs	3100	Dolo	15	15	4200	35	102	WF	Succ.
Salt Creek	12000	LS	20	12	6300	39	125	WF	Succ.
Slaughter North West Mallet	1048	Dolo	10	4	4950	32	105	WF	TETT
Slaughter West RKM Unit	1204	Dolo	9	4	4900	32	105	WF	TETT
South Welch	1160	Dolo	11	4	4900	34	98	WF	Succ.

Wasson Bennett Ranch Unit	1780	Dolo	11	8	5250	34	105	WF	Succ.
Wasson Denver Unit	27848	Dolo	12	8	5200	33	105	WF	Succ.
Wasson ODC Unit	7800	Dolo/LS	10	5	5100	34	110	WF	Succ.
Wasson Willard Unit	8500	Dolo	10	1.5	5100	32	105	WF	Succ.
West Welch	240	Dolo	10	3	4900	34	98	WF	Disc.
Dollarhide (Devonian) Unit	6183	Dolo	13.5	9	8000	40	122	Prim./WF	Succ.
Dollarhide (Clearfork"AB") Unit	160	Dolo	11.5	4	6500	40	113	Prim./WF	Prom.
Greater Aneth	1200	Dolo	12	18.3	5700	42	129	WF	Prom.
Wasson (Cornell Unit)	1923	Dolo	8.6	2	4500	33	106	WF	Succ.
Wasson (Mahoney)	640	Dolo	13	6	5100	33	110	WF	Succ.
Pembina	80	S	16	20	5300	41	128	WF	TETT

S: Sandstone, LS: Limestone, Dolo: Dolomite, Tripol: Tripolite, WF: Waterflood,

Prim: Primary, GI: Gas injection, Succ: Successful, Disc: Discouraging, TETT: Too early to tell

Recovery mechanisms related to CO_2 flooding include a swelling effect, a viscosity reduction,

an interfacial tension reduction and light components extraction (Pittaway, 1985; Mohammed, 2006; Zhang, 2015). Displacement of oil by CO_2 can develop miscibility through extraction of hydrocarbon components into a CO_2-rich phase (Orr, 1981). Generally, the displacement of oil by CO_2 does not depend on the presence of light hydrocarbon components (C_2-C_4) in crude oil. The extraction of hydrocarbons (~C_5 to C_{30}) contributes to miscibility and a reduction in interfacial tension (Holm, 1974). A significant alteration in gas-oil relative permeability occurs when the interfacial tension drops to 0.04 *dyne/cm* by CO_2 miscible flooding (Longeron, 1980). As shown in **Figure 3.1**, the oil swelling factor during CO_2 injection is larger in separator conditions than in reservoir conditions, which indicates that the liberation of solution gas does not impede oil swelling during CO_2 injection. This also explains why CO_2 flooding, as a tertiary process, has better recovery than as a secondary process. Compared to the CO_2 in the secondary process, the reservoir has been further depleted in the tertiary process and the pressure is far beyond the bubble point pressure. As shown in **Figure 3.1**, the oil has a more chance to swell and the increment in the oil recovery can be further enhanced.

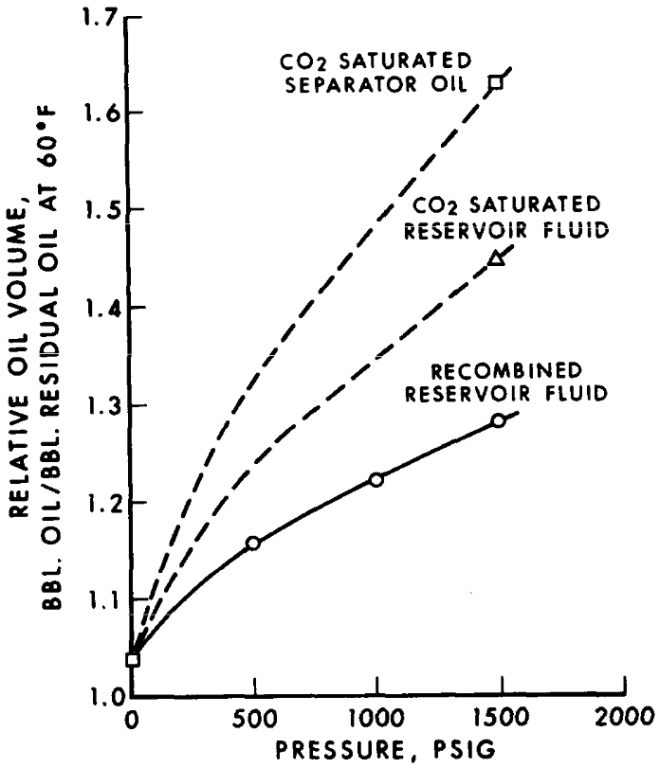

Figure 3.1 Relative Oil Volume vs Pressure at 144° *F*, West Texas Fluid (Holm, 1974)

During CO_2 flooding, the vaporizing and condensing gas drive contributes to improvement in oil recovery. The principle of the process is presented as follows.

To explain the process of vaporizing and condensing gas drive, oil compositions can be classified into essentially four groups of components. The first group consists of lean components including CO_2, N_2 and CH_4; the second group consists of light intermediate components including C_2-C_4; the third group contains middle intermediate components including C_5 to C_{30}; the fourth group consists of heavy components such as C_{30+} (Zick, 1986). In general, the displacement of oil by CO_2 does not depend on the presence of light hydrocarbon components (C_2-C_4) in crude oil. The extraction of hydrocarbons (~C_5 to C_{30}) contributes to miscibility and an interfacial tension reduction (Holm, 1974).

When gas contacts the oil, the light intermediates condense from the gas into the oil, and the middle intermediates are extracted from the oil into gas. The equilibrium gas is more mobile than the oil, and it moves ahead and is replaced by freshly injected gas. The equilibrium gas has a chance to contact fresh oil and the equilibrium oil left behind comes into contact with fresh gas. This forms a vaporizing gas drive (VGD) and condensing gas drive (CGD) in a reservoir. As CO_2 and oil keep contacting and propagating, multi-contact miscibility can be achieved in the transition zone before the condensation process reverts to the vaporization process (Zick, 1986), as shown in **Figure 3.2**. In general, 1.2 hydrocarbon pore volume (HCPV) of CO_2 injection can achieve CO_2 oil miscibility (Ahmadi, 2011). The extent of the hydrocarbon-CO_2 transition zone is a function of the displacement pressure. A longer transition zone is expected for flooding at a lower pressure (Ahmadi, 2011).

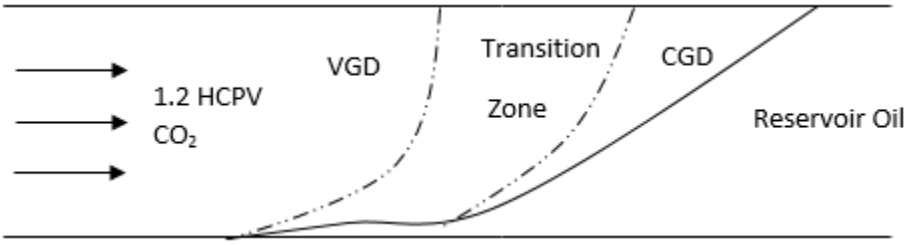

Figure 3. 2 CO_2 Drive Mechanisms Illustration (Zhang, 2016)

A ternary diagram represents phase behavior at a constant temperature and pressure (Martin, 1982). As shown in **Figure 3.3**, the curvature plot shows a bubble point curve representing oil mixtures at their bubble point and a dew point curve representing solvent mixtures at their dew point. The mixture inside the region bounded by the bubble and dew point curves consists of two phases; the mixture outside the region bounded by the dew point and bubble point is a single phase. The tie

line, shown as dashed lines, connects liquid and vapor compositions that are in equilibrium.

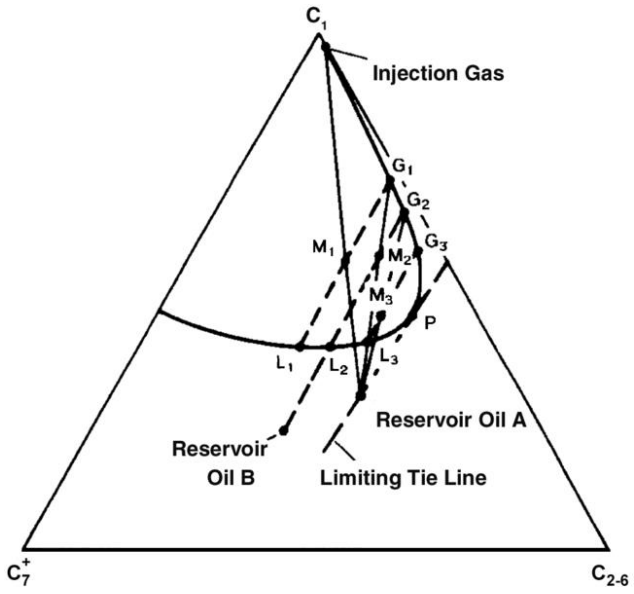

Figure 3.3 The Vaporizing Gas Drive Process (Martin, 1982)

In situ composition alterations when injected gas displaces oil is shown in **Figure 3.3**. Once the gas mixes with the reservoir fluid, an overall mixture composition such as M1 may result in. It is shown that M1 is inside the two-phase boundary of the diagram and can be flashed into dew point solvent G1 and bubble point liquid L1. As the gas injection process goes on, solvent G1 has a lower density than the liquid phase, it will move forward and contact with the fresh reservoir fluid. Another mixture can be formed by the G1 and reservoir fluid, resulting in an overall mixture composition M2, which will split into dew point solvent G2 and bubble point liquid L2. Afterwards, the vapor phase G2 will continue to move forward and make contact with the fresh reservoir fluid, forming an overall mixture M3, which consists of dew point solvent G3 and bubble point liquid L3. In this way, the vapor phase at the displacing front is progressively enriched by the extraction of the middle intermediates from the liquid phase. Once the vapor composition reaches a critical

composition, P, which drives the tie line length to be zero, the multi-contact miscibility is reached for the CO_2 with the reservoir fluid.

In the vaporizing drive process, as long as the reservoir fluid composition locates to the right of the limiting tie line through the critical point, multiple-contact miscibility is possible. If the oil composition lies to the left of the critical tie line, the multiple contacts enrichment can occur only to the composition of dew point solvent lying on the tie line that can be extended to pass through the oil composition. For example, reservoir oil A can reach miscibility with the injected gas, however, for reservoir oil B, enrichment of the solvent front can occur only up to dew point solvent G2.

During CO_2 flooding, it contains the extraction of oil components into the vapor phase and the gas phase can be condensed into the liquid phase. In condensing the gas drive mechanism, condensation of the light intermediates into the oil was thought to be the mechanism responsible for the development of multiple-contact miscibility. In this process, multiple contacts miscibility can be generated and propagated through the porous medium at the rear of the displacement front.

For example, solvent B comes into contact with oil, as seen in **Figure 3.4**. An overall composition, such as M1, may result in, which is in the two-phase region. It can be split into dew point solvent G1 and bubble point liquid L1, which are in equilibrium. Injection of fresh solvent B pushes the equilibrium vapor phase G1 ahead, which contacts the remaining oil around an injector with a composition L1. In this way, solvent B has a chance to mix with L1 and forms a new overall composition in the two-phase region, M2, which can be flashed into a new equilibrium

vapor phase G2 and equilibrium liquid phase L2 at reservoir conditions. Continued injection of fresh solvent B pushes the solvent G2 out of the way; B mixes with liquid L2 to form a new overall mixture M3. Afterwards, fresh solvent B successively contacts reservoir oil around the injector and enriches the oil by the condensation of the intermediates. The enrichment proceeds until the enriched liquid phase reaches the critical composition P, which has a zero tile line length. It indicates miscibility between the solvent and reservoir fluid.

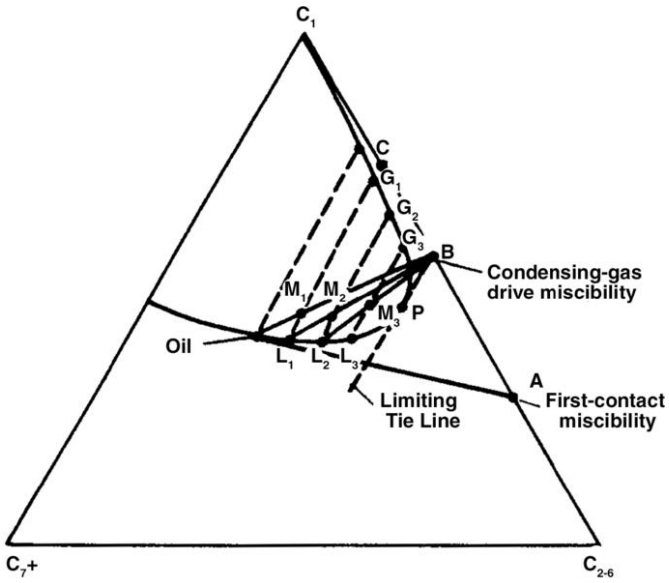

Figure 3.4 The Condensing Gas Drive Process (Martin, 1982)

If the composition of solvent locates to the left of the critical tie line, the displacement is immiscible because the oil cannot be enriched to the critical composition P. For solvent C injection, the reservoir oil can be enriched only to composition L1 on the dew point curve that passes through C when the tie line is extended. Further contact of L1 with solvent C can only give a new overall mixture on the tie line. Thus, the equilibrium vapor phase G1 on the tie line keeps displacing reservoir fluid, so the solvent G1 and the oil L1 are immiscible. The criterion for the condensing

drive mechanism is that the injected solvent composition must lie to the right of the critical tie line on the ternary diagram.

In general, the process of gas flooding is not just a vaporizing gas drive or condensing gas drive. For most reservoir oil, a combined mechanism that has both vaporizing and condensing drives can occur during gas flooding.

When the enriched gas comes into contact with the oil phase, the light intermediates including C2-C4 condense from the gas into the oil, which makes the oil lighter. The equilibrium gas is more mobile than the oil, so it moves forward and is replaced by fresh injection gas. As the light intermediates C2-C4 are condensing from the enriched gas phase into the oil, the middle intermediates C5-C30 are being extracted from the oil into the gas front, because the injection gas contains none of these middle intermediate components. After a few contacts between the oil and the injection gas, the reservoir oil will be saturated by the light intermediates C2-C4. The oil phase continues to lose the middle intermediates C5-C30, which are extracted out and carried ahead by the mobile gas phase. The light intermediates C2-C4 of the enriched gas cannot substitute for the middle intermediates C5-C30 because the oil is stripping. Therefore, the gas injection makes the oil lighter by net condensation of light intermediates after the first few contacts. Subsequent contacts make the oil much heavier by net vaporization of intermediates C5-C30.

Figure 3.5 shows that extraction of hydrocarbons from crude oil takes place at a certain pressure, and a large amount of CO_2 will dissolve into the oil prior to the extraction, resulting in an increment in a relative oil volume initially.

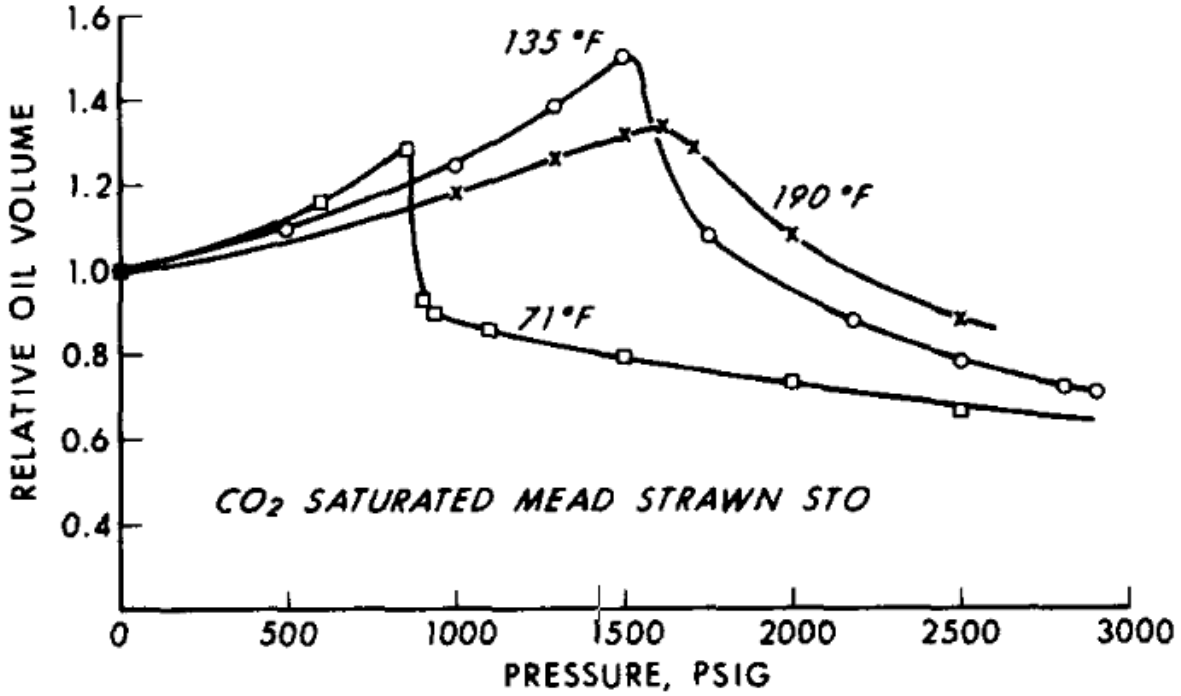

Figure 3.5 Change in Volume of Mead Strawn Stock Tank Oil (Holm, 1974)

A pseudoternary diagram can be used to characterize the condensing/vaporizing displacement in which the equilibrium vapor and liquid compositions are simulated in a slim tube displacement. Pseudo-components, lumped with different components based on the molecular weights of the fluid components, are plotted in the diagram. Instead of the minimum miscibility pressure determination in the three-phase diagram, the gas oil mixture behavior can be seen in the pseudoternary plot. As shown in **Figure 3.6**, the two-phase region has an hourglass shape instead of the two-phase envelope being shown in the three-phase diagram, in which the vapor and liquid are trying to reach a critical composition. Vapor and liquid compositions begin to diverge at the trailing part of the displacement prior to this occurring, which involves the gas oil mixture experiences from the vaporing to condensing gas drive (Martin, 1982).

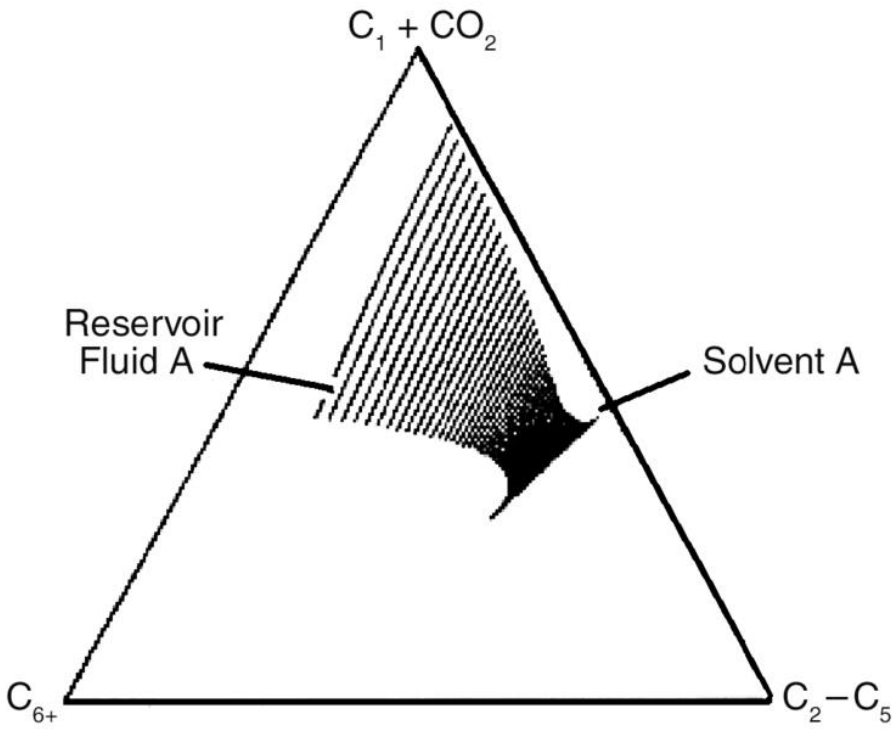

Figure 3.6 Pseudo-ternary Diagram (Martin, 1982)

Previous research shows that the CO_2 displacement efficiency is only related to the fluid composition, pressure and temperature (Martin, 1982). In tight oil reservoirs, a pore diameter is in the range of 30 to 2000 *nm* for sandstone and 2 *nm* to 100 *nm* for shale (Nelson, 2009). In such a confined system, alterations exist in van der Waals forces and molecular orientation and arrangement (Morishige, 1997; Zarragoicoechea, 2004; Singh, 2009; Travalloni, 2010; Devegowda, 2012; Pitakbunkate, 2015). The nanoscale pore confinement effect can cause fluid equilibrium alteration (Zhang, 2015) and critical properties shifts (Singh, 2009). The phase behavior of fluids deviates from that in the bulk state (Teklu, 2014). The transportation of hydrocarbons can also be affected by nanopores (Wu, 2015; Wu, 2015; Wu, 2016). When taking the confinement effect into consideration, variations in the CO_2 displacement between tight oil and

conventional oil reservoirs are evident (Zhang, 2015).

In the following section, the effects of nanoscale pores on phase equilibrium and fluid properties during CO_2 injection are investigated. As well, the CO_2 vaporizing gas drive (VGD) and condensing gas drive (CGD) with the confinement effect are studied and solubility parameters are applied to investigate gas-oil miscibility. The effects of nanopore confinement on CO_2 MMP are also investigated and the CO_2 stable and unstable displacements with the confinement effect are presented. In addition, alterations in gas-oil composition and interfacial tension during CO_2 injection are investigated to ascertain the results of the effect of nanopores on oil and gas relative permeability alteration and formation hysteresis.

3.1 Effects of Nanoscale Pore Confinement on the CO_2 Injection Process

During CO_2 flooding, the vaporizing and condensing gas drive mechanism will alter fluid compositions. In a nanopore, the molecular orientation and arrangement can be changed, resulting in a shift in the component's critical properties. In this way, the CO_2 injection process in tight oil reservoirs may vary from that in conventional oil reservoirs to some extent.

This section presents: the effect of nanoscale pore confinement on the CO_2 injection process, the fluid properties alteration during CO_2 injection and an analysis of the effect of nanoscale pore confinement on the stable and unstable CO_2 displacement.

Oil displacement by CO_2 can develop miscibility through the extraction of light hydrocarbon components into a CO_2-rich phase. In this process, a phase envelope of reservoir oil can be altered by CO_2 injection; a different volume of CO_2 injection results in various bubble point pressures. As shown in **Figure 3.7**, the bubble point pressure for reservoir oil rises as the amount of injected CO_2 increases.

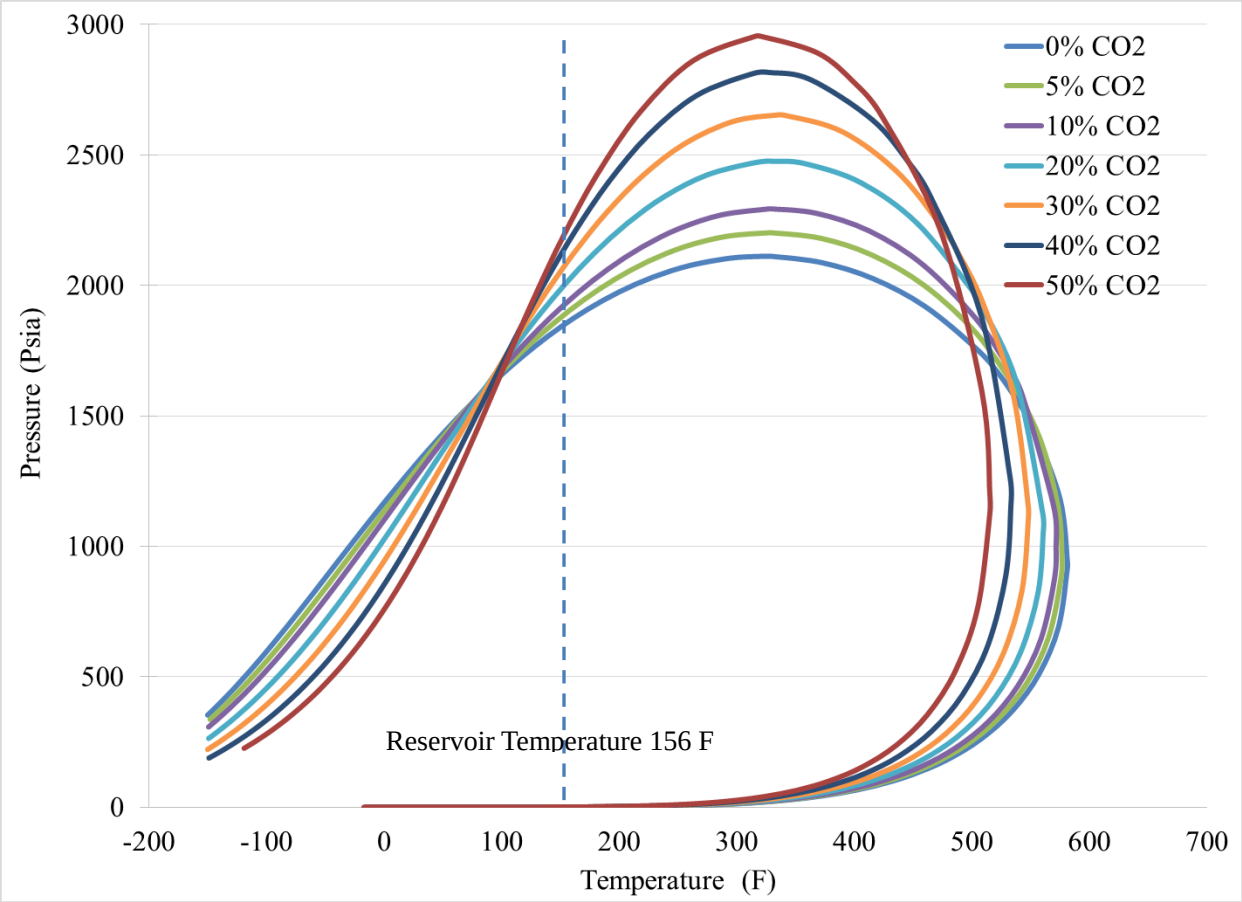

Figure 3.7 The Impact of CO_2 Concentration on Phase Envelope (Zhang, 2015)

In the process of CO_2 injection into tight oil reservoirs, the bubble point pressure is not only a function of the amount of CO_2 injected but also a function of the confinement effect caused by the nature of nanoscale pores. As shown in **Figure 3.8**, CO_2 injection has a chance of enlarging the bubble point pressure; however, the confinement effect decreases the bubble point pressure and the liquid region is further expanded by the confinement effect. The oil bubble point pressure is smaller with the confinement effect than that without the confinement effect during CO_2 injection.

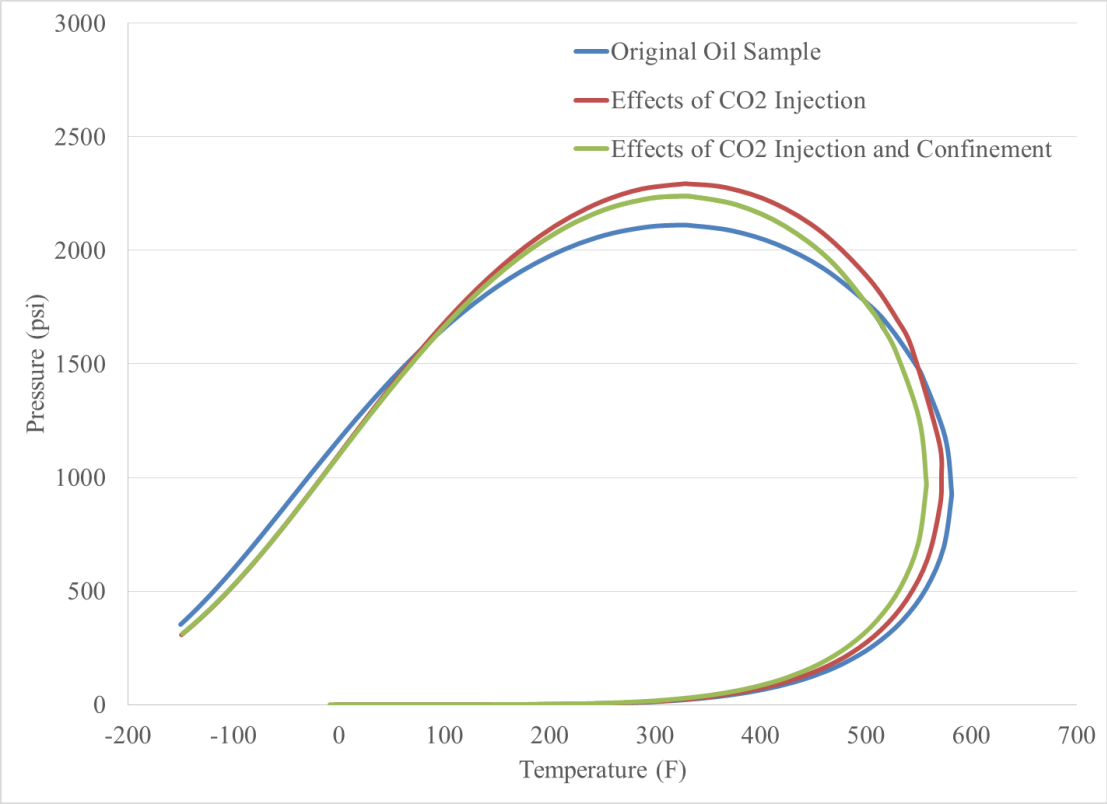

Figure 3. 8 Phase Envelope Alteration with Effects of CO_2 Injection and Confinement (Zhang, 2015)

When CO_2 is injected into an under-saturated oil reservoir, which is simultaneously producing fluids at a higher rate, the reservoir pressure decreases. The production and the bubble point pressure increase with an incremental injection of CO_2. For oil with API greater than 30, the bubble point pressure is related to the solution gas ratio R_s as given by the following equation (Curtis, 2000), and the solution gas-oil ratio increases as the bubble point pressure increases:

$$P_b = \left[a\left(\frac{R_s}{\gamma_{gc}}\right) b^{\left(\frac{-c*API}{T+460}\right)}\right]^d \tag{3.1}$$

A linear relationship between the oil formation volume factor and the solution gas-oil ratio at the bubble point pressure exists, as given by the following equation (Curtis, 2000):

$$B_{ob} = a + bR_s + cR_s\left(\gamma_g/\gamma_g\right) + dR_s(T-60)(1-\gamma_o) + e(T-60) \qquad (3.2)$$

The process path for CO_2 injection in tight oil reservoirs is shown in **Figure 3.9**. For conventional oil reservoirs, the process path during CO_2 injection is plotted as a solid line. The bubble point pressure in this case is only a function of the amount of CO_2 injection. In tight oil reservoirs, however, the increment of the oil bubble point pressure induced by injected CO_2 is less than that in conventional oil reservoirs. In this case, the oil formation volume factor and solution gas-oil ratio are smaller than those in conventional oil reservoirs. This is shown as a dashed line in **Figure 3.9**. The net effect is that the oil formation volume factor and solution gas-oil ratio are smaller than those without the confinement effect after a period of CO_2 injection.

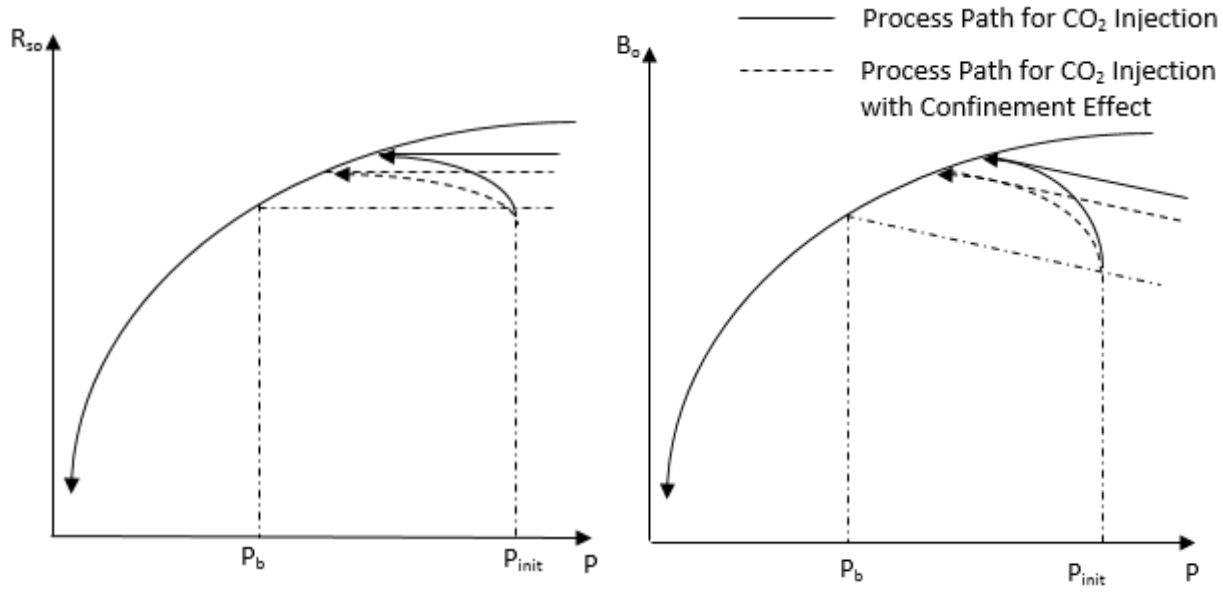

Figure 3.9 Process Path for CO_2 Injection in Conventional and Tight Oil Reservoirs (Zhang, 2015)

When CO_2 is flooding a reservoir, the vaporizing and condensing drive mechanism propels the gas and oil compositions close to each other. Assuming that 20 mole percentage of CO_2 makes

contact with the reservoir fluid, the phase envelope is presented in **Figure 3.10**. Once the CO_2 contacts with the reservoir fluid, more alteration can be recorded in the gas phase envelope than the liquid phase, and the gas and liquid phase envelopes approach each other during CO_2 flooding. Furthermore, with the confinement effect, the gap between gas and liquid is further decreased during CO_2 displacement.

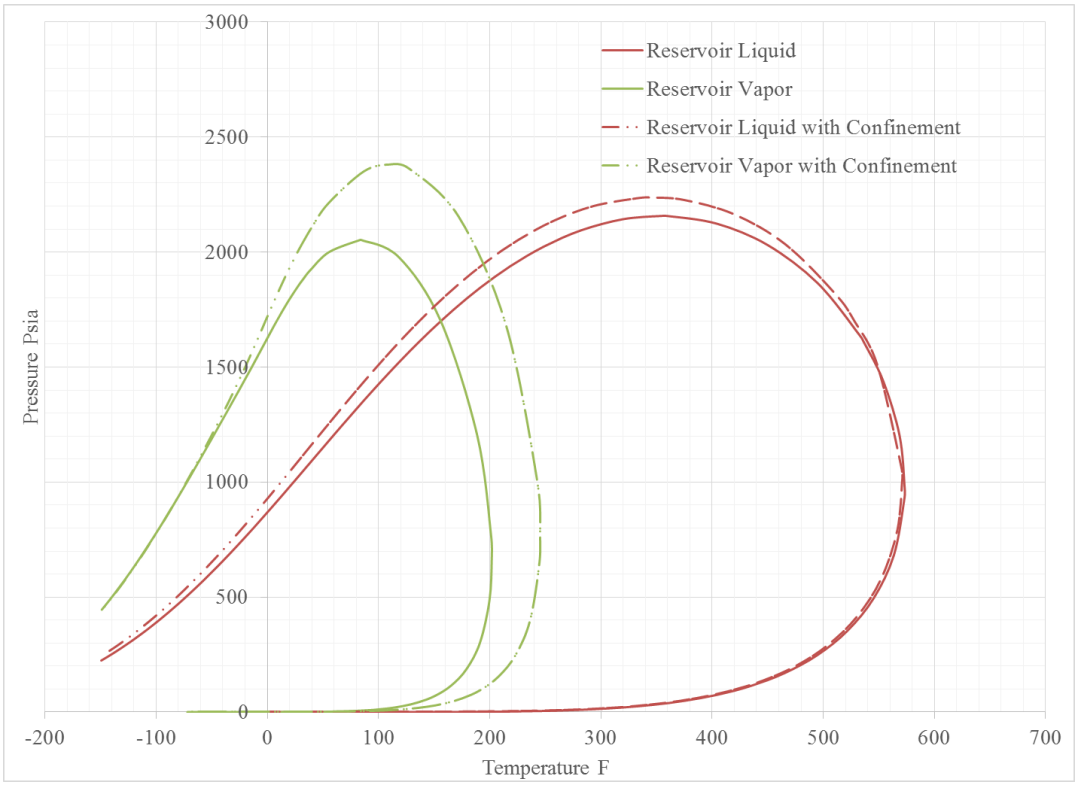

Figure 3.10 Phase Envelope for Reservoir Fluid Contacts with 20% CO_2 (Zhang, 2016)

In the vaporizing gas drive (VGD) process, the intermediate components from the oil will be liberated to the gas phase once CO_2 gets the first contact with oil. The equilibrium gas moves forward and maintains contact with fresh oil in the flooding front. At each contact of the equilibrium gas from the last stage and the fresh oil in the flooding front, the mixture formed will split into the new equilibrium gas and liquid phases. The composition alteration record as well as

the liquid and gas phase mole fraction during gas comes contact with the oil to be formed into new equilibrium phase are presented in **Figure 3.11**. A 20% mole fraction of CO_2 is in contact with fresh oil five times, and the liquid phase drops around 16% in mole fraction. Taking the confinement effect into consideration, the liquid phase alteration in mole fraction is about 19% and the efficiency of the VGD process is improved by 3%.

In the condensing gas drive (CGD) process, the mixture will split into the equilibrium gas and liquid phase once the CO_2 gets the first contact with oil, the light components from the gas will be condensed to the liquid phase. As the low density and viscosity of the equilibrium gas, it will move forward. And the equilibrium oil left behind comes into contact with the injected fresh gas. At each contact of the equilibrium oil and the fresh gas injected, the mixture formed will split into the new equilibrium gas and liquid phase.

The liquid and gas phase mole fraction alteration are presented in **Figure 3.12**. A 20% mole fraction of CO_2 is in contact with fresh oil five times and the liquid phase drops to around 12% in mole fraction. Assuming the process happens in a 10 *nm* pore size, taking the confinement effect into consideration, the liquid phase alteration in mole fraction is about 16%, and the efficiency of the CGD process is improved by 4%.

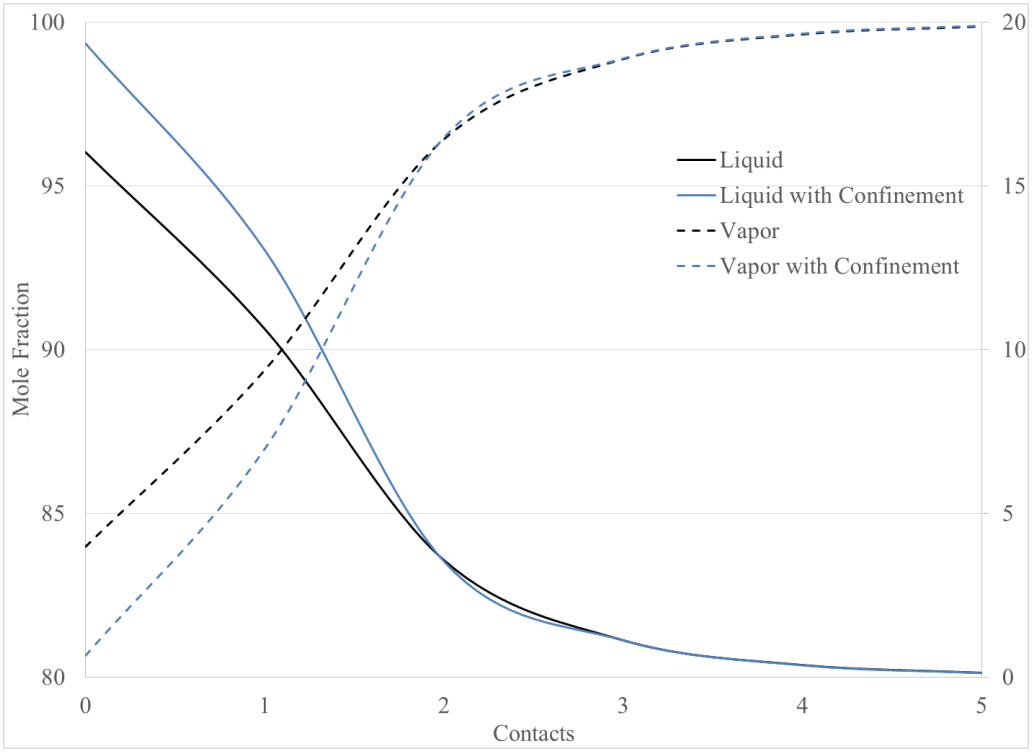

Figure 3. 11 Vaporizing Gas Drive (Zhang, 2016)

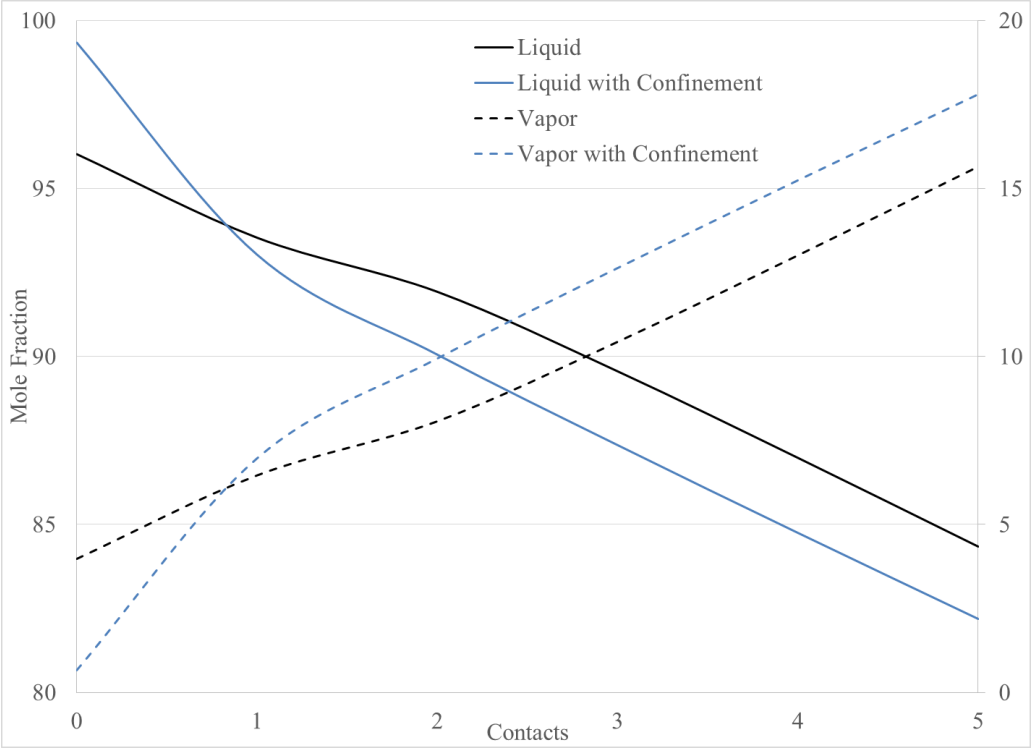

Figure 3.12 Condensing Gas Drive (Zhang, 2016)

In slim tube displacement, the equilibrium gas can be regarded as a solvent because it displaces oil through vaporization and condensation. The pseudo-ternary diagram is shown in **Figure 3.13**. The two-phase region has an hourglass shape. The vapor and liquid equilibrium compositions at first converge, as the simultaneous vaporizing and condensing drive mechanisms work. The vapor and liquid compositions begin to diverge at the trailing part of the displacement. Taking the nanoscale pore confinement effect into consideration, the molecular orientation can be altered. As shown in **Figure 3.14**, molecules are randomly distributed and oriented in a bulk state. The molecular orientation, however, alters into more parallelization in the confined system (Pitakbunkate, 2015). In this way, the multi-components dispersion can be suppressed by the confinement effect. As shown in **Figure 3.14**, molecules randomly disperse in the bulk state as the molecules are randomly oriented. The dispersion of multi-components is more parallel in a confined system. In this way, the efficiency of vaporizing and condensing gas drives can be improved. The equilibrium gas and oil compositions can be closer to each other with the nanoscale pore confinement effect. As shown in **Figure 3.13**, the dashed line represents the equilibrium gas and oil compositions, which is inside the solid line of compositions in the bulk state. The lower the gas dispersion, the smaller the residue oil saturation in the CO_2 VGD and CGD processes (Stalkup, 1987).

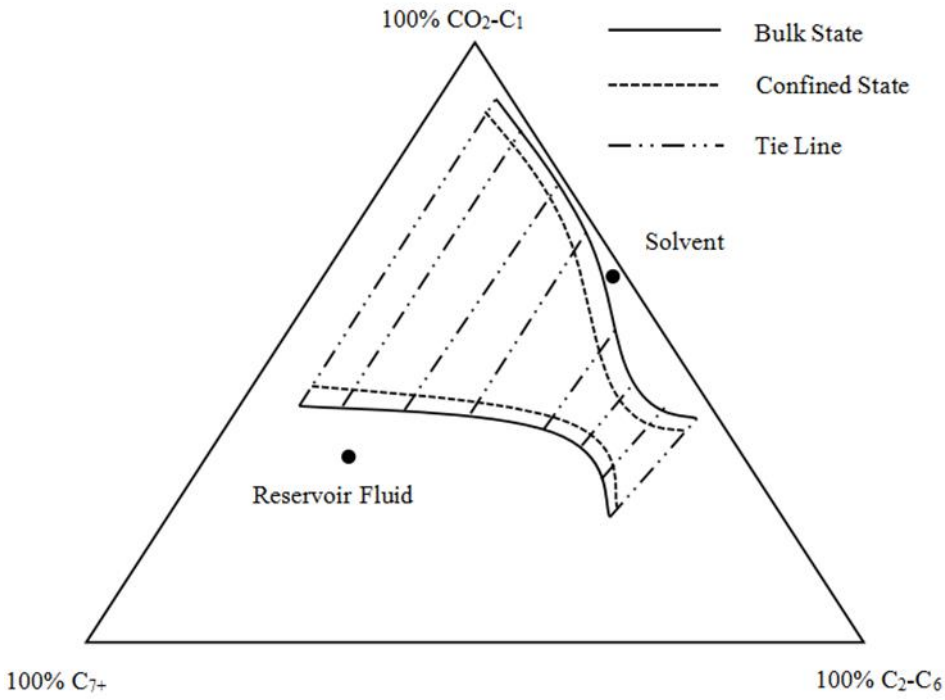

Figure 3.13 Pseudo-ternary Representation of Multi-contact Vaporizing and Condensing Drive (Zhang, 2016)

Figure 3.14 Molecular Dispersion in Bulk System (Left) and Confined System (Right) (Zhang, 2016)

The oil viscosity will be altered as the oil composition changes during CO_2 flooding. During CO_2 injection, the oil swelling causes a reduction in oil viscosity. The phase equilibrium of a CO_2 and oil system is recorded and the liquid and vapor viscosity is analyzed with the confinement effect. As shown in **Figure 3.15**, the greater the amount of CO_2 injected, the lower the liquid phase

viscosity. More CO_2 makes contact with oil and the gap between the liquid phase and gas phase viscosity gradually decreases. Taking the confinement effect into consideration, the difference in liquid and vapor viscosity is further reduced because the compositions of the gas and liquid phases tend to move closer to each other. The confinement effect contributes to a reduction in the liquid phase viscosity and an increment in the gas phase viscosity.

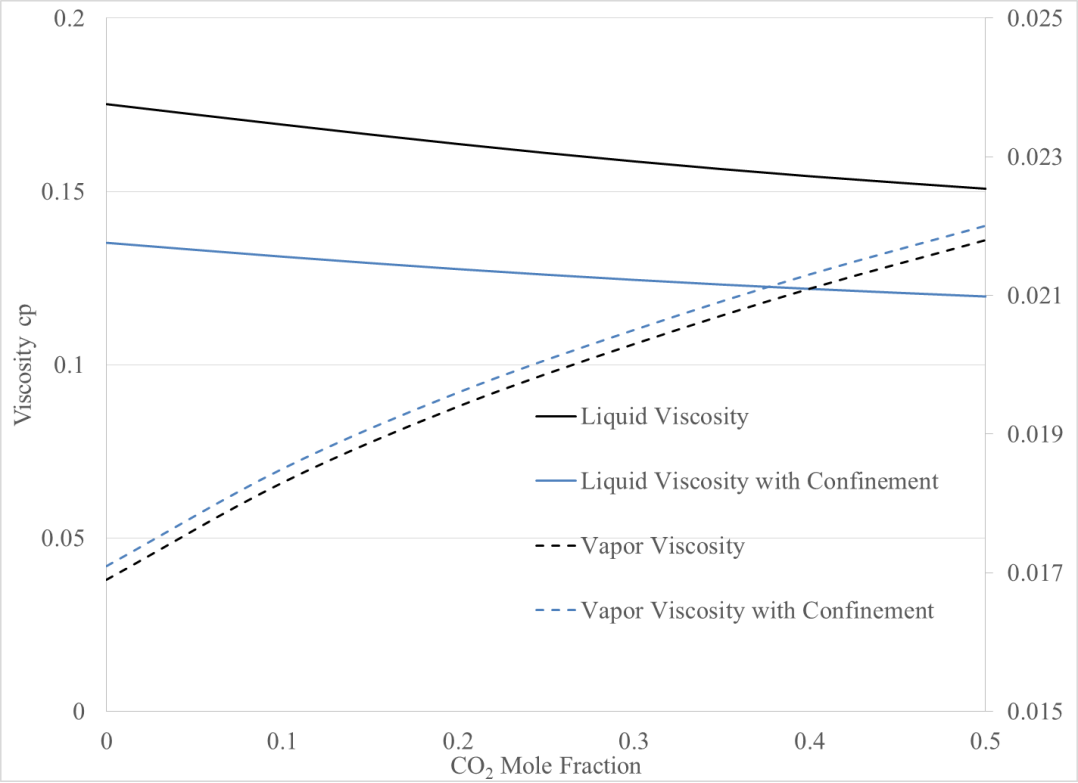

Figure 3.15 Phase Viscosity with Confinement Effect (Zhang, 2016)

The gas-oil mobility ratio is highly related to a vapor and liquid phase viscosity ratio. As shown in **Figure 3.16**, the liquid and vapor phase viscosity ratio decreases with the confinement effect. The smaller the pore size, the stronger the confinement effect and the lower the liquid-vapor viscosity ratio. As shown in **Figure 3.17**, the confinement effect on the viscosity ratio of the liquid and vapor phases cannot be negligible when a pore size is 100 *nm* or less.

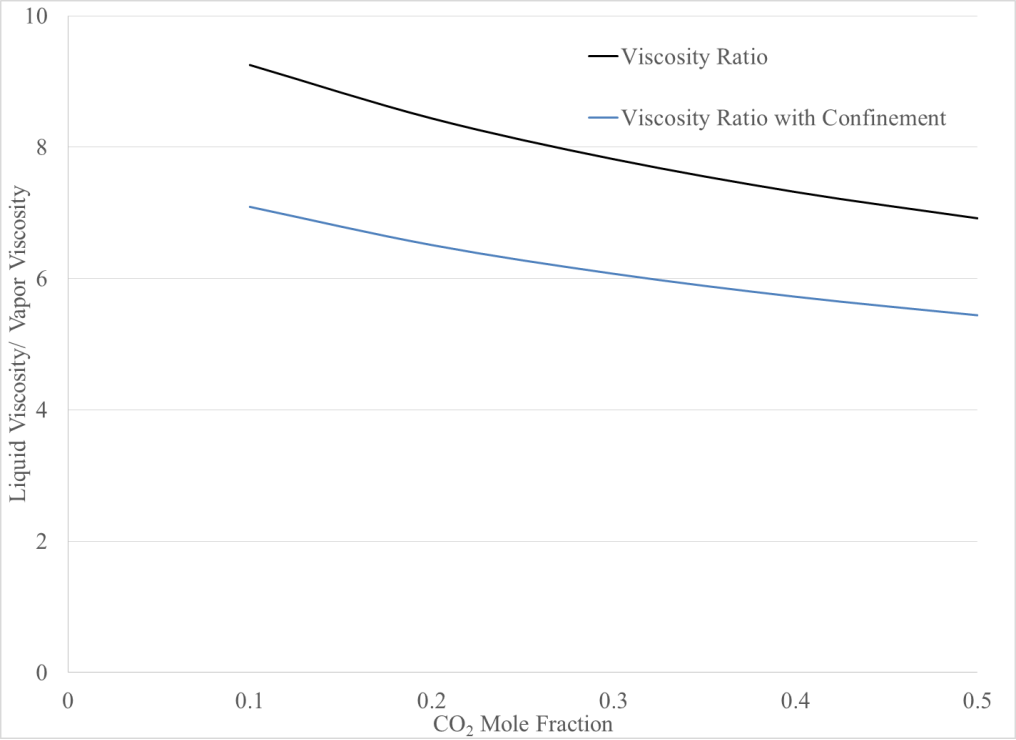

Figure 3.16 Liquid-vapor Viscosity Ratio (Zhang, 2016)

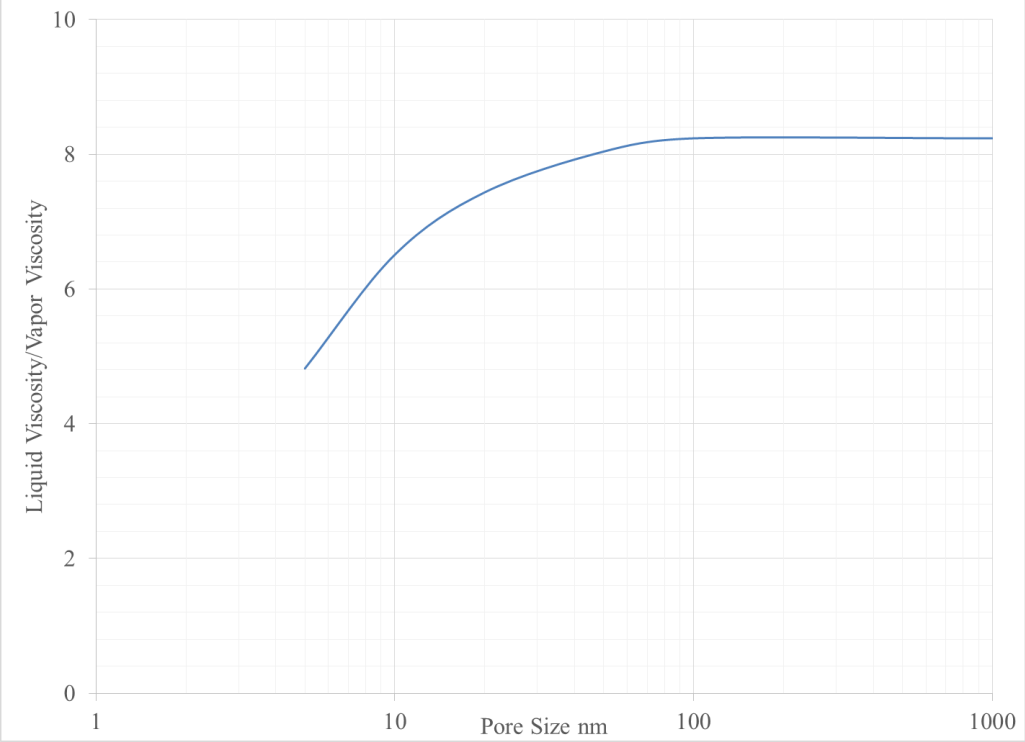

Figure 3.17 Liquid-vapor Viscosity Ratio at Various Radii (Zhang, 2016)

The gas-oil mobility alteration will affect the CO_2 stable and unstable displacement. In the case of a very low velocity of CO_2 injection, CO_2 moves forward and displaces oil downstream. Once the gas injection rate is high enough, the gas-oil interface is not horizontal and becomes unstable as shown in **Figure 3.18**. For a typical North Sea field, the critical gas-oil interface velocity is around 0.1378 *ft/day* (Kleppe, 2016).

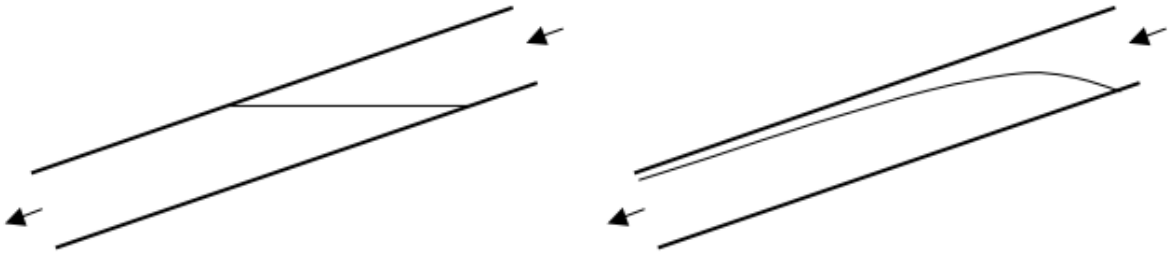

Figure 3. 18 Gas-oil Interface at Very Low Gas Injection Rate (Left) and Very High Gas Injection Rate (Right) (Kleppe, 2016)

Assuming a piston-like displacement, the Dietz principle (Hawthorne, 1960) is applied to capture the threshold velocity for stable CO_2 displacement. The assumptions is listed as follows (Kleppe, 2016):

1) Vertical equilibrium of oil and gas;
2) Piston displacement of oil by gas;
3) Gas-oil capillary pressure may be neglected;
4) Compressibility effects of rock and fluids may be neglected;

The gas front can be captured and the threshold velocity for a stable gas-oil interface movement can be obtained.

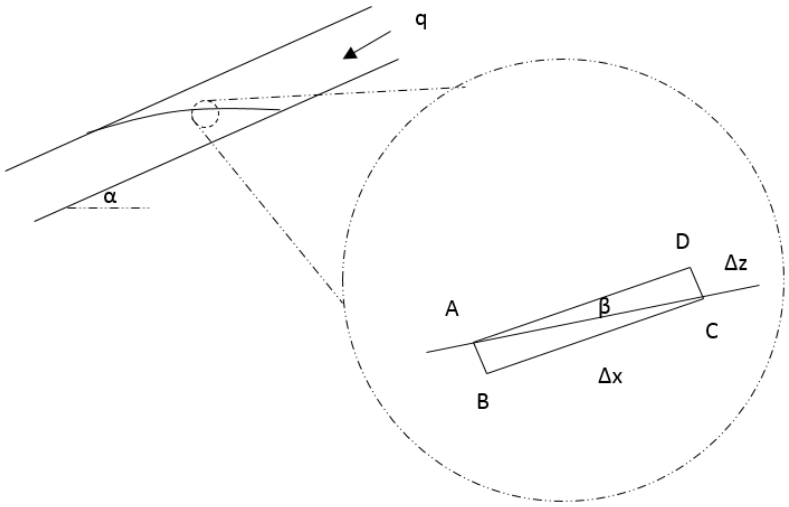

Figure 3.19 Dietz Analysis (Hawthorne, 1960)

As shown in **Figure 3.19**, the pressure balance at the interface becomes:

Vertically:

$$P_B = P_A + (AB)\rho_o g cos\alpha = P_A + \Delta z \rho_o g cos\alpha \tag{3.3}$$

$$P_C = P_D + (CD)\rho_g g cos\alpha = P_D + \Delta z \rho_g g cos\alpha \tag{3.4}$$

Along the direction of flow:

$$q = -\frac{kk'_{ro}A}{\mu_o}\left(\frac{dP}{dx} - \rho_o g sin\alpha\right) \tag{3.5}$$

$$q = -\frac{kk'_{rg}A}{\mu_g}\left(\frac{dP}{dx} - \rho_g g sin\alpha\right) \tag{3.6}$$

or

$$q = -\frac{kk'_{ro}A}{\mu_o}\left(\frac{P_B - P_C}{\Delta x} - \rho_o g sin\alpha\right) \tag{3.7}$$

$$q = -\frac{kk'_{rg}A}{\mu_g}\left(\frac{P_A - P_D}{\Delta x} - \rho_g g sin\alpha\right) \tag{3.8}$$

Combining the above four equations, the Dietz stability equation for CO_2 displacement of oil becomes:

$$tan\beta = \frac{1 - M_e}{M_e N_{ge} cos\alpha} + tan\alpha \tag{3.9}$$

The end-point gravity number for oil-gas is defined as:

$$N_{ge} = \frac{k'_{rg}}{\mu_o}\frac{Ak(\rho_o - \rho_g)g}{q} \tag{3.10}$$

The end-point mobility ratio is obtained by:

$$M_e = (\frac{k'_{rg}}{\mu_g})/(\frac{k'_{ro}}{\mu_o}) \tag{3.11}$$

In the case of unstable displacement, the gas injection rate is very high and the gas-oil interface becomes parallel to the reservoir dip where $\beta = 0$. Applying the Dietz stability criterion, $\beta > 0$, to the equation above, we get the requirement for stability:

$$\frac{1-M_e}{M_e N_{ge} cos\alpha} + tan\alpha > 0 \tag{3.12}$$

However, in the case of a gas-oil system, the mobility ratio is never less than 1. Thus, the gas-oil interface is always conditionally stable at low gas injection rate:

For $M_e > 1$:

$$tan\alpha > \frac{M_e - 1}{M_e N_{ge} cos\alpha} \tag{3.13}$$

the threshold fluid velocity becomes:

$$u_{ginj} < \frac{k\left(\frac{k'_{rg}}{\mu_g}\right)\Delta\rho_{og} g sin\alpha}{M_e - 1} \tag{3.14}$$

As the gas-oil mobility ratio benefits from the confinement effect, the threshold velocity in the stable displacement can be larger. As shown in **Figure 3.20**, when a reservoir has more dip, CO_2 can have a more stable displacement front since the gas prefers to go upwards. Taking the confinement effect into consideration, the threshold velocity for CO_2 injection can be increased, as shown by the blue line in **Figure 3.20**. The smaller a pore size, the more significant the confinement effect and the larger the threshold velocity allowed for a CO_2 stable displacement.

For the 30˚ reservoir dip case, as shown in **Figure 3.21**, the critical velocity for stable CO_2 displacement can increase by around 2 times at a 5 *nm* pore size.

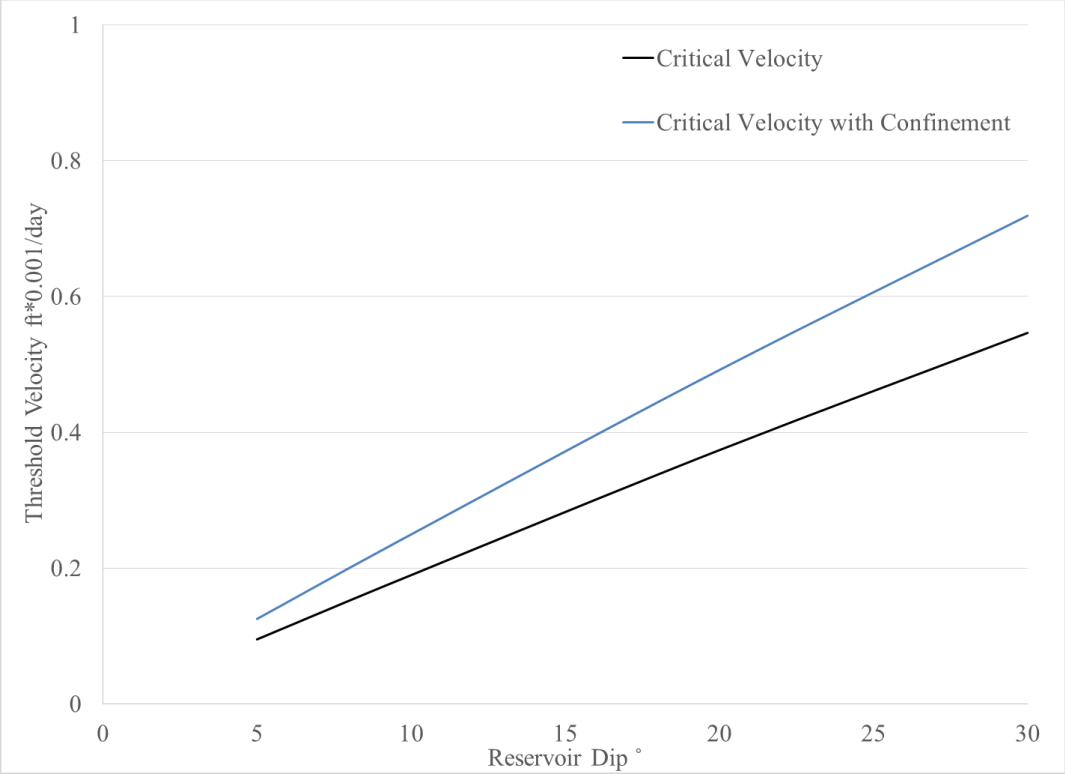

Figure 3.20 Threshold Velocity for Stable Displacement (Zhang, 2016)

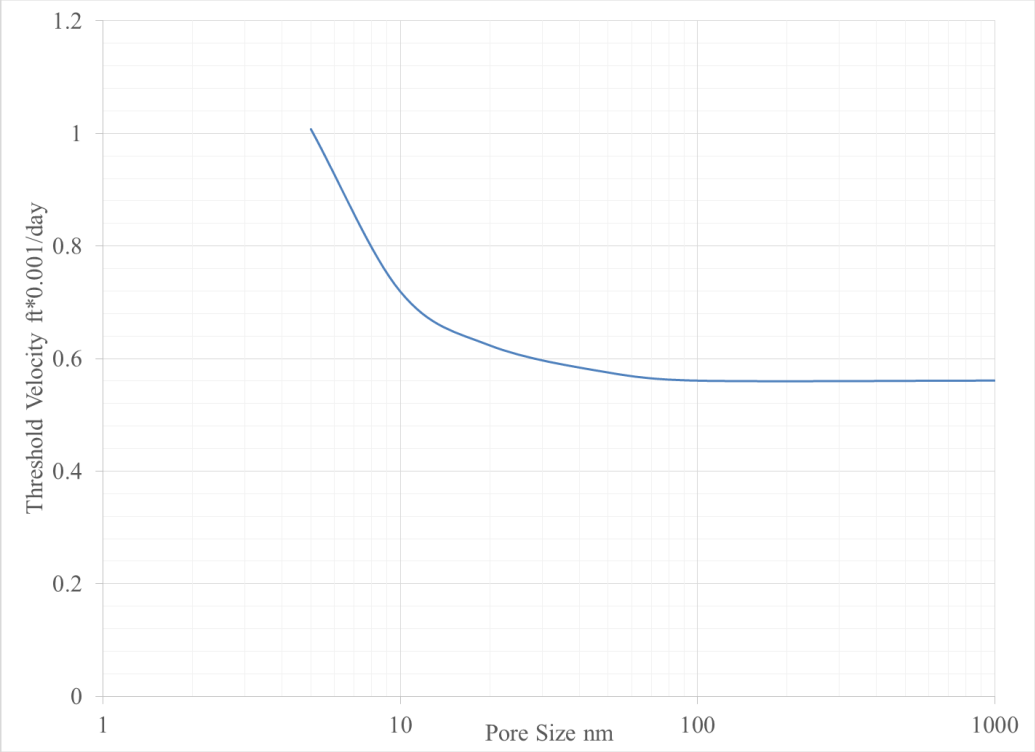

Figure 3. 21 Threshold Velocity for Stable CO_2 Displacement at Various Radii (Zhang, 2016)

Once the CO_2 velocity increases to a value larger than the threshold velocity, the viscosity difference between the vapor and liquid phases drives the fingers to grow during CO_2 displacement (Perkins, 1965). In the unstable CO_2 displacement, the initialization and growth of the finger zone can be recorded and plotted.

As shown in **Figure 3.22**, a viscous finger grows as the gas front travels. The width of the longitudinal mixed zones in a linear system is (Perkins, 1965):

$$Y_l = a\sqrt{\frac{D_o X}{F\phi U} + bd_p\sigma X} \tag{3.15}$$

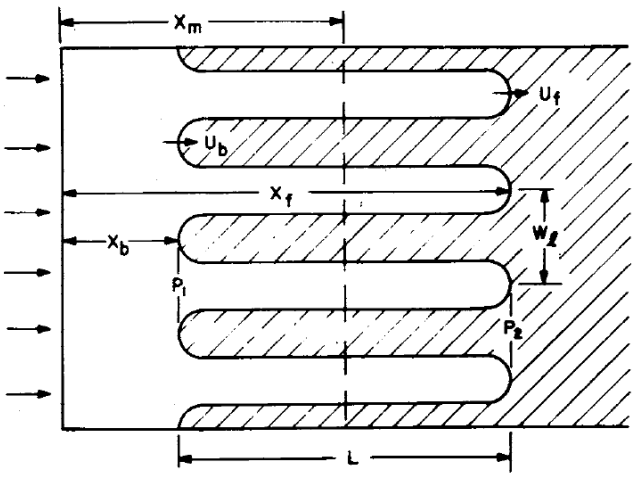

Figure 3. 22 Viscous Finger Illustration (Perkins, 1965)

The velocities of the leading and trailing edges of the fingers are given by (Perkins, 1965):

$$U_f = \frac{dX}{d\theta} = \frac{k(p_1 - p_2)}{\phi \mu_2 L} \tag{3.16}$$

$$U_b = \frac{dX_b}{d\theta} = \frac{k(p_1 - p_2)}{\phi \mu_1 L} \tag{3.17}$$

Assuming that viscous fingers start to grow at some distance, X_o, initially we have $X_o = X_f = X_b$, and the following equations can be obtained (Perkins, 1965):

$$X_f - X_o = \frac{\mu_1}{\mu_2}(X_b - X_o) \tag{3.18}$$

The relative finger width is around 0.5 (Perkins, 1965) so we have:

$$X_m = \frac{X_f + X_b}{2} \tag{3.19}$$

$$L = X_f - X_b \tag{3.20}$$

Substitution of the above equations results in (Perkins, 1965):

$$L = \frac{c(M_l - 1)}{M_l + 1}(X_m - X_o) \tag{3.21}$$

The initialization for finger growth can be obtained from the following equation (Perkins, 1965):

$$\left(\frac{dL}{dX_m}\right)_{x_o} = \left(\frac{dY_l}{dX_m}\right)_{x_o} \tag{3.22}$$

As shown in **Figure 3.23**, 20 mole percent of CO_2 is injected to displace oil at a high velocity. The viscosity difference between the gas and liquid phases drives the first finger to come out when the front travels 0.5 *ft* distance. Taking the confinement effect into consideration, assuming the front is traveled in a 10 *nm* porous medium, the dispersion of the gas phase is reduced by the confinement effect, and the improved efficiency of the VGD and CGD contributes to a better gas-oil mobility ratio. In this way, the initialization of the finger zone is delayed and the finger length is also reduced. The blue line in **Figure 3.23** represents the case with the confinement effect, where the first finger comes out when the front travels a 0.7 *ft* distance instead of 0.5 *ft*. In addition, when the front travels a 2 *ft* distance, the finger zone length drops from 1.7 *ft* to 1.4 *ft*. The initialization of the finger zone as the gas front travels is recorded and plotted in **Figure 3.24**. The confinement effect helps to delay the initialization of viscous fingers and is not negligible when a pore size is 100 *nm* or less.

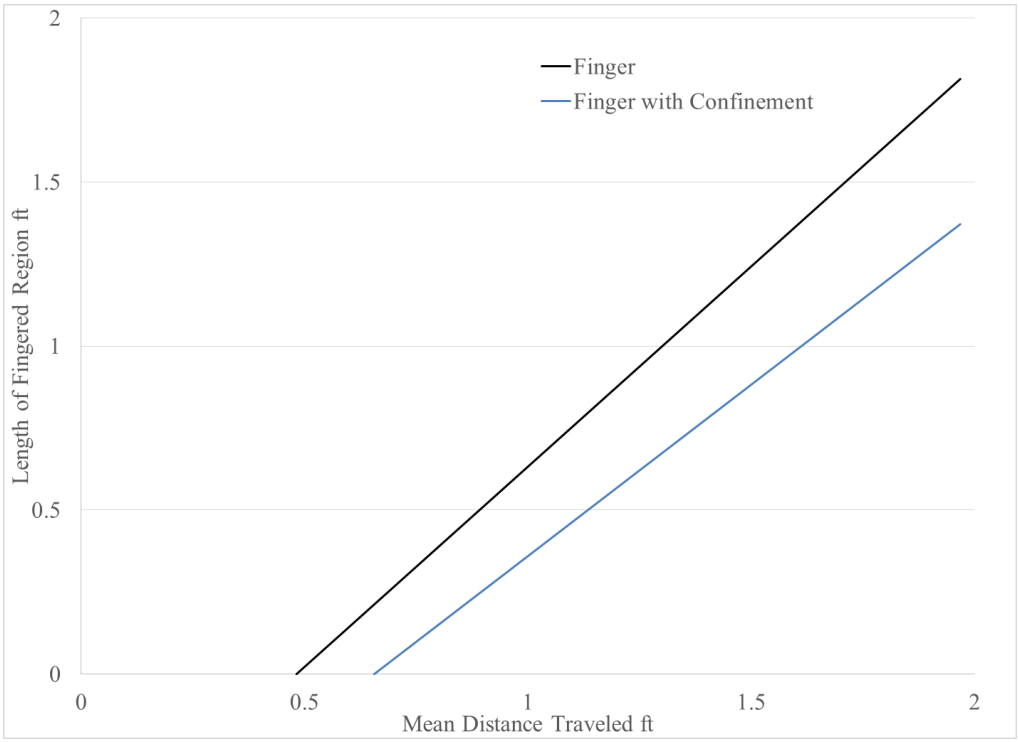

Figure 3.23 Growth of Fingers (Zhang, 2016)

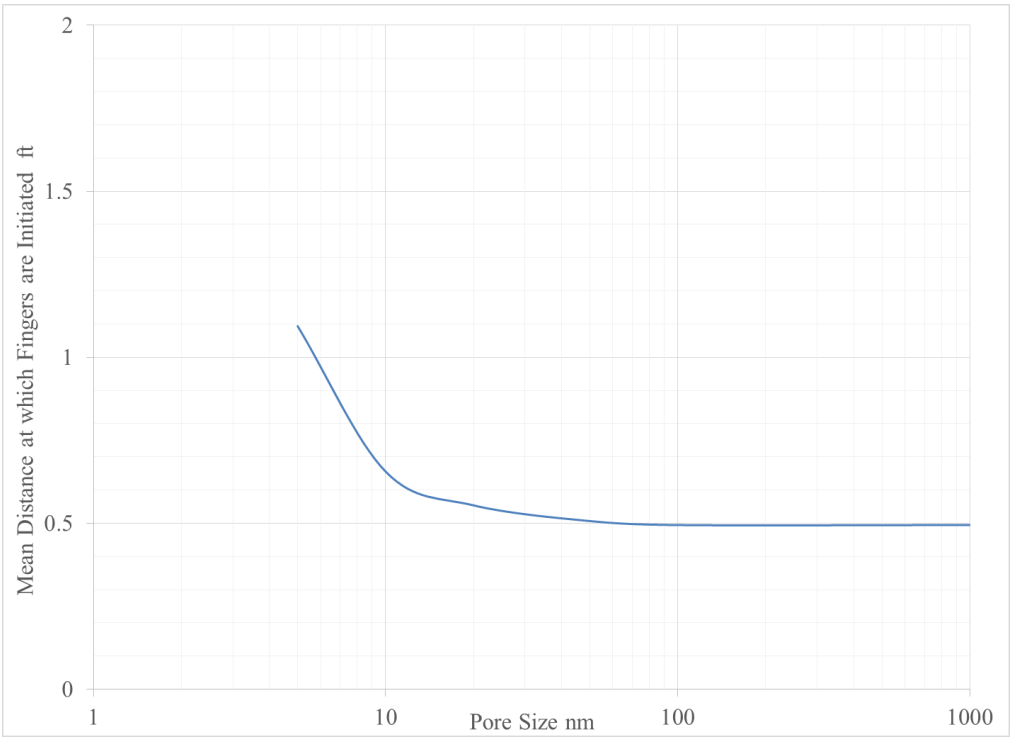

Figure 3. 24 Growth of Fingers with Confinement Effect (Zhang, 2016)

3.2 Effects of Nanoscale Pore Confinement on CO_2 Minimum Miscibility Pressure

As the vapor and liquid phase compositions can be altered, the CO_2 miscibility can be affected by the confinement as well. Miscible displacement indicates that the CO_2 and oil phases mix in all proportions without forming interfaces or two phases. In this part, the solubility parameter is introduced to investigate the gas-oil miscibility. The effects of nanoscale pore confinement on CO_2 minimum miscibility pressure (MMP) are presented.

A single PVT cell is commonly used to make repeated contacts between oil and gas in a forward or a backward manner to estimate the CO_2 miscibility. The criterion for the MMP is the pressure at which the converged tie line becomes the critical tie line. The key steps of the cell to cell simulation are summarized as follows:

Forward contacts are used in calculating the MMP for the vaporizing gas drive (Ahmadi, 2011).

1. Fill the cell with the original oil at specific pressure and temperature. The first pressure is chosen randomly and it can be far from the expected MMP range.
2. Gas is added into the cell, resulting in phase equilibrium with the mixture of the liquid and vapor phases.
3. Take the equilibrium gas and mix it with the original oil.
4. Repeat steps 2 and 3 until the equilibrium composition no longer changes with additional contacts, which means that the equilibrium composition converges to the oil tie line.
5. If the length of the tie line reaches zero or a specified tolerance, the pressure is the MMP; otherwise, pressure should be increased and steps 1 to 5 are repeated.

In a condensing gas drive, backward contacts can be used to evaluate the MMP, where the equilibrium liquid contacts the original gas at each step instead of the equilibrium gas contacting with the original oil. Repeated backward contacts converge to the gas tie line instead of the oil tie line. The procedure and criteria for the MMP remain the same for backward contacts (Ahmadi, 2011).

Except for the calculation of MMP, a slim tube test can be performed to estimate the CO_2 MMP.

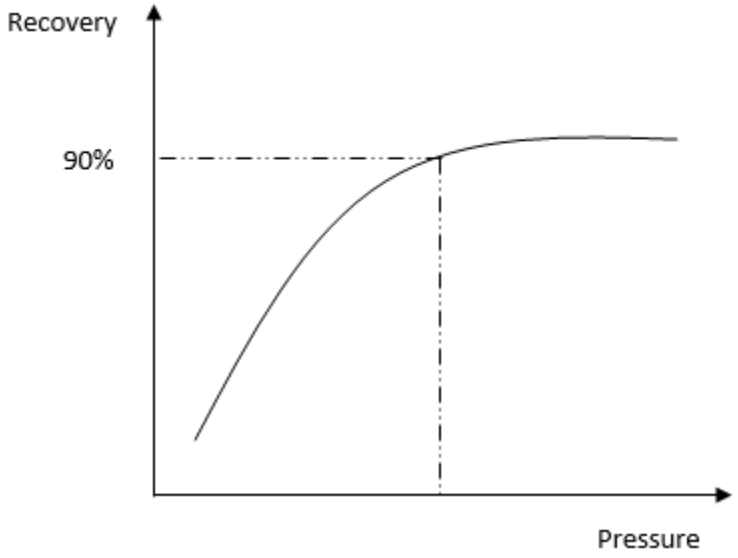

Figure 3.25 Slim Tube Displacements at Various Pressures (Wu, 1990)

In the experiments, CO_2 displaces oil from the fully oil-saturated slim tube at several pressures. Oil recovery is shown after 1.2 pore volume (PV) of injection for each pressure. As shown in **Figure 3.25**, oil recovery increases with pressure up to approximately 90% and increases very little thereafter. The pressure at which the break in the recovery curve occurs is said to be the minimum miscibility pressure (MMP) (Elsharkawy, 1996). Although it does not account for the effects of factors, such as gravity segregation and reservoir heterogeneity on volumetric sweep, a

slim tube is still a common way to evaluate the MMP (Elsharkawy, 1996).

Due to the existence of nanoscale pores in these reservoirs, which can affect phase equilibrium, there are some variations in CO_2 miscibility with the associated confinement effect. In the following section, the effects of nanoscale pore confinement on CO_2 MMP are studied.

When a liquid is heated to its boiling point, the amount of van der Waals forces that holds the molecules of the liquid together needed to be overcome. Similarly, when a solvent comes into contact with the liquid, miscibility can happen once the molecules of the liquid are physically separated by the molecules of the solvent, as shown in the **Figure 3.26**.

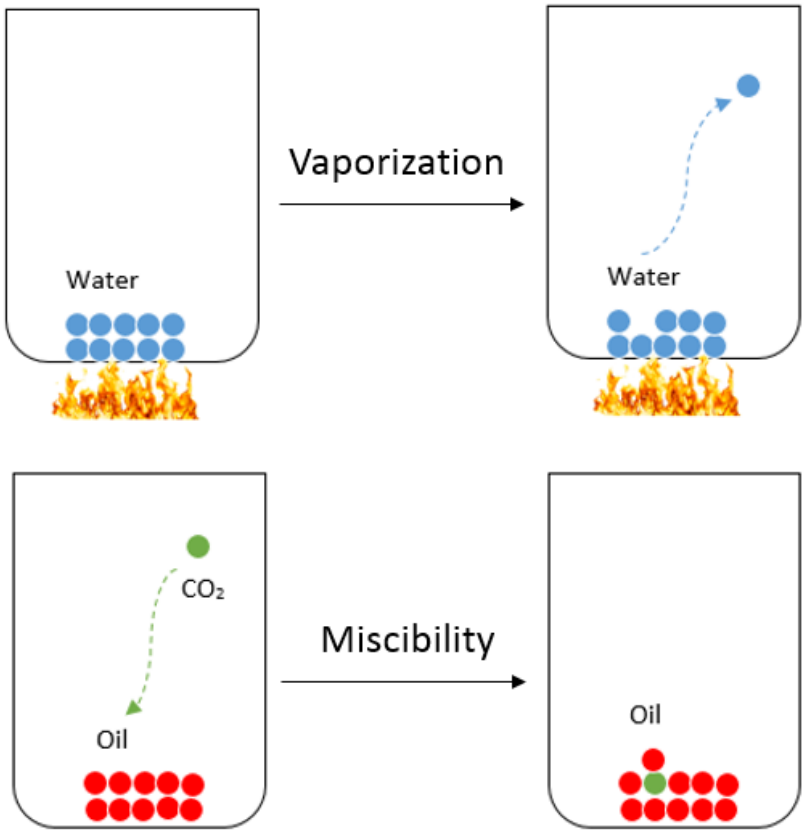

Figure 3. 26 Miscibility vs. Vaporization Process

The same intermolecular van der Waals forces must be overcome in both cases. Materials with similar solubility parameters will be able to interact with each other, resulting in miscibility or swelling. Solubility parameters can be used to indicate the gas-oil miscibility. The solubility parameter for CO_2 can be estimated by the following expression (Giddings, 1968):

$$\delta_g = 0.326 P_c^{0.5} \left({}^{\rho_r}/_{\rho_r(liq)} \right) \tag{3.23}$$

$$\delta_o = \sqrt{\frac{\Delta H - RT}{v}} \tag{3.24}$$

As the gas and oil compositions approach each other during CO_2 injection, the intermolecular van der Waals forces to be overcome are decreased. Solubility parameters indicate the amount of van der Waals forces that holds the molecules of the liquid together to be overcome. Materials with similar solubility parameters will be able to interact with each other, resulting in miscibility (Giddings, 1968). As shown in **Figure 3.27**, taking the confinement effect into consideration, the difference of solubility parameters in oil and gas decreases at a pore size in 100 *nm* or less, which indicates the miscible condition can be met in an easier way.

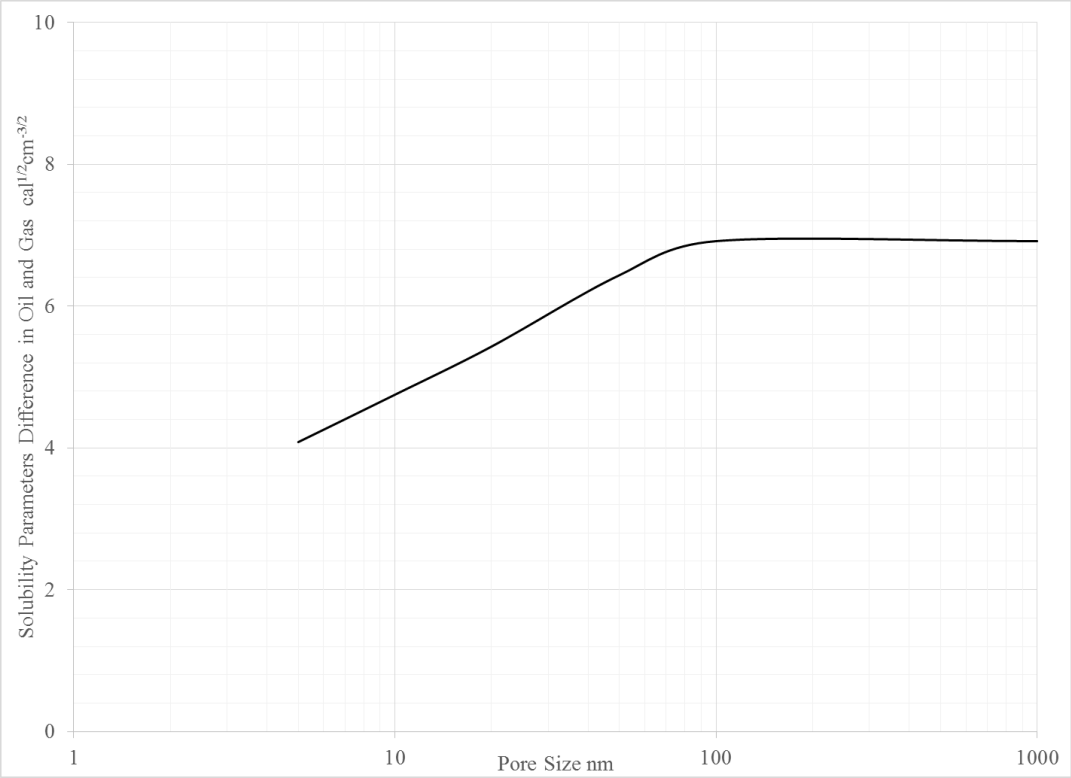

Figure 3.27 Solubility Parameters with the Confinement Effect (Zhang, 2016)

A semi-analytical method can be used to estimate CO_2 MMP. In this method, the tie line length is calculated and miscibility is achieved whenever one of the key tie lines reaches zero length (Johns, 1996).

The length of a tie line is calculated as follows (Johns, 1996):

$$tie - line\ length = \|x - y\| = \sqrt{\sum_{i=1}^{Nc}(x_i - y_i)^2} \tag{3.25}$$

The shifts in critical properties can suppress the two-phase region, which is shown as a dashed line in **Figure 3.28**. In this way, three contacts can drive the oil and CO_2 to become miscible instead of four contacts, as shown by the solid line.

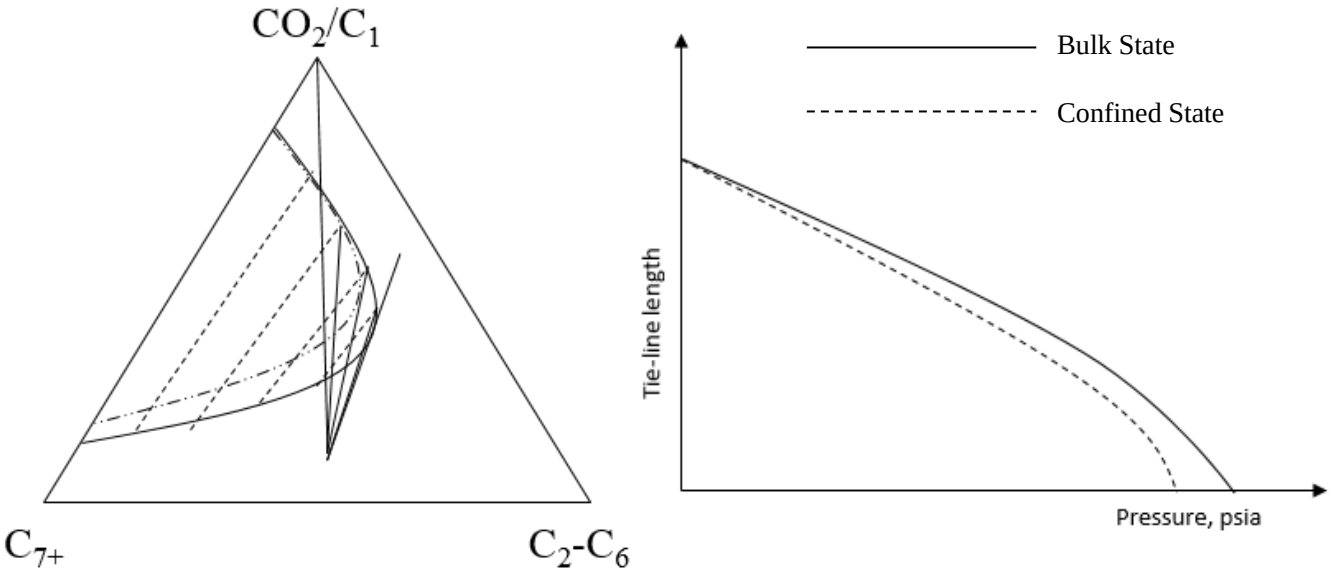

Figure 3.28 Semi-analytical Methods to Evaluate CO_2 MMP (Zhang, 2016)

By using the oil composition in **Table 2.1**, CO_2 MMP is calculated and listed in **Table 3.2.** It can be seen that CO_2 MMP decreases as the pore size decreases.

Table 3. 2 CO_2 Minimum Miscible Pressure versus Various Pore Radius (Zhang, 2015)

Pore Radius / *nm*	CO_2 Minimum Miscible Pressure / *psi*
Infinite	2920
10000	2920
500	2911
100	2895
50	2865
10	2635

3.3 Correlation and Prediction of MMP for CO_2 Injection in Nanopores

CO_2 MMP is a vital parameter in selecting CO_2 parameters for displacement (Wang, 1998; Zhang, 2015). A variety of correlations in the estimation of CO_2 MMP helps operators to determine injection conditions and to plan suitable surface facilities (Emera, 2005).

The main parameters influencing the CO_2 MMP are reservoir temperature, oil composition and injection gas properties (Johnson, 1981). In early times, the reservoir temperature was thought to have the most significant effect on CO_2 MMP (Yellig, 1980), however, some methods have large discrepancies compared with values gained from experiments (Holm, 1974; United, 1979). It was found that CO_2 MMP is further influenced by molecular weights of the reservoir oil (Holm, 1982). The prediction of CO_2 MMP needs to consider hydrocarbon composition for calculating MMP (Metcalfe, 1974). A high oil volatile fraction (e.g, C_1) in a reservoir increases the MMP, whereas a high intermediate (e.g, C_2-C_4) fraction reduces the MMP (Emera, 2007).

In general, the CO_2 MMP correlations can be classified into three categories. CO_2 MMP is only related to molecular weights (M), molecular weights and temperature (MT), or molecular weights, temperature and mole fractions (MTF). These correlations are helpful in screening candidate reservoirs for CO_2 flooding and in selecting CO_2 parameters without detailed characterizations. The existence of nanoscale pores in tight oil reservoirs can cause fluid equilibrium alterations and critical properties shifts, resulting in a lower CO_2 MMP. The correlations must be revised to accurately predict MMP for CO_2 injection in tight oil reservoirs. In this section, the existing CO_2 MMP correlations are summarized. These correlations successfully predicted the CO_2 MMP in a

variety of ways. None, however, can take the confinement effect into consideration in evaluating CO_2 MMP. The nanoscale pore confinement effect on CO_2 MMP is studied and incorporated into a new novel CO_2 MMP correlation. The proposed method is validated by CMG WINPROP by using tight oil samples including Cardium, Bakken, Monterey, Eagle Ford and Niobrara.

The way to capture the CO_2 MMP with the confinement effect is as follows:

The solubility parameters for a hydrocarbon component can be calculated by Equation (3.26), the solubility parameters A is 4.9- 6.5 * 10^8 $mol^{-1/3}$ (Barton, 1983).

$$\sigma = a\delta^2 v^{0.33}/A \tag{3.26}$$

The crude oil solubility parameters can be estimated from average molecular weights and reservoir temperature (Lange, 1998):

$$\delta_{oil} = 0.01M + 6.54 - 0.01(T - 25) \tag{3.27}$$

The solubility parameter for CO_2 can be estimated by the following expression (Giddings, 1968):

$$\delta_g = bP_c^{0.5}\left({\rho_r}/{\rho_r(liq)}\right) \tag{3.28}$$

The pressure condition that corresponds to $\left|\delta_o - \delta_g\right| \approx 3.0$ $(cal/cm^3)^{0.5}$ is the CO_2 MMP (Lange, 1998).

At reservoir temperature, the relationship between gas solubility and reduced density can be calculated by Equation (3.28). Then the CO_2 density can be obtained. According to **Figure 3.29**, the CO_2 MMP can be estimated.

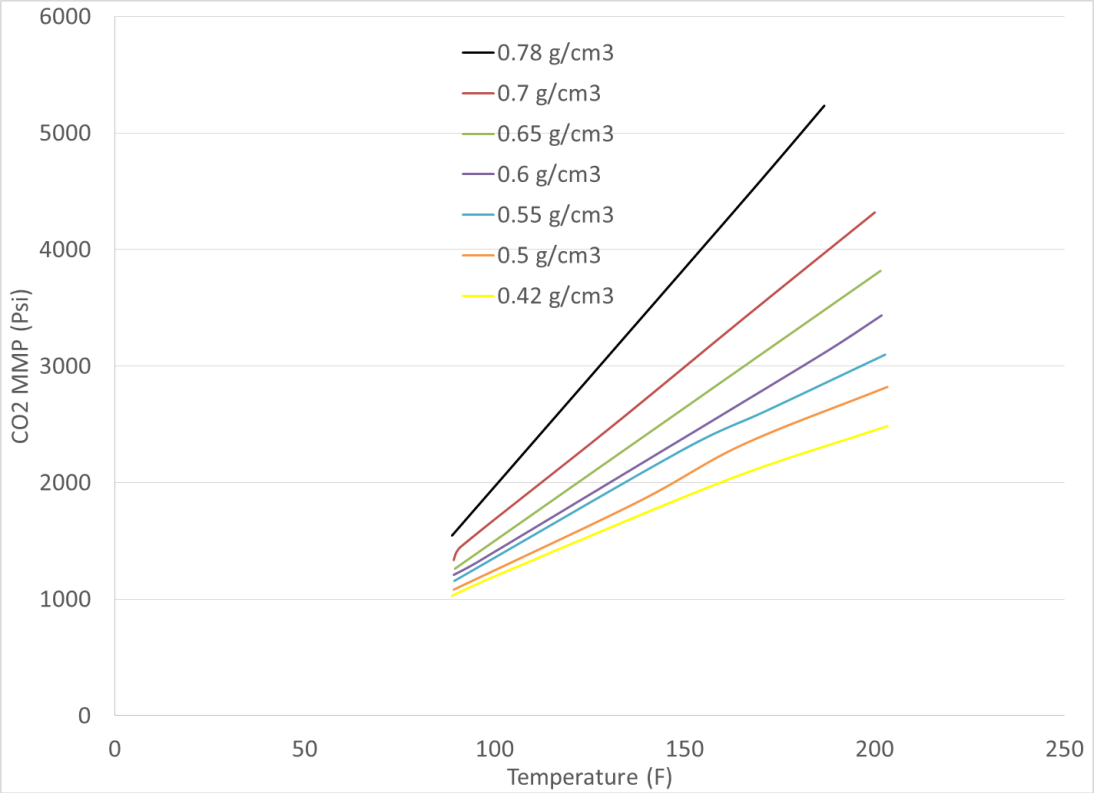

Figure 3.29 Density of CO_2 Required for Miscible Displacement (Holm, 1982)

Taking the confinement effect into consideration, a critical property shift is given by the following equations (Singh, 2009):

$$\Delta T_c^* = \frac{T_{cb} - T_{cp}}{T_{cb}} = a\frac{\sigma_{LJ}}{r_p} - b\left(\frac{\sigma_{LJ}}{r_p}\right)^2 \tag{3.29}$$

$$\Delta P_c^* = \frac{P_{cb} - P_{cp}}{P_{cb}} = a\frac{\sigma_{LJ}}{r_p} - b\left(\frac{\sigma_{LJ}}{r_p}\right)^2 \tag{3.30}$$

and

$$\sigma_{LJ} = c\sqrt[3]{\frac{T_{cb}}{P_{cb}}} \tag{3.31}$$

Following the above steps, the CO_2 density can be obtained. Afterwards, it needs to be revised by the following equation at various pore radii in 50 *nm* or less (Zhang, 2016). Then the revised CO_2 MMP, corresponding to **Figure 3.29** with the confinement effect, can be obtained.

$$\frac{\rho_{confined}}{\rho} = -0.0003\left(lnr_p\right)^4 + 0.0088\left(lnr_p\right)^3 - 0.0973\left(lnr_p\right)^2 + 0.4578lnr_p + 0.2179 \quad (3.32)$$

The CO_2 MMP can be predicted in various ways. A correlation or empirical model is an attractive solution to estimate CO_2 MMP. Although correlations should be applied in specific conditions, they are still a fast way to roughly estimate CO_2 MMP. Most of the CO_2 MMP correlations are summarized in **Table 3.3**. In general, they can be classified into three categories. The first one is only related to molecular weights (M), the second one involves molecular weights and temperature (MT), and the final one incorporates molecular weights, temperature and mole fractions (MTF).

Table 3. 3 Common CO_2 MMP Correlations (Zhang, 2016)

Author	Correlation	Remarks
Holm and Josendal 1974 (Holm, 1974)	It is a function of reservoir temperature and C_{5+} molecular weight of the crude oil.	MW_{C5+} within (180-240)
National Petroleum Council 1976 (Dong, 2015)	MMP is presented as a function of oil gravity and reservoir temperature.	API< 27, MMP =4003.04 *psi* 27< API < 30, MMP= 3002.28 *psi* API>30, MMP=1199.46 *psi*

		For 120.2 *F* < T< 150.08 *F*, ΔP=+200.15 *psi*, For 150.08 *F* < T < 199.94 *F*, ΔP=+349.98 *psi*, For 199.94 *F* < T< 249.8 *F*, ΔP=+500.38 *psi*.
Cronquist 1978 (Cronquist, 1978)	MMP=0.11027×T^{Y}, where Y=0.744206 +0.0011038 MW_{C5}+0.0015279 Vol	23.7 < °API < 44 159.82 < T < 478.4°*F*
Lee 1979 (Lee, 1979)	MMP =7.3924×$10^{b,}$ where b=2.772-(1519/(460+T))	If MMP < Pb, the Pb is taken as MMP.
Yellig and Metcalfe (Yellig, 1980)	MMP=12.6472+0.015531×T+1.24192×10^{-4}×T^{2} -716.9472/T	95 *F*< T <192.02 *F*
Holm	A graphic correlation that is a function of CO_2 density,	

1982 (Holm, 1982)	weight percentage of gasoline content and reservoir temperature	
Orr and Jensen 1984 (Orr, 1984)	MMP=0.101386exp(10.91-2015/(255.372+0.5556T))	T<121.64 *F*
Glaso's 1985 (Glass, 1985)	When C2-C6>18%: MMP =5.58657-0.02347739×MC_{7+} +(1.1725×10^{-11}×$MC_{7+}^{3.73}$×$e^{786.8}$×$MC_{7+}^{-1.058}$)×T-0.836×(C2-C6) When C2-C6<18%: MMP =20.33-0.02347739×MC_{7+} +(1.1725×10^{-11}×$MC_{7+}^{3.73}$×$e^{786.8}$×$MC_{7+}^{-1.058}$)×T-0.836×(C2-C6)	
Enick 1988 (Enick, 1988)	A graphical correlation that is a function of the reservoir temperature and molecular weight of C5+	
Lange (Lange, 1998)	MMP is a function of molecular weight, reservoir temperature and CO_2 density	
Huang (Huang, 2003)	The pure CO_2 MMP of a reservoir fluid (live oil) is correlated with the molecular weight of C5+ fraction, reservoir	

	temperature, and concentrations of volatile (methane) and intermediate (C2–C4) fractions in the oil.	
Yuan (Yuan, 2005)	$MMP= b_1+b_2M_{C7+} +b_3(C2\text{-}C6)$ $+(b_4+b_5M_{C7+} +b_6C2\text{-}C6 /M_{C7+}^2)T+$ $(b_7+b_8 M_{C7+}+b_9M_{C7+}^2+b_{10}(C2\text{-}C6)) T^2$ b_1 to b_{10} are constants	
Shengli SINOPEC (Dong, 2015)	$MMP=675.01\text{-}6.94M_{C6+}+1.7(T\text{-}T_{critical})$	
Recovery Institute (RI) CNPC (Dong, 2015)	$MMP=\text{-}4.8913+0.0415T\text{-}0.0015974T^2$	

Live oil samples listed in **Table 3.4** are used to validate the CO_2 MMP correlations of each category. Results are shown in **Table 3.5**. In general, the correlations, involving molecular weights and temperature (MT), provide a good prediction of CO_2 MMP. The correlations which only take temperature into consideration deviate the most from the results provided by the simulator. The results of the MT and MTF correlations are similar. The equations become more complex if the crude oil composition is involved in the estimation.

Table 3. 4 Live Oil Samples (Ghaderi, 2012; Teklu, 2014)

Cardium Oil		Bakken Oil		Monterey Oil		Eagle Ford Oil		Niobrara Oil	
T_{res}=156 ˚F		T_{res}=241 ˚F		T_{res}=210.00 ˚F		T_{res}=189 ˚F		T_{res}=230 ˚F	
Composition, %		Composition, %		Composition, %		Composition, %		Composition, %	
CO2	0.10	CO2	0.00	CO2	0.36	CO2	0.81	CO2	1.34
N2-C1	41.40	CH4	36.74	CH4	15.65	N2	0.07	N2	0.32
C2H6	7.60	C2H6	14.89	C2-3	8.15	CH4	65.54	CH4	42.26
C3H8	5.90	C3H8	9.33	C4-6	10.02	C2H6	12.97	C2H6	10.86
C4-C5	6.10	C4	5.75	C7-15	44.94	C3H8	6.17	C3H8	7.08
FC6	2.60	C5-6	6.41	C16-34	15.76	IC4	1.50	IC4	1.24
C7+	36.30	C7-12	15.85	C35+	5.12	NC4	2.42	NC4	3.71
Molecular Weight		C13-21	7.33	Molecular Weight		IC5	1.08	IC5	1.37
C7+	238.00	C22-80	3.70	C2-3	36.99	NC5	1.02	NC5	2.18
		Molecular Weight		C4-6	70.14	FC6	1.38	FC6	2.67
		C5-6	78.30	C7-15	135.20	C7+	7.04	C7+	26.97
		C7-12	120.56	C16-34	305.01	Molecular Weight		Molecular Weight	

	C13-21	220.72	C35+	644.85	C7+	177.11	C7+	180.60
	C22-80	443.52						

Table 3. 5 CO_2 MMP Correlation Validation for Each Category (Zhang, 2016)

Reservoir	T(psi)	MT(psi)	MTF(psi)	CMG(psi)
Cardium	1350	1917	2239	1790
Bakken	2899	3250	3092	3189
Monterey	2897	2969	3047	3719
Eagle Ford	2400	2657	2347	3268
Niobrara	2801	3250	2854	3599

Afterwards, the CO_2 MMP is predicted with the confinement effect at pore radii of 50 *nm* and 10 *nm*. As shown in **Table 3.6**, the method proposed in this thesis gives a reasonable prediction of CO_2 MMP. The CO_2 MMP calculated by the proposed correlation which also incorporates the nanoscale pore confinement matches the results provided by the CMG Winprop.

Table 3. 6 CO_2 MMP Correlation Validation for Nanoscale Pore (Zhang, 2016)

Reservoir	r=50 *nm* (psi)	r=50 *nm* by CMG (psi)	r=10 *nm* (psi)	r=10 *nm* by CMG (psi)
Cardium	1751	1771	1700	1745
Bakken	2850	3070	2650	2843
Monterey	2885	3548	2750	3171
Eagle Ford	3089	2999	2769	2701
Niobrara	3600	3410	3200	3150

In this section, most of the CO_2 MMP correlations are summarized and compared to the results by a CMG simulator. A solubility-based method is proposed to predict the CO_2 MMP, incorporating the CO_2 MMP alteration by the nanoscale pore confinement. In general, the correlations with molecular weights and reservoir temperature can give a rough estimation of a CO_2 MMP. For tight oil reservoirs, taking the confinement effect into consideration, CO_2 MMP is reduced and the solubility method in this thesis can incorporate the nanoscale pore confinement effect into the estimation.

3.4 Effects of Nanoscale Pore Confinement on CO_2 Immiscible and Miscible Flooding

CO_2 flooding is a promising technique in improving a tight oil recovery process. It can displace oil in either a miscible or immiscible way. High oil recovery by gas injection can be achieved at pressures over the MMP (Ahmed, 1997). If the reservoir pressure goes below MMP or the gas injection enrichment goes below minimum miscibility enrichment (MME), it will lead to immiscible displacement with lower oil recovery (Gao, 2010). In cases of pressure below MMP, immiscible displacement of oil takes place, in which the reduction of oil viscosity, swelling of reservoir oil and reduction of interfacial tension are major driving mechanisms. This combination enables a portion of the reservoir's remaining oil to be mobilized and produced. For pressures above MMP, the most dominant mechanism is the miscibility between CO_2 and reservoir oil. The CO_2 miscible displacement is a more favorable oil recovery process than the immiscible displacement (Fath, 2014). The displacement efficiency of the immiscible CO_2 process is highly related to reservoir pressure, temperature, crude composition and the amount of CO_2 injected (Bargas, 1992; Zekri, 2006). In the CO_2 miscible process, remaining oil saturation, trapped gas saturation, three phase relative permeability and injectivity are the main parameters that affect the displacement efficiency (Duchenne, 2014).

The nanoscale pores can exist in tight oil reservoirs. The common pore size is approximately 30 *nm* to 2000 *nm* in tight sandstone reservoirs and 2 *nm* to 100 *nm* in shale reservoirs (Nelson, 2009). Within such a confined system, the associated confinement can exert effects on component orientation and arrangement (Teklu, 2013; Teklu, 2014). In this way, interactions between surface

walls and fluid molecules can cause a change in the thermal dynamic behavior of the hydrocarbon phases, resulting in a variation in critical pressure and temperature (Pitakbunkate, 2015). Since crude oil phase behavior in such a confined system is deviated from their bulk state (Rahmani, 2015; Luo, 2015), the CO_2 immiscible and miscible processes can be affected by the confinement effect as well.

In this section, the gas-oil interfacial tension is investigated. Since the interfacial tension is related to the capillary pressure, it can be scaled in normalized residual oil saturation calculations. A reservoir can be treated as an immiscible or miscible zone during CO_2 injection. Consequently, nanoscale pore confinement on CO_2 immiscible and miscible processes can be evaluated.

The configuration that assumes a core sample is fully saturated with oil and that an immiscible zone, a miscible zone and an unswept area exist during CO_2 flooding is illustrated in **Figure 3.30**.

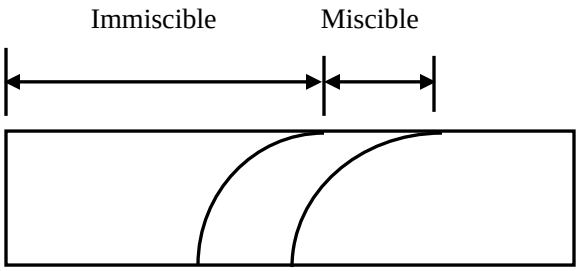

Figure 3. 30 CO_2 Flooding Schematic (Zhang, 2016)

The total oil recovery from the sample can be expressed by the following:

$$R_t = \frac{R_{im}L_{im}A\emptyset + R_mL_mA\emptyset}{L_tA\emptyset} \tag{3.33}$$

where

$$L_t = L_{im} + L_m \tag{3.34}$$

$$R_t = R_{im}\left(\frac{L_{im}}{L_t}\right) + R_m\left(\frac{L_m}{L_t}\right) \tag{3.35}$$

For multicomponent mixtures the gas-oil interfacial tension can be evaluated by the following equation (Weinaug, 1943):

$$\sigma_{go}^{1/4} = \sum_{i=1}^{N} P_i\left(x_i\frac{\rho_o}{M_o} - y_i\frac{\rho_g}{M_g}\right) \tag{3.36}$$

Once the interfacial tension is estimated, oil recovery can be evaluated (Li, 2006). Capillary force can be incorporated into the residual oil estimation.

Volumetric fluxes of the wetting and nonwetting phases in a core with a specific value of initial wetting phase saturation is given as follows (Li, 2006):

$$v_w = -\frac{k_w}{\mu_w}\left(\frac{\partial p_w}{\partial x} + \rho_w g\right) \tag{3.37}$$

$$v_{nw} = -\frac{k_{nw}}{\mu_{nw}}\left(\frac{\partial p_{nw}}{\partial x} + \rho_{nw} g\right) \tag{3.38}$$

The pressure of the wetting phase can be calculated by capillary pressure:

$$p_w = p_{nw} - p_c \tag{3.39}$$

Substituting equation (3.39) into (3.37):

$$v_w = M_w\left(\frac{\partial p_c}{\partial x} - \frac{\partial p_{nw}}{\partial x} - \rho_w g\right) \tag{3.40}$$

where

$$M_w = \frac{k_w}{\mu_w} \tag{3.41}$$

Equation (3.38) can be written as follows:

$$\frac{\partial p_{nw}}{\partial x} = -\left(\frac{v_{nw}}{M_{nw}} + \rho_{nw} g\right) \tag{3.42}$$

where

$$M_{nw} = \frac{k_{nw}}{\mu_{nw}} \tag{3.43}$$

Assuming the cocurrent flow occurs in the flux, which indicates that the flux of the non-wetting phase is equal to that of the wetting phase and both flow in the same direction:

$$v_w = v_{nw} \tag{3.44}$$

Equation (3.42) can be reduced:

$$\frac{\partial p_{nw}}{\partial x} = -\left(\frac{v_w}{M_{nw}} + \rho_{nw} g\right) \tag{3.45}$$

Substituting (3.45) into (3.40)

$$v_w = \frac{M_w M_{nw}}{M_{nw} - M_w}\left(\frac{\partial p_c}{\partial x} - \Delta\rho g\right) \tag{3.46}$$

where $\Delta\rho$ is the density difference between the wetting phase and the nonwetting phase.

$$\Delta\rho = \rho_w - \rho_{nw} \tag{3.47}$$

We define the effective mobility, representing the combined effect of the mobilities of both the wetting and nonwettting phases:

$$M_{eff} = \frac{k_e}{\mu_e} = \frac{M_w M_{nw}}{M_{nw} - M_w} \tag{3.48}$$

Assuming a piston like flux in the core:

$$\frac{\partial p_c}{\partial x} = \frac{p_c}{x_f} \tag{3.49}$$

$$v_w = M_{eff}\left(\frac{p_c}{x_f} - \Delta\rho g\right) \tag{3.50}$$

Assuming the distribution of S_{wi} in a porous medium is homogeneous, in this case, the cumulative volume of the wetting phase flux into the core can be calculated as follows:

$$N_{wt} = A x_f \emptyset\left(S_{wf} - S_{wi}\right) \tag{3.51}$$

$$q_w = A M_{eff}\left(\frac{p_c}{x_f} - \Delta\rho g\right) \tag{3.52}$$

Substituting (3.51) into (3.52), the following equation is obtained:

$$q_w = \frac{A^2 \emptyset M_{eff} p_c (S_{wf} - S_{wi})}{N_{wt}} - AM_e \Delta\rho g \tag{3.53}$$

Terms a_0, b_0, R_0, c_0, and R^* are defined as follows:

$$a_0 = \frac{AM_{eff}(S_{wf} - S_{wi})}{L_c} p_c \tag{3.54}$$

$$b_0 = AM_{eff} \Delta\rho g \tag{3.55}$$

$$R_0 = \frac{N_{wt}}{V_p} \tag{3.56}$$

$$c_0 = \frac{b_0}{a_0} \tag{3.57}$$

$$R^* = c_0 R_0 \tag{3.58}$$

and

$$t_d = c^2 \frac{k_e}{\emptyset} \frac{p_c}{\mu_e} \frac{S_{wf} - S_{wi}}{{L_c}^2} t \tag{3.59}$$

Substituting (3.57) - (3.59) into (3.53) results in (Li, 2006):

$$\frac{R^* dR^*}{dt_d} = 1 - R^* \tag{3.60}$$

In addition, solubility parameters can be used to indicate the CO_2 oil miscibility; the difference in solubility parameters in oil and gas decreases with the confinement effect. For nonpolar components including hydrocarbons and CO_2, the gas-oil interfacial tension can be correlated with the square of the difference in solubility parameters between crude oil and injected CO_2. There is a relationship between interfacial tension and solubility parameters, which is given by Equation (3.61) and a small solubility parameter difference may correspond to low IFT conditions, where good oil displacement efficiency should be observed (Lange, 1998):

$$\sigma_{go} \approx a \frac{v^{0.33}}{A} \left(\delta_g - \delta_o\right)^2 \tag{3.61}$$

Furthermore, the residual oil saturation during CO_2 injection can be correlated with the absolute

difference of oil and CO_2 solubility parameters (Lange, 1998):

$$S_{orm}/S_{orw} = 0.12|\delta_{oil} - \delta_g| - 0.11 \quad (3.62)$$

Taking the nanoscale pore confinement into consideration, the difference between crude oil and injected CO_2 in solubility parameters decreases with the nanoscale pore confinement effect, which indicates lower residual oil saturation. The following section presents the interfacial tension and residue oil saturations during CO_2 flooding with the confinement effect. The data used in the calculation is shown in **Table 3.7**, and the fluid properties refer to the above phase equilibrium calculations.

Table 3. 7 Reference Parameters for the Immiscible/Miscible Process Calculation

Core Length	Diameter	Porosity	Permeability	Oil Viscosity	Gas Phase Saturation at front	Initial Gas Saturation	k_{ro}	k_{rg}
cm	*cm*		*md*	*cp*				
100	4	0.03	0.085	0.17	0.75	0.25	1	0.49

In addition to the alteration in the two-phase region by the confinement effect, equilibrium compositions of the vapor and liquid phases and the interfacial tension (IFT) can be altered as well. Taking the confinement effect into consideration, the gas-oil interfacial tension reduces as the pore size decreases, which is shown in **Figure 3.31**. It is consistent with the previous work (Singh, 2010; Teklu, 2014).

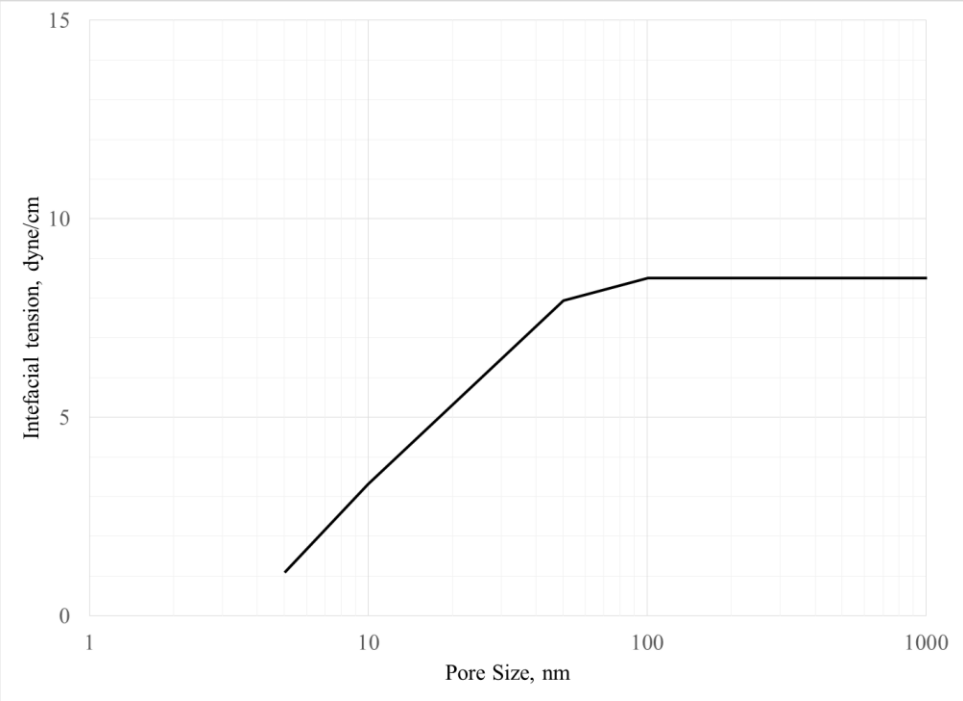

Figure 3.31 Gas-oil Interfacial Tension versus Pore Radius (Zhang, 2016)

Since this interfacial tension can be decreased this way, residual oil saturation can be decreased by the confinement effect as well. Because of the phase equilibrium alteration, the oil recovery in the immiscible zone can be altered by the confinement effect. In the miscible zone, the gas-oil interfacial tension is zero, so no oil remains. As shown in **Figure 3.32**, oil recovery improves as the pore radius decreases.

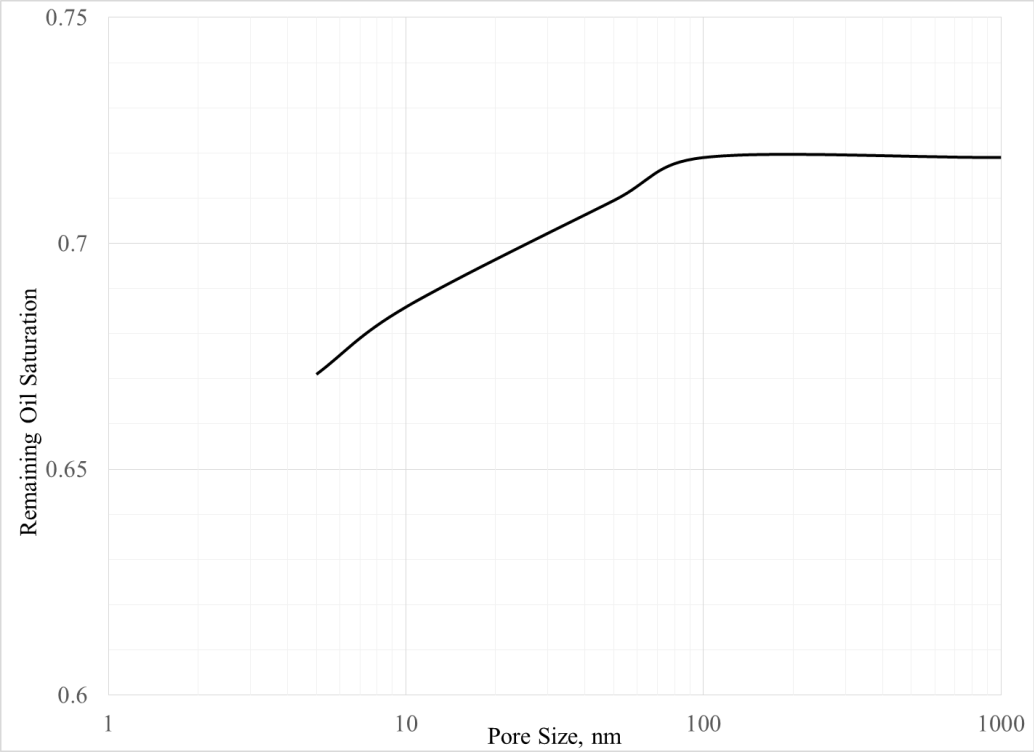

Figure 3.32 Remaining Oil Saturation in Immiscible Zone (Zhang, 2016)

Figure 3.33 shows that the CO_2 displacement efficiency in the immiscible zone is improved by the confinement effect and the length of the immiscible zone can be reduced.

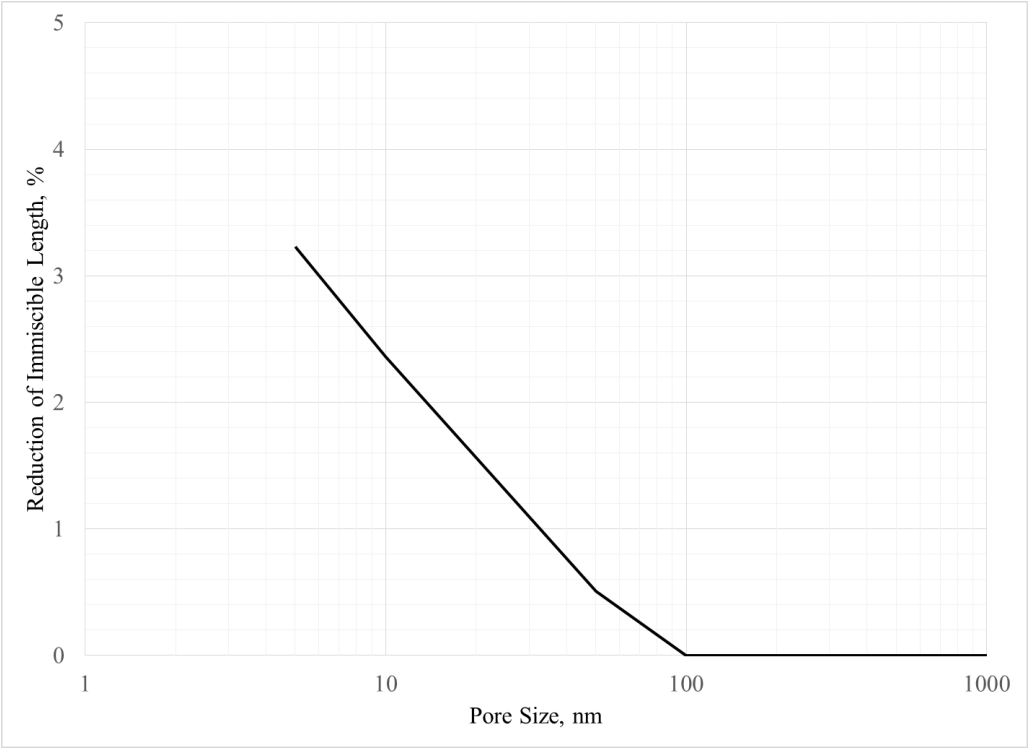

Figure 3. 33 Immiscible Zone Length Reduction (Zhang, 2016)

As the pore size is 100 *nm* or less, the effect of confinement on residual oil saturation during CO_2 injection cannot be negligible.

This section presents the effects of confinement on the CO_2 immiscible and miscible processes. The efficiency of immiscible flooding is improved, while the efficiency of miscible flooding is not affected by a confinement effect. The length of a CO_2 immiscible zone is decreased by the nanoscale pore confinement, resulting in lower CO_2 MMP.

3.5 Effects of Nanoscale Pore Confinement on Relative Permeability Alteration during CO_2 Flooding

During CO_2 flooding, a significant change in gas-oil relative permeability occurs when interfacial tension drops below 0.04 *dyne/cm* (Longeron, 1980). The curvature of gas-oil relative permeability can be straightened with a reduction in interfacial tension (Asar, 1988).

In addition, hysteresis cannot be ignored when interfacial tension is high and the reservoir permeability is low (Henderson, 1998; Fatemi, 2013). Hysteresis is much higher for the non-wetting phase (gas) compared to that for the wetting phase (oil) (Fatemi, 2012; Fatemi, 2013). The relative permeability for a given phase is greater when its saturation is increased (Fatemi, 2012; Fatemi, 2013). The variation in the drainage and imbibition relative permeability curves is highly related to the saturation history, which can cause gas phase trapping to some extent (Land, 1971).

In tight oil reservoirs, a large amount of nanoscale pores exist where the pore size is smaller than 100 *nm* for sandstone reservoirs and 10 *nm* for shale reservoirs (Nelson, 2009). Within a nanopore, the van der Waals forces and molecules orientation and arrangement can be altered to some extent (Morishige, 1997; Zarragoicoechea, 2004; Travalloni, 2010; Devegowda, 2012; Pitakbunkate, 2015). The confinement effect can cause fluid critical temperature and critical pressure shifts (Singh, 2009), resulting in an alteration in phase behavior (Teklu, 2014; Zhang, 2015). Furthermore, fluid transportation varies in a nanopore when it is in a bulk state (Wu, 2015; Wu, 2016).

As an interfacial tension reduction can occur during CO_2 injection, gas and oil relative

permeability has to be altered during CO_2 injection. Nanoscale pores are extensively distributed in tight oil reservoirs, and the associated confinement effect can affect gas and oil relative permeability during CO_2 injection as well. In this section, the interfacial tension of gas-oil is used to analyze the relative permeability curve with the hysteresis in a confined state.

The relative permeability of gas and oil can be altered by interfacial tension reduction. The curvatures of the gas-oil relative permeability curves decrease as the interfacial tension reduces (Asar, 1988). Once the fluid system approaches miscibility, the relative permeability of both phases show linear behavior and become diagonal lines (Fatemi, 2013). As shown in **Figure 3.34**, the gas-oil relative permeability is plotted as the black dashed line; the curve tends to straighten and the wetting phase is more sensitive to the interfacial tension reduction. The intersection of the gas-oil relative permeability curves shifts to the right to some extent, corresponding to a tendency in the water wet character (Asar, 1988). With the confinement effect, the interfacial tension can be further decreased, therefore, the curvature can be further reduced as well, as shown by the blue dashed line. In addition, the number of shifts in relative permeability depends on the amount of CO_2 injected and the pore size.

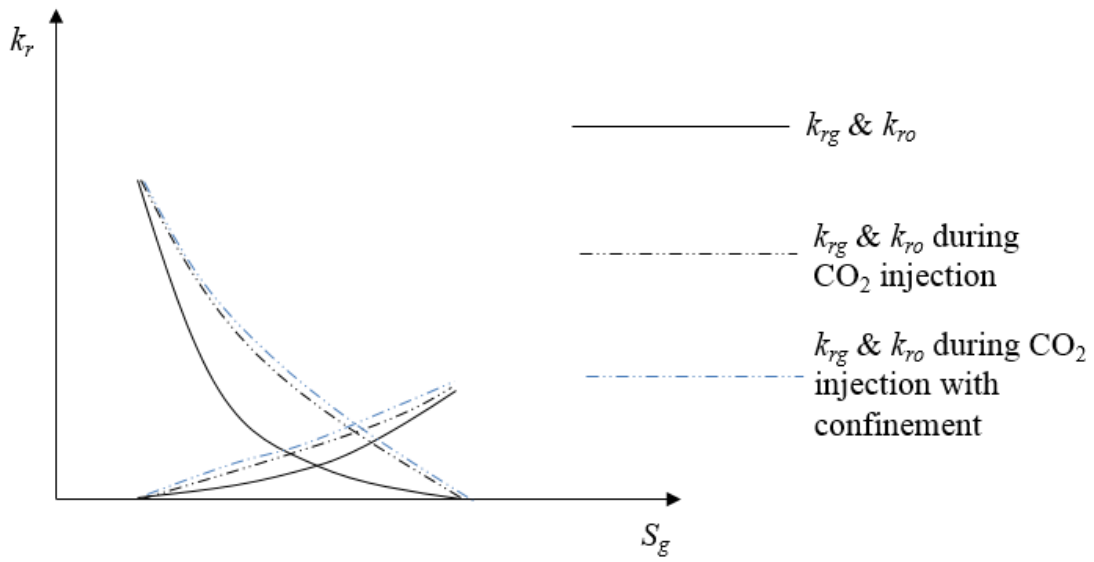

Figure 3.34 Relative Permeability Alteration during CO_2 Injection with Confinement Effect (Zhang, 2016)

Except for the alteration in relative permeability with the confinement effect, hysteresis can also be affected by the confinement effect.

In general, hysteresis for both the wetting and non-wetting phases is less in the high permeable zone compared to that in the low permeable area (Fatemi, 2013). For tight oil reservoirs, the hysteresis effect is non-negligible. In most cases, the hysteresis is caused by the contact angle difference during drainage and imbibition. As shown in **Figure 3.35**, the oil droplets are stable spreading on a solid surface. Once the CO_2 is introduced and oil is displaced, the immiscible interface moves forward in a porous medium. The effective angle of the advancing interface is different than the effective angle of the receding interface, which is as shown by the black dashed line. The contact angle difference is the root of the hysteresis, resulting in a relative permeability

variation in the drainage and imbibition curves. It is related to the degree of surface roughness and tortuosity of the porous medium (Fatemi, 2013).

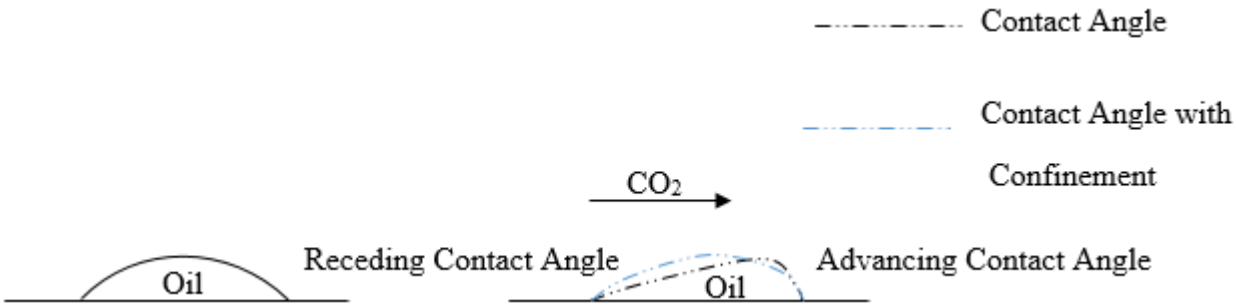

Figure 3.35 Contact Angle Hysteresis (Zhang, 2016)

The relative permeability with hysteresis is illustrated in **Figure 3.36**, where the solid line represents the process of drainage. Assuming the core is 100% saturated with oil initially, gas, the nonwetting phase, displaces the oil and the wetting phase saturation reduces in the drainage process. Under these conditions, the irreducible oil saturation will be reached. Afterwards, the oil is injected, displacing gas in the core sample; the process with the wetting phase saturation increment is imbibition. The difference between the primary drainage and the imbibition curves is caused by the hysteresis effect. Hysteresis is much higher for the non-wetting phase (gas) compared to that for the wetting phase (oil). If a saturation reversal occurs at an intermediate saturation level instead of the endpoint saturation, the relative permeability curve will follow an intermediate path between the drainage and imbibition curves, which is called a scanning curve (Fatemi, 2013).

In tight oil reservoirs, reservoir depletion is the primary way to recover the oil resources. Assuming the reservoir is under-saturated initially, after a certain time of depletion, the bubble

point pressure will be reached and the reservoir will become a saturated reservoir. In this case, the gas will liberate from the oil while the oil saturation is decreasing and the gas saturation is increasing. This occurs in the drainage process. Afterwards, CO_2 is injected into the reservoir, so the bubble point pressure of the reservoir oil can be increased (Zhang, 2015). Some gas can be dissolved in the oil and the resultant oil swelling makes the relative volume of oil increase. The liberated gas will be pushed upward in the reservoir due to the low density of gas phase. In this way, the oil saturation at the bottom of the reservoir is increased, which is in the imbibition process. Later on, as the CO_2 injection continues, the vaporizing gas drive will remove the oil phase. In this case, the relative volume of oil will be decreased, and the oil saturation is reduced again. This is during the drainage process. The alternation between the drainage and imbibition processes drives the hysteresis. The relative permeability for a given phase is greater when its saturation is increased (Fatemi, 2013). Once the injected CO_2 dissolved in the oil phase increases the oil volume, the gas saturation decreases and the relative permeability of the gas phase will be lower than that without the hysteresis effect. It indicates the critical gas saturation must be exceeded for gas to flow out. The gas phase trapping caused by hysteresis can impair oil recovery.

Taking the confinement effect into consideration, the gas and oil compositions, as well as the advancing and receding angles are closer to each other, as shown by the blue dashed line in **Figure 3.35**. In this case, the hysteresis effect can be weakened by the confinement effect. The gap between the relative permeability in the drainage and imbibition processes can be reduced by the confinement effect. As shown in **Figure 3.36**, the blue dashed line is inside the envelope of the

solid and black dashed lines. Since the production can be reduced by hysteresis during CO_2 injection, the confinement effect helps to extract hydrocarbon out, which is consistent with the gas and oil solubility parameters and interfacial tension analysis.

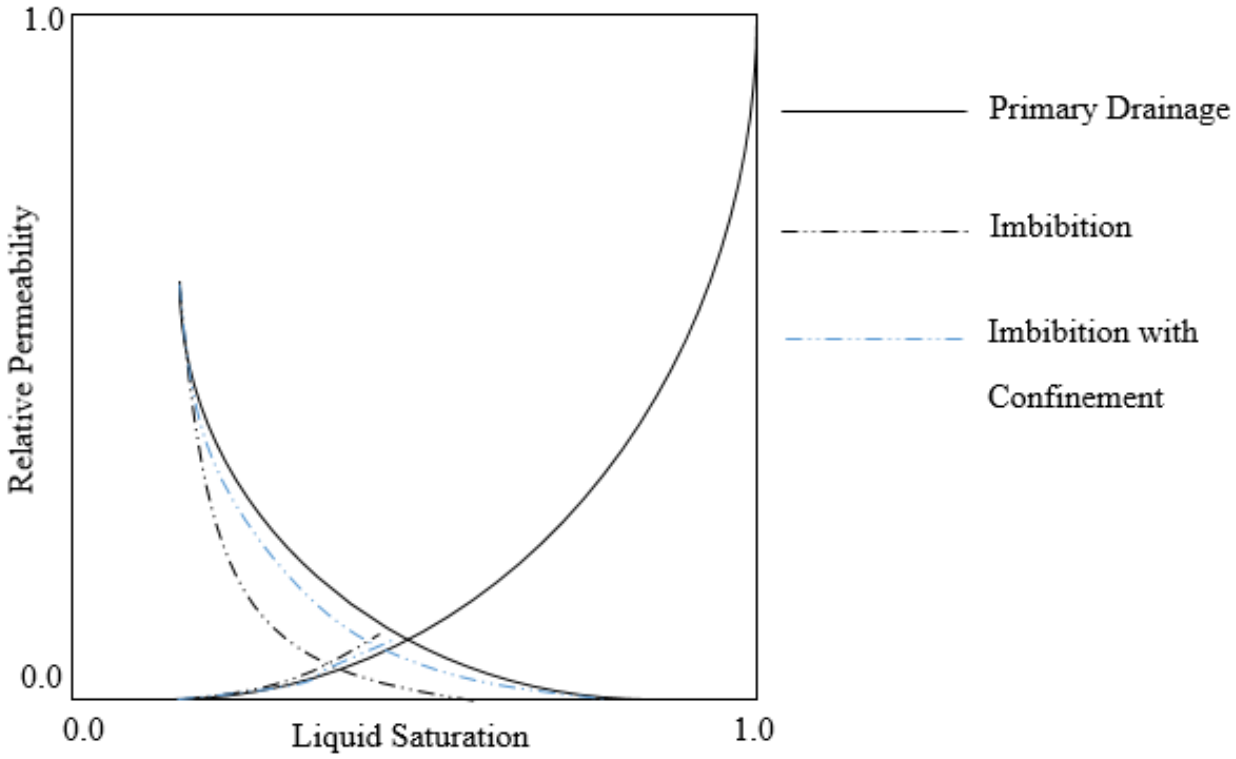

Figure 3.36 Relative Permeability with Hysteresis (Zhang, 2016)

3.6 Applications

It has been shown that nanopores in tight plays can help to modify the phase equilibrium and reduce the CO_2 MMP, resulting in a variation in the CO_2 injection process between conventional reservoirs and unconventional reservoirs. In this way, the development of tight oil reservoirs can be affected to some extent.

For tight oil reservoirs, reservoir depletion is the most common way to unlock the unconventional resources in Canada. CO_2 flooding has been regarded as a successful technique in

improving oil recovery for conventional oil reservoirs, where miscible flooding is generally applied. CO_2 miscible flooding, however, is not a necessity for tight oil reservoirs because of a reduction in CO_2 MMP by nanopores. Therefore, the screening process for CO_2 flooding in candidate reservoirs and CO_2 performance can be affected by the studies.

In the following sections, the least squares method, reservoir simulation and fuzzy analytical hierarchy process are combined to screen the candidate reservoirs for CO_2 flooding; reservoir simulations are applied to help to select CO_2 parameters and improve its performance. This research can help to maximize oil recovery with the lowest amount of CO_2 injected.

Chapter 4. Reservoir Models

In this chapter, theoretical reservoir models are introduced and reservoir simulations are performed to help to screen the candidate reservoirs and select CO_2 parameters.

The simulation models used in the following chapters are presented in this part. Reservoir properties are getting from the software Accumap, which is shown in **Table 4.1**. It is assumed that the reservoir pore sizes are 100 *nm*, 50 *nm* or 10 *nm* with the investigation of the nanopore effect.

Table 4. 1 Reservoir Properties (Zhang, 2015)

Permeability/*md*	0.085
Porosity	0.03
Thickness/*ft*	56.99
Reservoir Pressure/*psi*	3568
Oil Density/lb/ft^3	52.08
Top/*ft*	6945.9
K_v/K_h	0.1
Grid/*ft*	100*50 30*50 5*11.398
API	35
Temperature $^\circ F$	156
S_{wc}	0.25
S_{or}	0.25

On the basis of the properties, a homogenous model is created, as shown in **Figure 4.1.a**. A

heterogeneous model has an average permeability of 0.085 *md* with random permeability distribution, as shown in **Figure 4.1.b**. A dual porosity model is similar to the homogeneous model with the addition of natural fractures. Oil has an API of 35, and its composition is shown in **Figure 4.2**.

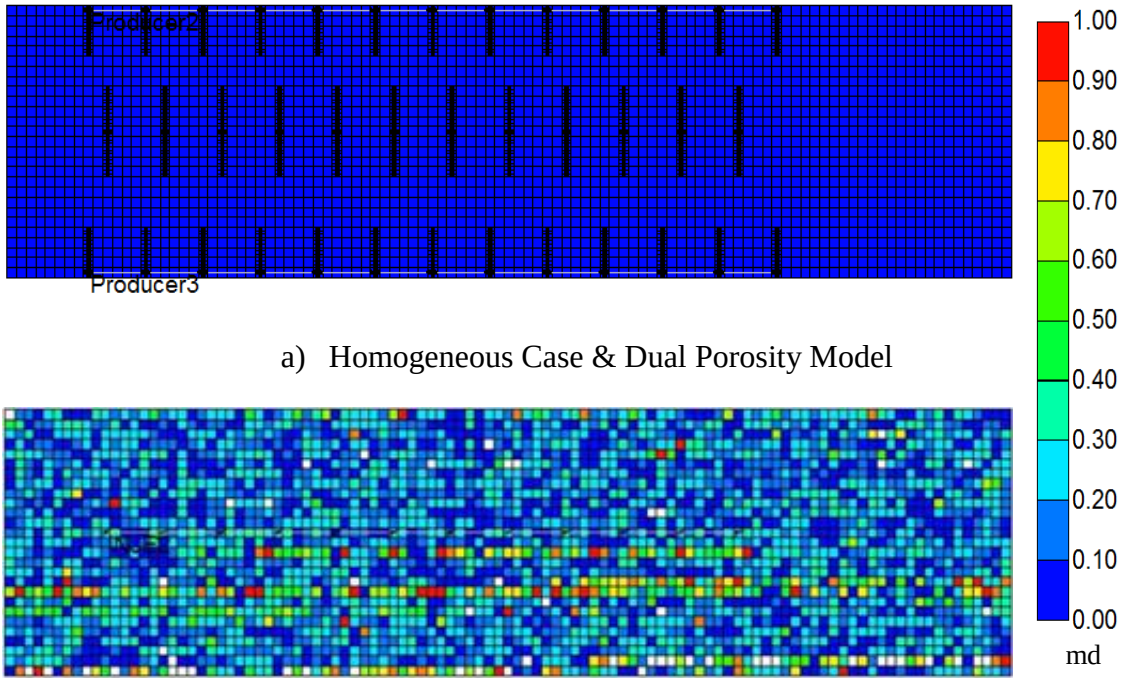

a) Homogeneous Case & Dual Porosity Model

b) Heterogeneous Model

Figure 4. 1 Permeability Distribution for Reservoir Models

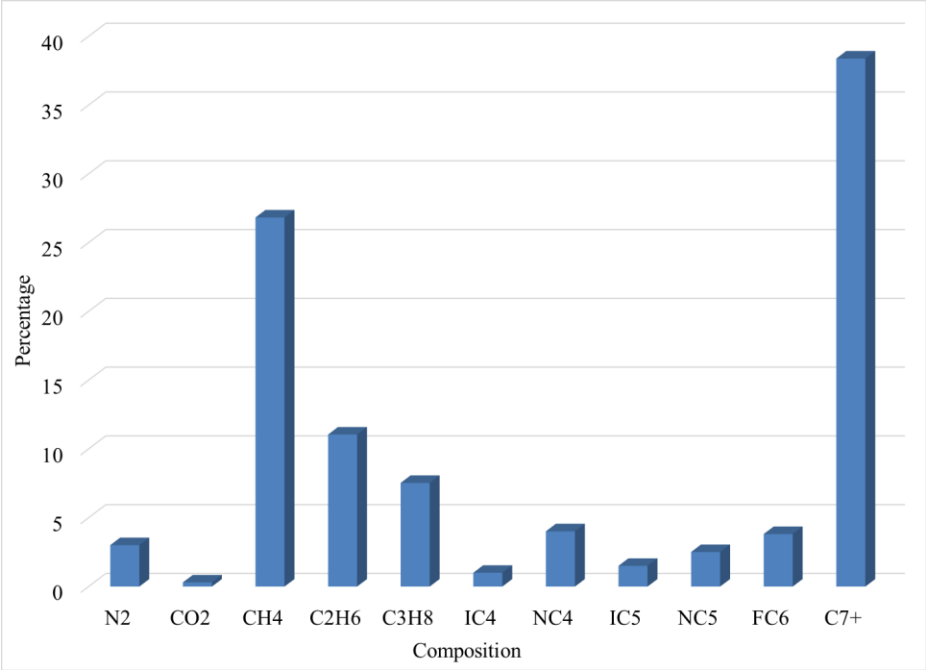

Figure 4. 2 Reservoir Fluid Composition

Hydraulic fractures are added into three models, as shown in **Figure 4.3-4.6**. All perforations of the well are fractured, with local grid refinement applied to simulate hydraulic fractures. Hydraulic fracture properties are shown in **Table 4.2**. In order to accurately capture the hydraulic fractures properties, permeability inside the hydraulic fractures has a reduction of 10 *md* at each feet along the fracture half length. And the initial water saturation in matrix is 0.3. The compressibility of the matrix and hydraulic fracture blocks is different. For the matrix, compressibility is constant; however, for hydraulic fractures, compressibility highly depends on pressure.

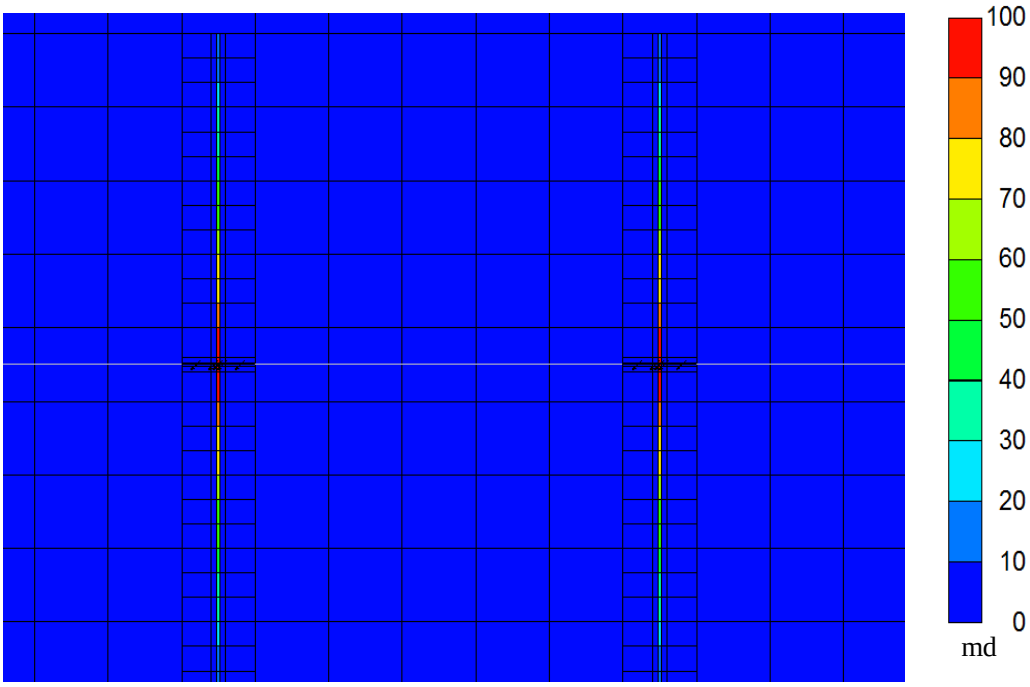

Figure 4. 3 Permeability in Fractures Varies with Distance to Wellbore

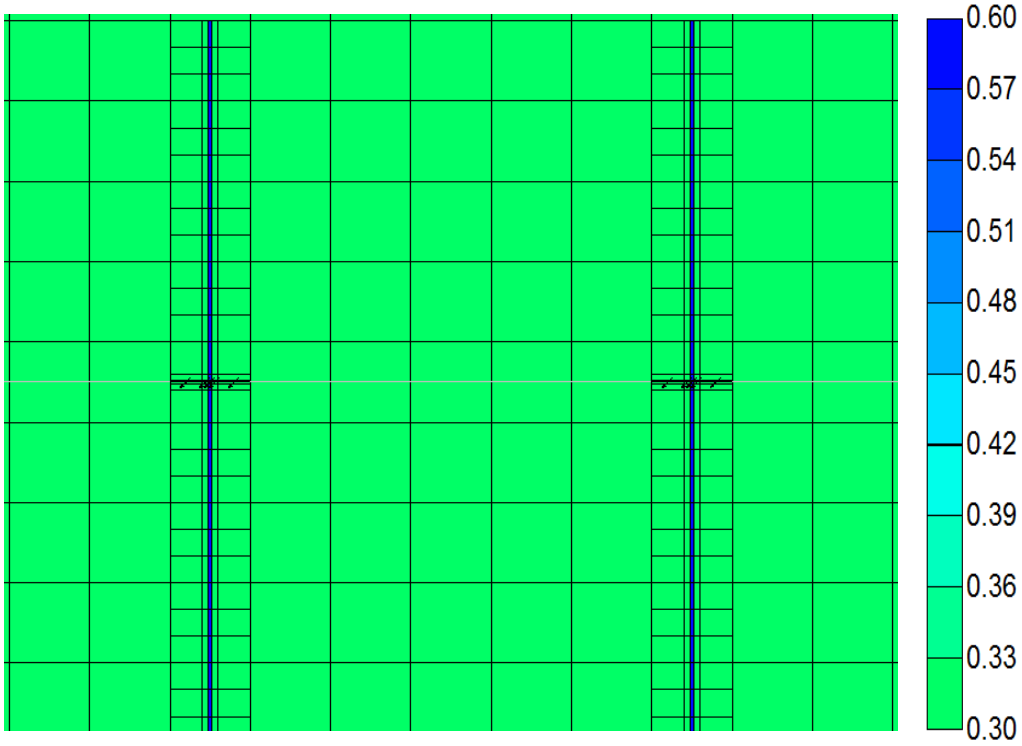

Figure 4. 4 Initial Water Saturation Configuration

As pressure drops in fractures, the fracture conductivity will drop, which leads to pressure

dependent compaction assigned to the hydraulic fractures, as shown in **Figure 4.6**.

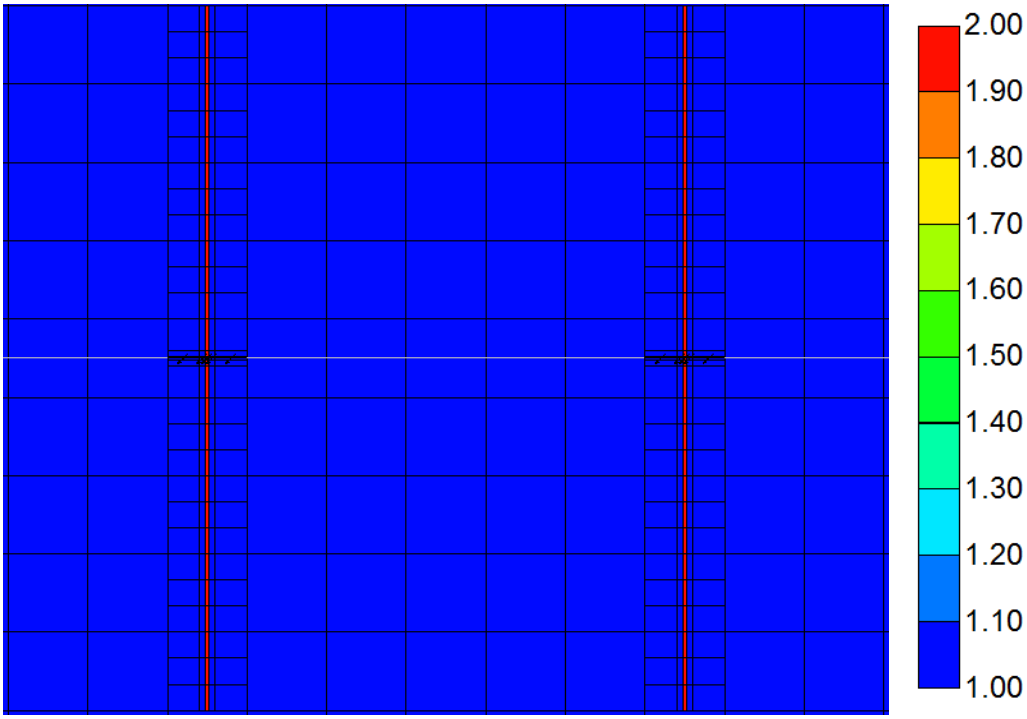

Figure 4. 5 Pressure Dependent Rock Compaction for Hydraulic Fractures

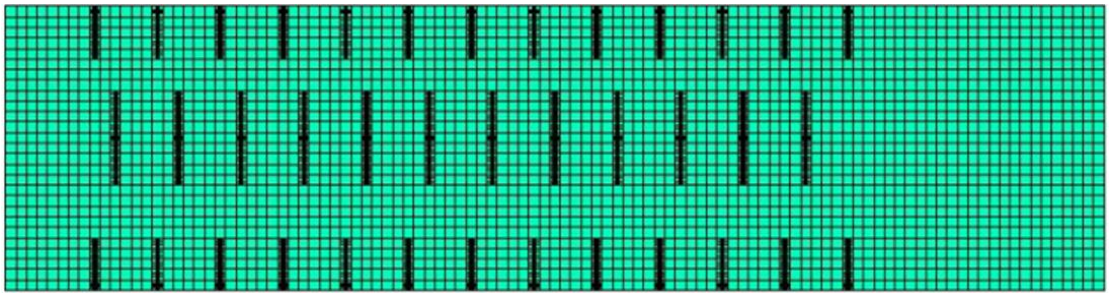

Figure 4. 6 Hydraulic Fracturing Distribution

Table 4. 2 Hydraulic Fracturing Properties (Zhang, 2015)

Half Length/*ft*	225
Fracture Conductivity/md-*ft*	200
Fracture Spacing/*ft*	200
S_{wi} in Matrix	0.30
Compressibility for Matrix/ *1/psi*	5.00×10^{-6}
Compressibility for Proppant	Pressure Dependent

Chapter 5. Integrated Method to Screen CO_2 Flooding for Tight Oil Reservoirs

Numerous field trials of CO_2 EOR projects have been reported. A CO_2 utilization value, defined as a cumulative CO_2 injection versus oil production, is a good technical economic index, ranging from 2.4 *Mcf/STB* to 13 *Mcf/STB* on a net basis (Brock, 1989). CO_2 utilization at an initial stage has a higher impact than if used at a mature stage (Matt, 2014). As reservoir permeability decreases, CO_2 utilization will increase, indicating more CO_2 must be injected to produce the same amount of oil. It is known that CO_2 flooding is a capital intensive process. Oil prices of \$90/*bbl* can support the \$37/*t* (\$2/*Mscf*) cost for CO_2 (Herb, 2013). In general, a CO_2 process will be economically feasible if enhanced oil recovery falls into the range of 6% to 20% (Zhang, 2009). Therefore, a screening process of CO_2 flooding for tight oil reservoirs should be much stricter than that for conventional oil reservoirs (Qin, 2016).

Screening criteria for CO_2 flooding is summarized in **Table 5.1.** It may be unsuccessful if the selection of suitable reservoirs for the CO_2 flooding process is only based on criteria for reservoir parameters. Popular methods to rank reservoirs for CO_2 flooding processes include reservoir simulation and a fuzzy analytical hierarchy process.

Table 5. 1 CO_2 Miscible Flooding Checklist (Carcoana, 1982; Taber, 1983; Klins, 1984; Zhao, 2001; Bachu, 2004; Zhang, 2009)

Experts	Depth	Temperature	Pressure	Permeability	API	Viscosity	Oil Saturation
	ft	*F*	*psi*	*md*		*cp*	%
Carcoana	< 9842	<194	>1203.8	>1	>40	<2	>30
Taber and Martin	> 2296				>26	<15	>30
Klins	>2999		>1493.9		>30	<12	>25
Fulin Zhao	>2500				>22	<10	>20
Bachu S		89.6-249.8	>1102.3		27-48		>25

In this section, an integrated method to screen tight oil reservoirs for CO_2 flooding is proposed. An alteration in MMP and phase equilibrium with the consideration of the confinement effect will occur and the screening process for CO_2 flooding in tight oil reservoirs can be affected this way.

There are three popular ways to calculate weight w_j, including the least squares method, reservoir simulation method and fuzzy analytical process.

5.1 Least Squares Method

To avoid subjectivity when evaluating an index weight for each property *j*, the least squares method is widely applied (Wang, 2010). In this way, minimizing weight errors is set as the objective, and weight w_j can be calculated through squares of the differences between weight w_j and relative significance matrix r_j together with squares of the differences between weight w_j and objective weight matrix u_j. Relative significance matrix r_j can be obtained through two property

performance comparisons, as shown in **Table 5.2**. In addition, an objective weight matrix is determined by the relative importance of a decisive matrix. The following formula shows the least squares method to calculate weight, w_j (Wang, 2010):

$$\begin{cases} \min H(w) = \sum_{i=1}^{m} \sum_{j=1}^{n} \left\{ \left[(r_j - w_j) b_{ij} \right]^2 + \left[(u_j - w_j) b_{ij} \right]^2 \right\} \\ \sum_{j=1}^{n} w_j = 1 \\ w_j \geq 0 \qquad j = 1,2,\cdots,n \end{cases} \tag{5.1}$$

Assuming candidate reservoirs of *i* are expected to perform CO_2 flooding, there are properties *j* for each reservoir. Reference values by experts are given in **Table 5.1.**

A base matrix can be built, in which *m* represents the number of reference experts and *n* is the total number of properties.

$$a_{ij} = \begin{bmatrix} a_{11} & a_{12} & \dots & a_{1n} \\ a_{21} & a_{22} & \dots & a_{2n} \\ \dots & \dots & \dots & \dots \\ a_{m1} & a_{m2} & \dots & a_{mn} \end{bmatrix}$$

The base matrix, a_{ij}, is given by the relative difference between each property, *j*, of the reservoir *i*, P_{ij} and reference value, P_r, are given by experts for property *j*:

$$a_{ij} = {(P_{ij} - P_r)}\Big/{P_r} \tag{5.2}$$

For each property *j*, it can be classified as a cost item, such as CO_2 price, an operating cost, a pipeline cost, or a compressor cost and a benefit item, including oil saturation, oil API, reservoir permeability, dip, or reservoir pressure.

For cost items, the decisive matrix b_{ij} is given by:

$$b_{ij} = {min\{a_{ij}|1 \le i \le m\}}/{a_{ij}} \tag{5.3}$$

For benefit items, the decisive matrix b_{ij} is given by:

$$b_{ij} = {a_{ij}}/{max\{a_{ij}|1 \le i \le m\}} \tag{5.4}$$

In this way, a decisive matrix can be obtained:

$$b_{ij} = \begin{bmatrix} b_{11} & b_{12} & \dots & b_{1n} \\ b_{21} & b_{22} & \dots & b_{2n} \\ \dots & \dots & \dots & \dots \\ b_{m1} & b_{m2} & \dots & b_{mn} \end{bmatrix}$$

A normalized matrix p_{ij} is defined as follows:

$$p_{ij} = {b_{ij}}/{\sum_{i=1}^{m} b_{ij}} \tag{5.5}$$

The information term E_j is defined as follows:

$$E_j = -(lnm)^{-1} \sum_{i=1}^{m} p_{ij} ln p_{ij} \tag{5.6}$$

The objective weight matrix u_j is given by:

$$u_j = {(1 - E_j)}/{\sum_{j=1}^{n} 1 - E_j} \tag{5.7}$$

For CO_2 flooding performance, the properties of each reservoir behave differently in the evaluation. A scale for a two-property comparison is proposed. In this comparison, the relative significance matrix r_{ij} can be obtained:

$$r_{ij} = \begin{bmatrix} r_{11} & r_{12} & \dots & r_{1n} \\ r_{21} & r_{22} & \dots & r_{2n} \\ \dots & \dots & \dots & \dots \\ r_{m1} & r_{m2} & \dots & r_{mn} \end{bmatrix}$$

It has the following characteristics:

1. $r_{ii} = 0.5, i = 1,2 \dots n$
2. $r_{ij} = 1 - r_{ji}, i, j = 1,2 \dots n$

3. $Constant = r_{ik} - r_{jk}, i, j, k = 1,2 \ldots n$

Table 5. 2 Scale for Two Properties Comparison (Zhang, 2000)

Significance	Definition	Comment
0.5	Equal Significance	Comparison between a and b effects on oil production or CO_2 utilization equal significance.
0.6	Somewhat Important	Comparison between a and b effects on oil production or CO_2 utilization, a is somewhat important than b.
0.7	More Important	Comparison between a and b effects on oil production or CO_2 utilization, a is more important than b.
0.8	Much More	Comparison between a and b effects on oil production or CO_2 utilization, a is much more important than b.
0.9	Extreme More	Comparison between a and b effects on oil production or CO_2 utilization, a is extremely more important than b.
0.1,0.2,0.3,0.4	Reverse	$r_{ij} = 1 - r_{ji}$

The steps to create the relative significance matrix r_{ij} are given as follows:

1. If one property has a more significant influence on CO_2 flooding performance in many trials, it will be less uncertain for r_{11}, r_{12},..., r_{1n}.

2. The difference in *r* for the same properties should be constant in rows 1 and 2. Otherwise, row 2 has to be adjusted.

3. The difference in *r* for the same properties should be constant in rows 1 and 3. Otherwise, row

3 has to be adjusted.

4. Follow the above steps until the differences in *r* for the same properties are constant in rows 1 and *n*.

The relative significance matrix used in the thesis is given in **Table 5.3**.

Table 5. 3 Relative Significance Matrix

	API	Oil Saturation	Permeability	Thickness	Dip	Pressure/MMP
API	0.5	0.6	0.2	0.3	0.6	0.5
Oil Saturation	0.4	0.5	0.1	0.2	0.5	0.4
Permeability	0.8	0.9	0.5	0.6	0.9	0.8
Thickness	0.7	0.8	0.4	0.5	0.8	0.7
Dip	0.4	0.5	0.1	0.2	0.5	0.4
Pressure/MMP	0.5	0.6	0.2	0.3	0.6	0.5

After the relative significance matrix r_{ij} is obtained, the vector *r* can be given by:

$$r_k = \sum_{j=1}^{n} r_{kj} \Big/ \sum_{r,j=1}^{n} r_{ij}$$

$$r = (r_1, r_2, \dots, r_n)$$

5.2 Reservoir Simulation

On the basis of the homogeneous model in **Chapter 4**, reservoir simulations are carried out to conduct an oil production comparison for each property *j*. Hundreds of simulations are run by CMG; CO_2 utilization or cumulative oil production with various API, oil saturation, permeability,

thickness, dip, and pressure/minimum miscible pressure (MMP) are recorded and plotted in **Figure 4.1**. The average slope for parameter *j* is expressed as (Rivas, 1994):

$$\alpha_j = \frac{\frac{|V_{oj} - V_{wj}|}{V_{oj}}}{\frac{|P_{oj} - P_{wj}|}{P_{oj}}} \tag{5.8}$$

The optimistic value for property *j* is given by simulation runs, and can be read from **Figure 5.1.** The worst value for property *j* is determined from the data bank of reservoirs to be ranked. For each specific property *j*, the value farthest away from the optimistic value will be the worst value for property *j*. The average relative importance of the slope for parameter *j* and α_j is used to determine the weight w_j for property *j* (Rivas, 1994):

$$w_j = \frac{\alpha_j}{\sum_{k=1}^{n} \alpha_k} \tag{5.9}$$

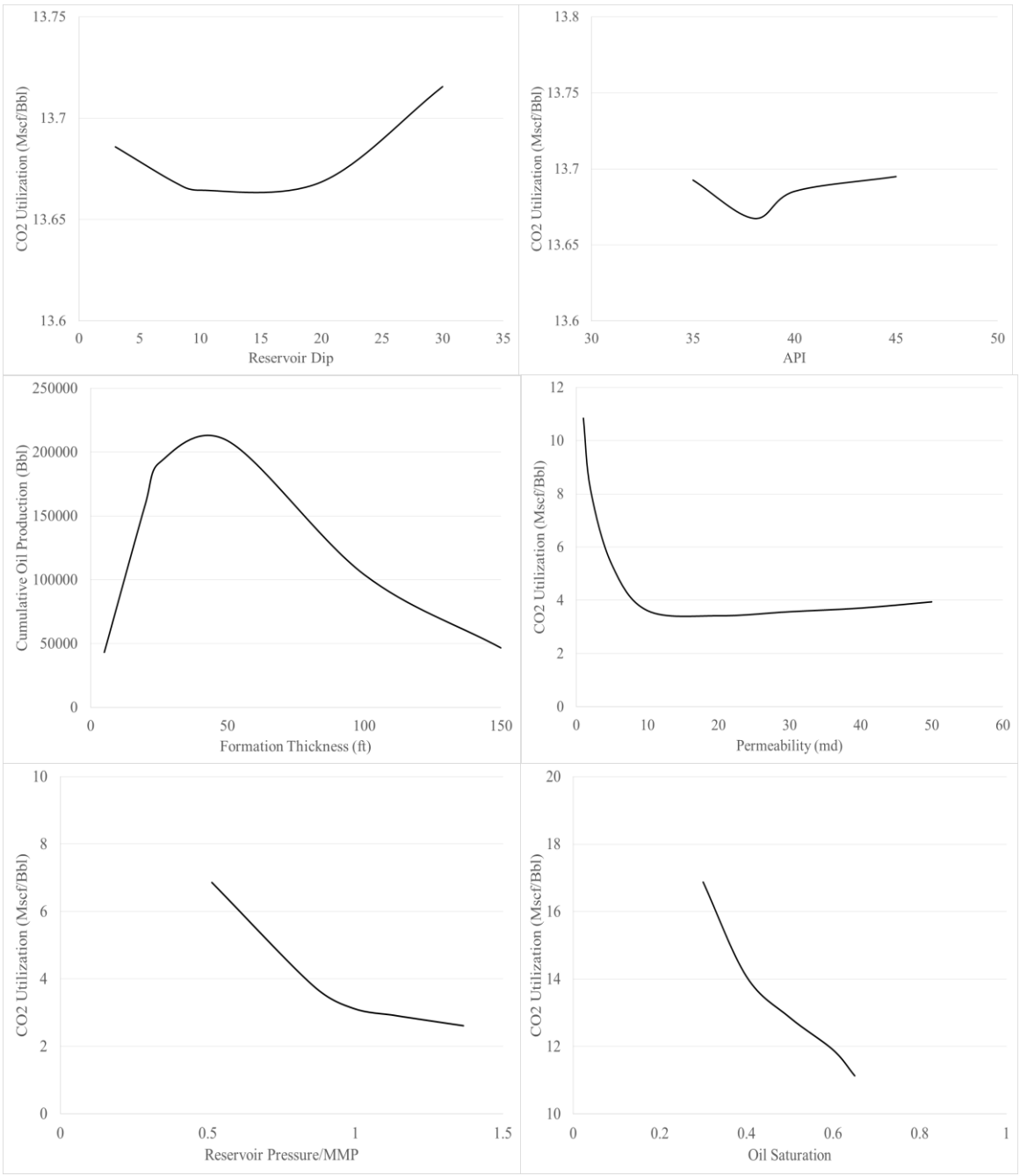

Figure 5. 1 Reservoir Simulations for Base Model (Zhang, 2015)

5.3 Fuzzy Analytical Hierarchy Process

The fuzzy analytical process involves a comparison between two factors at one time, resulting in a matrix for all factors. In this way, experience inadaptability and subjectivity can be avoided

(Zhang, 2000; Chen, 2007). In this method, a relative significance matrix r_{ij} is obtained from **Table 5.3**.

In the fuzzy analytical hierarchy process, the comparison of significance among properties results in a matrix r_{ij}. The weight for each property *j* is w_j. The following equation is established:

$$r_{ij} = 0.5 + a(w_i - w_j), i, j = 1,2, \dots, n \tag{5.10}$$

where a represents the uncertainty of the significance comparison among the properties. It represents the significance of the influence of the properties on the CO_2 flooding process. In general, a is in the range of (0, 0.5] (Zhang, 2000). In the case that a huge variation of different parameters works on CO_2 flooding performance, the constant a can be a larger value. Similar to the least squares method, instead of calculating the squares of weight errors, weight w_j for each property j can be calculated by the following equation:

$$\begin{Bmatrix} minz = \sum_{i=1}^{n} \sum_{j=1}^{n} [0.5 + a(w_i - w_j) - r_{ij}]^2 \\ \sum_{j=1}^{n} w_j = 1, w_j \geq 0 \end{Bmatrix} \tag{5.11}$$

A Lagrangian multiplier λ can be incorporated into the following equation:

$$minL(w, \lambda) = \sum_{i=1}^{n} \sum_{j=1}^{n} [0.5 + a(w_i - w_j) - r_{ij}]^2 + 2\lambda(\sum_{i=1}^{n} w_i - 1) \tag{5.12}$$

Taking the partial derivatives of L with respect to λ and driving it to be zero results in the equation:

$$a \sum_{j=1}^{n} [0.5 + a(w_i - w_j) - r_{ij}] - a \sum_{k=1}^{n} [0.5 + a(w_k - w_i) - r_{ki}] + \lambda = 0, \text{ i} = 1,2 \dots \text{n} \tag{5.13}$$

As $r_{ii} = 0.5$, it can be expressed as

$$\sum_{j=1}^{n} [2a^2(w_i - w_j) + a(r_{ji} - r_{ij})] + \lambda = 0 \tag{5.14}$$

It can be further expressed as:

$$\begin{cases} 2a^2(n-1)w_1 - 2a^2 w_2 - 2a^2 w_3 - \cdots - 2a^2 w_n + \lambda = a\sum_{j=1}^{n}\left(r_{1j} - r_{j1}\right) \\ -2a^2 w_1 + 2a^2(n-1)w_2 - 2a^2 w_3 - \cdots - 2a^2 w_n + \lambda = a\sum_{j=1}^{n}\left(r_{2j} - r_{j2}\right) \\ \quad ---------- \\ -2a^2 w_1 - 2a^2 w_2 - 2a^2 w_3 - \cdots + 2a^2(n-1)w_n + \lambda = a\sum_{j=1}^{n}\left(r_{nj} - r_{jn}\right) \\ w_1 + w_2 + \cdots + w_n = 1 \end{cases} \tag{5.15}$$

In this way, the weight w_j can be determined.

5.4 Ranking Candidate Reservoirs

Grading for candidate reservoirs is determined after weight w_j for each property *j* is calculated. The normalized parameter X_{ij} is determined by the relative difference between each property *j* of the reservoir *i*, P_{ij} and the optimistic and worst values, as shown in the following equation (Rivas, 1994):

$$X_{i,j} = \frac{\left|P_{i,j} - P_{o,j}\right|}{\left|P_{w,j} - P_{o,j}\right|} \tag{5.16}$$

The variable X_{ij} changes linearly between 0 and 1, and it is transformed to exponential varying parameters, A_{ij} (Rivas, 1994):

$$A_{ij} = 100e^{-4.6X_{i,j}^2} \tag{5.17}$$

To take into account the relative importance of the weight for each property, a weighted grading matrix W_{ij} is defined (Rivas, 1994):

$$W_{i,j} = A_{i,j}w_j \tag{5.18}$$

Grading is determined by multiplying the weight matrix W_{ij} by its transpose, W_{ji}, and normalizing it (Rivas, 1994).

$$R_g = {100\left(\sum W_{ij}W_{ji}\right)^{0.5}}\Big/{W_o} \tag{5.19}$$

Reservoirs with a grade R_g of over 80 will be considered towards the next step.

As an example, we have three candidate reservoirs for a CO_2 EOR evaluation. Reservoir parameters are shown in **Table 5.4** and oil composition is shown in **Figure 5.2**. The following presents the integrated method in detail.

Table 5. 4 Candidate Reservoirs for CO_2 Screen Process (Zhang, 2015)

Parameters	Reservoir 1	Reservoir 2	Reservoir 3
API	40	39	30
Oil Saturation	60	58	20
Permeability (*md*)	0.06	0.057	0.1
Thickness(*ft*)	44.3	54.1	32.8
Dip	8	4	3
Pressure/MMP	1.1	1.15	3.08
CO_2 price is \$1.5/*Mscf* for three reservoirs, all of which are initially saturated. The pore size is the same of 50 *nm* diameter.			

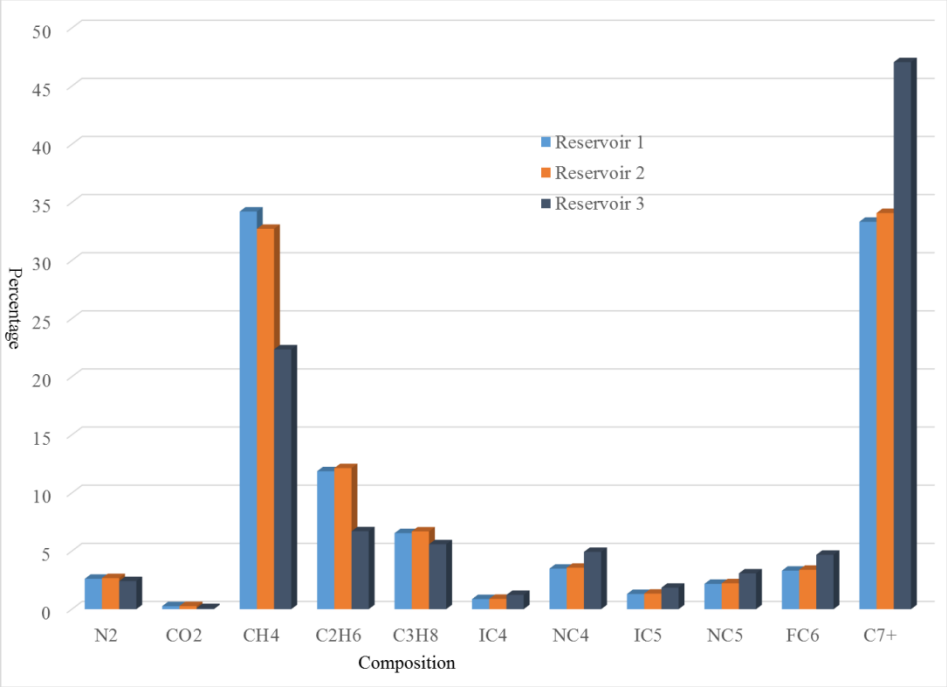

Figure 5. 2 Reservoir Fluids Composition (Zhang, 2015)

Based on the simulation runs, as shown in **Figure 5.1**, the optimistic value for API is 38, oil saturation is at the highest, permeability is 10 *md*, the thickness is 47 *ft*, the reservoir dip is 15, and the reservoir pressure is the highest from candidate reservoirs.

Weight w_j for each property *j* is calculated by the methods listed in **Table 5.5**.

Table 5. 5 Weight for Each Property (Zhang, 2015)

Parameters	Least Squares Method	Reservoir Simulation	Fuzzy Analytical Process
API	0.223	0.007	0.152
Oil Saturation	0.091	0.234	0.124
Permeability	0.316	0.576	0.240
Thickness	0.000	0.025	0.210
Dip	0.000	0.001	0.121
Pressure/MMP	0.169	0.157	0.152
CO_2 price	0.200	/	/

After the weight for each property w_j is obtained, grades for the reservoirs can be calculated, as shown in **Table 5.6**. Reservoir 1 has a better potential in the CO_2 EOR process with a grade of over 80 for all three methods and thus it will move forward for the next consideration.

Table 5. 6 Grades for Candidate Reservoirs (Zhang, 2015)

Grade	Reservoir 1	Reservoir 2	Reservoir 3
Least Square Method	0.835	0.824	0.704
Reservoir Simulation	0.834	0.822	0.557
Fuzzy Analytical Process	0.857	0.693	0.531

In tight oil reservoirs, a significant chance exists in underground nanoscale pores. The nanoscale pore confinement can alter crude oil phase behavior and MMP in tight oil reservoirs.

Uncertainties for the grade of candidate reservoirs become more complex because of the existence of nanoscale pores.

The CO_2 MMP is reduced by the confinement effect, however, the oil recovery is still higher with a larger reservoir pressure. The weight for reservoir pressure does not change, while the oil recovery benefits from the confinement effect because of the bubble point suppression. Taking the confinement effect into consideration, the term of the reservoir/MMP will become larger, and the grades of the candidate reservoir will be increased for all cases. It will not affect the ranking for candidate reservoirs in screen CO_2 flooding.

After the grades of candidate reservoirs are obtained, reservoir simulations will only focus on the high score reservoirs. In general, a CO_2 process will be economically feasible if enhanced oil recovery falls into the range of 6% to 20% (Zhang, 2009).

The results for simulation runs based on the reservoir 1 properties are shown in **Figure 5.3**. CO_2 flooding following water flooding over two years has an oil recovery incremental of 10% compared to water flooding performance. A good chance exists for reservoir 1 to dramatically improve oil recovery by CO_2 flooding.

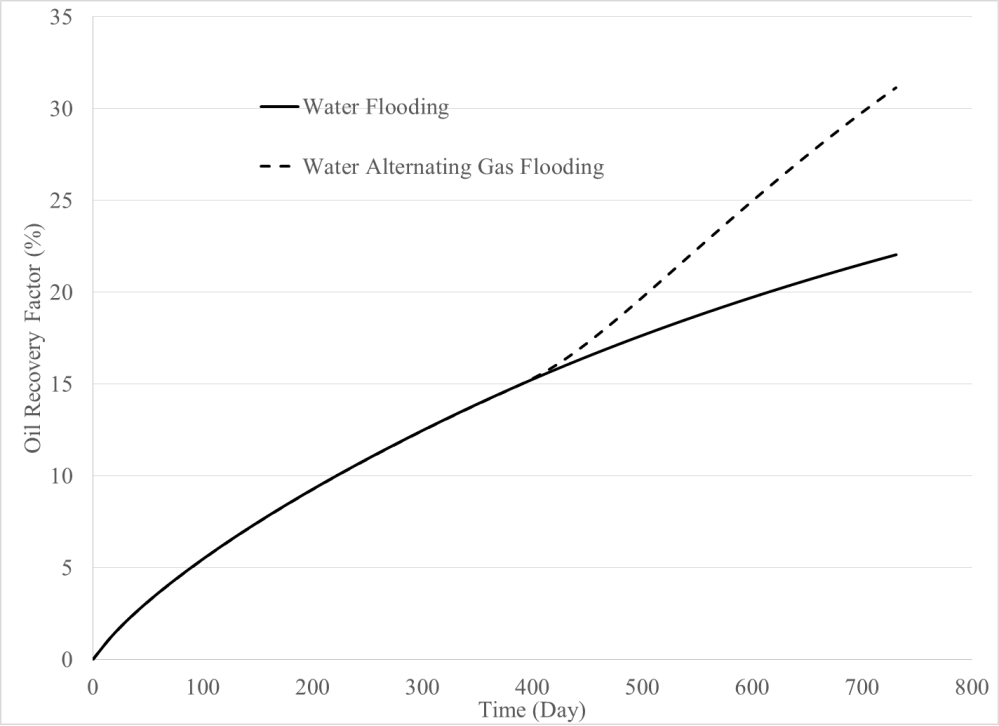

Figure 5. 3 CO_2 Flooding Reservoir Simulation for Reservoir 1 (Zhang, 2015)

Good candidate reservoirs are moved towards an asphaltene precipitation analysis and CO_2 parameters design. CO_2-induced asphaltene precipitation may cause a severe problem during CO_2 flooding even with good miscibility conditions. It is necessary to take asphaltene precipitation into consideration in the screening process for CO_2 flooding. First, the asphaltene to resin ratio is checked and an asphaltene precipitation equation of state (EOS) calculation is made. Finally, production experience is used as a reference for risk evaluation.

Figure 5.2 shows a low ratio of asphaltene to resin for the reservoir 1 oil sample. This implies good colloidal stabilization as there is less chance for asphaltene to be precipitated in formation (Carnahan, 2007). EOS calculations are conducted to analyze asphaltene precipitation. As shown in **Figure 5.4**, all of these solid precipitation plots are overlapped, and only the green line with the

case of 500 *psia* can be seen because it is plotted at the very end. No solid precipitation appears for the reservoir 1 oil sample during CO_2 injection under various reservoir pressures and amounts of CO_2 injected in mole fraction, even at a low pressure of 500 *psia* with 0.9 mole fraction of CO_2.

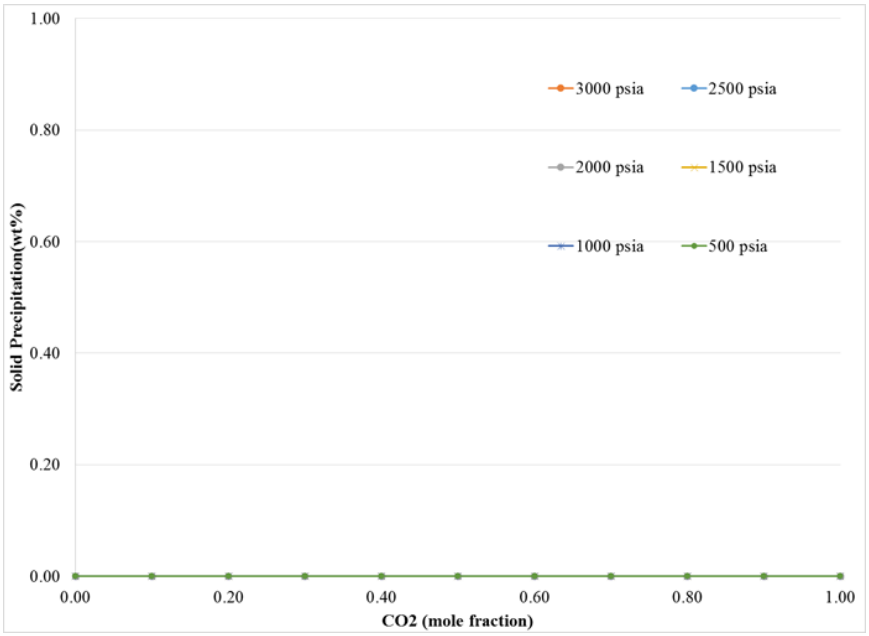

Figure 5. 4 Solid Precipitation Prediction (Zhang, 2015)

Asphaltene precipitation is not linked to any severe problem for the presented oil sample. In some cases, it can cause severe problems even when a low amount of asphaltene is precipitated; field experience of CO_2 induced asphaltene precipitation problems are shown in **Figure 5.5**. Reservoir 1 is initially saturated with an oil density of 51.47 lb/ft^3. As observed on the plot in the **Figure 5.5**, reservoir 1 has no asphaltene problem.

Based on an oil composition analysis, asphaltene precipitation calculations and a field trial plot, reservoir 1 is not likely to have asphaltene problems. It can move towards the CO_2 parameters design in order to maximize oil recovery.

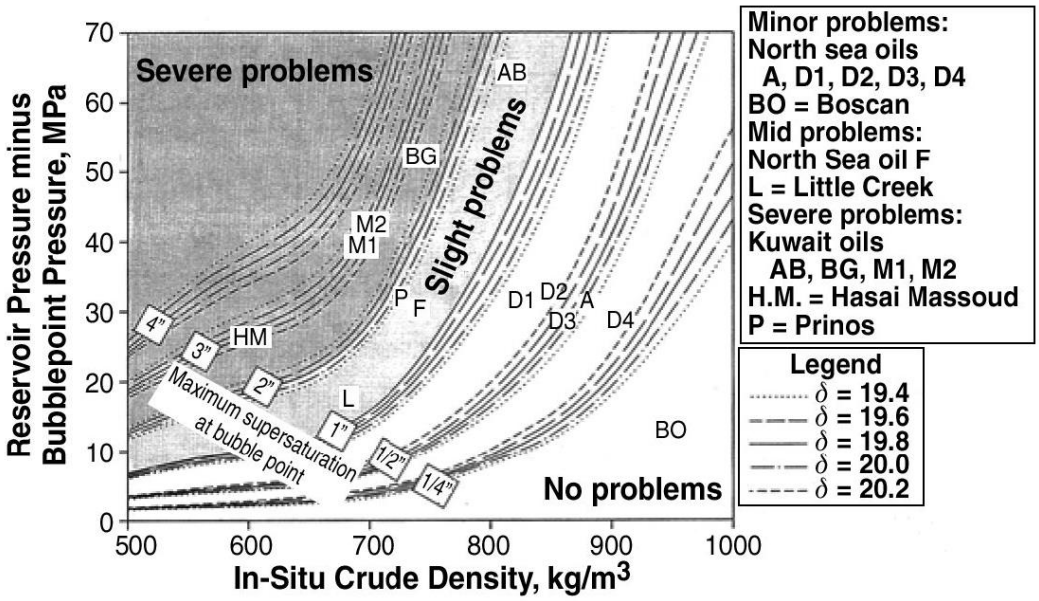

Figure 5. 5 Screen for Asphaltene Precipitation (Boer, 1995)

5.5 Pros and Cons

In general, these three methods offer similar results for candidate reservoirs. Only the least squares method, however, can take the CO_2 price into account as a cost item, which is not applicable for the other two methods. The factors can be classified into cost and benefit items in the least squares method. In this way, it is easier to carry out an economic analysis and minimize a system error. Even so, in some cases, numerical instabilities exist in calculations.

Only six factors are involved in the analysis. If thousands of candidate reservoirs with 10 properties or more are needed to be screened for a CO_2 flooding process, it is easier to carry out a simulation analysis as a weight calculation for each property is simple and it can be also used for production forecast. For others, the calculation of weight w_j will become too complex and simplified models may create deviated results to some extent.

Experience, inadaptability and subjectivity can be avoided in the least squares method and fuzzy analytical process. For the fuzzy analytical process, there is no squared term in calculation, resulting in higher efficiency than with the least squares method.

The integrated method in this section is based on experience from experts, associated with mathematical methods and reservoir simulation, together with asphaltene precipitation calculations for CO_2 flooding projects. It is applicable in broad scenarios for risk, cost and benefit analysis.

Chapter 6. CO_2 Parameters Selection

With the goal to maximize oil recovery, a miscible CO_2 process is preferred over the immiscible one. A CO_2 near-miscible flooding, with formation pressure slightly below MMP, can also economically recover oil from tight formations (Holm, 1976; Pittaway, 1985; Manrique, 2006). Laboratory studies and field pilots show that oil recovery can also be high in a near-miscible region (Holm, 1976; Shyeh, 1991; Hadlow, 1992; Bardon, 1994; Dong, 2001; Arshad, 2009; Ren, 2011). Additionally, the presence of non-CO_2 (e.g., CH_4, N_2, or intermediate hydrocarbons components such as C_2 and C_3) in the injected gas can exert a big impact on the CO_2-oil MMP, either to raise or to decrease the MMP depending on the components, resulting in a variation in gas flooding performance.

Reservoir simulations are run to investigate the confinement effect of 10 *nm* and 50 *nm* pores on CO_2 injection performance; the pure and impure gas performances are presented.

6.1 CO_2 Operation Pressure

With the effect of nanoscale pore confinement, CO_2 MMP is lower, as shown in **Table 3.2**. On the basis of the homogeneous model in **Chapter 4**, assuming that all reservoir pores are 50 *nm* or 10 *nm*, the reservoir simulations are carried out to select CO_2 parameters for tight oil exploitation in a more reasonable way.

If a pore size is small without much standard deviation, then interfacial tension optimization will be key to oil recovery. If the pore size is big and its distribution is of a broader variation, the viscosity force will dominate in the determination of an oil rate. Since a pore size is quite small in

a tight formation, the confinement can exert effects on a reservoir fluid phase envelope, especially with the presence of nanopore (Teklu, 2013; Teklu, 2014), resulting in lower CO_2 MMP (Teklu, 2014). As the reservoir pore size has a broad distribution, one can operate injectors in a near-miscible region, where pressure is slightly less than MMP, as measured in the lab. Oil flow in large pores is dominated by the viscosity force and oil can still be extracted effectively in a near-miscible region. The miscible phenomenon can appear in small pores with the confinement effect. In this way, operating wells in a near-miscible region can offer similar oil production to that in a miscible condition for tight oil reservoirs, but the volume of CO_2 injected can be reduced.

The confinement effect caused by the nanoscale pore can boost oil production to some extent. A well injection pressure can be lower with the confinement effect to achieve a similar amount of oil production. In this case, there is a great chance for a CO_2 near-miscible process to lead to competitive oil production with the miscible process in tight oil reservoirs, where nanoscale pores can be extensively distributed. On the basis of the homogeneous reservoir model in **Chapter 4**, reservoir simulations are run to investigate the confinement effect of 10 *nm* and 50 *nm* pores on CO_2 injection performance.

Miscibility of CO_2 injection is determined by a well operation pressure. As CO_2 is injected into a reservoir, while the reservoir fluid is producing at a high rate, the reservoir pressure will depend on the volume of CO_2 injected. For the reservoir fluids in this simulation, CO_2 MMP is around 2920 *psi*. Recovery of 20 years of CO_2 injection is shown in **Figure 6.1**; when the well injection pressure is 3500 *psi* and CO_2 flooding is under the immiscible condition. When the well

injection pressure is 3900 *psi*, the average reservoir pressure can approach 2900 *psi* and CO_2 flooding is in a near-miscible condition. The CO_2 injection process is converted to a miscible condition with a well injection pressure of 4000 *psi* and above. In this case, the average reservoir pressure keeps above 2920 *psi*. The slope of the oil recovery factor starts to decrease as the well injection pressure approaches 4000 *psi*. The more CO_2 injected, the more reduced the efficiency of the oil viscosity reduction, as shown in **Figure 6.2**. The CO_2 process is transformed from a near-miscible process into the miscible condition. It indicates that CO_2 EOR efficiency goes down as the pressure approaches MMP. The CO_2 near-miscible process benefits from mobility control since CO_2 mobility decreases with decreasing pressure (Shyeh, 1991).

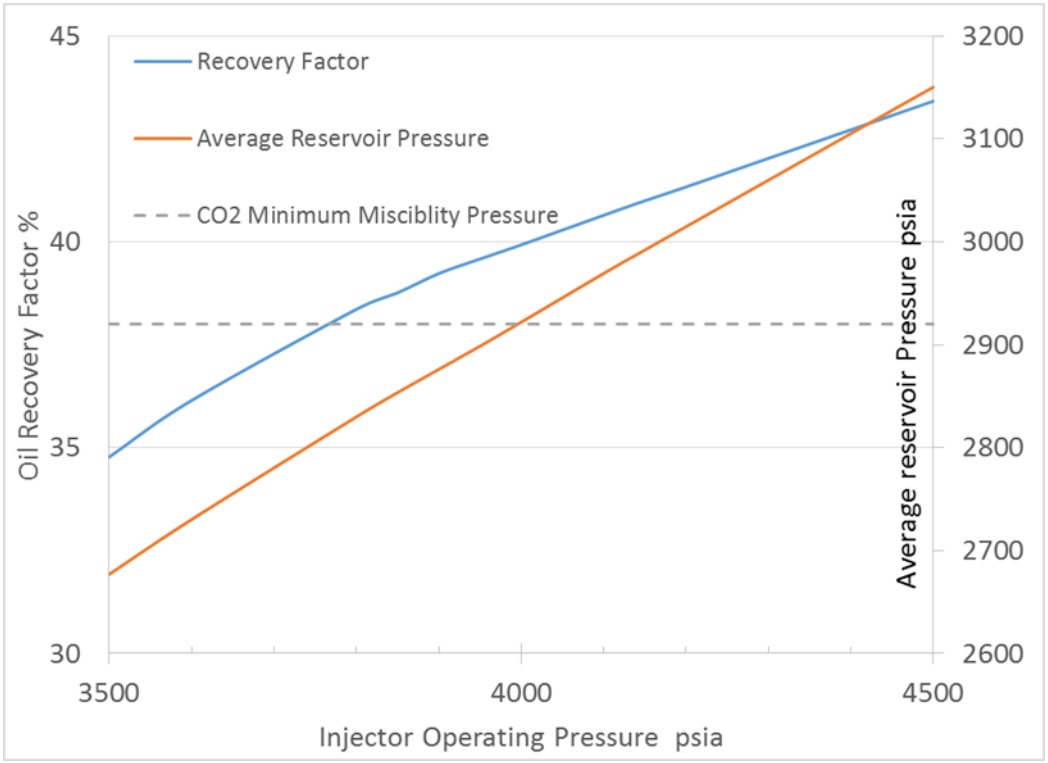

Figure 6. 1 Oil Recovery Factor with Various CO_2 Operation Conditions (Zhang, 2015)

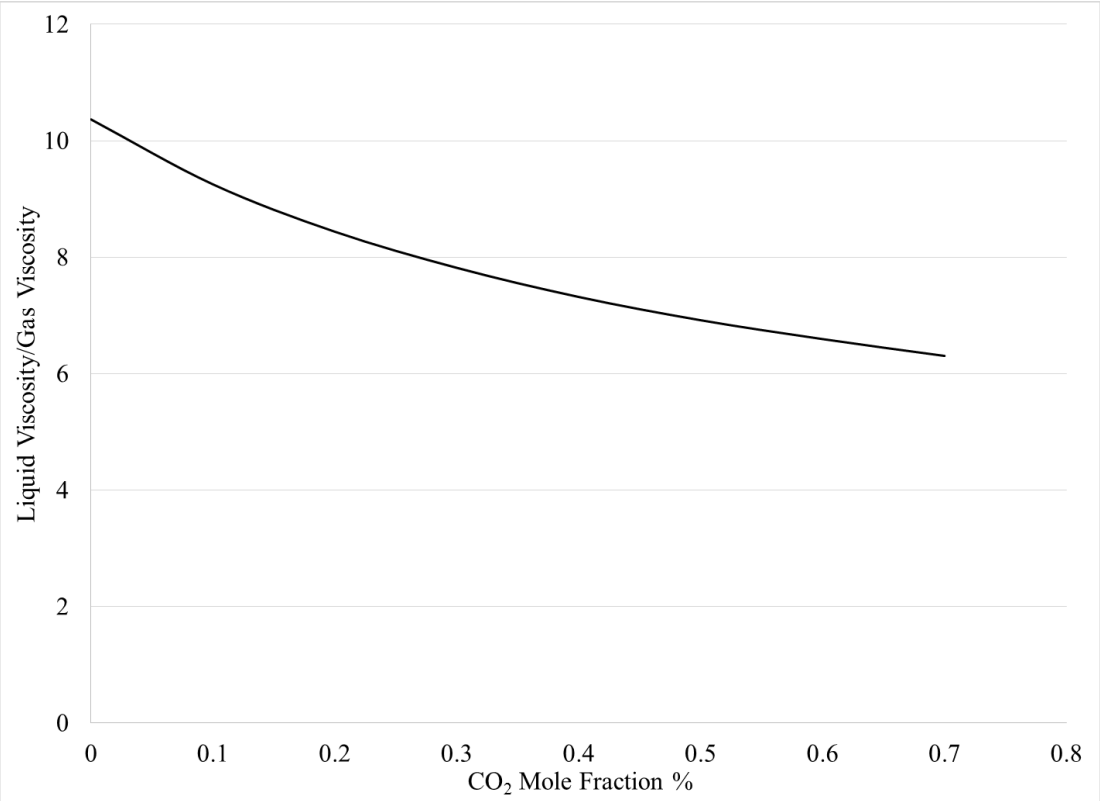

Figure 6. 2 Liquid-vapor Viscosity Ratio (Zhang, 2016)

As shown in **Figures 6.3 - 6.6**, CO_2 injection is designed as a near-miscible process with the well operation pressure at 3900 *psi* and 3600 *psi*, respectively. CO_2 is at the miscible condition with the well operation pressure of 4000 *psi* as the reservoir pressure reaches 2920 *psi*, which is the MMP for this reservoir fluid. For the 50 *nm* pore size, cumulative oil production at a well operation pressure of 3900 *psi* with the effect of confinement is similar to that at a well operation pressure of 4000 *psi*, however, cumulative CO_2 injection is less with a lower injection pressure. For the 10 *nm* pore size, operating pressure can drop to 3600 *psi* with the confinement effect to achieve a similar amount of oil production as operating pressure is 4000 *psi* without the confinement effect. Due to the effect of confinement in nanoscale pores, CO_2 flooding designed

in a near-miscible condition can also approach a similar amount of oil production with the CO_2 miscible flooding process, however, the volume of CO_2 injected can be lower in this situation.

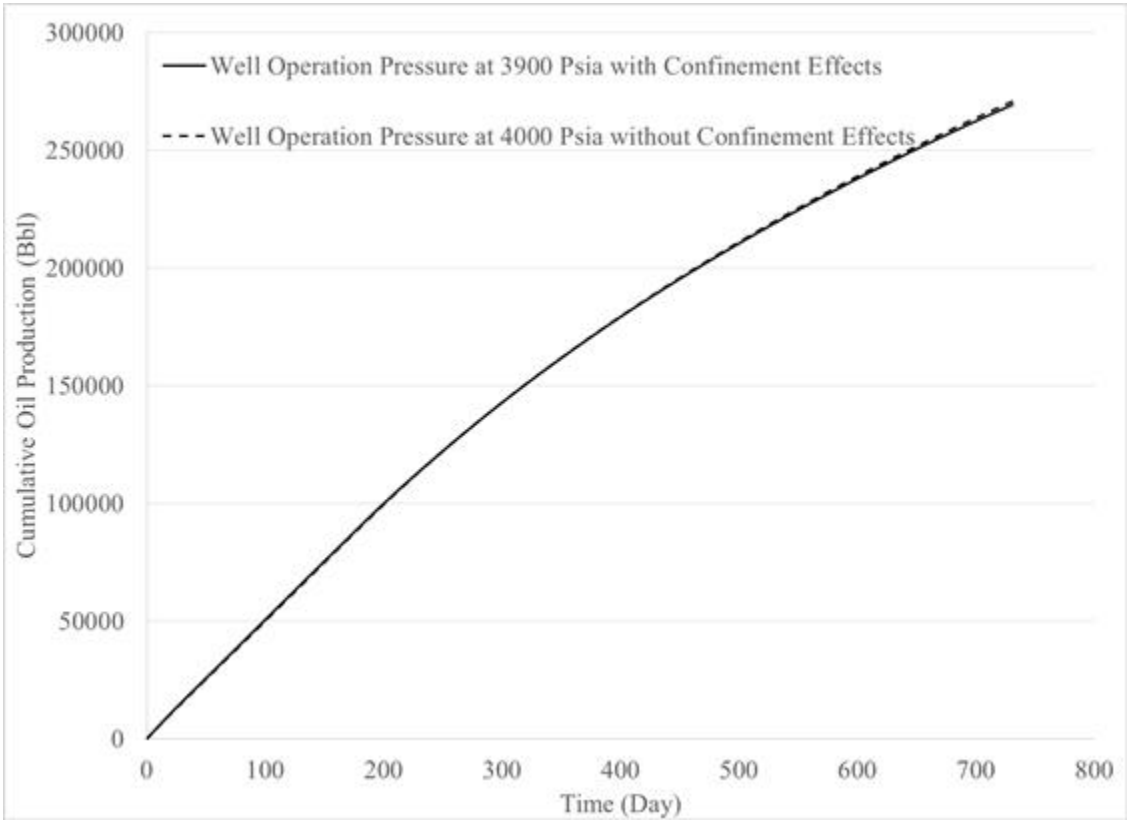

Figure 6. 3 Oil Production for CO_2 Near-miscible and Miscible Process with 50 *nm* Pores (Zhang, 2015)

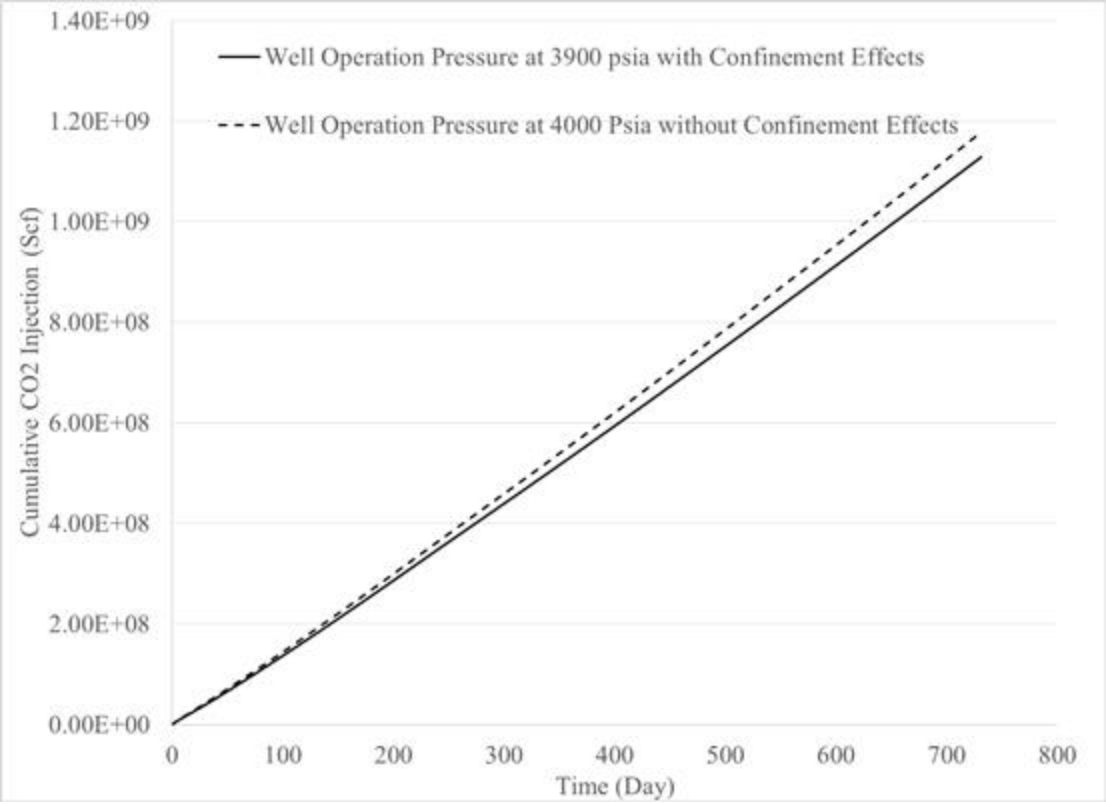

Figure 6. 4 CO_2 Injection for Near-miscible and Miscible Process with 50 *nm* Pores (Zhang, 2015)

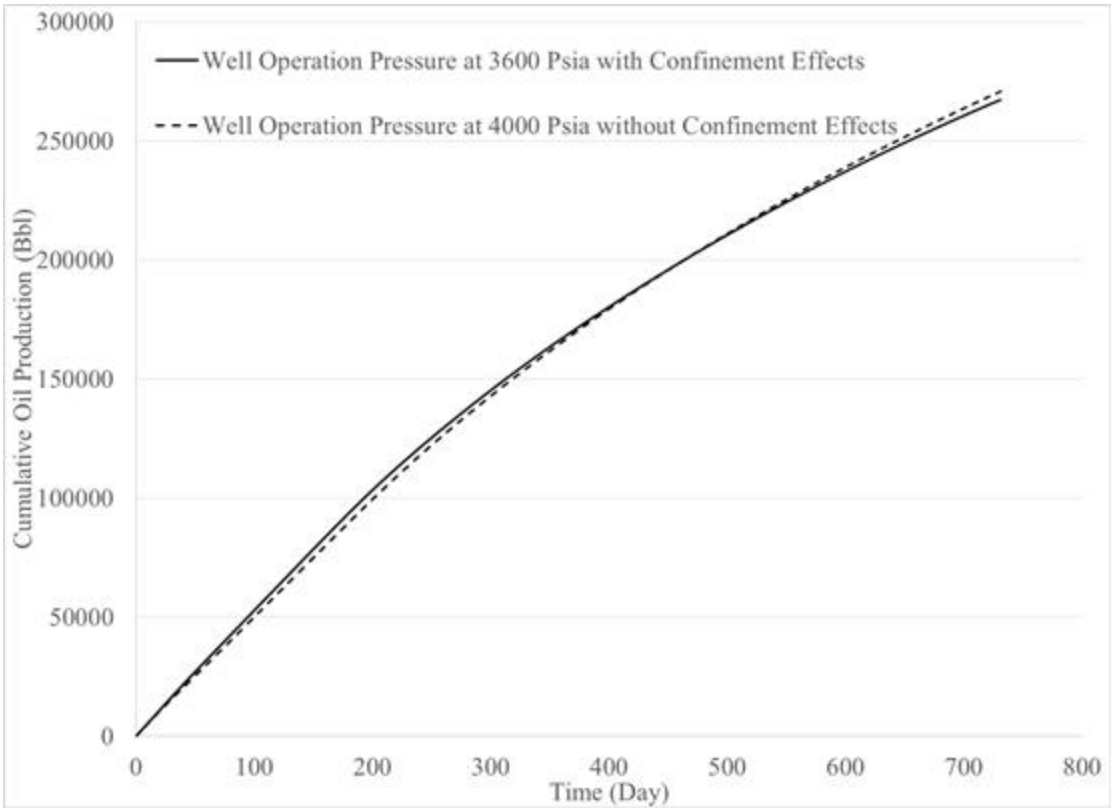

Figure 6. 5 Oil Production for CO_2 Near-miscible and Miscible Process with 10 *nm* Pores (Zhang, 2015)

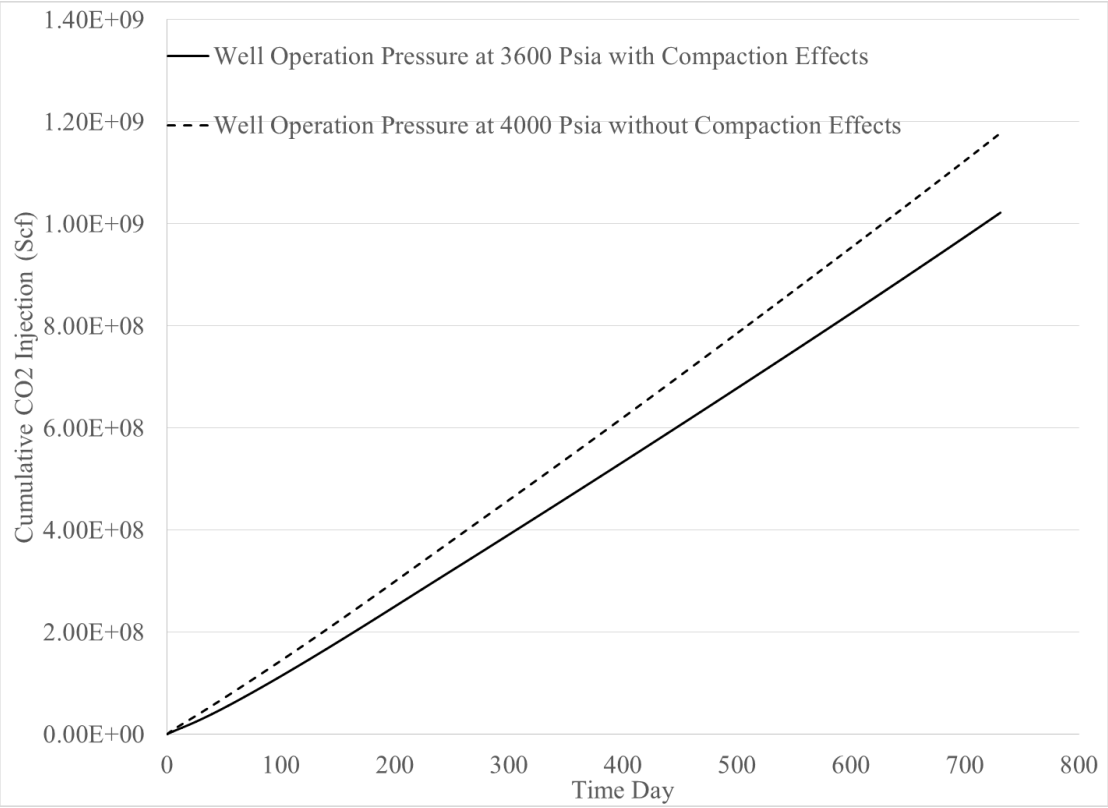

Figure 6. 6 CO_2 Injection for Near-miscible and Miscible Process with 10 *nm* Pores (Zhang, 2015)

As the reservoir pore sizes can have a broad distribution in a tight formation, one can operate a well in a near-miscible region where pressure is slightly less than MMP. Oil flow in large pores is dominated by the viscous force and oil can still be extracted effectively in the near-miscible region. The miscible phenomenon can appear in smaller pores with the confinement effect. It is not necessary for CO_2 to operate above the MMP condition in tight formations where the nanoscale pores can be present.

6.2 Pure or Impure Gas

Gas flooding is a common way to improve oil recovery. The previous experiences are shown in **Figure 6.7**. It can be seen that 79% of the gas injections are miscible cases. Sand and dolomite are dominant in the gas applications. Also 47% of the gas flooding projects are CO_2 and 42% of the gas flooding projects are hydrocarbon gas (Christensen, 1998).

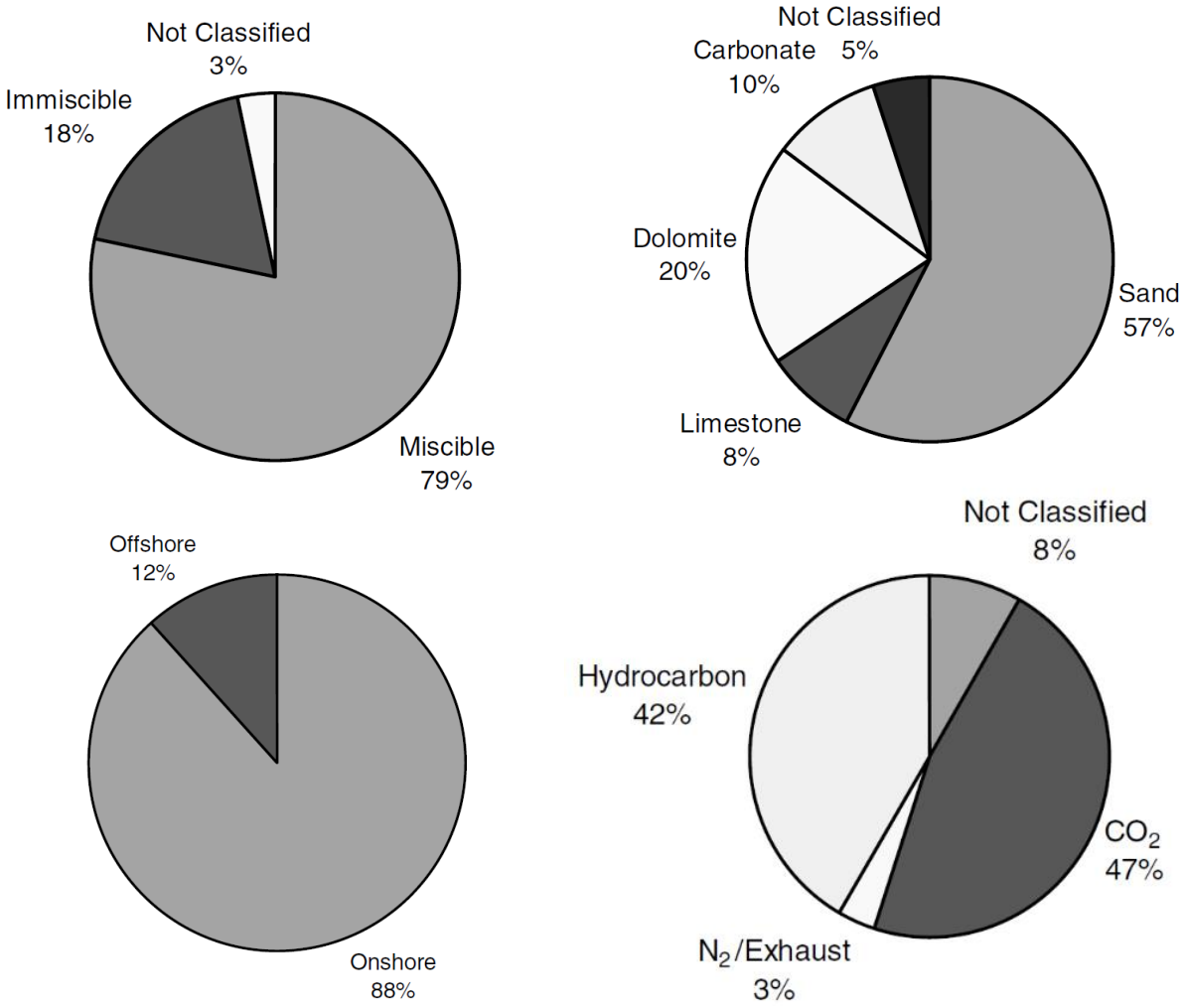

Figure 6. 7 Gas Injection Field Experience (Christensen, 1998)

Various gases have a different diffusion in a porous medium, as shown in **Figure 6.8**. CO_2 and C_2H_6 can have a high pore pressure at the same gas injectivity because the diffusion of CO_2

and C_2H_6 is lower compared to that of CH_4.

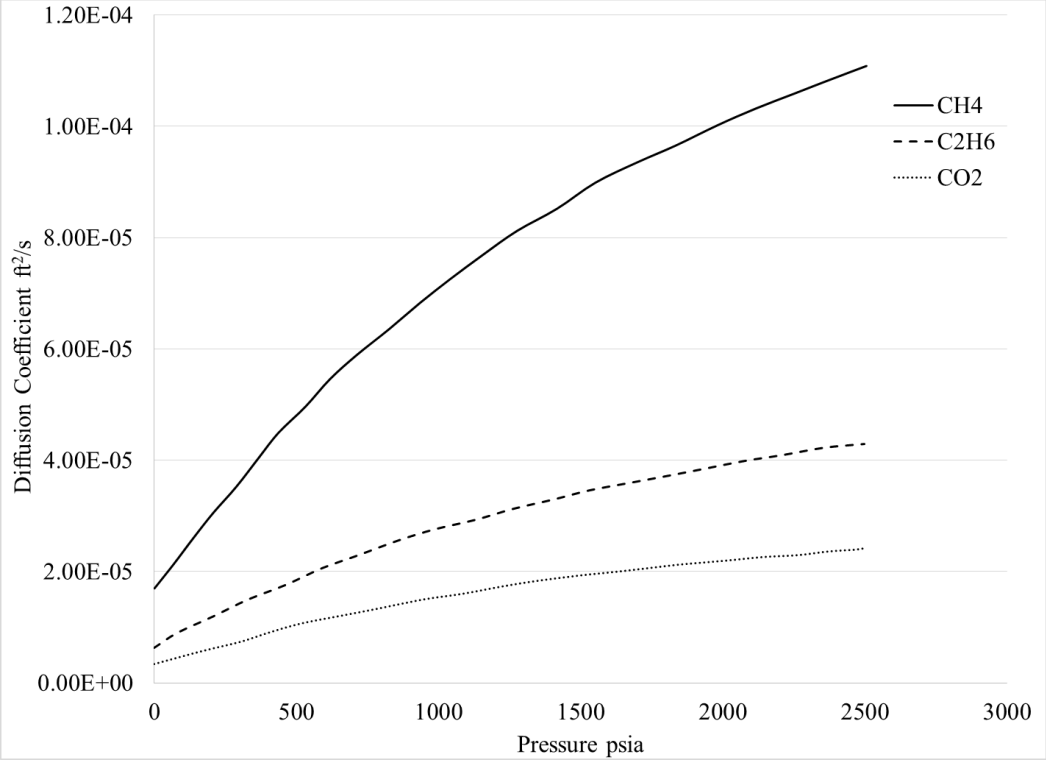

Figure 6. 8 Diffusion Coefficient at Different Pore Pressure (Wu, 2015)

CO_2 displacement efficiency does not depend on the presence of light hydrocarbons (C_2-C_4) in reservoir oil. Impure gas components in CO_2 may affect MMP in the CO_2 flooding process, resulting in varying performances (Holm, 1974). In general, the presence of CH_4 or N_2 can substantially increase the CO_2 MMP while the presence of H_2S, C_2H_6, or intermediate hydrocarbons (such as C_3 and C_4) can reduce the CO_2 MMP (Lake, 1989; Lansangan, 1993; Adekunle, 2014). In addition, rich gas (C_2-C_4) helps to reduce the potential of CO_2-induced organic deposition (Monger, 1987). Nitrogen miscibility pressure is too high (Teklu, 2014) to use nitrogen as an injection gas. Although CH_4 and C_3H_8 can improve oil recovery, the cost of hydrocarbons injected does not offer a viable payback due to its induced oil rate improvement.

Based on the fluid composition of reservoir 1, impure CO_2 MMP is calculated and shown in **Table 6.1**. The presence of N_2 significantly boosts the MMP, which drives the process to be immiscible. CH_4 also helps to increase the MMP, but not as much as N_2. C_3H_8 helps to reduce the MMP, which contributes to a first contact miscible process.

The flooding performances of these four scenarios are shown in **Figure 6.9**. The blue bar representing the presence of C_3H_8 has the highest oil production and the presence of N_2 has the lowest oil production. The presence of CH_4 in injection gas reduces the oil production a little bit compared to the pure CO_2 injection case. The oil production results are consistent with the MMP calculations.

Based on the above analysis, nitrogen miscibility pressure is too high (Teklu, 2014) for nitrogen to be an injection gas for reservoir 1. Although C_3H_8 can improve oil recovery, the oil recovery factor only improves a little with 20% of hydrocarbon additives. As the cost of injecting hydrocarbons does not offer a viable return for its induced oil rate improvement, pure CO_2 flooding is a better choice.

Table 6. 1 Impure Gas MMP (Zhang, 2015)

Injection Gas	MMP/ *psi*
80 % CO_2 + 20 % C_3H_8	2000
CO_2 + N_2	5175
80 % CO_2 + 20 % CH_4	3825
CO_2	2920

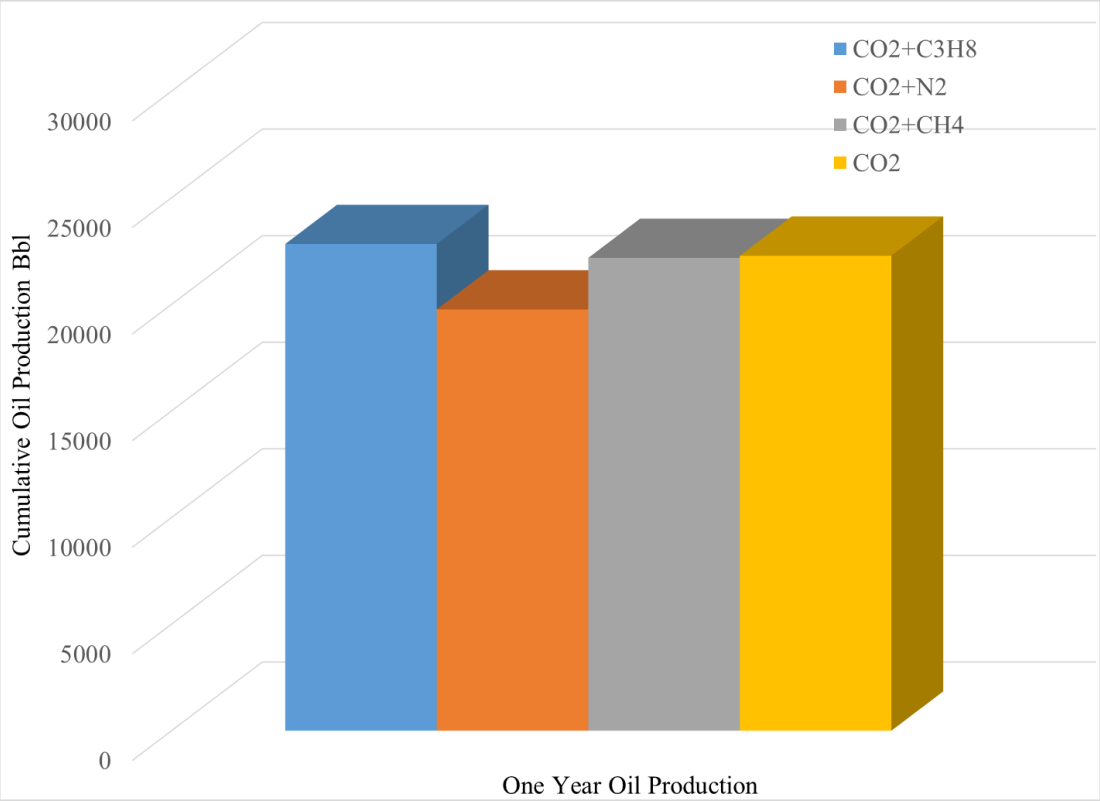

Figure 6. 9 Impure CO_2 MMP and Flooding Performance (Zhang, 2015)

Chapter 7. CO_2 Performance Improvement

CO_2 flooding is a promising technique in improving tight oil recovery. **Table 7.1** shows the pros and cons of CO_2 flooding. Oil recovery can be improved by oil viscosity reduction, oil swelling, and surface tension reduction. Although CO_2 injection can extract oil at a high water cut in some cases, this process suffers from viscous fingering, gravity override, channeling of gas and unfavorable gas mobility in heterogeneous formations (Le, 2008).

Table 7. 1 Pros and Cons of CO_2 Flooding

Pros and Cons	
Positive Effects	Negative Effects
Oil viscosity reduction	CO_2 viscosity < Oil viscosity
Oil swelling	Viscous Fingers
Oil surface tension reduction	CO_2 density < Oil density
Residue oil decrease	Gravity over-ride, accentuated by reservoir heterogeneity

A capillary number usually characterizes the ratio of viscous forces to interfacial tension forces in the fluid flow analysis. The flow in the reservoir is dominated by the capillary force when a capillary number is below the critical capillary number of 10^{-5} and the flow is dominated by the viscous force at a capillary number above the critical capillary number of 10^{-5} (Lake, 1989). As shown in **Figure 7.1**, if the pore size is small without much standard deviation, flow of the mobile oil is controlled by the capillary force, then interfacial tension optimization will be key to oil recovery. If the pore size is big and in a broader variation, the viscosity force will dominate in

determination of an oil rate (Lake, 1989).

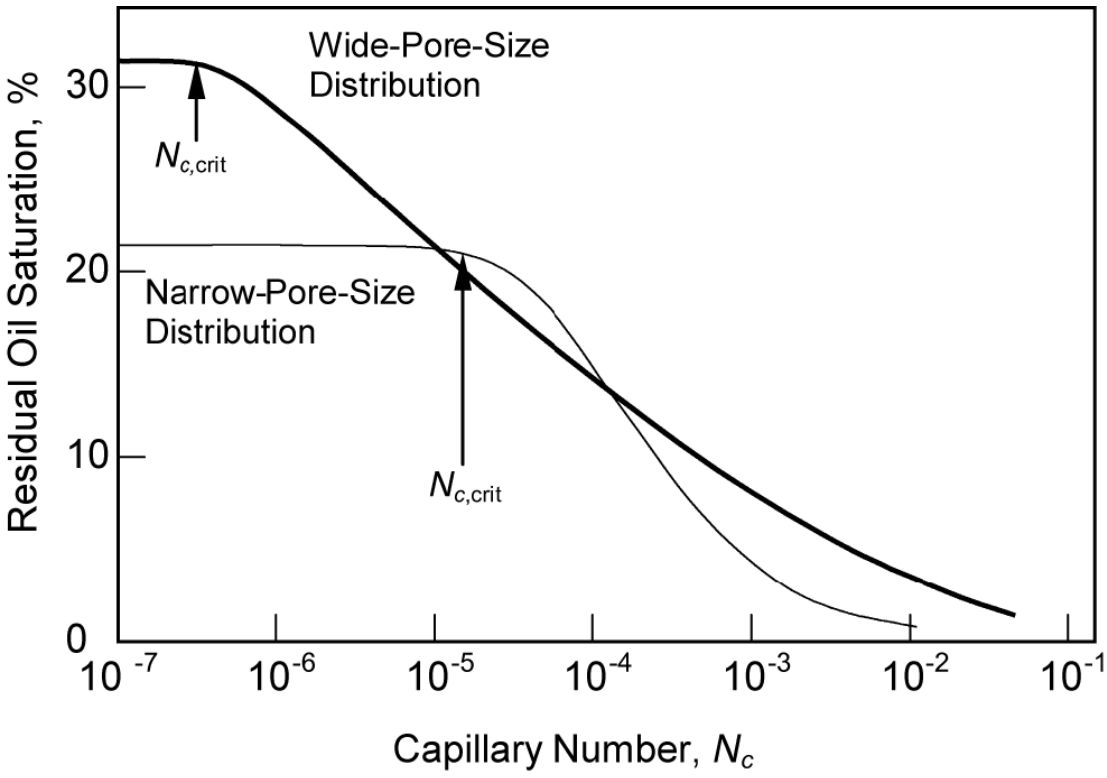

Figure 7. 1 Typical Behavior of Relationships for Mobilization of Residual Oil (Lake, 1989)

CO_2 can reduce oil viscosity and interfacial tension, resulting in proper recovery in both large and small pore media.

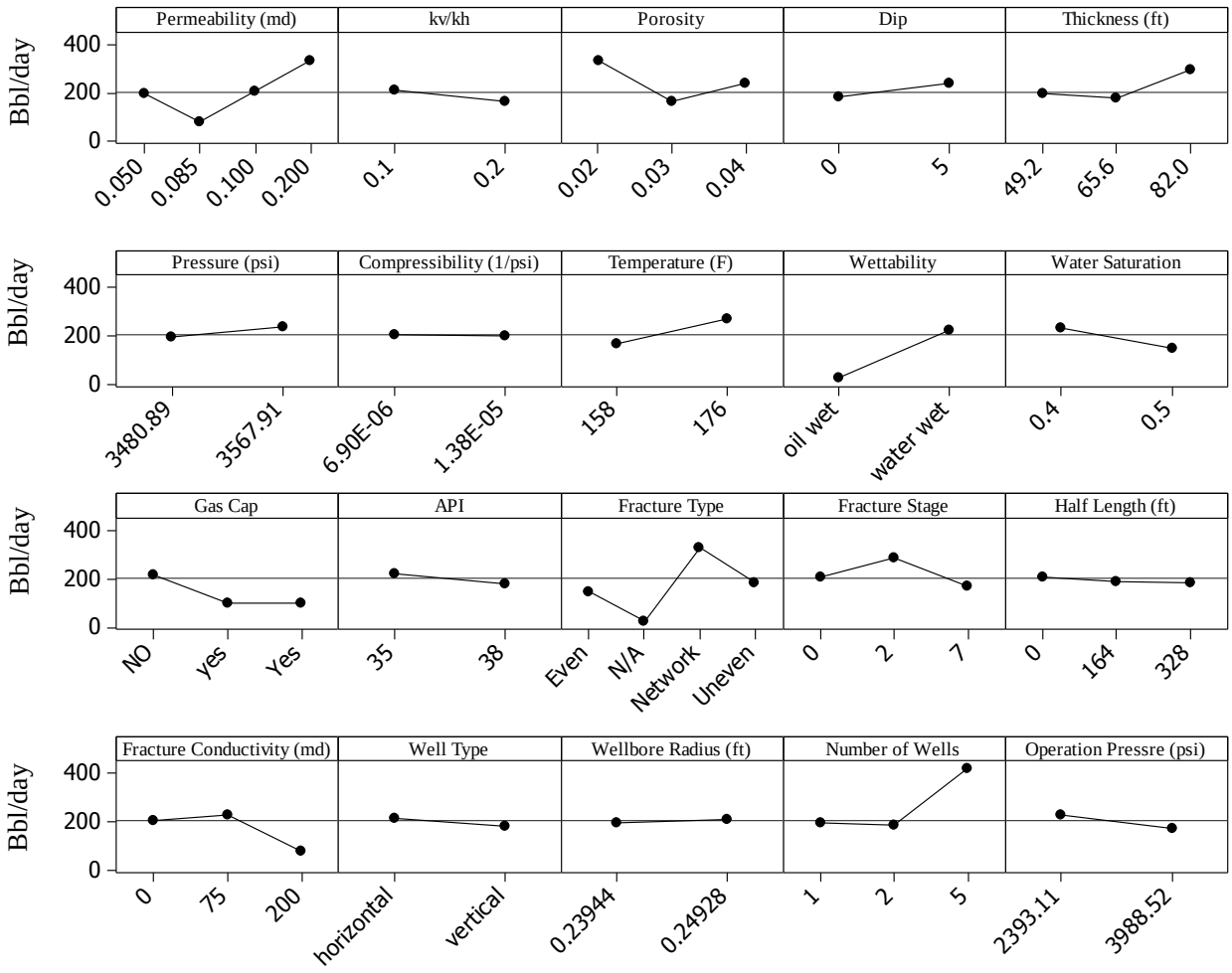

Figure 7. 2 Cumulative Oil Production versus Different Parameters

The main effects of various factors on oil rate are analyzed by the analysis of variance (ANOVA), with results shown in **Figure 7.2**. The parameters considered to have significant effects on oil production include: reservoir properties, such as permeability, a vertical and horizontal permeability ratio, porosity, oil saturation, reservoir dip, thickness, reservoir pressure, reservoir temperature, wettability, oil API and gas cap, as well as operation variables, such as a fracturing type, a fracturing stage, fracture half-length, fracture conductivity, the number of wells, a well type

and well operating pressure. Only some of these factors can be controlled or altered during operation. Taking Darcy's law into consideration, enhanced oil recovery potential for tight oil reservoirs exists in enlarging formation permeability, improving oil relative permeability, reducing oil viscosity and altering wettability.

If the pore size is small without much standard deviation, then interfacial tension and wettability optimization will be key to oil recovery. If the pore size is big and in a broader variation, the viscosity force will dominate an oil rate (Lake, 1989).

CO_2 can reduce oil viscosity and interfacial tension, resulting in proper recovery of both large and small pores. In addition, previous work showed that the WAG process was a better technique compared to continuous CO_2 flooding in tight formations (Figuera, 2014).

Reservoir simulations of CO_2 flooding have been performed, as discussed in **Chapter 6**. The gas saturation profile is shown in **Figure 7.3**. The injector is located in the middle and the production wells are in the margin of the reservoir. It can be seen that CO_2 is fingering in the reservoir; the CO_2 breaks through at the left parts more easily than in the others.

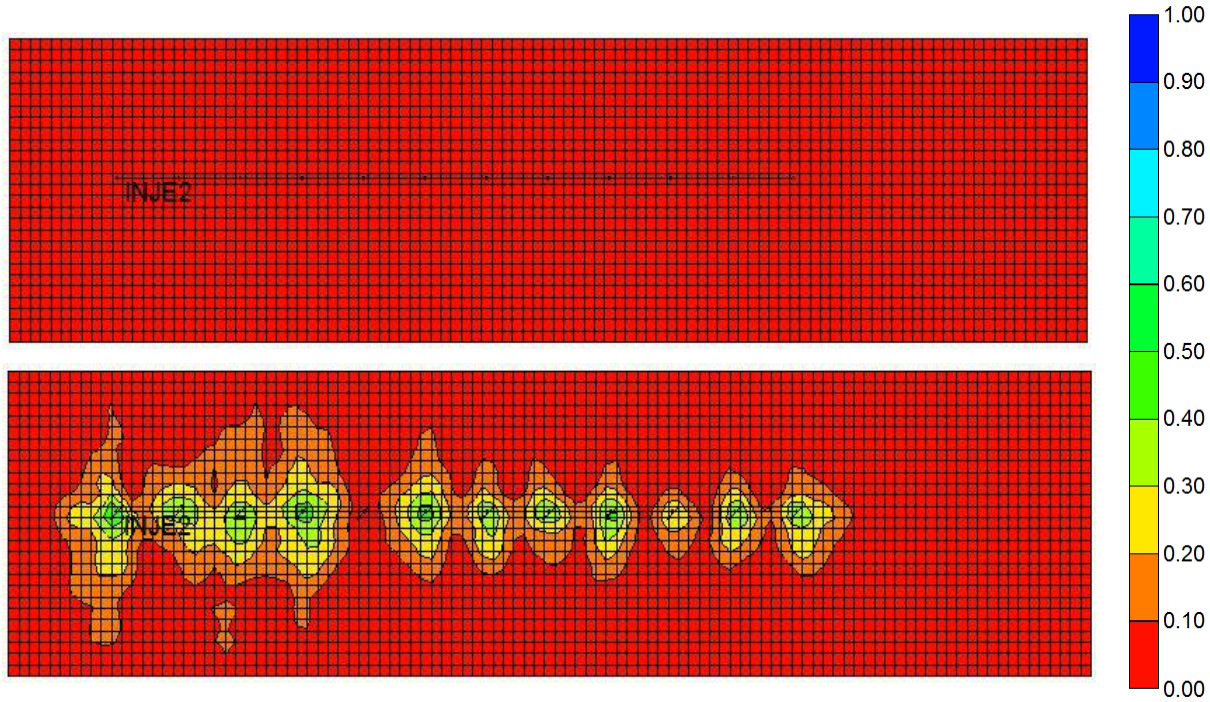

Figure 7. 3 Gas Saturation Profile during CO_2 Injection

Changing a well from water to gas injection after a prolonged water cycle can lead to a short-lived increase in production (Lake, 1989). The following content presents the CO_2 performance improvement. The fluid is tuned to match the confinement effect in the 100 *nm* nanopore.

7.1 Water Alternating CO_2 Flooding

In the water alternating gas (WAG) process, the slug size and cycle length are key parameters that affect the performance. On the basis of reservoir 1 in **Table 5.3**, reservoir simulations are performed.

Slug size: Generally, the more miscible the gas injected, the higher the incremental oil recovery (Jin, 2015). Therefore, a CO_2 slug size is investigated in a cycle length study; the amount of CO_2 injected depends on an oil rate requirement and project budget.

Cycle length: The time span of WAG may have a considerable effect on oil production. Three

scenarios, listed in **Table 7.2**, are made for a CO_2 flooding performance in reservoir 1. As shown in **Figure 7.4**, the cycle length of CO_2 injection in 12 months has a better oil rate. A small length of the WAG cycle with high frequency applied to another WAG cycle is a good choice for reservoir 1.

Table 7. 2 Various Scenarios for WAG Cycle Length

Scenario	Cycle length /Months	Gas injection /Months	Water Injection/Months
1	12	6	6
2	24	12	12
3	36	18	18

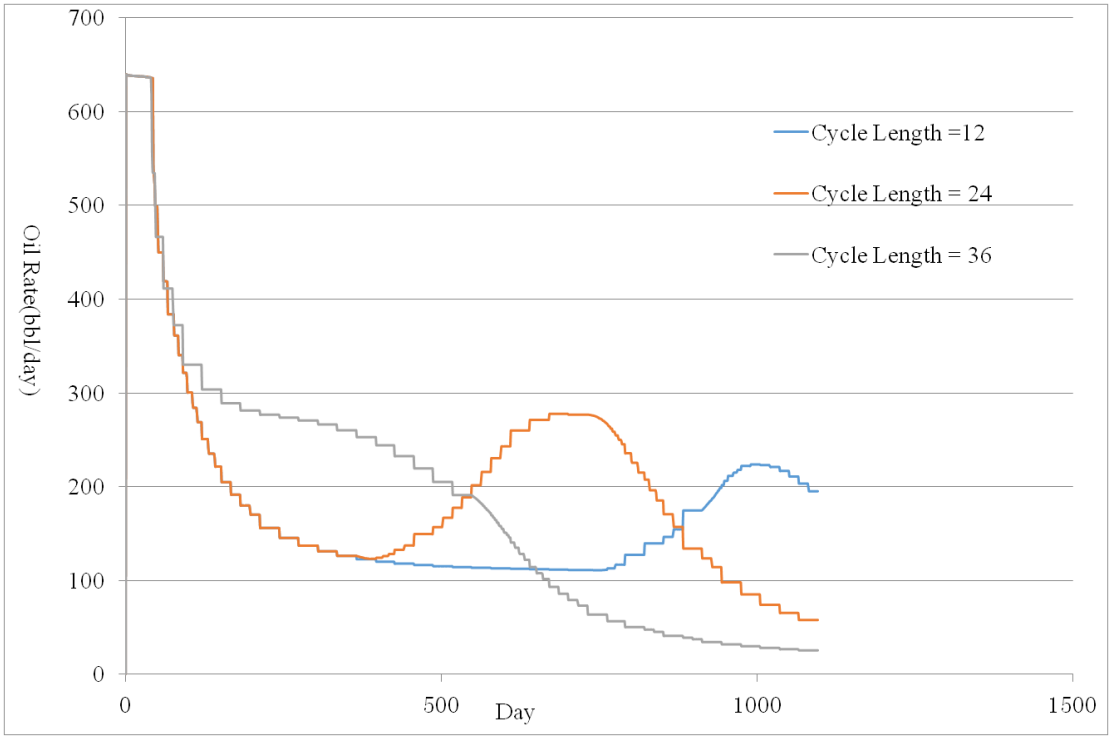

Figure 7. 4 WAG Cycle Length Investigations

WAG Ratio: The ratio of the volume of injected water to that of gas in reservoir conditions. Several

scenarios of the WAG ratio are investigated for reservoir 1, listed in **Table 7.3**. A WAG performance plot is shown in **Figure 7.5**. The oil rate declines quickly in the case where CO_2 is injected into reservoir 1 for three years production, which is even lower than the oil rate with waterflooding for three years. In general, CO_2 flooding after water performs better than either gas flooding or water flooding. The WAG ratio of 1:2 gives the best oil rate; a similar oil rate is found with a WAG ratio of 1:1. An optimal WAG ratio for reservoir 1 may be determined with the consideration of an oil rate requirement and project budget.

Table 7. 3 WAG Ratio Investigation for Reservoir 1

Scenario	WAG Ratio
1	0-1
2	1-2
3	5-1
4	1-0
5	3.5-1
6	1-1
7	1.25-1
8	2-1

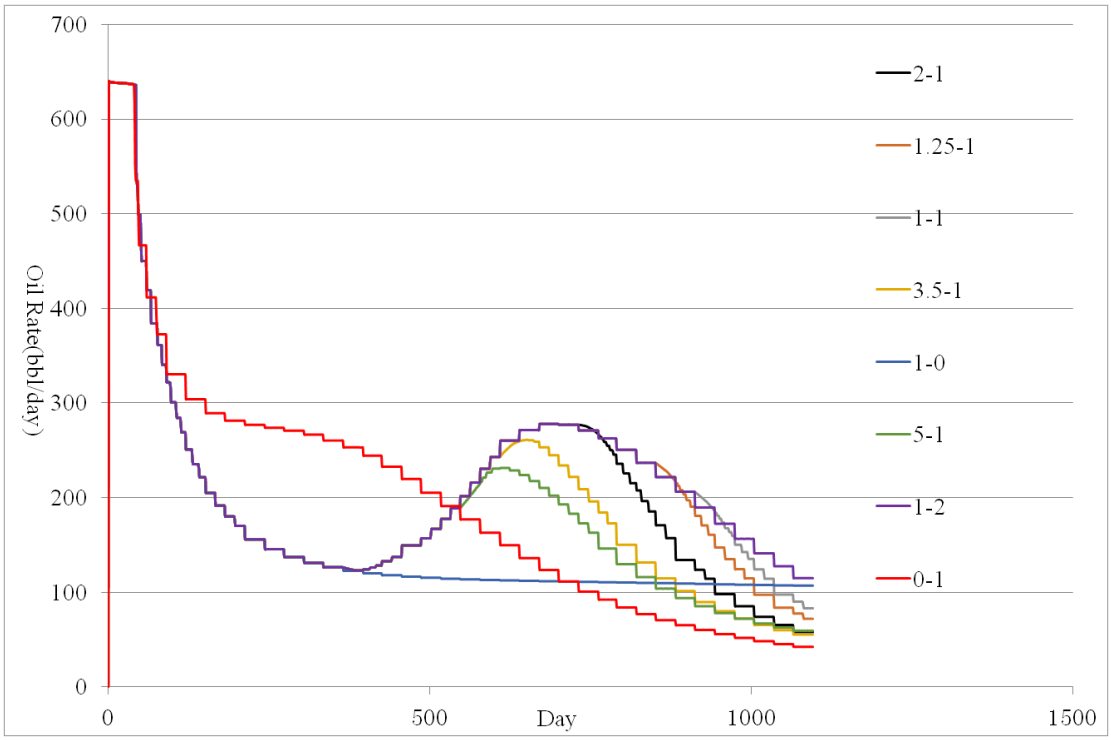

Figure 7. 5 WAG Performance

It has been shown that the WAG process can boost oil production compared to continuous CO_2 injection. The water injectivity, however, is low and it is not applicable for shale reservoirs, as discussed in **Chapter 3**. It is still possible for water flooding to apply in tight sandstone, limestone, and dolomites reservoirs. Furthermore, an analytical model for the WAG process is preferred to figure out the potential alternatives in improving the WAG performance.

Assumptions (Jenkins, 1984):

1. The reservoir model is horizontal and homogeneous.
2. During WAG operations, a gas mobile zone is only formed at the top, a water mobile zone is only formed at the bottom, and the mixture of gas and water is in the gas and water mobile zone, as illustrated in **Figure 7.6**.

3. The reservoir is under a steady state condition.

For water and gas flow in a porous medium, based on Darcy's law and mass conservation, the following equations can be obtained (Jenkins, 1984):

$$q_g = -\lambda_{gg} k W h_g \frac{dp}{dx} \tag{7.1}$$

$$q_m = -(\lambda_g + \lambda_w)_m k W h_m \frac{dp}{dx} \tag{7.2}$$

$$q_w = -\lambda_{ww} k W h_w \frac{dp}{dx} \tag{7.3}$$

$$q_t = q_g + q_m + q_w \tag{7.4}$$

$$f_g q_t = q_g + f_g q_m \tag{7.5}$$

$$f_w q_t = q_w + f_w q_m \tag{7.6}$$

$$h_t = h_g + h_m + h_w \tag{7.7}$$

$$(q_w + q_g) f_w f_g = \Delta\rho k_V f_g (\lambda_w)_m W_x \tag{7.8}$$

Incorporating equations (7.5) and (7.6):

$$\frac{q_w(x)}{q_g(x)} = WAG \tag{7.9}$$

Equation (7.8) shows that the ratio of flow rates in the water and gas zones is equal to the WAG ratio of the injection mixture. Substituting equations (7.1) and (7.3) into equation (7.9) results in:

$$\frac{h_w(x)}{h_g(x)} = M_{gw} WAG \quad \text{where} \quad M_{gw} = \frac{\lambda_{gg}}{\lambda_{ww}} \tag{7.10}$$

The unit in the horizontal distance along reservoir is normalized by *x/L*, vertical height is normalized by h/h_t, which can be extended to different scales.

Substitute equations (7.10) to (7.7):

$$h_w(x \geq L_G) = \left(1 - \frac{1}{1 + M_{gw} WAG}\right) h \tag{7.11}$$

The solution to the above equations can be written as:

$$h_w(x) = \frac{M_{gw}WAG\ h}{\alpha+\beta/x} \tag{7.12}$$

where

$$\alpha = 1 + M_{gw}WAG - M_{gm} \tag{7.13}$$

$$\beta = M_{gm}\,VGR\,L_r \tag{7.14}$$

$$M_{gm} = \frac{\lambda_{gg}}{(\lambda_g)_m} \tag{7.15}$$

$$VGR = \frac{q_t(constant)}{\Delta\rho k_V a(\lambda_g+\lambda_w)_m} \tag{7.16}$$

The mobility ratio in the mixture is equal to the WAG ratio:

$$\frac{(\lambda_w)_m}{(\lambda_g)_m} = WAG \tag{7.17}$$

Recovery efficiency can be expressed by the following equation:

$$E_{inc} = \frac{N_{WAG}-N_{wf}}{N_i-N_{wf}} = \frac{E_{tot}-E_{wf}}{1-E_{wf}} \tag{7.18}$$

The height of the water zone-mixture zone boundary can be integrated as follows:

$$E_{inc} = \left(1-\frac{S_{org}}{S_{orw}}\right)\left[1-\frac{\int_0^{L_G} h_w(x)dx}{hL}-\frac{h_w(L_G)}{h}\left(1-\frac{L_G}{L}\right)\right] \tag{7.19}$$

It can be simplified as:

$$E_{inc} = \left(1-\frac{S_{org}}{S_{orw}}\right)(1-V_{wu}-V_{ws}) \tag{7.20}$$

Afterwards, the volumes occupied by water in unsegregated and segregated zones can be obtained:

$$V_{wu}(VGR \le 1) = \frac{VGR\,M_{gw}\,WAG}{\alpha^2}\left[\alpha - M_{gm}\ln\left(1+\frac{\alpha}{M_{gm}}\right)\right] \tag{7.21}$$

$$V_{ws}(VGR \le 1) = \frac{1-VGR}{1+\frac{1}{M_{gw}WAG}} \tag{7.22}$$

$$V_{wu}(VGR > 1) = \frac{VGR\,M_{gw}\,WAG}{\alpha^2}\left[\alpha - M_{gm}VGR\ln\left(1+\frac{\alpha}{VGR\,M_{gm}}\right)\right] \tag{7.23}$$

$$V_{ws}(VGR > 1) = 0 \tag{7.24}$$

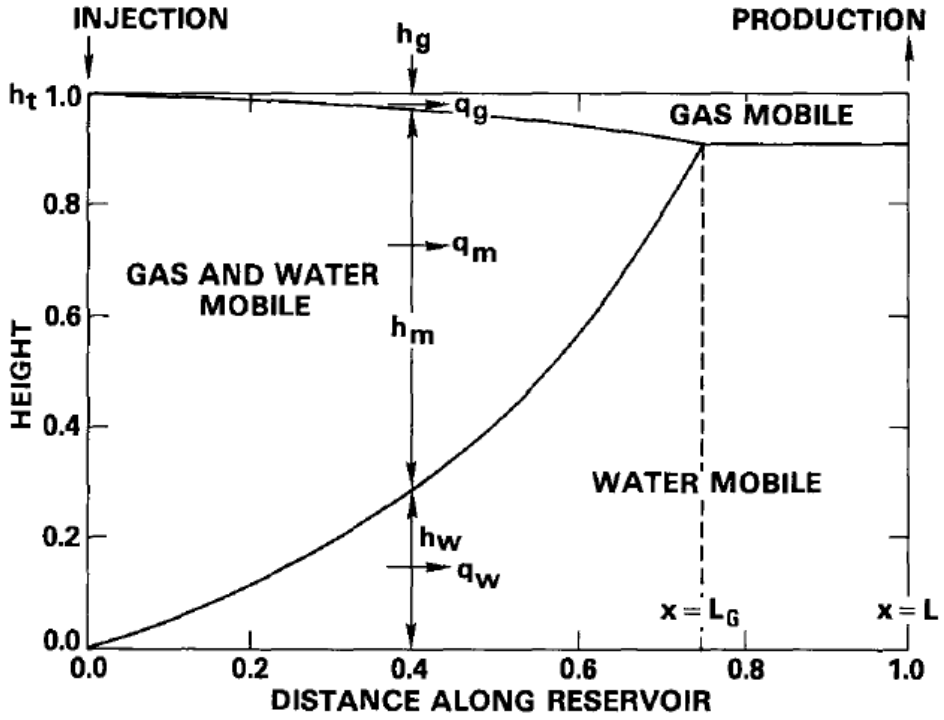

Figure 7. 6 Fluid Zone Illustration in Analytical Model (Jenkins, 1984)

As shown in **Figure 7.7**, the smaller the viscosity gravity ratio (VGR), the bigger the dimensionless volume occupied by water in the gas and water mobile zones. It indicates higher sweep efficiency and recovery. To lower VGR and improve WAG performance, advanced knowledge should be focused on mobility control, wettability alteration and interfacial tension management.

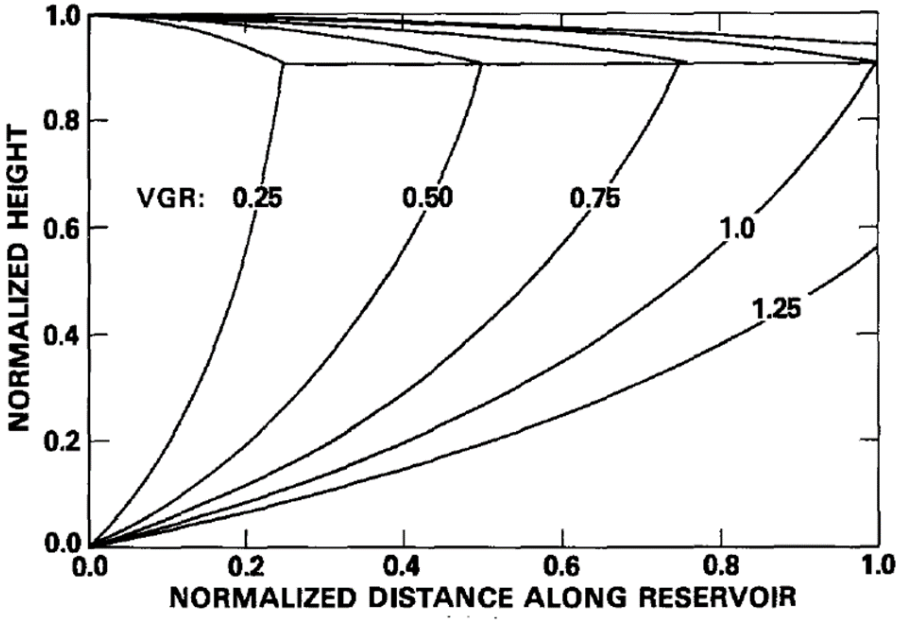

Figure 7. 7 Zone Boundaries for Different VGR in a Rectangular Homogeneous Reservoir. (Jenkins, 1984)

7.2. Nanofluid Alternating CO_2 Flooding

Based on the above analysis in the last section, improved oil recovery by WAG injection can be affected by mobility control, wettability alteration and interfacial tension management (Christensen, 1998; Mohanty, 2013; Zhang, 2015).

Chemical additives, like polymer or foam, can help to improve mobility (Li, 2014), but they are limited to a reservoir permeability of 50 *md* and higher (Mohan, 2009). Alkaline can offer a reduction in interfacial tension, resulting in an increment in oil production (Donaldson, 1966; Longeron, 1980). A candidate for alkaline flood should have an acid number above 0.5 *mg* OH^-/*g* oil, corresponding to oil with API below 30. It is not suitable for an enhanced oil recovery (EOR) process in tight reservoirs (Fan, 2006). Surfactant, low salinity water and nanofluids have potential

in improving WAG performance for tight oil exploitation (Rotondi, 2014; Zhang, 2015). Surfactant additives offer a reduction in interfacial tension and an increment in the capillary number, resulting in an increment in both k_{rl} and k_{rg} (Donaldson, 1966; Longeron, 1980). The retention of surfactant is not negligible (Bernard, 2002; Wulff, 2009) because the surfactant particles are around 10 *nm* to 30 *nm* in diameter and the nano-emulsion formed by surfactant can be 20 *nm* to 500 *nm*. Low salinity water and nanofluids cause an alteration in wettability (Dang, 2013; Dang, 2014; Zhang, 2015) resulting in an increment in k_{ro} and a reduction in k_{rw} (Anderson, 1987). Furthermore, low salinity water exchanges ions in the second layer of a water film, resulting in a highly negative electrokinetic charge of the oil-water interface, which causes instability in an electrical double layer (Nasralla, 2011). This, however, is limited to sandstone and carbonate reservoirs with clay minerals (Rotondi, 2014). For nanofluids, the fluid suspension of nanoparticles can be 1 to 7 *nm* in diameter (Li, 2013). When they are introduced into an oil-water-rock system, the net force of van der Waals, electrostatic, and structural or solvation interactions are altered by the nanofluids (Chengara, 2004; Kondiparty, 2012) which impair the water film stability (Abdallah, 1986). In this section, the nanofluid alternating gas process is investigated.

The spreading of nanofluids varies with the spreading of liquids without nanoparticles. Nikolov studied the complex solid-nanofluid-oil interactions using the combined differential and common light interferometric method of the self-structuring of nanoparticles confined in a thin film (Nikolov, 2010). The excess pressure within the wedge-film region separates the two surface confining nanofluids (**Figure 7.8**), and the disjoining pressure has an oscillatory exponential decay

with a thicker film (**Figure 7.9**) with both the period of oscillation and the decay factor equal to the effective diameter of the nanoparticles. The structural disjoining pressure dominates at scales longer than the effective diameter of a nanoparticle, below which other disjoining pressure components (such as van der Waals, electrostatic, and solvation forces) are prevalent (Chengara, 2004).

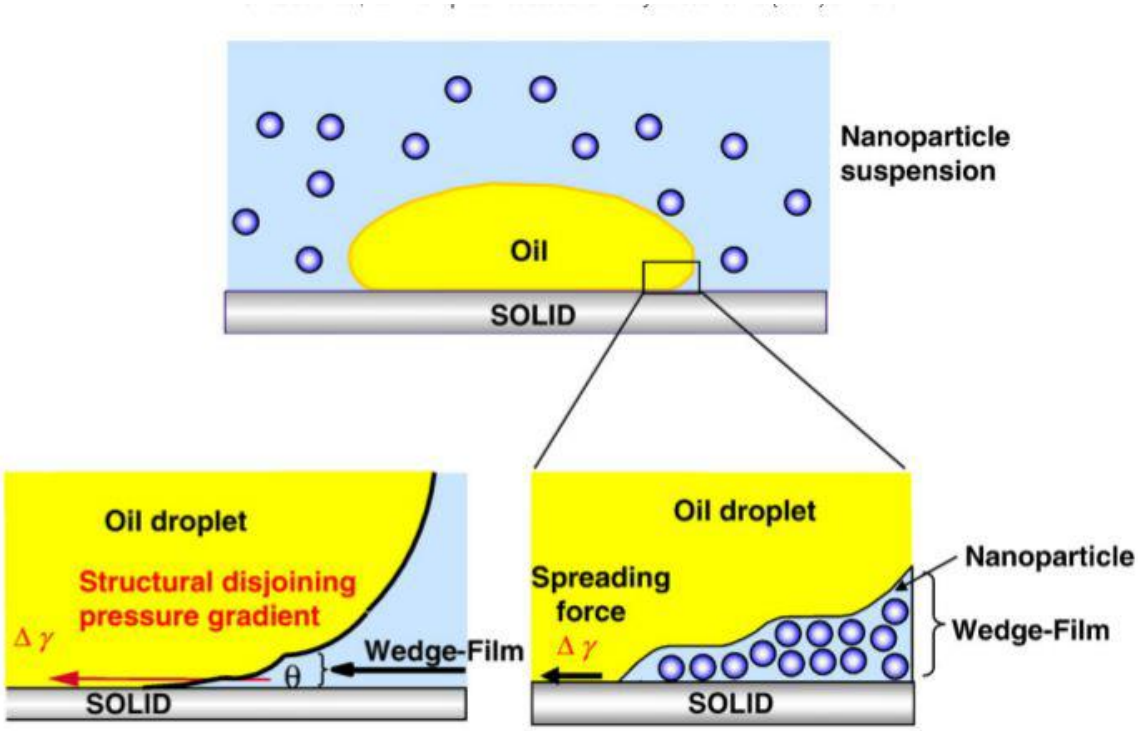

Figure 7. 8 Nanoparticle Structuring in the Wedge Film (Kondiparty, 2012)

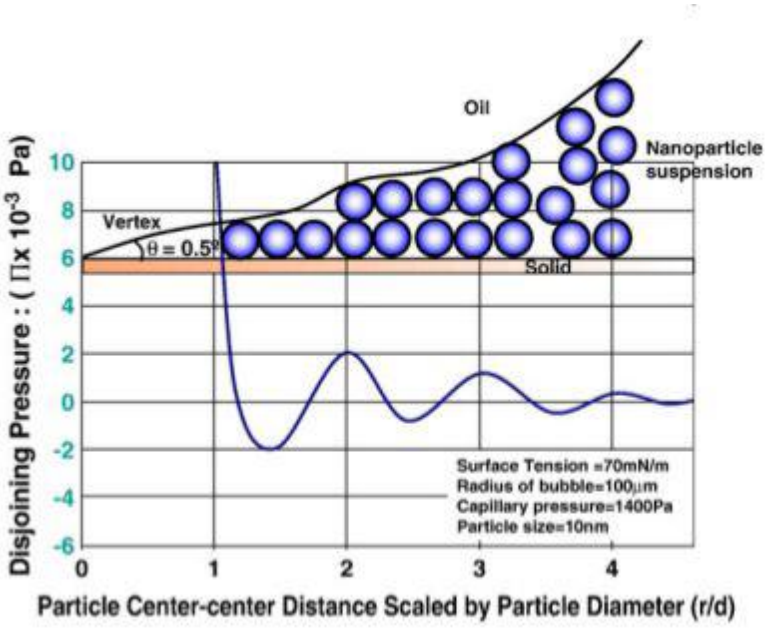

Figure 7. 9 Pressure on the Walls of Wedge for 0.5°Contact Angle at the Vertex as a Function of Radial Distance (Kondiparty, 2012)

As the film thickness decreases toward the wedge vertex, the structural disjoining pressure increases. The driving force for the spreading of the nanofluid is the structural disjoining pressure gradient or film tension gradient directed toward the wedge from the bulk solution. As the film tension increases toward the vertex of the wedge, it drives the nanofluid to spread at the wedge tip (the three-phase contact line moves), thereby enhancing the dynamic spreading behavior of the nanofluid (**Figure 7.8**).

Since the rate of oil recovery in tight oil reservoirs can be increased with wettability alteration (Mohanty, 2013), nanoparticle additives in the WAG process can boost oil recovery to some extent. In general, the k_{ro} and k_{rw} curves can be affected individually by additives that change the wettability of an oil-brine-rock system. For example, sodium tripolyphosphate only affects the k_{ro}

curve without alteration in interfacial tension. Dilute NaOH, while giving a slight effect on the interfacial tension, only affects the k_{rw} curve. Detergent, while lowering the interfacial tension, affects both the k_{ro} and k_{rw} curves (Donaldson, 1966). Nanoparticle additives can alter wettability and reduce interfacial tension, resulting in various residual oil saturations. Although there is some permeability and porosity reduction by the retention of nanoparticles (Li, 2013; Khezrnejad, 2014), it is still a promising technique to recover more oil in tight formations.

Nanofluid properties are summarized as follows:

Nanoparticles, having a very high surface to volume ratio (Marthe, 2013), can easily move into the tight formation without external forces. Nanoparticles are added into water as an injection fluid, which can alter wettability (Marthe, 2013) and reduce oil-water interfacial tension (Ayatollahi, 2012) resulting in higher oil recovery.

As shown in **Table 7.4**, density and viscosity of brine almost remain constant in the range of 0.01 *wt%* to 0.1 *wt%* of nanoparticles. Also, nanoparticle additives in the range of 0.01 *wt%* and 0.1 *wt%* do not affect the viscosity and density of oil (Marthe, 2013).

Table 7. 4 Density and Viscosity Measurement (Anne, 2013)

Properties of Brine and Hydrophilic Nano-Silica in Brine at 70.7 °*F*				
	Brine 3 *wt%*	0.01 *wt%*	0.1 *wt%*	0.5 *wt%*
Density (*lb/ft*^{3})	63.677	63.614	63.677	63.801
Viscosity (*cp)*	1.007	0.983	1.137	1.453
Properties of Oil and Hydrophobic Nano-Silica in Oil at 70.7 °*F*				
	Oil	0.01 *wt%*	0.1 *wt%*	0.5 *wt%*
Density (*lb/ft*^{3})	45.51	45.198	45.135	45.323
Viscosity (*cp*)	0.9	0.894	0.894	0.903

Although the viscosity and density of an oil-water system do not change by adding nanoparticles within 0.01 *wt%* and 0.1 *wt%*, a contact angle of the oil-water system is altered by the addition of nanoparticles. As shown in **Table 7.5**, this contact angle reduces by half when the nanoparticle concentration approaches 0.03 *wt%*. This indicates that the wettability of the water-oil system is changing. In this way, oil molecules become more spherical in water, which means that oil can be flooded away more easily. The contact angle of the oil and water system decreases as the concentration of nanoparticles increases; the reduction of the contact angle becomes less when the nanoparticle concentration approaches 0.05 *wt%*.

Table 7. 5 Oil/Water Contact Angle Measurement (Manrique, 2010)

Sample	Contact Angel ˚
Pure Water(3 *wt%* NaCl)	34.81
Pure Water(3 *wt%* NaCl, 0.01% Nano-Silica)	27.62
Pure Water(3 *wt%* NaCl, 0.02% Nano-Silica)	20.81
Pure Water(3 *wt%* NaCl, 0.03% Nano-Silica)	16.77
Pure Water(3 *wt%* NaCl, 0.04% Nano-Silica)	24.57
Pure Water(3 *wt%* NaCl, 0.05% Nano-Silica)	12.83
Pure Water(3 *wt%* NaCl, 0.06% Nano-Silica)	11.42
Pure Water(3 *wt%* NaCl, 0.07% Nano-Silica)	13.81
Pure Water(3 *wt%* NaCl, 0.08% Nano-Silica)	12.44
Pure Water(3 *wt%* NaCl, 0.09% Nano-Silica)	7.89
Pure Water(3 *wt%* NaCl, 0.10% Nano-Silica)	12.71

Besides the contact angle alteration, the interfacial tension of the oil water system can also be reduced by nanoparticles. As shown in **Table 7.6**, interfacial tension has a 25 % reduction with 0.05 *wt%* of nanoparticles.

Table 7. 6 Interfacial Tension Reduction by Nanoparticles (Gunnar, 2014)

Fluid	Concentration *wt%*	IFT *dyne/cm*
Brine	-	16.41
Nanosilica	0.05	11.65
Nanosilica	0.05	12.67
Nanosilica	0.05	12.99
Nanosilica	0.05	14.52
Nanosilica	0.05	11.96
Nanosilica	0.05	12.15

In the oil and water system, contact angle alternation and interfacial tension reduction have effects on oil and water relative permeability. Relative permeability to oil decreases and relative permeability to water increases at a given saturation as the rock preferential of water decreases (Owens, 1971). In this way, nanofluid flooding can have a different residual oil saturation compared with water flooding. As shown in **Table 7.7**, for Berea sandstone, nanoparticles with 0.05 *wt%* concentration added into a water flooding process has residual oil saturation reduced by 6% as compared to water flooding.

Table 7. 7 Berea Sandstone Core Flooding Summary (Gunnar, 2014)

Fluid	Concentration *wt%*	S_{or} for water flooding	S_{or} for nanofluids flooding
Nanosilica	0.05	0.41	0.39
Nanosilica	0.05	0.41	0.36
Nanosilica	0.05	0.50	0.46
Nanosilica	0.05	0.38	0.37
Nanosilica	0.05	0.30	0.28
Nanosilica	0.05	0.48	0.46

Nanofluid can experimentally improve oil recovery, however, retention of nanoparticles also has a potential to decrease permeability and porosity. As shown in **Tables 7.8** and **7.9**, there are around 1~2% reduction in porosity and 1~9% reduction in permeability during nanofluid flooding. High concentration of nanoparticles, for example, 0.5 *wt*% of nanoparticles, as additive in the water flooding process, is out of interest since a permeability reduction cannot be negligible (Anne, 2013).

Table 7. 8 Porosity and Permeability Measurement Scenarios (Anne, 2013)

Core type	Nano-silica	Core plug	Nanofluid concentration
Water-wet Berea Sandstone	Hydrophilic	# 1	0.01 %
		# 7	0.01 %
		# 3	0.1 %
		# 12	0.1 %
		# 4	0.5 %
		# 8	0.5 %
	Hydrophobic	# 5	0.01 %
		# 14	0.01 %
		# 11	0.1 %
		# 13	0.1 %
		# 15	0.5 %
		# 16	0.5 %

Table 7. 9 Porosity and Permeability Measurement (Anne, 2013)

Core Plug	Original Porosity	New Porosity	Deviation	Original Permeability (*md*)	New Permeability (*md*)	Deviation
# 1	17.49 %	15.34 %	-2.14 %	334.4	354.6	6.04 %
# 7	17.03 %	14.68 %	-2.36 %	336.7	334.4	-0.68 %
# 3	17.88 %	15.44 %	-2.45 %	319.2	335.3	5.04 %
# 12	16.42 %	15.13 %	-1.29 %	319.6	333.8	4.44 %
# 4	15.95 %	14.67 %	-1.28 %	359.6	275.4	-23.41 %
# 8	16.19 %	15.12 %	-1.07 %	361.2	141.1	-60.94 %
# 5	18.96 %	16.61 %	-2.35 %	367.9	373	1.39 %
# 14	16.63 %	14.70 %	-1.93 %	332.4	328.1	-1.29 %
# 11	18.55 %	16.41 %	-2.14 %	384	348.9	-9.14 %
# 13	17.89 %	15.96 %	-1.93 %	383.1	378.4	-1.23 %
# 15	16.61 %	15.33 %	-1.28 %	346.4	230	-33.60 %
# 16	16.39 %	15.33 %	-1.06 %	345.9	171	-50.56 %

A nanoparticle concentration of 0.05 *wt%* has a good chance of wettability alteration and interfacial tension reduction, however, permeability and porosity reduction are not negligible when the nanoparticle concentration is increased to 0.1 *wt%* or higher. Hence, 0.05 *wt%* of nanoparticle additive in the water flooding process offers the best performance during core flooding (Gunnar,

2014).

On the basis of the models in **Chapter 4**, reservoir simulations are carried out to investigate nanofluid alternating gas (NAG) performance.

Modeling of NAG (Zhang, 2015):

1. Obtain an understanding of where nanoparticles go underground and their concentration in a reservoir after injection.
2. Modify formation permeability or transmissibility based on nanoparticle concentration underground.
3. Involve wettability alteration and interfacial tension reduction that are captured by multiple relative permeability sets with various residue oil saturations. Multiple relative permeability sets are used to represent wettability alteration and interfacial tension reduction, as shown in **Figure 7.10**. For the matrix, there will be multiple relative permeability sets based on the concentration of nanoparticles underground; for fractures, a linear curve is set for k_{rw} and k_{ro}.

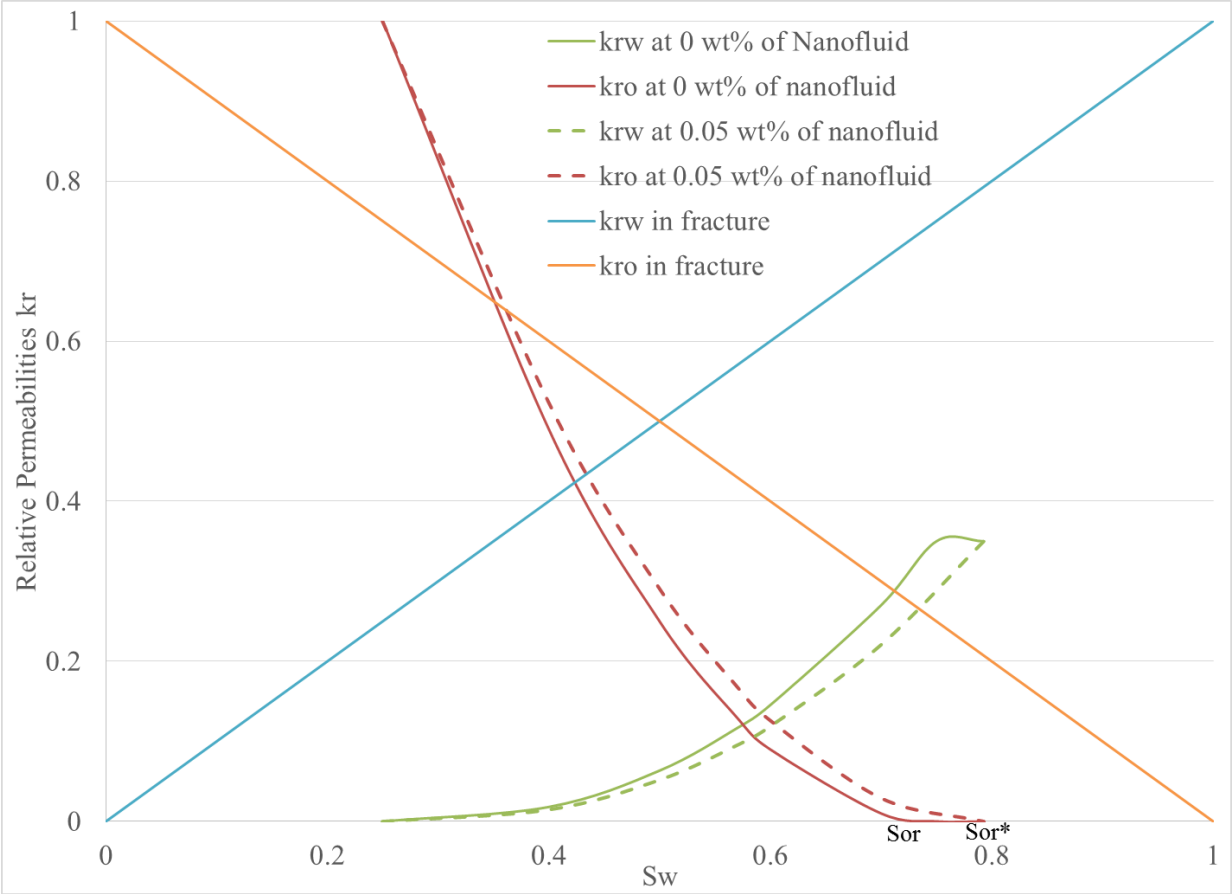

Figure 7. 10 Multiple Relative Permeability Sets (Zhang, 2015)

4. Gain a phase envelope that may change during fluids injection; especially at the bubble point pressure, compositional modeling is required.

Homogeneous and Heterogonous Models without Hydraulic Fracturing

The nanoparticle concentration underground after nanofluid injection in the homogeneous and heterogeneous models is captured by the tracer in Eclipse and as shown in **Figure 7.11**. It can be seen that nanoparticles mainly stay around the injection well and highly permeable zone.

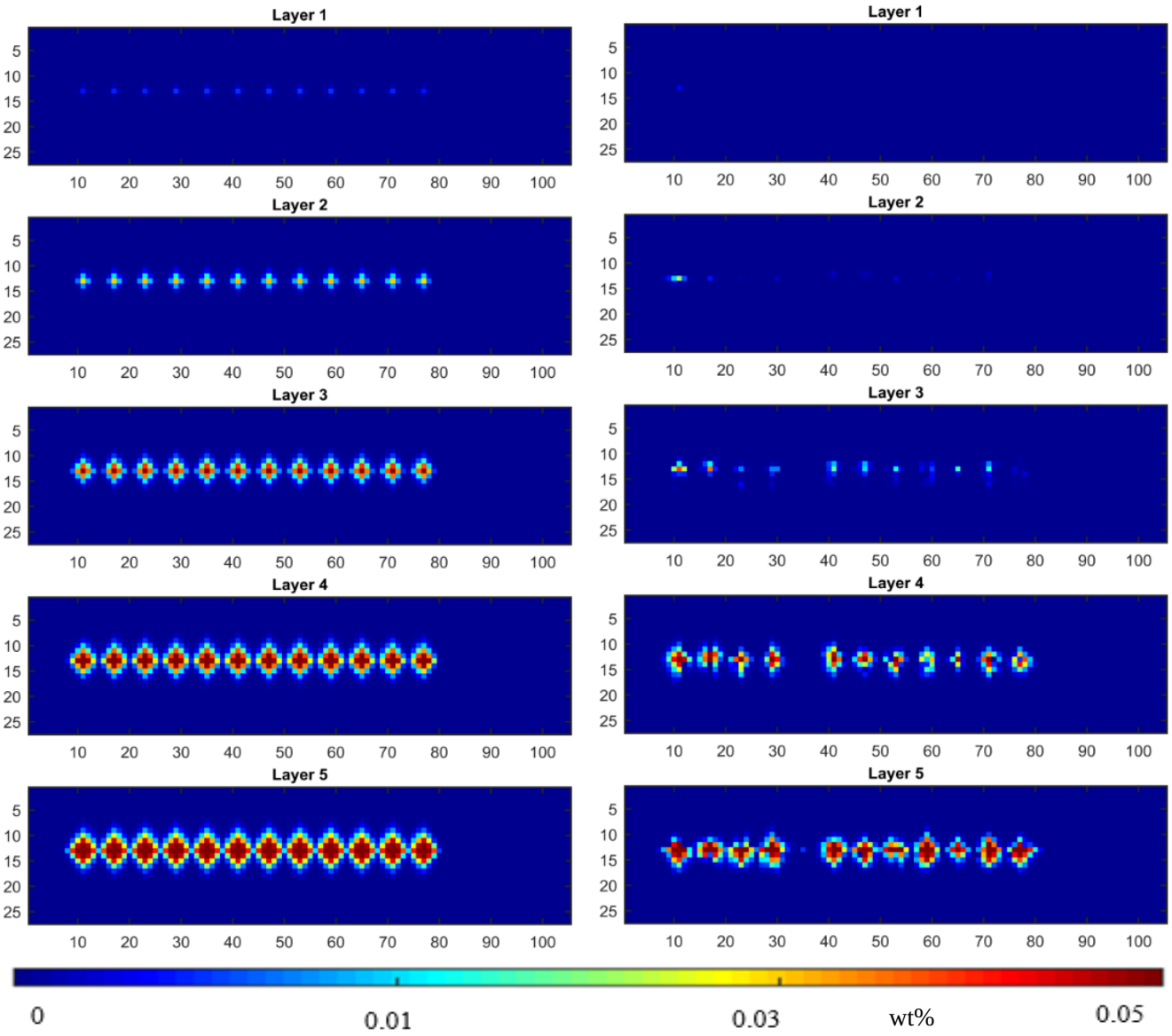

Figure 7. 11 Nanofluids Concentration in a Reservoir after 3 Years' Injection for Homogeneous (left) and Heterogonous (right) Model (Zhang, 2015)

Permeability is modified based on the nanoparticle concentration underground. As shown in **Table 7.10**, a permeability reduction is negligible as the concentration of nanoparticles is less than 0.01 *wt%*, 3% of permeability reduction is set for a concentration of nanoparticles between 0.01 *wt%* and 0.025 *wt%*, and 5% of permeability reduction is set for a concentration of nanoparticles

between 0.025 *wt%* and 0.05 *wt%*.

Table 7. 10 Permeability Modification Based on Nanoparticle Concentration (Zhang, 2015)

Concentration	Permeability Multiplier
0.025-0.05	0.95
0.01-0.025	0.97
<0.01	1

Dual Porosity Model without Hydraulic Fracturing

Massive natural fractures exist in the dual porosity model. As shown in **Figure 7.12**, the existence of natural fractures boosts the injectivity of nanofluid, and more nanofluid can enter into the matrix and fractures system in this case. Nanoparticles mainly stay in the natural fractures and highly permeable zone.

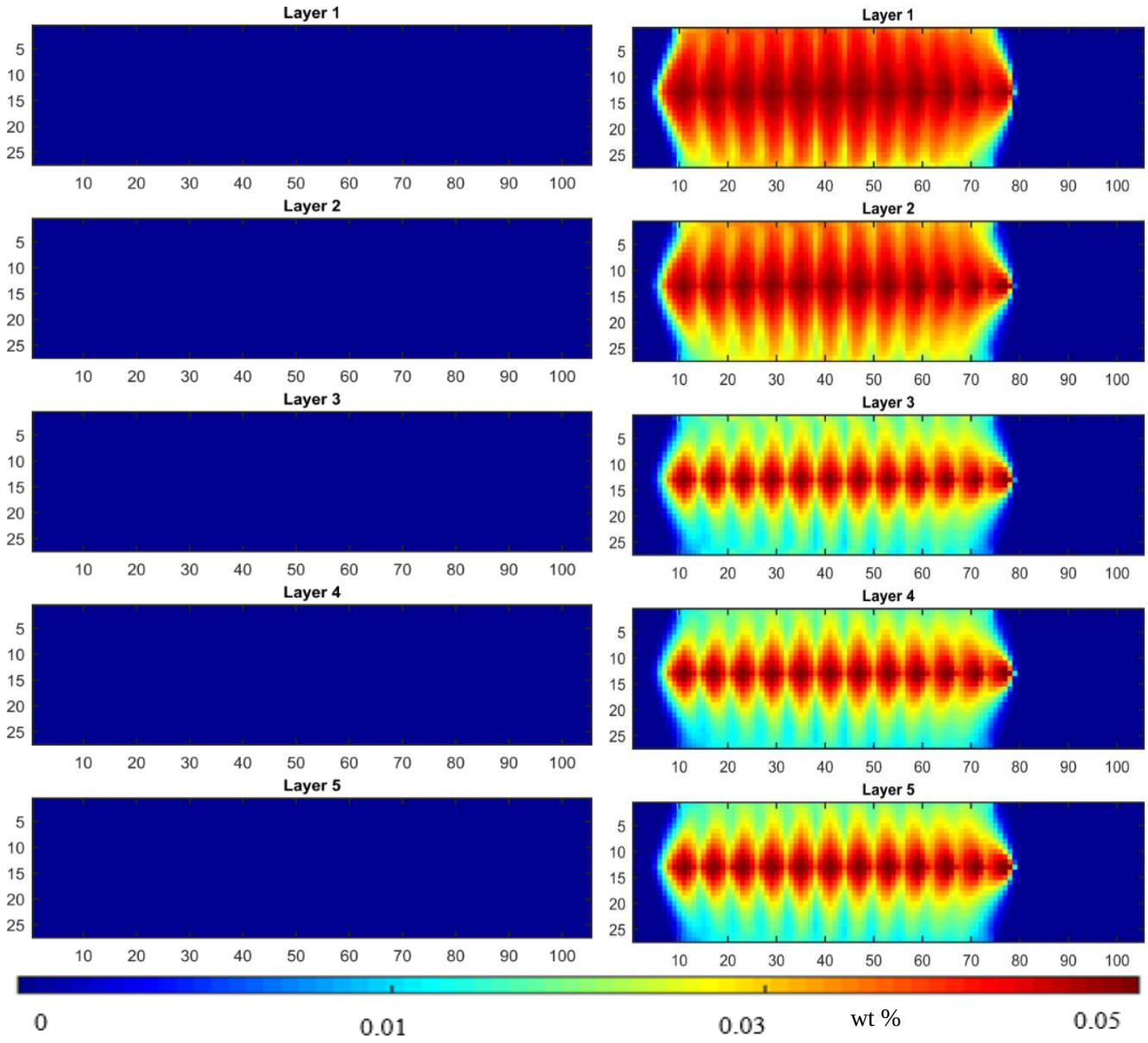

Figure 7. 12 Nanofluids Concentration in Reservoir after 3 Years' Injection for Matrix (left) and Fracture (right) in Dual Porosity Model (Zhang, 2015)

The following results show the NAG performance in various models.

Reservoir simulations are run by using Eclipse and CMG simulators. As shown in **Figures 7.13** and **7.14**, oil production by NAG is around 7% higher than WAG in both the homogeneous model and the heterogeneous system. The results given by Eclipse are consistent with those of CMG.

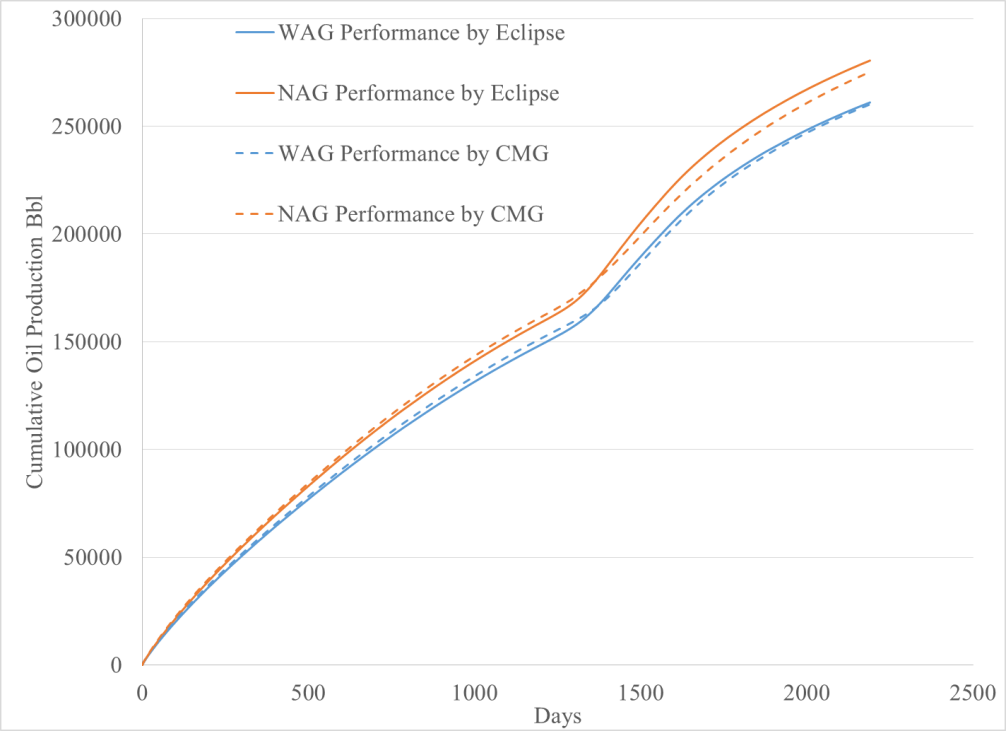

Figure 7. 13 Cumulative Oil Production for Homogeneous Model (Zhang, 2015)

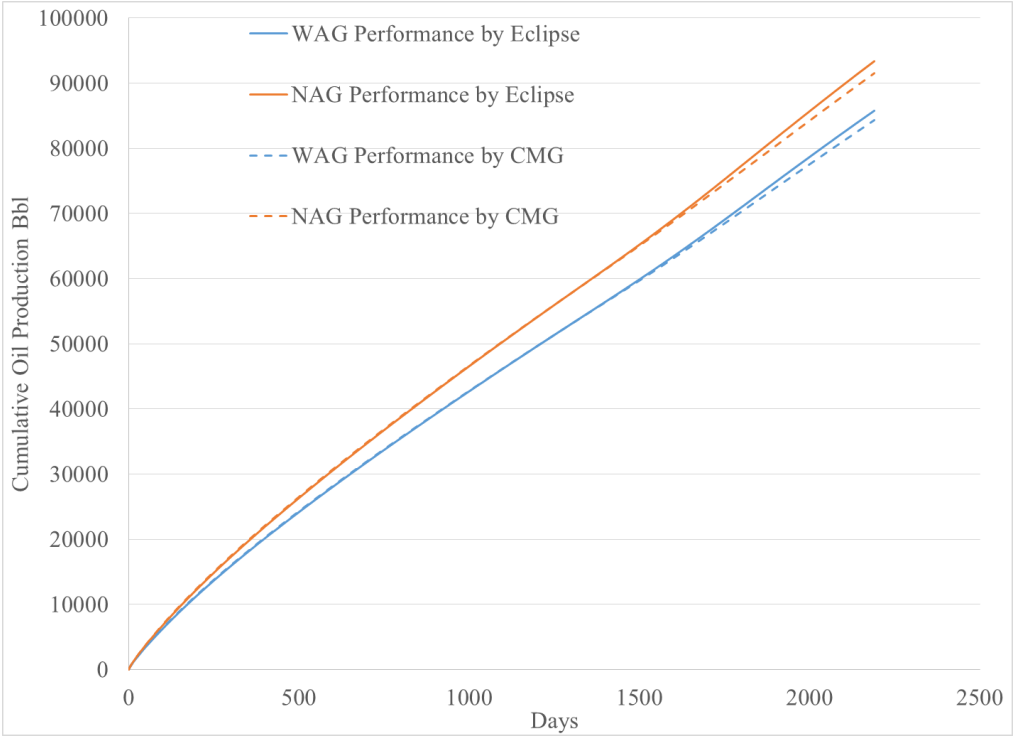

Figure 7. 14 Cumulative Oil Production for Heterogeneous System (Zhang, 2015)

As shown in **Figure 7.15**, oil production by NAG is around 11% higher than WAG, and NAG has a higher increment of oil recovery with the existence of natural fractures. The results given by Eclipse are consistent with those of CMG.

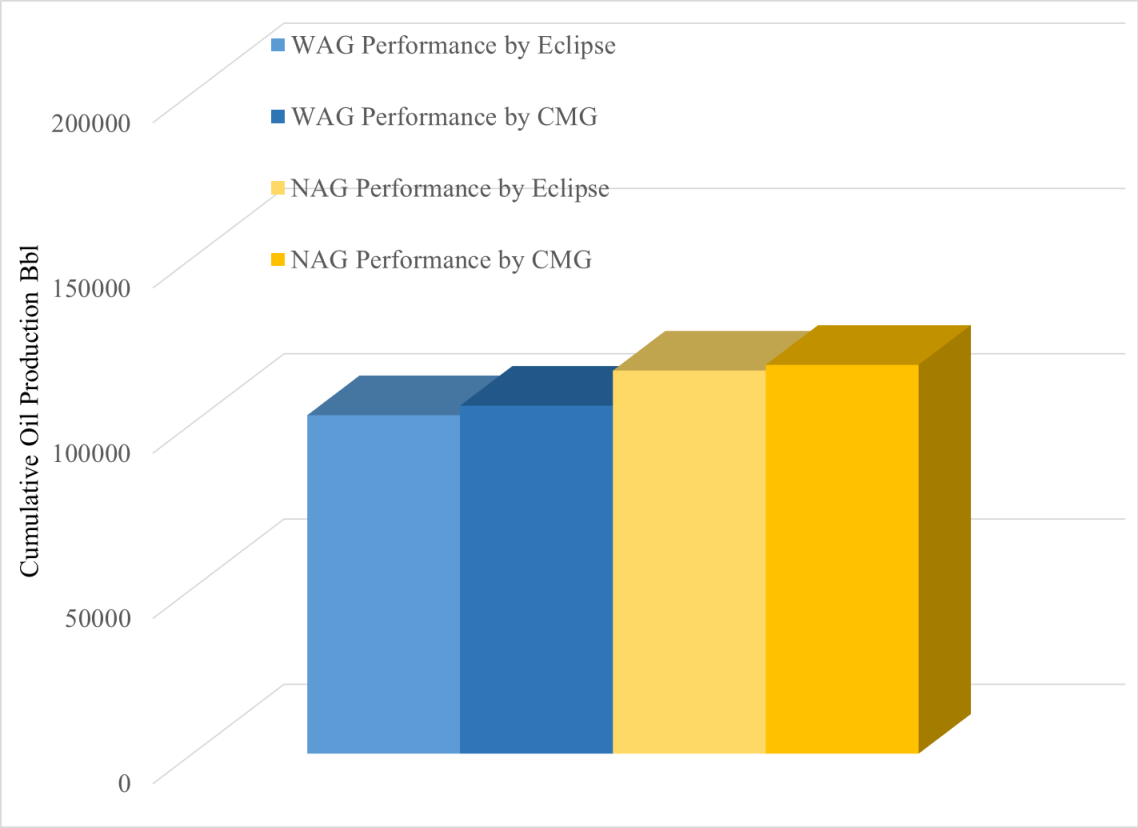

Figure 7. 15 Cumulative Oil Production for Dual Porosity Model (Zhang, 2015)

When natural fractures exist in a reservoir, the injectivity of nanofluid is at a high increment. More nanofluid has a chance to flood the matrix and nanoparticles retain predominately in fractures instead of the matrix. Reduction of permeability in natural fractures will not impede well productivity too much, however, the contact area between the nanofluid and matrix becomes much larger with the existence of natural fractures.

In addition, in the dual porosity model, the matrix functions as storage of oil and fractures act

as flow channels. The reduction of interfacial tension can play a significant role in improving final recovery in the fractured system due to increased gravity effects, which, in turn, changes the process from capillary countercurrent flow to gravity drive cocurrent flow (Karimaie, 2007).

The inverse Bond number, N_B^{-1} for showing the relative importance of capillary forces to gravity, is expressed by the following equation (Karimaie, 2007):

$$N_B^{-1} = \frac{\sigma_{wo}\sqrt{\emptyset/k}}{\Delta\rho g H} \tag{7.25}$$

If N_B^{-1} is reduced by a decrease in interfacial tension, the gravity force becomes more important. As interfacial tension is reduced, there is a transition from the countercurrent capillary dominated flow to cocurrent gravity-driven flow during an imbibition process (Karimaie, 2007). This means that water and oil are produced in the same direction as the water is injected, and less resistance of flow can occur in this case, as shown in **Figure 7.16.**

.

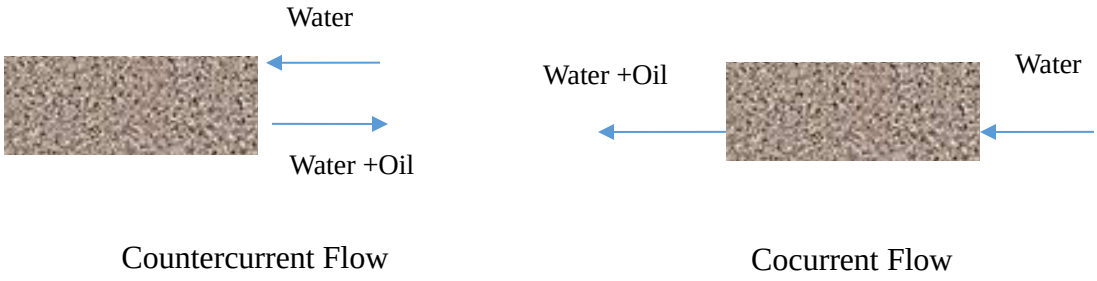

Figure 7. 16 Countercurrent Flow vs. Cocurrent Flow during Water Flooding (Zhang, 2015)

Nanofluid flooding with the reduction of interfacial tension contributes to cocurrent flow in the dual porosity system, resulting in higher oil recovery.

Chapter 8. Conclusions and Future work

This thesis presents the effects of nanopores on the CO_2 EOR process. The CO_2-oil miscibility in nanopores is investigated and further illustrations with respect to miscibility, including solubility parameters, vaporizing and condensing drive, and immiscible and miscible processes, are presented. The effect of nanopores can be applied in screening tight oil reservoirs and selecting CO_2 parameters for CO_2 flooding. The investigation highlights the following:

1. Gas and oil or water and oil are co-produced at an early stage of production. Many tight oil producers have seen that the water cut remains constant or undergoes a reduction as production goes on within the first 36 months. Fluid flooding can maintain reservoir pressure and keep the oil production for tight oil reservoirs, but for conventional oil reservoirs, water flooding can suddenly increase the oil production rate which then drops after a certain time of production.
2. The confinement effect in nanoscale pores helps to drive molecules to remain horizontal to pore wall surfaces.
3. The confinement effect in nanoscale pores helps to suppress the bubble point pressure and decrease a solution gas-oil ratio and an oil formation volume factor.
4. The confinement effect in nanoscale pores drives the vapor and liquid phase composition close to each other.
5. The confinement effect in nanoscale pores helps to decrease the difference in solubility parameters between crude oil and injected CO_2, resulting in lower gas-oil interfacial tension, which, in turn, contributes to CO_2-oil miscibility.

6. The confinement effect of nanoscale pores may impair multi-component dispersion and improve the vaporizing and condensing drive efficiency during CO_2 displacement, which contributes to a lower CO_2 MMP.
7. The nanopores effect mainly applies to the range of a pore diameter from 100 *nm* to 5 *nm*. The heavy components in the reservoir oil are difficult to cross over at a pore size less than 5 *nm*.
8. The hysteresis effect can be weakened by the confinement effect.
9. Nanopores mainly affect the CO_2 parameters selection and an integrated method to screen CO_2 flooding for tight oil reservoirs is presented.
10. A CO_2 near-miscible process is more suitable than miscible flooding for tight oil reservoirs.
11. The nanofluid alternating gas process can be an alternative solution to improve WAG performance. It has a potential to enhance oil recovery for tight reservoirs, not including shale reservoirs.

Future work

The nanoscales effect in this study is only for homogeneous reservoirs with a unique pore size. Intraparticle nanopores can have somewhat irregular, ellipsoidal shapes, but other morphologies are also present (Loucks, 2009; Curtis, 2010). The arrangement of carbon atoms can be different as well.

Molecules Static/Dynamic Properties with High Pore Structure Complexity

As shown in **Figure 8.1**, carbon bonds can rotate and have different arrangements; molecules' diffusion and mean square displacement can be affected by the carbon bonds arrangement in the Armchair and Zig-zag nanotubes.

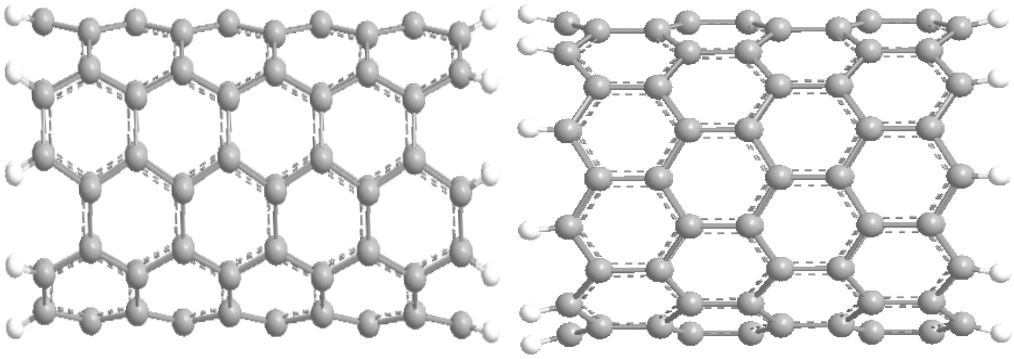

Figure 8. 1 Armchair Nanotube (Left) vs. Zig-zag Arrangement of Carbon Nanotube (Right); the Grey Atoms Represent the Carbon and the White Molecules are Hydrogens.

A methane molecule is placed inside nanotubes to investigate the mean square displacement and diffusion. The trajectory can be captured with time and the mean square displacement can be characterized by the following (Sofos, 2010):

$$MSD(t) = \frac{1}{N}\sum_{j=1}^{N}\left[r_j(t) - r_j(0)\right]^2 \quad (8.1)$$

The channel diffusion coefficient can be evaluated (Sofos, 2010):

$$D_{ch} = \lim_{t\to\infty} \frac{1}{6t}\, MSD(t) \tag{8.2}$$

In an Armchair (8,8) nanotube, a molecule has a similar mean square displacement and diffusion with the one in the zig-zag nanotube, as shown by the solid line in **Figures 8.2** and **8.3**. A minor variation between the molecules inside the Armchair and Zig-zag nanotubes is shown by the dashed line.

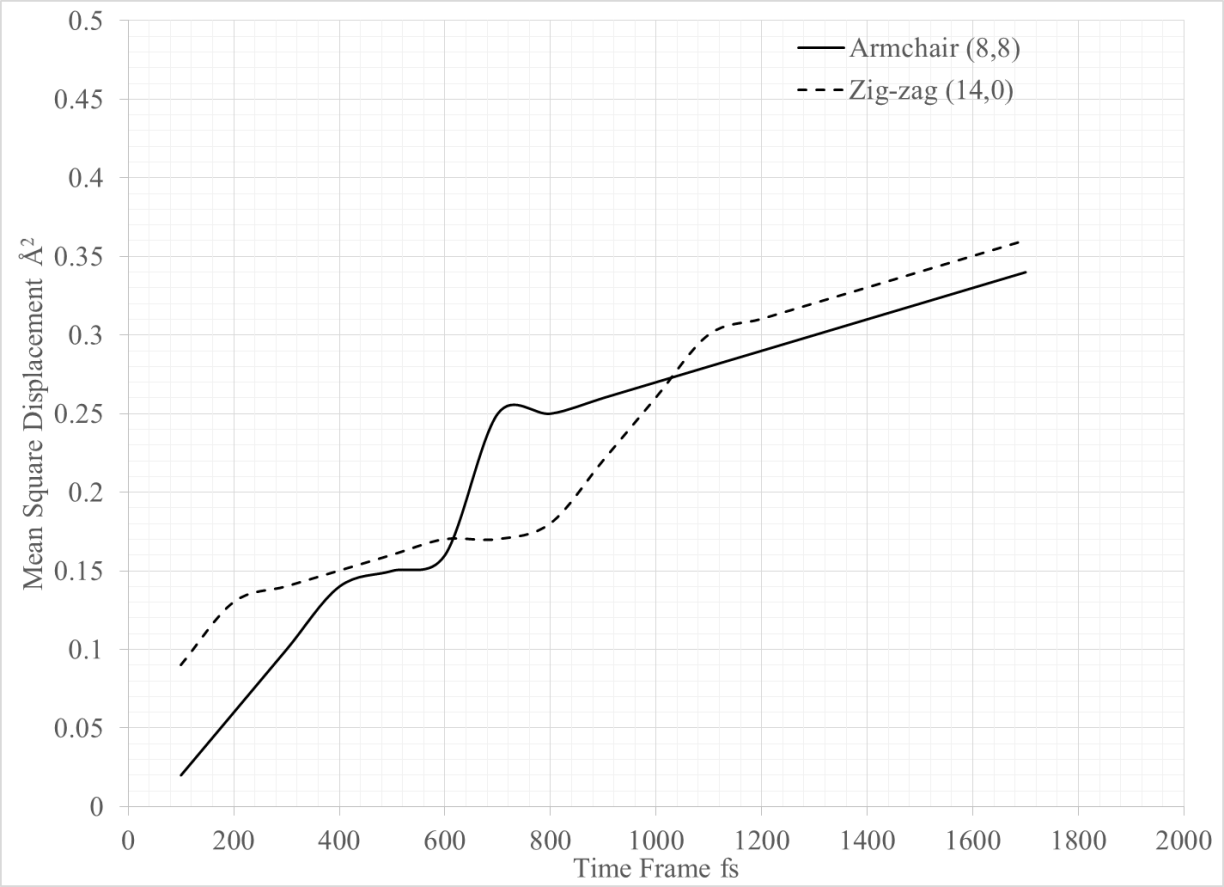

Figure 8. 2 Mean Square Displacement in a Nanotube

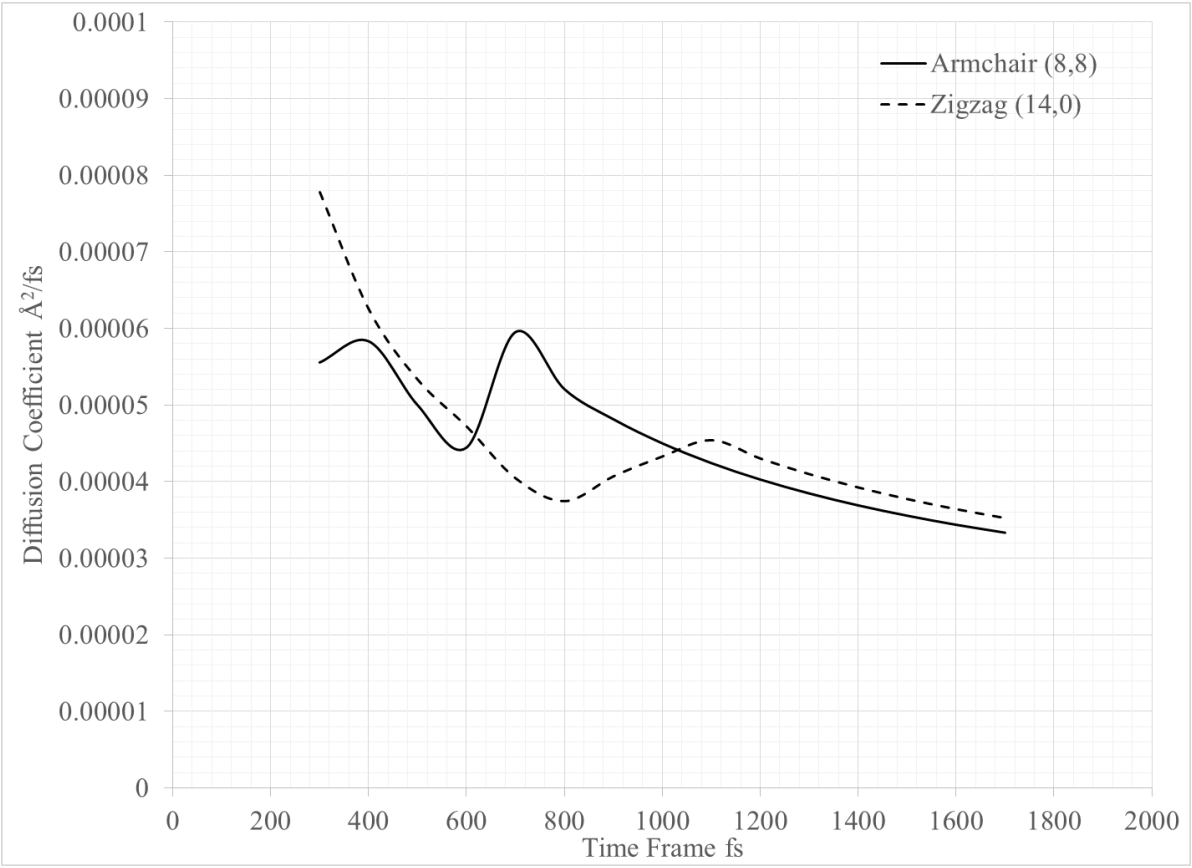

Figure 8. 3 Diffusion in a Nanotube

The variation in the mean square displacement inside the armchair and zig-zag nanotubes is associated with the different interactions inside the nanotubes. The fluid shear stress and potential energy can be affected by the carbon atoms arrangement, which will be studied in the future.

In addition, coalescence of multiple ellipsoidal pores can further accelerate the complexities of pore structures. The surface roughness can be altered in this way. Instead of a nanotube, a cubic shaped nano-channel is created to study the effect of surface roughness of a nano-channel on the interaction between molecules and the nano-channel. As shown in **Figure 8.4**, the surface roughness increases from left to right. The grey atoms represent carbon bonds and the white molecules are the hydrogens. The left model illustrates an approximately smooth nano-channel

surface while the rest shows roughness. The models have a uniform lateral around 1 *nm*. The methane is placed inside the nano-channel to investigate the molecules' trajectory and acceleration.

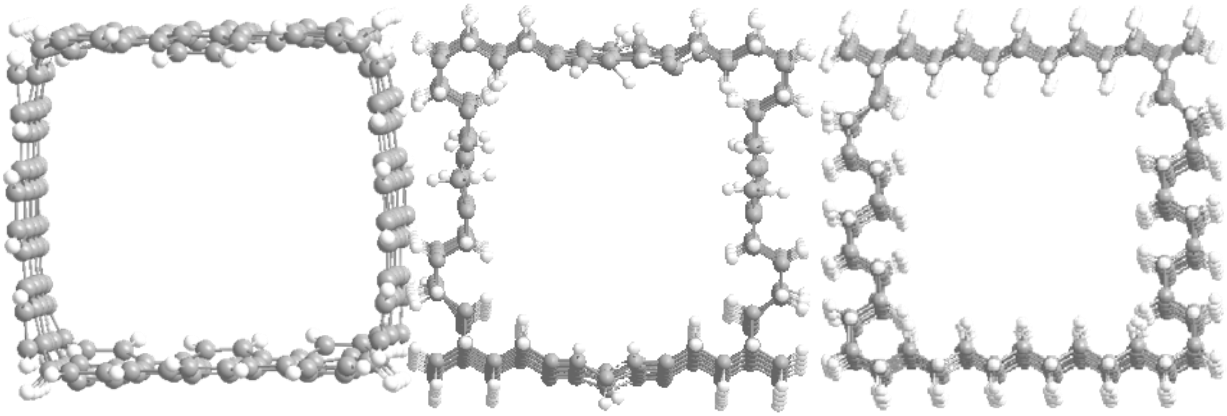

Figure 8. 4 Surface Roughness Variation in the Nano-channel

As the roughness of pore wall surfaces alters, the mean square displacement of molecules inside pores can be different. As shown in **Figures 8.5** and **8.6**, the mean square displacement and diffusion in a smooth nano-channel varies with the degree of roughness. The molecular diffusion is also different with the smooth surface case. As shown in the solid line, the molecule can travel more distance inside a smooth pore wall surface within a certain period as compared to the smooth nano-channel. The curvature is caused by the different interactions between the molecule and pore wall surface, the van der Waals force varies when the molecule locates in a different part of the nano-channel, either close to the center of the pore or near the pore wall surface. The variation in the interactions, based on the molecule trajectory, drives the mean square displacement and the diffusion has a curvature shape.

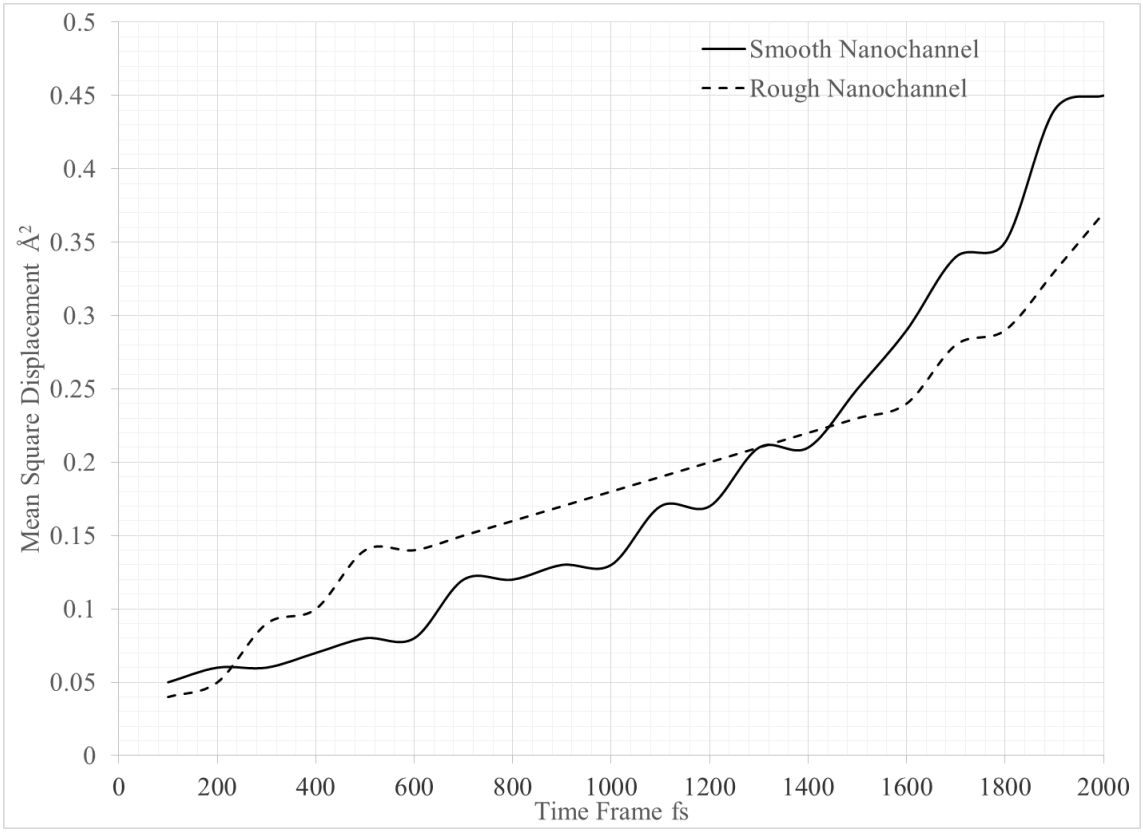

Figure 8. 5 Mean Square Displacement in a Nano-channel

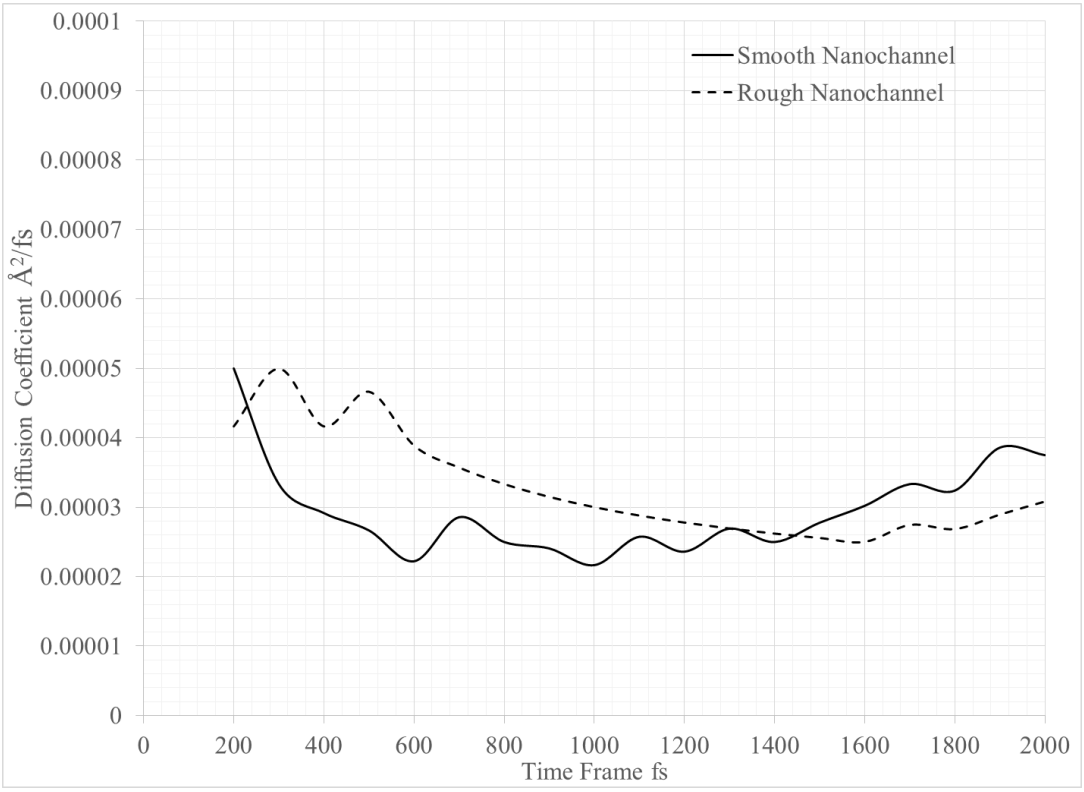

Figure 8. 6 Diffusion in a Nano-channel

The molecule can have a larger capacity in dynamic energy when it locates at the center of the pore. As the roughness of the pore increases, the interaction between the pore wall and the molecule will be stronger and the diffusion of the molecule decreases, which can be seen in **Figure 8.7**. Especially for a molecule located in the area near the rough pore wall surface, movement is strongly limited by the reduction of the diffusion near the rough pore wall surface. The previous research shows that the diffusion decreases as the surface roughness increases, as illustrated in **Figure 8.8**.

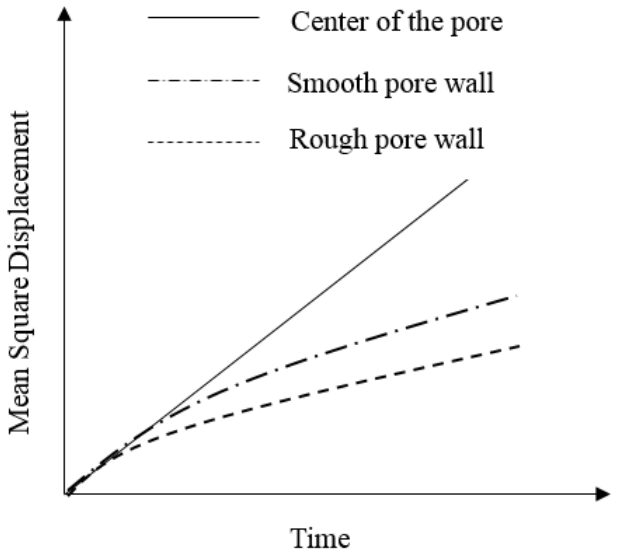

Figure 8. 7 Mean Square Displacement in Smooth and Rough Pore Walls (Sofos, 2010)

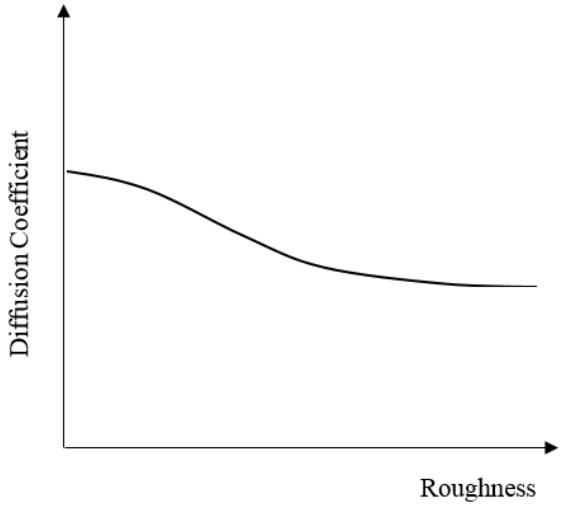

Figure 8. 8 Diffusion Coefficient of Pore Wall Roughness (Sofos, 2010)

The molecule has the highest diffusion and velocity when it is located at the center of the pore. The molecule has the most acceleration once it is close to the pore wall surface, and the pore wall surface roughness can further accelerate the gap between the diffusion coefficient at the center and the pore wall surface, as shown by the dashed line in **Figure 8.9**.

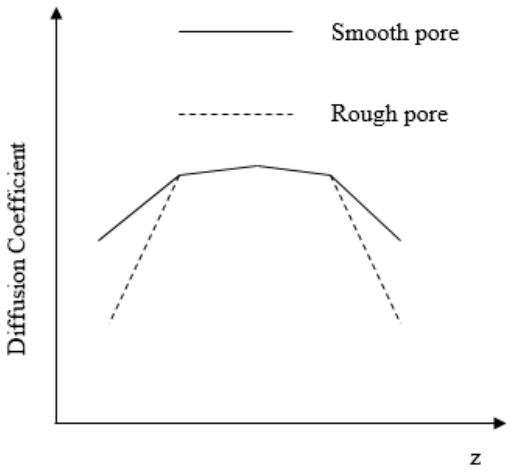

Figure 8. 9 Diffusion Coefficient in Smooth and Rough Pore Walls (Sofos, 2010)

The diffusion and mean square displacement of molecules can be affected by the pore wall surface roughness, in which the interaction between molecules and the pore wall can be altered. A CO_2 molecule is placed into the cube-shape nano-channel model and the rough one to see the potential energy difference: One is parallel to the nano-channel surface, and the other is perpendicular to the nano-channel surface. As shown in **Figures 8.10** and **8.11**, the variations between the energy at a specific position and the energy at the center of the nanotube are recorded. The CO_2 molecule in a parallel configuration to the surface has a larger bond energy parameters at the molecular separation distance, which indicates the molecule has a less energy; the molecule will prefer to stay parallel to the surface of the nano-channel. In addition, the comparisons between the energy difference in the smooth and rough nano-channels are made. The CO_2 has lower energy when it is located parallel to the rough nano-channel surface. The strength parameter of the Lennard-Jones potential, ε_{LJ}, is around 3.1 kcal/mol in the rough case and 2.8 kcal/mol in the smooth one, which indicates that the interactions between the molecules and the pore wall surface

are stronger in the rough case. The size parameter of the Lennard-Jones potential σ_{LJ} in the rough pore is around 0.32 *nm* and around 0.35 *nm* in the smooth one.

The critical properties shifts are summarized by the following equations (Singh, 2009):

$$\Delta T_c^* = \frac{T_{cb} - T_{cp}}{T_{cb}} = a\frac{\sigma_{LJ}}{r_p} - b\left(\frac{\sigma_{LJ}}{r_p}\right)^2 \tag{8.3}$$

$$\Delta P_c^* = \frac{P_{cb} - P_{cp}}{P_{cb}} = a\frac{\sigma_{LJ}}{r_p} - b\left(\frac{\sigma_{LJ}}{r_p}\right)^2 \tag{8.4}$$

As the pore wall surface roughness increases, the size parameter of the Lennard-Jones potential σ_{LJ} decreases, resulting in an reduction in the term ΔT_c^* ΔP_c^*; the pore critical properties, including critical temperature and critical pressure, T_{cp}, P_{cp}, will be increased.

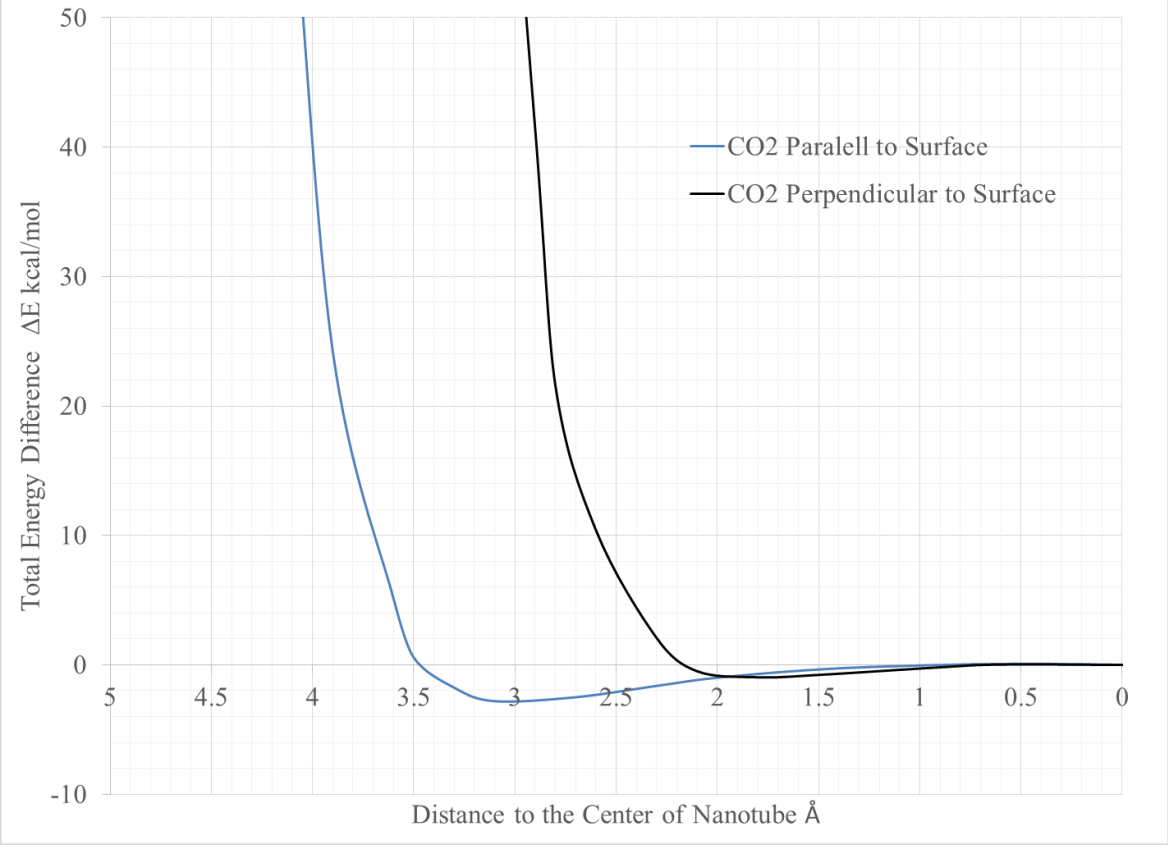

Figure 8. 10 Energy Difference in Smooth Nano-channel

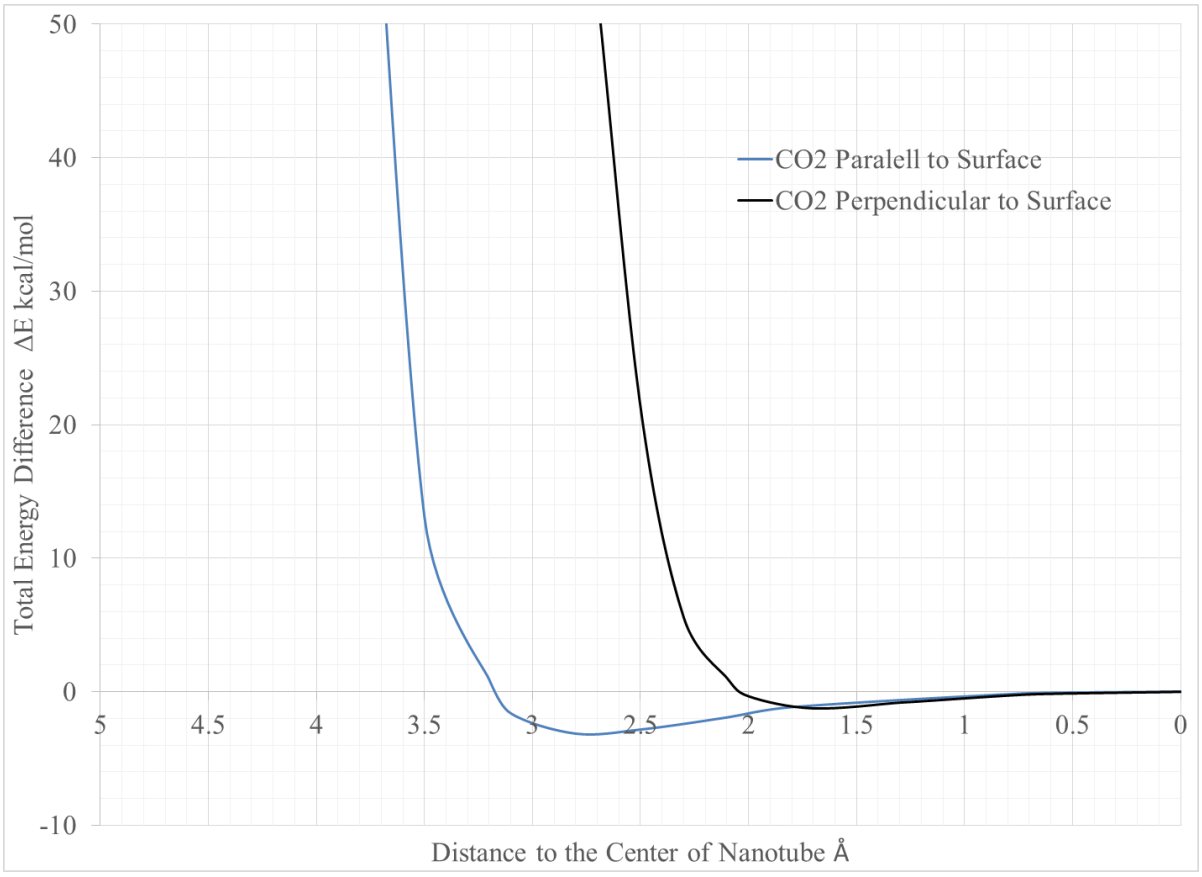

Figure 8. 11 Energy Difference in Rough Nano-channel

In a soft rough nano-channel, the heat transfer increases with regard to the hard and smooth cases (Nicol, 1966). The roughness in nanopores contributes to the formation of multiple bridges and slow kinetics of condensation (Banerjee, 2012), and molecules will prefer to stay in a gas phase. The pore wall surface roughness drives molecules to stay further beyond the pore wall surface. The adsorption decreases as the pore wall surface roughness increases, resulting in a reduction in inhomogeneity of molecules' density at the boundary of a pore and that at the center of the pore. The nanopore confinement effect is weakened by the incremental of the nanopore wall surface roughness. Compared to the smooth case, the nanopore wall roughness contributes to an increment of critical properties, resulting in a broader two-phase region.

The preceding analysis does not include a functional group; only carbon bonds are considered in a nanopore, which is a hydrophobic system. Instead, models with the functional group –OH are created to represent the cases of hydrophilic properties in part of a nano-channel. As shown in **Figure 8.12**, the functional group –OH is added into the rough nano-channel case, where the grey bonds represent the carbons, the white atoms show the hydrogens, and the red molecules present the functional group –OH.

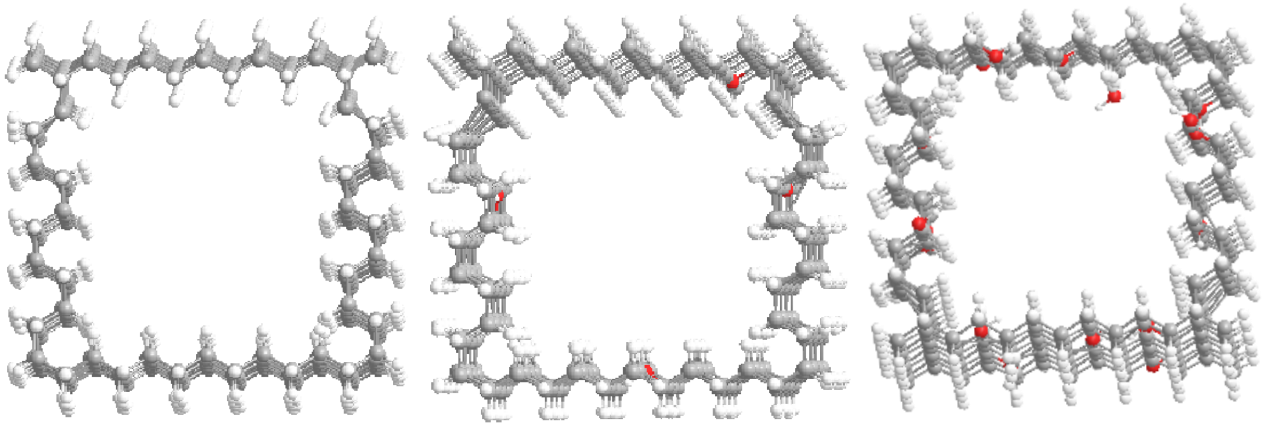

Figure 8. 12 Functional Group OH in the Rough Nano-channel

Methane is placed in the models, both left and right in **Figure 8.12** to see the molecule movement; the mean square displacement and diffusion are recorded. The functional group OH is hydrophilic. Once the methane enters the system, the chemical bonds of the functional group repel the hydrocarbon and the mean square displacement and the diffusion can be increased, as shown by the dashed line in **Figures 8.13** and **8.14**.

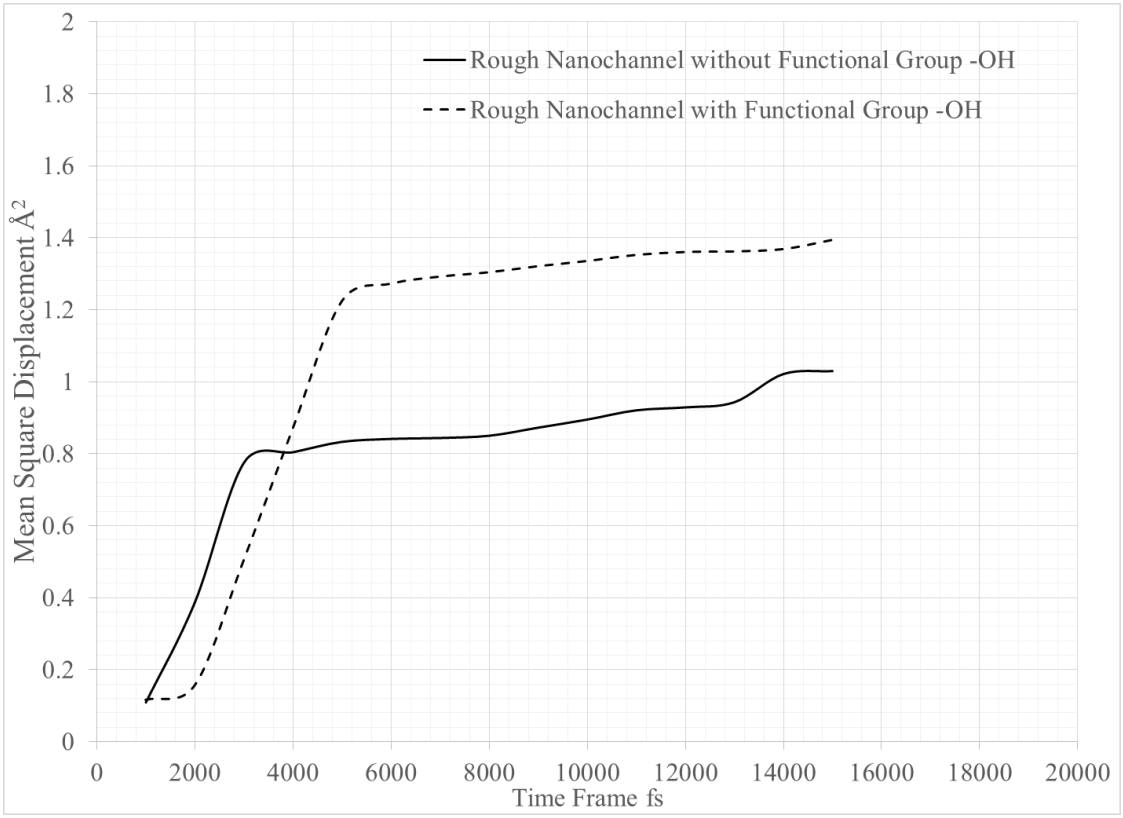

Figure 8. 13 Mean Square Displacement in the Rough Nano-channel with Functional Group OH

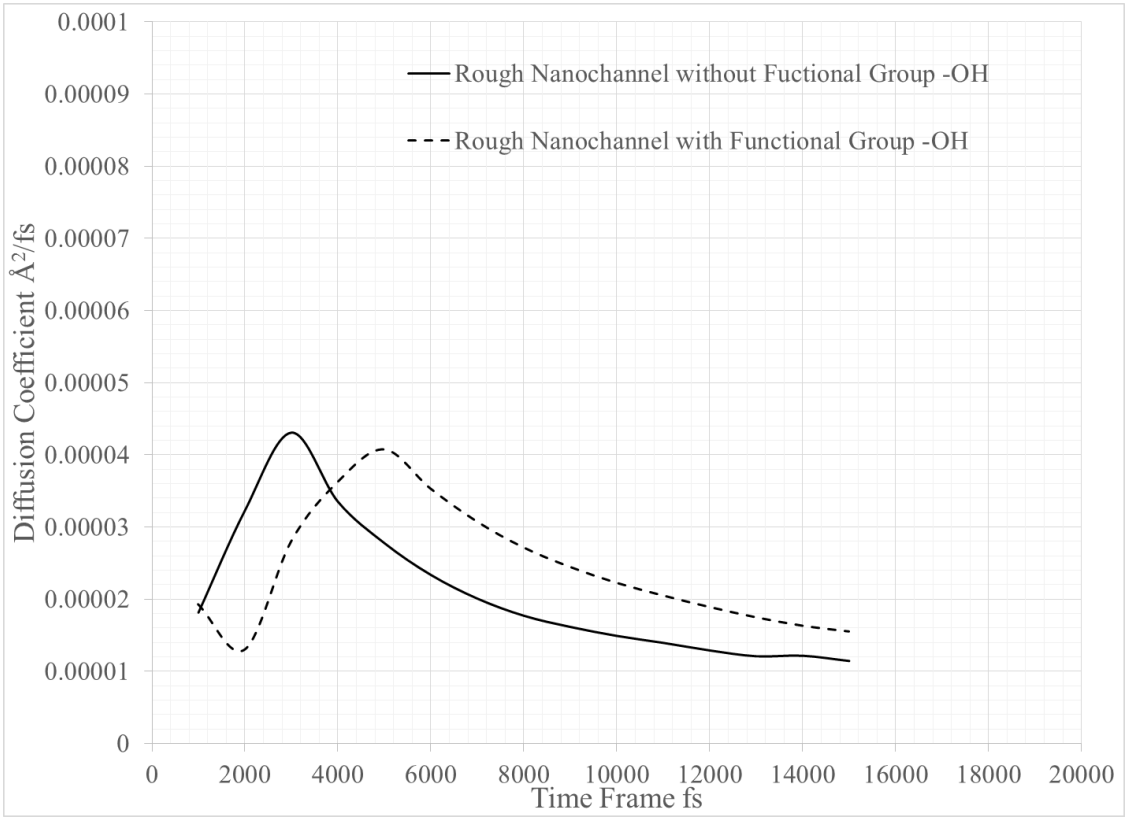

Figure 8. 14 Diffusion in the Rough Nano-channel with Functional Group OH

In the case of a broad nanopore size distribution, the integrated nanopore geometry will be taken into consideration. As shown in the **Figure 8.15**, the pore with high complexity will be created with different size, varying roughness and different amount of the functional group, which can be used to mimic a molecule's travel in a broad pore distribution. Dodecane is planned to be used to represent the oil and CO_2 is flooding from an edge of the pore, the mixture behavior and the interactions of the molecules and complex pore structure will be further studied by the molecular dynamics.

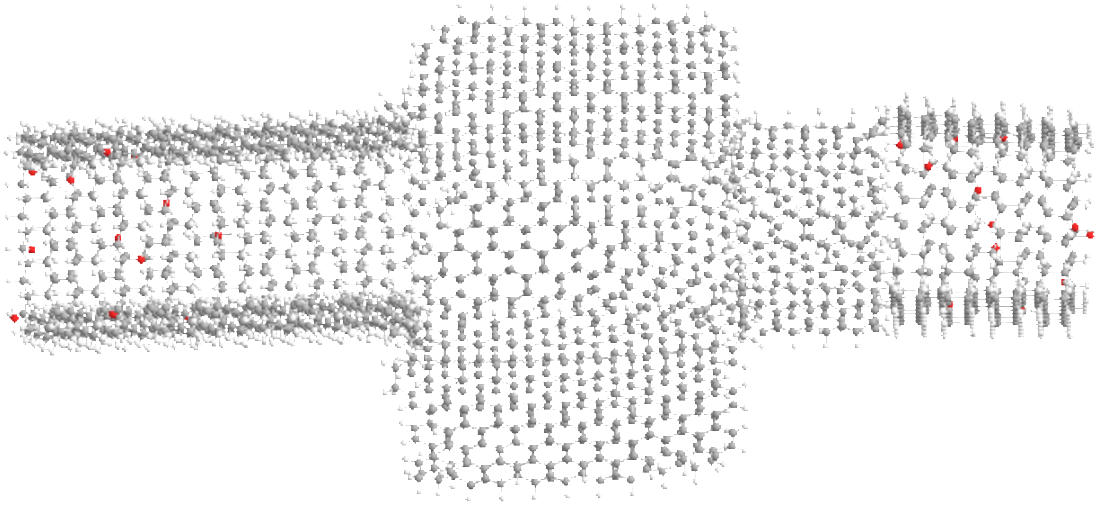

Figure 8. 15 Pore Connections

The adsorption of hydrocarbons on the pore wall surface can reduce a pore diameter to some extent, which can contribute to a variation in the interactions between the molecules and nanopore. Research has also shown that the critical properties are dependent on parameters including pore sizes, geometry, wall shape, chemical properties, and gas properties (Derycke, 1991; Hamada, 2007; Singh, 2011). These factors affect the geometric constraints on molecules or the van der Waals forces, which are areas for future studies.

Identifying the CO_2 Sequestration Sweet Spot in Shale Plays

The thesis works on the interaction between hydrocarbons and the pore wall surface, the hydrocarbons are expected to travel through the porous media. Instead, the non-hydrocarbon such as CO_2, which is expected to store in the reservoirs. In the future, the study on CO_2 diffusion and movement in the nanopores can help to determine where the CO_2 will be secured in the porous media. The

The surface diffusivity of CO_2 is around a quarter of CH_4 in nanopores. It indicates that the

transfer capacity for CH_4 is better than CO_2 in a reservoir. Hydrocarbon recovery by CO_2 injection benefits from a preferable mobility ratio with a higher absorption ability to displace reservoir gas (Zhang, 2016). In this way, the CO_2 injection can provide dual benefits of enhanced recovery of absorbed methane and sequestrate CO_2, especially in shale gas condensate reservoirs. The interactions between CO_2 and pore surfaces with a different pore size, a pore type and pore surface roughness will be studied by a molecular dynamic simulation, which helps to identify the sweet spots for CO_2 sequestration in the porous media.

References

Allinger, Norman L. Conformational analysis. 130. MM2. A hydrocarbon force field utilizing V1 and V2 torsional terms. Journal of the American Chemical Society 99.25: 8127-8134. 1977.

Abdallah, Wael, et al. Fundamentals of wettability. Technology 38.1125-1144: 268. 1986.

Anderson, W. G. Wettability Literature Survey Part 5: The Effects of Wettability on Relative Permeability. Society of Petroleum Engineers. doi:10.2118/16323-PA. 1987.

Asar, H., & Handy, L. L. Influence of Interfacial Tension on Gas/Oil Relative Permeability in a Gas-Condensate System. Society of Petroleum Engineers. doi:10.2118/11740-PA. 1988.

Ahmed, T. A Generalized Methodology for Minimum Miscibility Pressure. Society of Petroleum Engineers. doi:10.2118/39034-MS. 1997.

Arshad, Aziz, et al. Carbon dioxide (CO_2) miscible flooding in tight oil reservoirs: A case study. Kuwait International Petroleum Conference and Exhibition. 2009.

Ahmadi Rahmataba, Kaveh. Advances in calculation of minimum miscibility pressure. Diss. 2011.

Ayatollahi S, Zerafat M. Nanotechnology-assisted EOR techniques: New solutions to old challenges, SPE International Oilfield Nanotechnology Conference. 2012.

Anne. Investigation of how Silica Nanoparticle Adsorption Affects Wettability in Water-Wet Berea Sandstone. NTNU. 2013.

Ashraf, M., and M. Satapathy. "The Global Quest for Light Tight Oil: Myth or Reality." Energy Perspectives: 16-23. 2013.

Akkutlu, I. Y., & Didar, B. R.. Pore-size Dependence of Fluid Phase Behavior and Properties in Organic-Rich Shale Reservoirs. Society of Petroleum Engineers. doi:10.2118/164099-MS. 2013.

Adekunle O O, Hoffman B T. Minimum Miscibility Pressure Studies in the Bakken, SPE Improved Oil Recovery Symposium. Society of Petroleum Engineers. 2014.

Allawe, E. M., Stockdale, A. P., Aminiaa, K., & Ameri, S. Impact of Nanoscale Pore Confinement on Estimation of Gas Resources and Gas/Condensate Behavior in Shale Reservoirs. Society of Petroleum Engineers. doi:10.2118/177285-MS. 2015.

Barton. A.F.M. Handbook of Solubility Parameters and Other Cohesion Parameters, CRC Press, Boca Raton, Florida 1983.

Brock, W. R., and L. A. Bryan. Summary Results of CO2 EOR Field Tests 1972-1987. Low Permeability Reservoirs Symposium. Society of Petroleum Engineers. 1989.

Bargas, C. L., Montgomery, H. D., Sharp, D. H., & Vosika, J. L. Immiscible CO2 Process for the Salt Creek Field. Society of Petroleum Engineers. doi:10.2118/21577-PA. 1992.

Bardon, C. Gas/Oil Relative Permeability and Residual Oil Saturations in a Field Case of a Very Light Oil, in the Near-Miscibility Conditions. Society of Petroleum Engineers. doi:10.2118/28625-MS. 1994.

Bernard P. Binks. Particles as surfactants—similarities and differences, Current Opinion in Colloid & Interface Science, Volume 7, Issues 1–2, Pages 21-41, ISSN 1359-0294. 2002.

Bachu S , Shaw J C. Pears on R M. Estimation of oil recovery and CO_2 storage capacity in CO_2 EOR incorporat ing the effect of underlying aquifers. Society of Petroleum Engineers. 2004.

Bui, Ly Huong, Jyun-Syung Tsau, and G. Paul Willhite. Laboratory Investigations of CO_2 Near Miscible Application in Arbuckle Reservoir. SPE Improved Oil Recovery Symposium. Society of Petroleum Engineers. 2010.

Banerjee, Soumi, et al. Effect of surface roughness and softness on water capillary adhesion in apolar media. The Journal of Physical Chemistry A 116.25: 6481-6488. 2012.

Cronquist, C. Carbon dioxide dynamic displacement with light reservoir oils. Paper presented at the 1978 U.S. DOE Annual Symposium, Tulsa, Aug. 28–30. 1978.

Carcoana A N. Enhanced oil recovery in Rumania. Society of Petroleum Engineers. 1982.

Christensen, J. R., Stenby, E. H., & Skauge, A. Review of WAG Field Experience. Society of Petroleum Engineers. doi:10.2118/39883-MS. 1998.

Curtis H. Whitson, et al. Phase Behavior, Monograph Vol. 20. Society of Petroleum. 2000.

Chengara, Anoop, et al. Spreading of nanofluids driven by the structural disjoining pressure gradient. Journal of colloid and interface science, 280.1: 192-201. 2004.

Carnahan, Norman, Jean Louis Salager, and Raquel Anton. Effect of resins on stability of asphaltenes. Offshore Technology Conference. Offshore Technology Conference. 2007.

Chen, Zhangxin. Reservoir Simulation, University of Calgary. 2007

Changqing Wang, etc. Research of Determining Index Weights Based on Least Squares Method in Post- Evaluation Process. Journal of Jilin University. 2010.

Curtis, M. E., Ambrose, R. J., & Sondergeld, C. H. Structural Characterization of Gas Shales on the Micro- and Nano-Scales. Society of Petroleum Engineers. doi:10.2118/137693-MS. 2010.

Clarkson, C. R., & Pedersen, P. K. Production Analysis of Western Canadian Unconventional Light Oil Plays. Society of Petroleum Engineers. doi:10.2118/149005-MS. 2011.

Chalmers, G. R., Bustin, R. M., & Power, I. M. Characterization of gas shale pore systems by porosimetry, pycnometry, surface area, and field emission scanning electron microscopy/transmission electron microscopy image analyses: Examples from the Barnett, Woodford, Haynesville, Marcellus, and Doig units. AAPG bulletin, 96(6), 1099-1119. 2012.

Clarkson, C. R., Solano, N., Bustin, R. M., Bustin, A. M. M., Chalmers, G. R. L., He, L. & Blach, T. P. Pore structure characterization of North American shale gas reservoirs using USANS/SANS, gas adsorption, and mercury intrusion. Fuel, 103, 606-616. 2013.

CSUR. Understanding Tight Oil. Canadian Society for Unconventional Resources. 2017.

Donaldson, Erle C., Philip B. Lorenz, and Rex D. Thomas. The effects of viscosity and wettability on oil and water relative permeabilities. Fall Meeting of the Society of Petroleum Engineers of AIME. Society of Petroleum Engineers. 1966.

Derycke, I., et al. "Physisorption in confined geometry." The Journal of chemical physics 94.6: 4620-4627. 1991.

De Boer R B, Leerlooyer K, Eigner M R P, et al. Screening of Crude Oils for Asphalt Precipitation: Theory Practice and the Selection of Inhibitors. Society of Petroleum Engineers. 1995.

Dong, M., Huang, S. S., & Srivastava, R. A Laboratory Study on Near-Miscible CO_2 Injection in Steelman Reservoir. Petroleum Society of Canada. doi:10.2118/01-02-05. 2001.

Devegowda, D., Sapmanee, K., Civan, F., & Sigal, R. F. Phase Behavior of Gas Condensates in Shales Due to Pore Proximity Effects: Implications for Transport, Reserves and Well Productivity. Society of Petroleum Engineers. doi:10.2118/160099-MS. 2012.

Didar, B. R., & Akkutlu, I. Y. Pore-Size Dependence of Fluid Phase Behavior and the Impact on Shale Gas Reserves. Society of Petroleum Engineers. doi:10.1190/URTEC2013-183. 2013.

Dang, C. T. Q., Nghiem, L. X., Chen, Z. J., & Nguyen, Q. P. Modeling Low Salinity Waterflooding: Ion Exchange, Geochemistry and Wettability Alteration. Society of Petroleum Engineers. doi:10.2118/166447-MS. 2013.

Dang, C. T. Q., Nghiem, L. X., Chen, Z., Nguyen, N. T. B., & Nguyen, Q. P. CO2 Low Salinity Water Alternating Gas: A New Promising Approach for Enhanced Oil Recovery. Society of Petroleum Engineers. doi:10.2118/169071-MS. 2014.

Duchenne, S., Puyou, G., Cordelier, P., Bourgeois, M., & Hamon, G. Laboratory Investigation of Miscible CO2 WAG Injection Efficiency in Carbonate. Society of Petroleum Engineers. doi:10.2118/169658-MS. 2014.

Dhanapal, K., Devegowda, D., Zhang, Y., Contreras-Nino, A. C., Civan, F., & Sigal, R. Phase Behavior and Storage in Organic Shale Nanopores: Modeling of Multicomponent Hydrocarbons in Connected Pore Systems and Implications for Fluids-in-place Estimates in Shale Oil and Gas Reservoirs. Society of Petroleum Engineers. doi:10.2118/169008-MS. 2014.

Dong, Xiaohu, Huiqing Liu, and Zhennan Gao. Experimental investigation of miscible gas injection with different gases in petroleum reservoirs. International Journal of Oil, Gas and Coal Technology 9.3: 280-295. 2015.

Enick, R.M., Holder, G.D., Morsi, B.I. A thermodynamic correlation for the minimum miscibility pressure in CO2 flooding of petroleum reservoirs. SPERE, 81– 92. 1988.

Elsharkawy, Adel M., Fred H. Poettmann, and Richard L. Christiansen. Measuring CO2 minimum miscibility pressures: slim-tube or rising-bubble method?. Energy & fuels 10.2: 443-449. 1996.

Emera, M. K., & Sarma, H. K. Use of genetic algorithm to estimate CO2–oil minimum miscibility pressure—a key parameter in design of CO2 miscible flood. Journal of petroleum science and engineering, 46(1), 37-52. 2005.

Emera, M. K., Javadpour, F., & Sarma, H. K. Genetic Algorithm (GA)-Based Correlations Offer More Reliable Prediction of Minimum Miscibility Pressures (MMP) Between Reservoir Oil and CO2 or Flue Gas. Petroleum Society of Canada. doi:10.2118/07-08-01. 2007.

Fan, T., & Buckley, J. S. Acid Number Measurements Revisited. Society of Petroleum Engineers. doi:10.2118/99884-MS. 2006.

Forrest, J., et al. Working document of the NPC North American resource development study-unconventional oil. 2011.

Fatemi, S. M., Jamiolahmady, M., Sohrabi, M., & Ireland, S. Experimental and Theoretical Investigation of Oil/Gas Relative Permeabilities Hysteresis in the Presence of Immobile Water:

under Low Oil/Gas IFT and Mixed-Wet Conditions. Society of Petroleum Engineers. doi:10.2118/154530-MS. 2012.

Fatemi, S. Mobeen, and Mehran Sohrabi. Recovery mechanisms and relative permeability for gas/oil systems at near-miscible conditions: effects of immobile water saturation, Wettability, hysteresis, and permeability. Energy & Fuels 27.5: 2376-2389. 2013.

Fath, Aref Hashemi, and Abdol-Rasoul Pouranfard. "Evaluation of miscible and immiscible CO_2 injection in one of the Iranian oil fields." Egyptian Journal of Petroleum 23.3: 255-270. 2014.

Figuera, Luis Alfredo, et al. Performance Review and Field Measurements of an EOR-WAG Project in Tight Oil Carbonate Reservoir-Abu Dhabi Onshore Field Experience. Abu Dhabi International Petroleum Exhibition and Conference. Society of Petroleum Engineers. 2014.

Girifalco L.A. and Good, R.J.: A Theory for the Estimation of Surface and Interfacial Energies. I., Derivation and Application to Interfacial Tension, J. Phys. Chem. 61, 904. 1957.

Giddings, J.C., et al.: High Pressure Gas Chromatography of Nonvolatile Species, Science 162, 67. 1968.

Goodrich, J.H.: Target Reservoirs for CO_2 Miscible Flooding, Report DOE/MC/08341-17, U.S. DOE, Washington, DC. 1980.

Glass, O. Generalized Minimum Miscibility Pressure Correlation (includes associated papers 15845 and 16287). Society of Petroleum Engineers. doi:10.2118/12893-PA. 1985.

Gregory et. al. Tight reservoirs. Journal of Petroleum Technology, 2010.

Gao, P., Towler, B. F., & Pan, G. Strategies for Evaluation of the CO2 Miscible Flooding

Process. Society of Petroleum Engineers. doi:10.2118/138786-MS. 2010.

Ghaderi, S. M, et al. Evaluation of Recovery Performance of Miscible Displacement and WAG Processes in Tight Oil Formations. SPE/EAGE European Unconventional Resources Conference & Exhibition-From Potential to Production. 2012.

Gunnar, Investigation of how Hydrophilic Silica Nanoparticles Affect Oil Recovery in Berea Sandstone. NTNU. 2014.

Guo, Chaohua, et al. Study on gas flow through nano pores of shale gas reservoirs. Fuel 143: 107-117. 2015.

Hoffmann, A.E., Crump, J.S., and Hocott, C.R.: Equilibrium Constants for a Gas-Condensate System, *Trans.*, AIME **198,** 1.46 PHASE BEHAVIOR. 1953.

Hawthorne, Robert G. Two-phase flow in two-dimensional systems-effects of rate, viscosity and density on fluid displacement in porous media. 1960.

Holm, L. W., & Josendal, V. A. Mechanisms of Oil Displacement By Carbon Dioxide. Society of Petroleum Engineers. doi:10.2118/4736-PA. 1974.

Holm, L.W.: Status of CO_2 and Hydrocarbon Miscible Oil Recovery Methods, JPT 76. 1976.

Holm, L. W., & Josendal, V. A. Effect of Oil Composition on Miscible-Type Displacement by Carbon Dioxide. Society of Petroleum Engineers. doi:10.2118/8814-PA. 1982.

Hadlow, R. E. Update of industry experience with CO_2 injection. SPE Annual Technical Conference and Exhibition. Society of Petroleum Engineers. 1992.

Henderson, G. D., Danesh, A., Tehrani, D. H., Al-Shaidi, S., & Peden, J. M. Measurement and

Correlation of Gas Condensate Relative Permeability by the Steady-State Method. Society of Petroleum Engineers. doi:10.2118/30770-PA. 1998.

Huang, Y.F., Huang, G.H., Dong, M.Z. Development of an artificial neural network model for predicting minimum miscibility pressure in CO2 flooding. J. Pet. Sci. Eng. 37, 83– 95. 2003.

Hamada, Yoshinobu, Kenichiro Koga, and Hideki Tanaka. "Phase equilibria and interfacial tension of fluids confined in narrow pores." The Journal of chemical physics 127.8: 084908. 2007.

Honarpour, M. M., Nagarajan, N. R., Orangi, A., Arasteh, F., & Yao, Z. Characterization of Critical Fluid PVT, Rock, and Rock-Fluid Properties - Impact on Reservoir Performance of Liquid Rich Shales. Society of Petroleum Engineers. doi:10.2118/158042-MS. 2012.

Herb.L et. al. Barriers to CO2 Ehanced Oil Recovery(CO2 EOR) in Alberta. Energy and Environment Solutions, Alberta Innovates. 2013.

Islam, Akand W., Tad W. Patzek, and Alexander Y. Sun. "Thermodynamics phase changes of nanopore fluids." Journal of Natural Gas Science and Engineering 25: 134-139. 2015.

Johnson, J. P., & Pollin, J. S. Measurement and Correlation of CO2 Miscibility Pressures. Society of Petroleum Engineers. doi:10.2118/9790-MS. 1981.

Jenkins, M. K. An Analytical Model for Water/Gas Miscible Displacements. Society of Petroleum Engineers. doi:10.2118/12632-MS. 1984.

Johns, R.T. and Orr, J. Miscible Gas Displacement of Multicomponent Oils. SPE Journal, 1(1). doi: 10.2118/30798-PA. 1996.

Jensen, Craig RC, et al. Prediction of multicomponent adsorption equilibrium using a new

model of adsorbed phase nonuniformity. Langmuir 13.5: 1205-1210. 1997.

Jana, Subimal, Jayant K. Singh, and Sang Kyu Kwak. Vapor-liquid critical and interfacial properties of square-well fluids in slit pores." The Journal of chemical physics 130.21: 214707. 2009.

Jin, L., Ma, Y., & Jamili, A. Investigating the Effect of Pore Proximity on Phase Behavior and Fluid Properties in Shale Formations. Society of Petroleum Engineers. doi:10.2118/166192-MS. 2013.

Jin, Z., & Firoozabadi, A. Thermodynamic Modeling of Phase Behavior in Shale Media. Society of Petroleum Engineers. doi:10.2118/176015-PA. 2015.

Klins, M.A.: CO2 Flooding, Basic Mechanisms, and Project Design, Intl. Human Resources Development Corp., Boston. 1984.

Klins M A. Carbon dioxide flooding: Basic mechanisms and project design. International Human Resources Development Corporation. 1984.

Kast, W., and C-R. Hohenthanner. Mass transfer within the gas-phase of porous media. International Journal of Heat and Mass Transfer 43.5: 807-823. 2000.

Karimaie .H, Torsæter .O. Effect of injection rate, initial water saturation and gravity on water injection in slightly water-wet fractured porous media. NTNU. 2007.

Kondiparty, Kirtiprakash, et al. Dynamic Spreading of Nanofluids on Solids. Part I: Experimental. Langmuir, 28.41: 14618-14623. 2012.

Khezrnejad, Ayub, L. A. James, and T. E. Johansen. Water Enhancement Using Nanoparticles

in Water Alternating Gas (WAG) Micromodel Experiments. SPE Annual Technical Conference and Exhibition. Society of Petroleum Engineers. 2014.

Khoshghadam, M., Khanal, A., & Lee, W. J. Numerical Study of Impact of Nano-Pores on Gas-Oil Ratio and Production Mechanisms in Liquid-Rich Shale Oil Reservoirs. Society of Petroleum Engineers. doi:10.15530/urtec-2015-2154191. 2015.

Kleppe Jon. Reservoir Recovery Techniques, Dietz Stability Analysis. Norwegian University of Science and Technology. 2016.

Land, C. S. Comparison of Calculated with Experimental Imbibition Relative Permeability. Society of Petroleum Engineers. doi:10.2118/3360-PA. 1971.

Lee, J.I. Effectiveness of carbon dioxide displacement under miscible and immiscible conditions. Report RR-40, Petroleum Recovery Inst., Calgary. 1979.

Longeron D G. Influence of very low interfacial tensions on relative permeability. Society of Petroleum Engineers Journal, 20(05): 391-401. 1980.

Lake, L. Enhanced Oil Recovery. Saddle River, NJ, Prentice-Hall, Inc. 1989.

Lake, L.W. Enhanced Oil Recovery; Prentice Hall. 1989.

Lansangan, R. M., and J. L. Smith. Viscosity Density and Composition Measurements of CO2/West Texas Oil Systems. Society of Petroleum Engineers. 1993.

Lange, E. A. Correlation and Prediction of Residual Oil Saturation for Gas Injection EOR Processes. Society of Petroleum Engineers. doi:10.2118/35425-PA. 1998.

Li, K., & Horne, R. N. Generalized Scaling Approach for Spontaneous Imbibition: An

Analytical Model. Society of Petroleum Engineers. doi:10.2118/77544-PA. 2006.

Leena Koottungal, Worldwide EOR survey, drilling and production. 2008.

Le, Viet Quoc, Quoc Phuc Nguyen, and Aaron Sanders. A novel foam concept with CO_2 dissolved surfactants. SPE Symposium on Improved Oil Recovery. Society of Petroleum Engineers. 2008.

Loucks, Robert G., et al. Morphology, genesis, and distribution of nanometer-scale pores in siliceous mudstones of the Mississippian Barnett Shale. Journal of Sedimentary Research 79.12: 848-861. 2009.

Lin, Sen-hu et al. Status quo of tight oil exploitation in the United States and its implication. Lithologic Reservoirs 23.4: 25-30. 2011.

Liu, Yangyang, and Jennifer Wilcox. Molecular simulation of CO2 adsorption in micro-and mesoporous carbons with surface heterogeneity. International Journal of Coal Geology 104: 83-95. 2012.

Li, Shidong, Luky Hendraningrat, and Ole Torsaeter. Improved Oil Recovery by Hydrophilic Silica Nanoparticles Suspension: 2 Phase Flow Experimental Studies. International Petroleum Technology Conference. 2013.

Li, W., Dong, Z., Sun, J., & Schechter, D. S. Polymer-Alternating-Gas Simulation:A Case Study. Society of Petroleum Engineers. doi:10.2118/169734-MS. 2014.

Li, B., Mezzatesta, A., Li, Y., Ma, Y., & Jamili, A. A Multilevel Iterative Method To Quantify Effects of Pore-Size-Distribution on Phase Equilibrium of Multicomponent Fluids in

Unconventional Plays. Society of Petrophysicists and Well-Log Analysts. 2015.

Luo, S., Lutkenhaus, J. L., & Nasrabadi, H. Experimental Study of Confinement Effect on Hydrocarbon Phase Behavior in Nano-Scale Porous Media Using Differential Scanning Calorimetry. Society of Petroleum Engineers. doi:10.2118/175095-MS. 2015.

Liu, Bing, et al. Displacement mechanism of oil in shale inorganic nanopores by supercritical carbon dioxide from molecular dynamics simulations. Energy & Fuels. 2016.

Laredo Energy. Hydraulic Fracturing Unlocking America's Natural Gas Resources. 2017.

Metcalfe R. S., Y. L. Discussion. J Petrol Technol.(12), 1436-1437. 1974.

Martin, W.E. The Wizard Lake D-3A Pool Miscible Flood. Presented at the International Petroleum Exhibition and Technical Symposium, Beijing, China, 17-24 March 1982. SPE-10026-MS. http://dx.doi.org/10.2118/10026-MS. 1982.

Monger, T. G., and J. C. Fu. The nature of CO2-induced organic deposition. SPE Annual Technical Conference and Exhibition. Society of Petroleum Engineers. 1987.

Morishige, K., et al. Capillary critical point of argon, nitrogen, oxygen, ethylene, and carbon dioxide in MCM-41. Langmuir 13.13: 3494-3498. 1997.

Mohammed-Singh, Lorna Jennifer, Ashok Kumar Singhal, and Steve Soo-Khoon Sim. Screening Criteria for CO_2 Huff'n'Puff Operations. SPE/DOE Symposium on Improved Oil Recovery. Society of Petroleum Engineers. 2006.

Manrique, E. J., Muci, V. E., & Gurfinkel, M. E. EOR Field Experiences in Carbonate Reservoirs in the United States. Society of Petroleum Engineers. doi:10.2118/100063-MS. 2006.

Mohan, K. Alkaline Surfactant Flooding for Tight Carbonate Reservoirs. Society of Petroleum Engineers. doi:10.2118/129516-STU. 2009.

Manrique, Eduardo, et al. EOR: current status and opportunities. SPE Improved Oil Recovery Symposium. 2010.

Marthe et. al. Investigation of Nanoparticle Effect on Wettability and Interfacial tension. NTNU. 2013.

Ma, Y., Jin, L., & Jamili, A. Modifying van der Waals Equation of State to Consider Influence of Confinement on Phase Behavior. Society of Petroleum Engineers. doi:10.2118/166476-MS. 2013.

Mohanty, Kishore, and Prateek Kathel. EOR in Tight Oil Reservoirs through Wettability Alteration. SPE Annual Technical Conference and Exhibition. 2013.

Matt Wallace, et al. Near-Term Projections of CO2 Utilization for Enhanced Oil Recovery, National Energy Technology Laboratory, US Department of Energy. 2014.

Ma, Y., & Jamili, A. Using Simplified Local Density/ Peng-Robinson Equation of State to Study the Effects of Confinement in Shale Formations on Phase Behavior. Society of Petroleum Engineers. doi:10.2118/168986-MS. 2014.

Ma, Y., & Jamili, A. Modeling the Effects of Porous Media in Dry Gas and Liquid Rich Shale on Phase Behavior. Society of Petroleum Engineers. doi:10.2118/169128-MS. 2014.

Nicol, A. A., and J. O. Medwell. The effect of surface roughness on condensing steam. The Canadian Journal of Chemical Engineering 44.3: 170-173. 1966.

Nelson, Philip H. Pore-throat sizes in sandstones, tight sandstones, and shales. AAPG bulletin 93.3: 329-340. 2009.

Nikolov, Alex, Kirti Kondiparty, and Darsh Wasan. Nanoparticle self-structuring in a nanofluid film spreading on a solid surface. Langmuir 26.11: 7665-7670. 2010.

Nasralla, R. A., Bataweel, M. A., & Nasr-El-Din, H. A. Investigation of Wettability Alteration by Low Salinity Water. Society of Petroleum Engineers. doi:10.2118/146322-MS. 2011.

Nagarajan, N. R., Honarpour, M. M., & Arasteh, F. Critical Role of Rock and Fluid - Impact on Reservoir Performance on Unconventional Shale Reservoirs. Society of Petroleum Engineers. doi:10.1190/URTEC2013-194. 2013.

Nicholas, Holly A., and Per Kent Pedersen. Comparison of porosity and permeability within the Cardium Formation between East Pembina 02-16-049-08W5 and West Pembina 04-32-047-10W5, West-Central AB. 2015.

Owens, W. W., and DLj Archer. The effect of rock wettability on oil-water relative permeability relationships. Journal of Petroleum Technology. 1971.

Orr Jr, F. M., A. D. Yu, and C. L. Lien. Phase behavior of CO_2 and crude oil in low-temperature reservoirs. Society of Petroleum Engineers Journal 21.04: 480-492. 1981.

Orr Jr., F.M., Jensen, C.M. Interpretation of pressurecomposition phase diagrams for CO2/crude–oil systems. SPEJ, 485– 497. 1984.

Perkins, T. K., Johnston, O. C., & Hoffman, R. N. Mechanics of Viscous Fingering in Miscible Systems. Society of Petroleum Engineers. doi:10.2118/1229-PA. 1965.

Pittaway, K. R., Hoover, J. W., & Deckert, L. B. Development and Status of the Maljamar CO_2 Pilot. Society of Petroleum Engineers. doi:10.2118/12600-PA. 1985.

Pitakbunkate, T., Balbuena, P., Moridis, G. J., & Blasingame, T. A. Effect of Confinement on PVT Properties of Hydrocarbons in Shale Reservoirs. Society of Petroleum Engineers. doi:10.2118/170685-MS. 2014.

Pitakbunkate, T., Balbuena, P. B., Moridis, G. J., & Blasingame, T. A. Effect of Confinement on Pressure/Volume/Temperature Properties of Hydrocarbons in Shale Reservoirs. Society of Petroleum Engineers. doi:10.2118/170685-PA. 2015.

Parsa, E., Yin, X., & Ozkan, E. Direct Observation of the Impact of Nanopore Confinement on Petroleum Gas Condensation. Society of Petroleum Engineers. doi:10.2118/175118-MS. 2015.

Qanbari, F., Haghshenas, B., & Clarkson, C. R. Effects of Pore Confinement on Rate-Transient Analysis of Shale Gas Reservoirs. Society of Petroleum Engineers. doi:10.2118/171637-MS. 2014.

Qin, T., Chen, Z., Zhang, K., Han, J., & Wu, K. Redevelopment of the Pembina Cardium Field by CO2-EOR Using Existing Wells. Society of Petroleum Engineers. doi:10.2118/180178-MS. 2016.

Rivas O, Embid S, Bolivar F. Ranking reservoirs for carbon dioxide flooding processes. Society of Petroleum Engineers. 1994.

Raju, K. U., Nasr-El-Din, H. A., Hilab, V. V., Siddiqui, S., & Mehta, S. Injection of Aquifer Water and GOSP Disposal Water into Tight Carbonate Reservoirs. Society of Petroleum Engineers. doi:10.2118/87440-MS. 2004.

Raju, K. U., Nasr-El-Din, H. A., Hilab, V., Siddiqui, S., & Mehta, S. Injection of Aquifer Water and GOSP Disposal Water into Tight Carbonate Reservoirs. Society of Petroleum Engineers. doi:10.2118/87440-PA. 2005.

Rickman R, Mullen M, Petre J, et al. A practical use of shale petrophysics for stimulation design optimization: All shale plays are not clones of the Barnett Shale[C]//SPE Annual Technical Conference and Exhibition. 2008.

Ross, D. J., & Bustin, R. M. The importance of shale composition and pore structure upon gas storage potential of shale gas reservoirs. Marine and Petroleum Geology, 26(6), 916-927. 2009.

Ren, Bo, et al. Laboratory Assessment and Field Pilot of Near Miscible CO_2 Injection for IOR and Storage in a Tight Oil Reservoir of ShengLi Oilfield China. SPE Enhanced Oil Recovery Conference. 2011.

Rotondi, M., Callegaro, C., Masserano, F., & Bartosek, M. Low Salinity Water Injection: eni's Experience. Society of Petroleum Engineers. doi:10.2118/171794-MS. 2014.

Rahmani Didar, B., & Akkutlu, I. Y. Confinement Effects on Hydrocarbon Mixture Phase Behavior in Organic Nanopore. Society of Petroleum Engineers. doi:10.15530/urtec-2015-2151854. 2015.

Sommerfeld, Arnold. Ein beitrag zur hydrodynamischen erklaerung der turbulenten fluessigkeitsbewegungen. Atti del 4: 116-124. 1908.

Shindo, Yuji, et al. Gas diffusion in microporous media in Knudsen's regime. Journal of chemical engineering of Japan 16.2: 120-126. 1983.

Stalkup, F. I. Displacement behavior of the condensing/vaporizing gas drive process. SPE Annual Technical Conference and Exhibition. Society of Petroleum Engineers. 1987.

Shyeh-Yung, J. G. Mechanisms of miscible oil recovery: effects of pressure on miscible and near-miscible displacements of oil by carbon dioxide. SPE Annual Technical Conference and Exhibition. Society of Petroleum Engineers. 1991.

Sohrabi, M., Danesh, A., & Tehrani, D. H. Oil Recovery by Near-Miscible SWAG Injection. Society of Petroleum Engineers. doi:10.2118/94073-MS. 2005.

Singh, Sudhir K., et al. Vapor− liquid phase coexistence, critical properties, and surface tension of confined alkanes. The Journal of Physical Chemistry C 113.17: 7170-7180. 2009.

Singh, Sudhir K., Ashim K. Saha, and Jayant K. Singh. "Molecular Simulation Study of Vapor− Liquid Critical Properties of a Simple Fluid in Attractive Slit Pores: Crossover from 3D to 2D." The Journal of Physical Chemistry B 114.12: 4283-4292. 2010.

Sofos, F., Theodoros E. Karakasidis, and Antonios Liakopoulos. Effect of wall roughness on shear viscosity and diffusion in nanochannels. International Journal of Heat and Mass Transfer 53.19: 3839-3846. 2010.

Singh, Sudhir K., and Jayant K. Singh. Effect of pore morphology on vapor–liquid phase transition and crossover behavior of critical properties from 3D to 2D. Fluid Phase Equilibria 300.1: 182-187. 2011.

Swami, Vivek, Christopher R. Clarkson, and Antonin Settari. Non-Darcy flow in shale nanopores: do we have a final answer?. SPE Canadian Unconventional Resources Conference.

Society of Petroleum Engineers, 2012.

Sanaei, A., Jamili, A., & Callard, J. Effect of Pore Size Distribution and Connectivity on Phase Behavior and Gas Condensate Production From Unconventional Resources. Society of Petroleum Engineers. doi:10.2118/168970-MS. 2014.

Siripatrachai, N., Ertekin, T., & Johns, R. 2016. Compositional Simulation of Discrete Fractures Incorporating the Effect of Capillary Pressure on Phase Behavior. Society of Petroleum Engineers. doi:10.2118/179660-MS.

Steven Jones. Producing Gas-Oil Ratio Behavior of Tight Oil Reservoirs. Unconventional Resources Technology Conference. DOI 10.15530-urtec-2016-2460396. 2016.

Song, Wenhui, et al. Apparent gas permeability in an organic-rich shale reservoir. Fuel 181: 973-984. 2016.

Taber J J, Martin F D. Technical screening guides for the enhanced recovery of oil. Society of Petroleum Engineers. 1983.

Thomas, F. B., et al. Miscible or Near-Miscible Gas Injection Which Is Better?. SPE/DOE Improved Oil Recovery Symposium. Society of Petroleum Engineers. 1994.

Travalloni, L., Castier, M., Tavares, F. W., & Sandler, S. I. Critical behavior of pure confined fluids from an extension of the van der Waals equation of state. The Journal of Supercritical Fluids, 55(2), 455-461. doi: 10.1016/j.supflu.2010.09.008. 2010.

Teklu, T. W., Brown, J. S., Kazemi, H., Graves, R. M., & AlSumaiti, A. M. Residual Oil Saturation Determination - Case Studies in Sandstone and Carbonate Reservoirs. Society of

Petroleum Engineers. doi:10.2118/164825-MS. 2013.

Teklu, Tadesse Weldu, et al. Minimum Miscibility Pressure in Conventional and Unconventional Reservoirs. Unconventional Resources Technology Conference. Society of Petroleum Engineers. 2013.

Teklu, T. W., Alharthy, N., Kazemi, H., Yin, X., & Graves, R. M. Hydrocarbon and Non-hydrocarbon Gas Miscibility with Light Oil in Shale Reservoirs. Society of Petroleum Engineers. doi:10.2118/169123-MS. 2014.

Teklu, Tadesse Weldu, et al. Vanishing interfacial tension algorithm for MMP determination in unconventional reservoirs. SPE Western North American and Rocky Mountain Joint Meeting. Society of Petroleum Engineers. 2014.

Teklu, Tadesse Weldu, et al. Phase behavior and minimum miscibility pressure in nanopores. SPE Reservoir Evaluation & Engineering 17.03: 396-403. 2014.

Tsau, J. S., & Ballard, M. Single Well Pilot Test of Near Miscible CO_2 Injection in a Kansas Arbuckle Reservoir. Society of Petroleum Engineers. doi:10.2118/169084-MS. 2014.

Thomas, A., Kumar, A., Rodrigues, K., Sinclair, R. I., Lackie, C., Galipeault, A., & Blair, M. Understanding Water Flood Response in Tight Oil Formations: A Case Study of the Lower Shaunavon. Society of Petroleum Engineers. doi:10.2118/171671-MS. 2014.

Teklu, T. W., Alameri, W., Kazemi, H., & Graves, R. M. Contact Angle Measurements on Conventional and Unconventional Reservoir Cores. Society of Petroleum Engineers. doi:10.15530/urtec-2015-2153996. 2015.

United, S., & Bartlesville, E. T. C. Contracts and grants for cooperative research on--enhancement of recovery of oil and gas. Enhanced oil and gas recovery and improved drilling technologyMar. 31, 1979, 21-24. 1979.

Vishnyakov, A., et al. Critical properties of Lennard-Jones fluids in narrow slit-shaped pores. Langmuir 17.14: 4451-4458. 2001.

Weinaug, C.F. and Katz, D.L. Surface Tensions of Methane-Propane Mixtures, Ind. & Eng. Chem. 35, 239. 1943.

Whitson, C.H. and Torp, S.B.: Evaluating Constant Volume Depletion Data, *JPT*; *Trans.*, AIME, **275.** 1983.

Whittaker, A. H., Mud logging, in Bradley, H. B., ed., Petroleum Engineering Handbook: Richardson, TX, Society of Petroleum Engineers. 1987.

Wu, R. S., and J. P. Batycky. Evaluation of miscibility from slim tube tests. Journal of Canadian Petroleum Technology 29.06. 1990.

Wang, Y., & Orr, F. M. Calculation of Minimum Miscibility Pressure. Society of Petroleum Engineers. doi:10.2118/39683-MS. 1998.

Wulff-Pérez M. et al. Stability of emulsions for parenteral feeding: Preparation and characterization of o/w nanoemulsions with natural oils and Pluronic f68 as surfactant, Food Hydrocolloids, Volume 23, Issue 4, Pages 1096-1102, ISSN 0268-005X. 2009.

Wang, C, etc. Research of Determining Index Weights Based on Least Squares Method in Post-Evaluation Process. Journal of Jilin University. 2010.

Wang, L., Neeves, K., Yin, X., & Ozkan, E. Experimental Study and Modeling of the Effect of Pore Size Distribution on Hydrocarbon Phase Behavior in Nanopores. Society of Petroleum Engineers. doi:10.2118/170894-MS. 2014.

Wilson, A. Multiscale Simulation of WAG Flooding in Naturally Fractured Reservoirs. Society of Petroleum Engineers. Journal of Petroleum Technology. 2014.

Wang, L., Parsa, E., Gao, Y., Ok, J. T., Neeves, K., Yin, X., & Ozkan, E. Experimental Study and Modeling of the Effect of Nanoconfinement on Hydrocarbon Phase Behavior in Unconventional Reservoirs. Society of Petroleum Engineers. doi:10.2118/169581-MS. 2014.

Wu, K., Li, X., Wang, C., Yu, W., & Chen, Z. Model for surface diffusion of adsorbed gas in nanopores of shale gas reservoirs. Industrial & Engineering Chemistry Research, 54(12), 3225-3236. 2015.

Wu, Keliu, Zhangxin Chen, and Xiangfang Li. Real gas transport through nanopores of varying cross-section type and shape in shale gas reservoirs. Chemical Engineering Journal 281: 813-825. 2015.

Wu, Keliu, et al. A model for multiple transport mechanisms through nanopores of shale gas reservoirs with real gas effect–adsorption-mechanic coupling. International Journal of Heat and Mass Transfer 93: 408-426. 2016.

Xiao, Jirong, and James Wei. Diffusion mechanism of hydrocarbons in zeolites—I. Theory. Chemical Engineering Science 47.5: 1123-1141. 1992.

Xiong, X., Devegowda, D., Civan, F., Sigal, R. F., & Jamili, A. Compositional Modeling of

Liquid-Rich Shales Considering Adsorption, Non-Darcy Flow Effects and Pore Proximity Effects on Phase Behavior. Society of Petroleum Engineers. doi:10.1190/URTEC2013-248. 2013.

Xiong, Y., Winterfield, P. H., Wu, Y.-S., & Huang, Z. Coupled Geomechanics and Pore Confinement Effects for Modeling Unconventional Shale Reservoirs. Society of Petroleum Engineers. doi:10.15530/urtec-2014-1923960. 2014.

Yellig, W. F., & Metcalfe, R. S. Determination and Prediction of CO_2 Minimum Miscibility Pressures (includes associated paper 8876). Society of Petroleum Engineers. doi:10.2118/7477-PA. 1980.

Yuan, H., Johns, R. T., Egwuenu, A. M., & Dindoruk, B. Improved MMP Correlation for CO_2 Floods Using Analytical Theory. Society of Petroleum Engineers. doi:10.2118/89359-PA. 2005.

Yong, C., Wu, O., Bridle, M. K., Xiao, J., & Klotz, E. Reinjecting Produced Water Into Tight Oil Reservoirs. Society of Petroleum Engineers. doi:10.2118/162863-MS. 2012.

Yang, Hua, S. X. Li, and X. Y. Liu. Characteristics and resource prospects of tight oil and shale oil in Ordos Basin. Acta Pet Sin 34.1: 1-6. 2013.

Zick, A. A. A combined condensing/vaporizing mechanism in the displacement of oil by enriched gases. SPE annual technical conference and exhibition. Society of Petroleum Engineers. 1986.

Zhang Ji jun. Fuzzy Analytical Hierarchy Process, Fuzzy Systems and Mathematics. 2000.

Zhao Fu lin. The principle of EOR. Dongying: Petroleum University Press. 2001.

Zarragoicoechea, Guillermo J., and Víctor A. Kuz. van der Waals equation of state for a fluid

in a nanopore. Physical Review E 65.2: 021110. 2002.

Zarragoicoechea, Guillermo J., and Victor A. Kuz. Critical shift of a confined fluid in a nanopore. Fluid phase equilibria 220.1: 7-9. 2004.

Zhang, Xianren, and Wenchuan Wang. Square-well fluids in confined space with discretely attractive wall-fluid potentials: Critical point shift. Physical Review E 74.6: 062601. 2006.

Zekri, A. Y., Almehaideb, R. A., & Shedid, S. A. Displacement Efficiency of Supercritical CO2 Flooding in Tight Carbonate Rocks Under Immiscible Conditions. Society of Petroleum Engineers. doi:10.2118/98911-MS. 2006.

Zhangxin Chen. Reservoir Simulation, University of Calgary. 2007.

Zhang L. et. al. Assessment of CO_2 EOR and its geo- storage potential in mature oil reservoirs, Shengli Oilfield, China, Petroleum Exploration and Development. 2009.

Ziarani, Ali S., and Roberto Aguilera. Knudsen's permeability correction for tight porous media. Transport in porous media 91.1: 239-260. 2012.

Zhang, Kai. Potential technical solutions to recover tight oil: Literature and simulation study of tight oil development. 2014.

Zhang, K., Qin, T., Wu, K., Jing, G., Han, J., Hong, A. Chen, Z. Integrated Method to Screen Tight Oil Reservoirs for CO2 Flooding. Society of Petroleum Engineers. doi:10.2118/175969-MS. 2015.

Zhang, K., Wang, M., Liu, Q., Wu, K., Yu, L., Zhang, J., & Chen, S. Effects of Adsorption and Confinement on Shale Gas Production Behavior. Society of Petroleum Engineers.

doi:10.2118/176296-MS. 2015.

Zhang, K., Li, Y., Hong, A., Wu, K., Jing, G., Torsæter, O. Chen, Z. Nanofluid Alternating Gas for Tight Oil Exploitation. Society of Petroleum Engineers. doi:10.2118/176241-MS. 2015.

Zhang, K., Perdomo, M. E. G., Kong, B., Sebakhy, K. O., Wu, K., Jing, G. Chen, Z. CO2 Near-Miscible Flooding for Tight Oil Exploitation. Society of Petroleum Engineers. doi:10.2118/176826-MS. 2015.

Zhang, K., Sebakhy, K., Wu, K., Jing, G., Chen, N., Chen, Z. Torsæter, O. Future Trends for Tight Oil Exploitation. Society of Petroleum Engineers. doi:10.2118/175699-MS. 2015.

Zhang, K., Dong, X., Li, J., Lv, J., Wu, K., Kusalik, P., & Chen, Z. Effect of Nanoscale Pore Confinement on Multi-Component Phase Equilibrium. Unconventional Resources Technology Conference. doi:10.15530/URTEC-2016-2456191. 2016.

Zhang, K., Liu, Q., Wang, S., Feng, D., Wu, K., Dong, X. Chen, Z. Effects of Nanoscale Pore Confinement on CO2 Displacement. Unconventional Resources Technology Conference. doi:10.15530/URTEC-2016-2454564. 2016.

Zhang, K., Seetahal, S., Hu, Y., Zhao, C., Hu, Y., Wu, K. Alexander, D. A Way to Improve Water Alternating Gas Performance in Tight Oil Reservoirs. Society of Petroleum Engineers. doi:10.2118/180858-MS. 2016.

Zhang, K., Seetahal, S., Alexander, D., He, R., Lv, J., Wu, K. Chen, Z. Correlation for CO2 Minimum Miscibility Pressure in Tight Oil Reservoirs. Society of Petroleum Engineers. doi:10.2118/180857-MS. 2016.

Zhang, K., Seetahal, S., Alexander, D., Lv, J., Hu, Y., Lu, X. Chen, Z. Effect of Confinement on Gas and Oil Relative Permeability During CO2 Flooding in Tight Oil Reservoirs. Society of Petroleum Engineers. doi:10.2118/180856-MS. 2016.

Zhang, K., Kong, B., Zhan, J., He, R., Qin, T., Wu, K. Zhang, J. Effects of Nanoscale Pore Confinement on CO2 Immiscible and Miscible Processes. Society of Petroleum Engineers. doi:10.2118/180256-MS. 2016.

Zhang, K., Liu, Q., Wang, M., Kong, B., Lv, J., Wu, K. Chen, Z. Investigation of CO2 Enhanced Gas Recovery in Shale Plays. Society of Petroleum Engineers. doi:10.2118/180174-MS. 2016.

Appendix A: Phase Behavior

This section shows that the process of the phase equilibrium calculations involves the wellstream composition determination, phase envelop evaluation, phase equilibrium calculations, fluid properties and critical properties shifts in nanopores.

Well Stream Compositions

An oil Pressure/Volume/Temperature study is usually based on an oil sample during production tests and bottom hole sampling is commonly taken in oil reservoirs (Curtis, 2000).

The composition of a recombined reservoir fluid is determined as the follows (Curtis, 2000):

1. Flashing the sample to atmospheric conditions.
2. Measuring the volumes of surface gas, $V_{\bar{g}}$, and surface oil, $V_{\bar{o}}$.
3. Determining the normalized weight fractions, $w_{\bar{g}i}$ and $w_{\bar{o}i}$, of surface samples by gas chromatography.
4. Measuring the surface-oil molecular weight, $M_{\bar{o}}$, and specific gravity, $\gamma_{\bar{o}}$.
5. Converting $w_{\bar{g}i}$ weight fractions to normalized mole fractions y_i and x_i.
6. Recombining mathematically to the wellstream composition, z_i.

$$z_i = F_g y_i + (1 - F_g) x_i \tag{A.1}$$

$$F_g = \frac{1}{1+\left[\frac{188800\left(\frac{\gamma}{M}\right)_{\bar{o}}}{R_s}\right]} \tag{A.2}$$

where $R_s = GOR = {V_{\bar{g}}}/{V_{\bar{o}}}$ in scf/STB from the single-stage flash

$$y_i = \frac{w_{\bar{g}i}/M_i}{\sum_{j \neq C_{7+}}(w_{\bar{g}j}/M_j)+(w_{\bar{g}C_{7+}}/M_{\bar{g}C_{7+}})} \tag{A.3}$$

$$x_i = \frac{w_{\bar{o}i}/M_i}{\sum_{j \neq C_{7+}}(w_{\bar{o}j}/M_j)+(w_{\bar{o}C_{7+}}/M_{\bar{o}C_{7+}})} \quad \text{(A.4)}$$

and

$$M_{\bar{o}C_{7+}} = \frac{w_{\bar{o}C_{7+}}}{\left(\frac{1}{M_{\bar{o}}}\right)-\sum_{j \neq C_7}\left(\frac{w_{\bar{o}j}}{M_j}\right)} \quad \text{(A.5)}$$

Phase Envelop

Once the well stream composition is obtained, the phase envelop can be determined. In the phase envelop evaluation, a convergence pressure is first determined by matching either the bubble point pressure or dew point pressure at the reservoir temperature. Afterwards, the phase envelop can be obtained by driving the sum of the gas or liquid equilibrium phase to be one at different temperature.

Whitson and Torp (Whitson, 1983) suggested a generalized form of the Hoffman *et al* (Hoffmann, 1953) equation in terms of the convergence pressure and acentric factor:

$$\mathrm{K_i} = \left(\frac{\mathrm{p_{ci}}}{\mathrm{p_k}}\right)^{\mathrm{A_1}-1} \frac{\exp[5.37\mathrm{A_1}(1+\omega_\mathrm{i})(1-\mathrm{T_{ri}^{-1}})}{\mathrm{p_{ri}}} \quad \text{(A.6)}$$

where A_1 is a function of pressure with A_1 =1 at p=psc and A_1=0 at $p=p_k$.

$$\mathrm{A_1} = 1 - (\mathrm{p}/\mathrm{p_k})^{\mathrm{A_2}} \quad \text{(A.7)}$$

where A_2 ranges from 0.5 to 0.8

We define the following terms for the bubble point pressure and dew point pressure calculations(Curtis, 2000):

$$\mathrm{hBp} = 1 - \mathrm{sum}(\mathrm{z_i K_i}) \quad \text{(A.8)}$$

$$\mathrm{hDp} = 1 - \mathrm{sum}(\mathrm{z_i}/\mathrm{K_i}) \quad \text{(A.9)}$$

The convergence pressure is calculated by driving the *hBp* term to 0 with changing the convergence pressure; the saturation pressure at different temperatures can be obtained by driving either the hBp term or *hDp* term to 0 with changing the pressure.

In addition, the gas and oil compositions at a specific pressure and temperature can be calculated as follows (Curtis, 2000):

Introduce the quantity c_i

$$c_i = {}^{1}/_{(K_i - 1)} \tag{A.10}$$

where $c_i = \infty$ for $K_i = 1$,

The vapor fraction F_v can be used to determine the compositions of the gas and liquid phases:

$$h(F_v) = \sum_{i=1}^{n} \frac{z_i}{F_v + c_i} = 0 \tag{A.11}$$

$$x_i = \frac{z_i}{F_v(K_i - 1) + 1} \tag{A.12}$$

$$y_i = \frac{z_i K_i}{F_v(K_i - 1) + 1} = K_i x_i \tag{A.13}$$

Phase Equilibrium

The phase stability determines that the CO_2-oil mixture can attain lower energy by splitting into two or more phases. The mixture will be split into two phases if the mixture Gibbs energy, G_{mix}, is less than G_z, where G_{mix} is given by (Curtis, 2000):

$$G_{mix} = \sum_{i=1}^{n} n[F_v y_i + (1 - F_v)x_i]\mu_i \tag{A.14}$$

The normalized Gibbs energy function for overall composition is evaluated as follows (Curtis, 2000):

$$G_z = \sum_{i=1}^{n} z_i ln f_i(z) \tag{A.15}$$

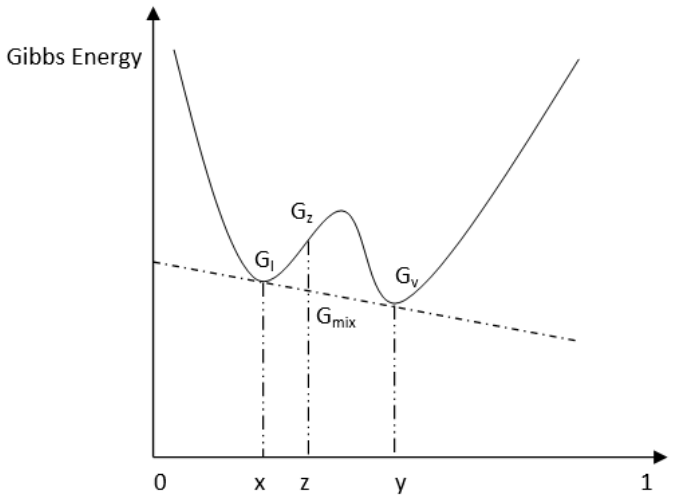

Figure A. 1 Gibbs Energy Surface for a Binary System (Curtis, 2000)

For a binary system, the energy surface G_z represents the curve shown as the solid line in **Figure A.1**. When the overall composition z_i is between the equilibrium compositions y_i and x_i, the mixture is unstable and will be split into the equilibrium composition y_i and x_i with $G_{mix} < G_z$ (Curtis, 2000).

If the mixture in one phase is unstable, it will be split into two phases. The way to determine the gas and liquid phase equilibrium composition is shown as follows (Chen, 2007):

The Peng-Robinson Equation of State is given by:

$$\mathrm{P} = \frac{RT}{v-b} - \frac{a}{v(v+b)+b(v-b)} \tag{A.16}$$

$$\mathrm{A} = \frac{aP}{R^2T^2} \tag{A.17}$$

$$\mathrm{B} = \frac{bP}{RT} \tag{A.18}$$

Introducing the compressibility term:

$$\mathrm{Z} = \frac{PV}{RT} \tag{A.19}$$

the Peng-Robinson Equation of State can be expressed by the following:

$$Z^3 - (1-B)Z^2 + (A - 2B - 3B^2)Z - (AB - B^2 - B^3) = 0 \quad \text{(A.20)}$$

If only one root is availbale, it is selected for the following calculations. Normally the equation has three roots, $Z_1 > Z_2 > Z_3$, the smallest positive root will be selected (Chen, 2007).

The fugacity expression is given by (Curtis, 2000):

$$\ln\frac{f}{P} = ln\emptyset_f = Z - 1 - ln(Z - B) - \frac{A}{2\sqrt{2}B}\ln\left[\frac{Z+(1+\sqrt{2})B}{Z-(1-\sqrt{2})B}\right] \quad \text{(A.21)}$$

Fluid Properties

In the evaluation of the fluid propeoties, the density and viscosity are calculated in the thesis.

The following gives the expressions for the gas and oil density and viscosity evaluations (Curtis, 2000):

$$\rho_g = {}^{PM}/_{ZRT} \quad \text{(A.22)}$$

$$\rho_o = \frac{a\gamma_o + b\gamma_g R_s}{B_o} \quad \text{(A.23)}$$

For the gas viscosity (Curtis, 2000):

$$\mu_g = (\mu_g)_{uncorrected} + \Delta\mu_{N_2} + \Delta\mu_{CO_2} + \Delta\mu_{H_2S} \quad \text{(A.24)}$$

$$(\mu_g)_{uncorrected} = a + (b - c\gamma_g)T - dlog\gamma_g \quad \text{(A.25)}$$

$$\Delta\mu_{N_2} = y_{N_2}(alog\gamma_g + b) \quad \text{(A.26)}$$

$$\Delta\mu_{CO_2} = y_{CO_2}(alog\gamma_g + b) \quad \text{(A.27)}$$

$$\Delta\mu_{H_2S} = y_{H_{2S}}(alog\gamma_g + b) \quad \text{(A.28)}$$

For the oil viscosity, the dead oil or stock tank oil viscosity is given by (Curtis, 2000):

$$\mu_{oD} = \left(a + \frac{b}{\gamma_o^c}\right)\left(\frac{d}{T+e}\right)^A \quad \text{(A.29)}$$

where

$$\mathrm{A} = a^{\left(b+{}^{c}/_{\gamma_o}\right)} \tag{A.30}$$

The bubble point oil viscosity is obtained (Curtis, 2000):

$$\mu_{ob} = A_1 \mu_{oD}^{A_2} \tag{A.31}$$

$$A_{1,2} = a(R_s + b)^c \tag{A.32}$$

The undersaturated oil viscosity is expressed (Curtis, 2000):

$$\frac{\mu_o - \mu_{ob}}{a(P - P_b)} = b\mu_{ob}^c + \mathrm{d}\mu_{ob}^e \tag{A.33}$$

Critical Properties Shifts

The critical shift of a confined fluid in a nanopore is given as follows (Zarragoicoechea, 2004):

For a Lennard-Jones fluid confined in a nanopore, the Helmholtz free energy can be obtained (Zarragoicoechea, 2002):

$$A = f(T) - NkT\ln\left(V_p - Nb\sigma^3\right) + 2\frac{N^2}{V_p}\varepsilon\sigma^3\left(-\frac{a}{2} + \frac{c_1}{\sqrt{A_p}} + \frac{c_2}{A_p}\right) \tag{A.34}$$

From the free energy, the axial pressure is derived:

$$p_{zz}^* = \frac{T^*}{v^* - b} - \frac{a - 2\left(c_1/\sqrt{A_p}\right) - 2(c_2/A_p)}{v^{*2}} \tag{A.35}$$

where the reduced variables are $p_{zz}^* = p_{zz}\,{}^{\sigma^3}/_{\varepsilon}$, $P_{zz} = -\left(1/A_p\right)\left({}^{\partial A}/_{\partial L_z}\right)_{T,Ap}$, $T^* = kT/\varepsilon$, and $v^* = \left({}^{V_p}/_{N}\right)\sigma^3$

The adjusted parameters are used for the correction of the confined equation of state (Zarragoicoechea, 2002):

$$p_{zz}^* = \frac{T^*}{v^* - b_{adj}} - \frac{(a_{adj}/a)\left(a - 2\left(c_1/\sqrt{A_p}\right) - 2(c_2/A_p)\right)}{v^{*2}} \tag{A.36}$$

The critical parameters that characterize the capillary condensation for a confined fluid are as follows (Zarragoicoechea, 2002):

$$T_{cp}^{*} = \frac{8}{27b_{adj}} \frac{a_{adj}}{a} \left(a - 2\frac{c_1}{\sqrt{A_p}} - 2\frac{c_2}{A_p}\right) \tag{A.37}$$

$$p_{cp}^{*} = \frac{(a_{adj}/a)(a - 2\left(c_1/\sqrt{A_p}\right) - 2(c_2/A_p))}{27\mathrm{b}_{adj}^{2}} \tag{A.38}$$

$$v_{cp}^{*} = 3b_{adj}. \tag{A.39}$$

The corresponding bulk critical parameters are shown (Zarragoicoechea, 2002):

$$T_{c}^{*} = \frac{8a_{adj}}{27b_{adj}} \tag{A.40}$$

$$p_{c}^{*} = \frac{a_{adj}}{27\mathrm{b}_{adj}^{2}} \tag{A.41}$$

$$v_{c}^{*} = 3b_{adj}. \tag{A.42}$$

The shift for the critical parameters is obtained (Zarragoicoechea, 2002):

$$\frac{\left(T_c^{*} - T_{cp}^{*}\right)}{T_c^{*}} = 2\frac{c_1}{\sqrt{\pi}a}\frac{\sigma}{r_p} + 2\frac{c_2}{\pi a}\left(\frac{\sigma}{r_p}\right)^2 \tag{A.43}$$

Its numerical expression is shown by the following equation (Zarragoicoechea, 2002):

$$\frac{\left(T_c^{*} - T_{cp}^{*}\right)}{T_c^{*}} = 0.9409\frac{\sigma}{r_p} - 0.2415\left(\frac{\sigma}{r_p}\right)^2 \tag{A.44}$$

Appendix B: Molecular Dynamics

Molecular dynamic simulation is employed in the thesis to investigate the interactions between the molecules and nano-channel surfaces. Furthermore, the movement of the molecules inside a nano-channel is studied.

Different models are created by Software ChemBioOffice, and the system energy optimization and molecules dynamics calculations are performed by the Chem3D. Several models are chosen to display in **Table B.1**.

In the creation of a nanotube, the chains of benzene are connected such that double and single bonds are connected in the alternating order, yielding a nanotube.

In the creation of cubic nano-channel, the construction of the flat cubes begins with the symmetrical planes. The planes are composed of linear carbon chains containing conjugated double bonds (-CH=CH-CH=CH-). The chains are connected such that double and single bonds are connected in the alternating order, yielding a flat plane. Geometrically, all carbons are sp^2 hybridized, such that each C-C and C-H bond is at approximately 120°.

In the creation of a rough nano-channel, linear alkyl chains are connected to form a mesh of cyclohexanes. All carbons are then in tetravalent and sp^3 hybridized. The planes are symmetrical to the vertical axis and horizontal axes, wherein one pair of planes are composed of cyclohexanes in the boat conformation, and the other pair are composed of planes in the chair conformation. As the chair conformation is the most stable of cyclohexane, with C-C-C bonds at 109.5° and free of angle strain, the chair surfaces are stable and maintain structural integrity. On the other hand, the

boat conformation is also free of angle strain, but the eclipsed bonds at the sides of the boat does exert considerable torsional strain, in addition to the steric interactions of hydrogen atoms pointing towards each other both inside and outside the cube.

In the creation of a nano-channel with functional group –OH, oxygen atoms are inserted directly into the surface as ketones and ethers. The oxygen atoms replace carbons already in place. When the oxygen atoms are placed upon the edge of the plane, they replace double-bonded carbons as ketones. As both the carbon and oxygen atoms in the carbonyl double bond are sp^2 hybridized, the bond angles between the molecules are approximately 120° and the bond is therefore parallel to the plane. When the oxygen atoms are placed in the proximal center of the plane, the oxygen atoms replace alkenyl components as ethers, without disrupting the smoothness of the plane. The ether oxygen is, however, sp^3 hybridized.

Table B. 1 Sample Models Description

Model	Formula	Bond Angle (°)	Bound Type	Surface Charge	Polar Surface Area (Å)
Armchair (10, 10)	C200H40	119.6	Single/Double	0	0
Zig-zag (15,0)	C150H30	118.9	Single/Double	0	0
Cubic nano-channel lateral around 1 *nm*	C200H80	119.5	Single/Double	0	0
Cubic nano-channel lateral around 2 *nm*	C716H164	116.3	Single/Double	0	0
Rough nano-channel	C368H414	109.5	Single	0	0
Nano-channel with Functional Group -OH	C355H414O17	109.5	Single	0	343.91
Combined	C2204H1493O24	98.3-120.5	Single/Double	0	485.525

The system is optimized under the molecular mechanics force field MM2, which is mainly for a conformational analysis of hydrocarbons and other small organic molecules. The models approach a steady state after 20000 fs of simulations. The interactions between two atoms separated by a distance greater than a pre-defined distance, the cut-off distance, are ignored. In addition, the cut off radius in the simulations is set to 10 Å.

The MM2 is designed to reproduce the equilibrium covalent geometry of molecules as accurately as possible. The total energy is the sum of the stretching, bending, torsion and the van der Waals forces. **Table B.2** gives the force field MM2 parameters. Moreover, the equations involved in the calculation are as follows:

Energy variation caused by stretching (Allinger, 1977):

$$E_s = 71.94k_s(l - l_0)^2\big(l - 2(l - l_0)\big) \tag{B.1}$$

where length is in Å and k_s is in mdyn/Å.

Energy variation caused by bending (Allinger, 1977):

$$E_\theta = 0.021914k_\theta(\theta - \theta_0)^2(1 + 7 \times 10^{-8}(\theta - \theta_0)^4) \tag{B.2}$$

where θ is in deg and k_θ in mdyn/Å rad^2

Energy variation caused by stretch-bending (Allinger, 1977):

$$E_{s\theta} = 2.51124k_{s\theta}(\theta - \theta_0)((l - l_0)_a + (l - l_0)_b) \tag{B.3}$$

where bonds *a* and *b* are attached with an angle θ

Energy variation caused by torsion (Allinger, 1977):

$$E_{\theta_t} = \frac{V_1}{2}(1 + \cos\theta_t) + \frac{V_2}{2}(1 - \cos 2\theta_t) + \frac{V_3}{2}(1 + \cos 3\theta_t) \tag{B.4}$$

Table B. 2 Force-Field Parameters for MM2 (Allinger, 1977):

Stretching		
Bond	k_s	l_0
C-C	4.4	1.523
C-H	4.6	1.113

Bending			
Angle	k_θ	Θ_0	
C-C-C	0.45	109.5	
C-C-H	0.36	109.4	
H-C-H	0.32	109.4	
Stretch-Bend			
Angle	$k_{s\theta}$		
C-C-C	0.12		
C-C-H	0.09		
H-C-H	0		
Torsion			
Atoms	V_1	V_2	V_3
C-C-C-C	0.2	0.27	0.093
C-C-C-H	0	0	0.267
H-C-C-H	0	0	0.237

Energy variation caused by van der Waal force (Liu, 2016):

$$E_{ij} = 4\varepsilon_{ij}\left[\left(\frac{\sigma_{ij}}{r_{ij}}\right)^{12} - \left(\frac{\sigma_{ij}}{r_{ij}}\right)^{6}\right] \quad \text{(B.5)}$$

The interaction among atoms can be characterized by the Lorentz Berthelot rule (Liu, 2016):

$$\sigma_{ij} = {}^{\sigma_{ii} + \sigma_{jj}}/_{2} \quad \text{(B.6)}$$

$$\varepsilon_{ij} = \left(\varepsilon_{ii}\varepsilon_{jj}\right)^{1/2} \quad \text{(B.7)}$$

The value employed in the interaction can refer to **Table B.3**.

Table B. 3 Reference Parameters for Molecular Interaction (Liu. 2016)

Site	σ (Å)	ε (KJ/mol)
C(CO_2)	2.757	0.234
O(CO_2)	3.033	0.669
Pair Interaction	σ_{ii} (Å)	ε_{ii}/k_B (K)
C-C	3.4	28
CH4-CH4	3.73	148
CH3-CH3	3.775	104.1
k_B the Boltzmann constant 0.0083144621 KJ/(mol·K)		

The total energy E_t involved in this system can be characterized by (Allinger,1977):

$$E_t = E_s + E_\theta + E_{s\theta} + E_{\theta_t} + E_{ij} \quad \text{(B.8)}$$

Appendix C: Reservoir Simulation

In the continuum flow regime, the mean free path is small compared with a pore diameter. In this case, the collision among molecules dominates over the molecule-wall collisions (Kast, 2000). The mass flux of viscous flow can be calculated by the Darcy law.

The mean free path of gas molecules is characterized by the following equation (Song, 2016):

$$\lambda = \sqrt{\frac{\pi z R T}{2 M_w}} \frac{\mu}{P} \tag{C.1}$$

The Knudsen number used to define the gas flow regime can be expressed as follows (Song, 2016):

$$K_n = \frac{\lambda}{r} \tag{C.2}$$

The Reynolds number used to characterize the liquid flow regime is generally defined (Sommerfeld, 1908)

$$Re = \frac{\rho v D}{\mu} \tag{C.3}$$

During primary production, gas will liberate from oil as the pressure depletes from reservoir pressure 3568 *psi* to bubble point pressure 1800 *psi* and less, and the gas molecules flow regime is evaluated by the Knudsen number. The gas Knudsen number is investigated in different porous media as shown in **Figure C.1**. The producer operates in the pressure of 1000 *psi*, and the gas molecules have a maximum Knudsen number of 0.00259 at the pore size of 5 *nm*. Furthermore, the Knudsen number of equilibrium gas can be enlarged by the CO_2 introduced. As shown in **Figure C.2**, during CO_2 flooding, the equilibrium gas molecules have a maximum Knudsen number of 0.00261 at the pore size of 5 *nm*. Darcy's law is applicable for the fluid with Knudsen number of 0.01 and less where the continuum theory is valid and the no-slip boundary is applicable

(Guo, 2015). Darcy's law is applicable in the flowing of the gas phase.

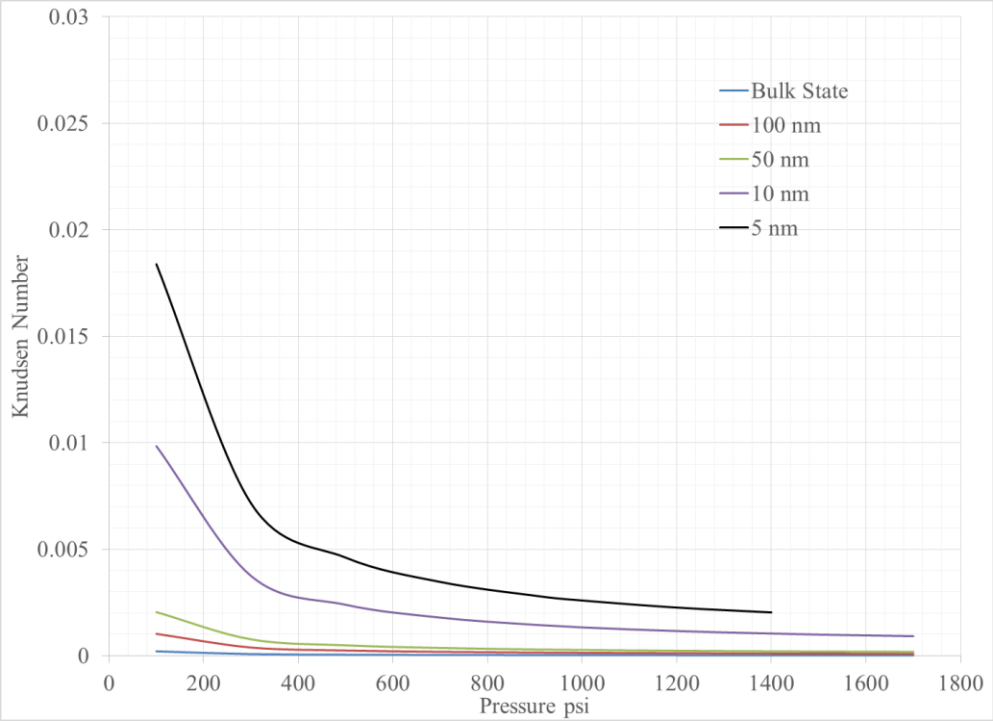

Figure C. 1 Knudsen Number of Reservoir Gas

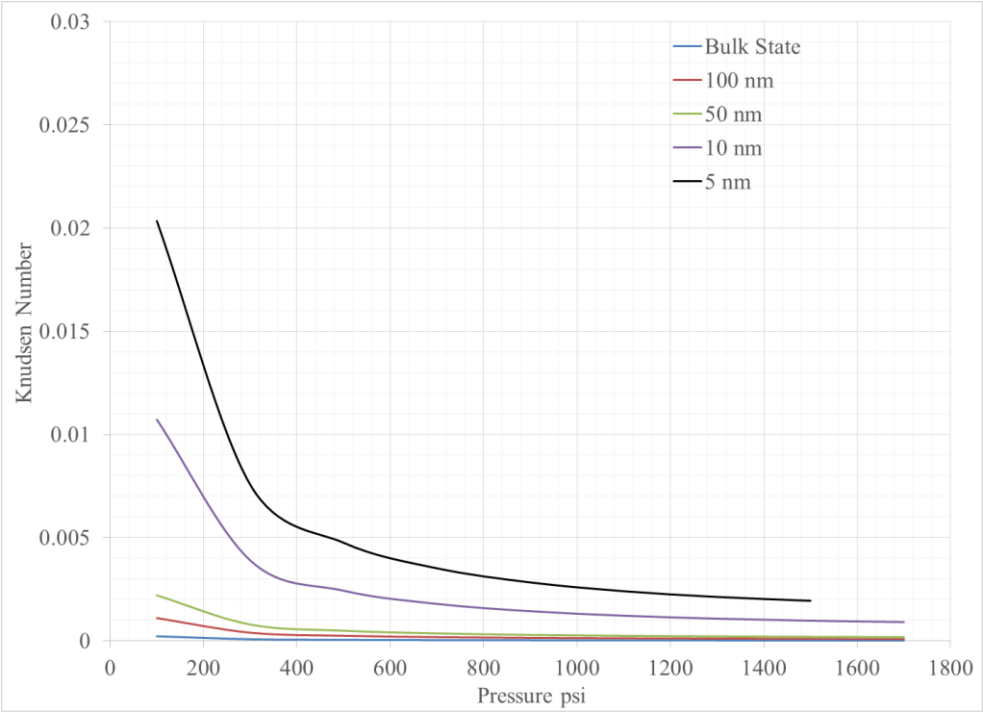

Figure C. 2 Knudsen Number of Equilibrium Gas during CO_2 Flooding

In addition, the Reynolds number of the equilibrium oil is examined to eliminate the effect of the non-Darcy flow. As shown in **Figures C.3** and **C.4**, in the process of the primary recovery, the highest Reynolds number is found to be 3.23 at the pore size of 5 *nm*, and it is 3.66 at the pore size of 5 *nm* during the CO_2 flooding process. Darcy's law is applicable at a Reynolds number of 10 or less (Ziarani, 2012). All of these investigations show that Darcy's law is applicable in the flowing of the oil phase, and the reservoir simulations in the thesis are valid with Darcy's law applied.

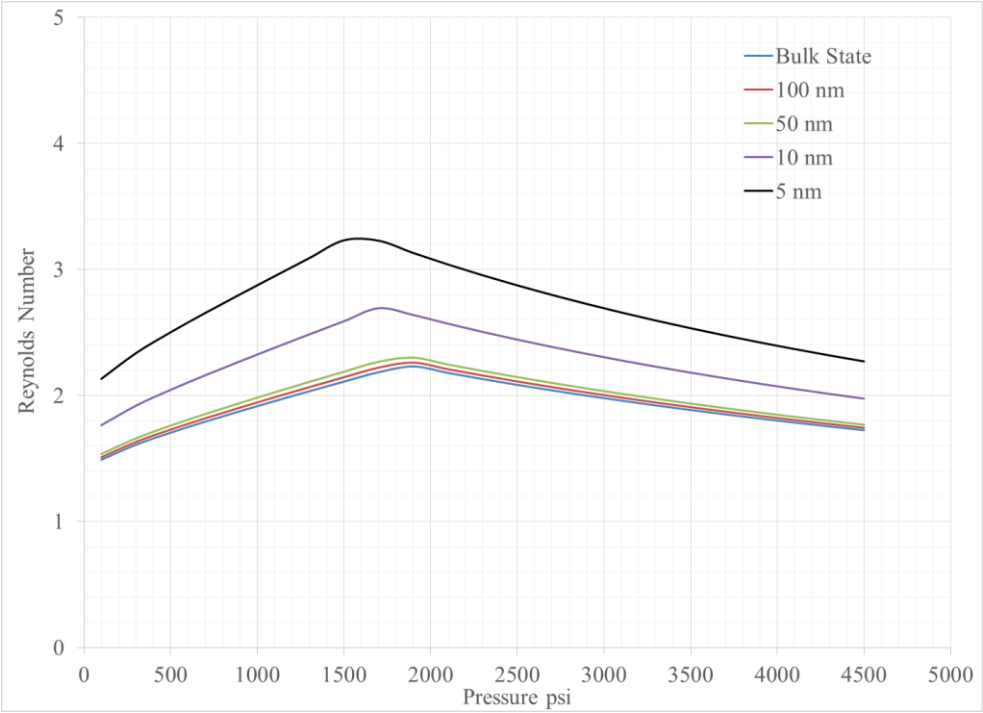

Figure C. 3 Reynolds Number of Reservoir Oil

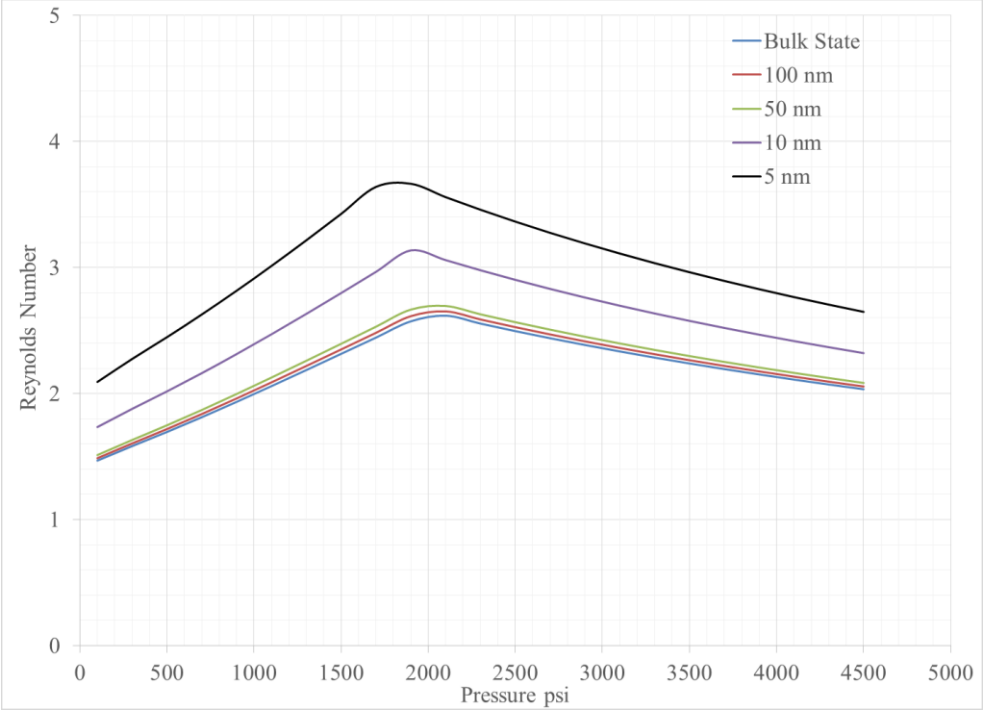

Figure C. 4 Reynolds Number of Equilibrium Oil during CO_2 Flooding

The compositional model in the reservoir simulation is shown as follows (Chen, 2007):

$$\frac{\partial(\emptyset\rho_w S_w)}{\partial t} = -\nabla(\rho_w v_w) + q_w \tag{C.4}$$

$$\frac{\partial\left(\emptyset(y_i\rho_{gi}S_g + x_i\rho_{oi}S_o)\right)}{\partial t} = -\nabla\left(y_i\rho_{gi}v_g + x_i\rho_{oi}v_o\right) + q_i \tag{C.5}$$

$$v_w = -\frac{kk_{rw}}{\mu_w}(\nabla P_w - \rho_w g\nabla z) \tag{C.6}$$

$$v_o = -\frac{kk_{ro}}{\mu_o}(\nabla P_o - \rho_o g\nabla z) \tag{C.7}$$

$$v_g = -\frac{kk_{rg}}{\mu_g}\left(\nabla P_g - \rho_g g\nabla z\right) \tag{C.8}$$

The porous medium is saturated with reservoir fluids at all time of the exploitation

$$S_w + S_o + S_g = 1 \tag{C.9}$$

$$P_{cgo} = P_g - P_o \tag{C.10}$$

$$P_{cow} = P_o - P_w \tag{C.11}$$

$$\sum_{i=C1}^{C7+} x_i = 1 \tag{C.12}$$

$$\sum_{i=C1}^{C7+} y_i = 1 \tag{C.13}$$